Modeling of Thermal Joint Resistance for Sphere-Flat Contacts in a Vacuum

by

Majid Bahrami

A thesis
presented to the University of Waterloo
in fulfillment of the
thesis requirement for the degree of
Doctor of Philosophy
in
Mechanical Engineering

Waterloo, Ontario, Canada, 2004

I hereby declare that I am the sole author of this thesis. This is a true copy of the thesis, including any required final revisions, as accepted by my examiners.

I understand that my thesis may be made electronically available to the public.

Majid Bahrami

Abstract

As a result of manufacturing processes, real surfaces have roughness and surface curvature. The real contact occurs only over microscopic contacts, which are typically only a few percent of the apparent contact area. Because of the surface curvature of contacting bodies, the macrocontact area is formed, the area where microcontacts are distributed randomly. The heat flow must pass through the macrocontact and then microcontacts to transfer from one body to another. This phenomenon leads to a relatively high temperature drop across the interface. Thermal contact resistance (TCR) is a complex interdisciplinary problem, which includes geometrical, mechanical, and thermal analyses. Each part includes a micro and a macro scale sub-problem. Analytical, experimental, and numerical models have been developed to predict TCR since the 1930's. Through comparison with more than 400 experimental data points, it is shown that the existing models are applicable only to the limiting cases and none of them covers the general non-conforming rough contact. The objective of this study is to develop a compact analytical model for predicting TCR for the entire range of non-conforming contacts, i.e., from conforming rough to smooth sphere-flat in a vacuum.

The contact mechanics of the joint must be known prior to solving the thermal problem. A new mechanical model is developed for spherical rough contacts. The deformation modes of the surface asperities and the bulk material of contacting bodies are assumed to be plastic and elastic, respectively. A closed set of governing relationships is derived. An algorithm and a computer code are developed to solve the relationships numerically. Applying Buckingham Pi theorem, the independent non-dimensional parameters that describe the contact problem are specified. A general pressure distribution is proposed that covers the entire spherical rough contacts, including the Hertzian smooth contact. Simple correlations are offered for the general pressure distribution and the radius of the macrocontact area, as functions of the non-dimensional parameters. These correlations are compared with experimental data collected by others and good agreement is observed. Also a criterion is offered to identify the flat surface, where the effect of surface curvature on the contact pressure is negligible.

Thermal contact resistance is considered as the superposition of macro and micro thermal components. The flux tube geometry is chosen as the basic element in the thermal analysis of microcontacts. Simple expressions for determining TCR of non-conforming rough joints are

derived which cover the entire range of TCR by using the general pressure distribution and the flux tube solution. A complete parametric study is performed; it is seen that there is a value of surface roughness that minimizes TCR. The thermal model is verified with more than 600 data points, collected by many researchers during the last 40 years, and good agreement is observed.

A new approach is taken to study the thermal joint resistance. A novel model is developed for predicting the TCR of conforming rough contacts employing scale analysis methods. It is shown that the microcontacts can be modeled as heat sources on a half-space for engineering applications. The scale analysis model is extended to predict TCR over the entire range of non-conforming rough contacts by using the general pressure distribution developed in the mechanical model. It is shown that the surface curvature and contact pressure distribution have no effect on the effective micro thermal resistance. A new non-dimensional parameter is introduced as a criterion to identify the three regions of TCR, i.e., the conforming rough, the smooth spherical, and the transition regions.

An experimental program is designed and data points are collected for spherical rough contacts in a vacuum. The radius of curvature of the tested specimens are relatively large (in the order of m) and can not be seen by the naked eye. However, even at relatively large applied loads the measured joint resistance (the macro thermal component) is still large which shows the importance of surface out-of-flatness/curvature. Collected data are compared with the scale analysis model and excellent agreement is observed. The maximum relative difference between the model and the collected data is 6.8 percent and the relative RMS difference is approximately 4 percent.

Additionally, the proposed scale analysis model is compared/verified with more than 880 TCR data points collected by many researchers. These data cover a wide range of materials, surface characteristics, thermal and mechanical properties, mean joint temperature, directional heat transfer effect, and contact between dissimilar metals. The RMS difference between the model and all data is less than 13.8 percent.

Acknowledgements

I would like to express my sincere appreciation to my supervisors, Dr. M. M. Yovanovich, J. R. Culham, and G. E. Schneider for their guidance, support and encouragement during the course of this investigation. I have learned that the most important part of modeling is to follow the "physics" of the phenomenon and understand the "big picture".

I thank Mr. J. Boldt and B. Whitfield of the Engineering Machine Shop for their care and patience in the fabrication of the test specimens. I would also appreciate the assistance of Mr. P. Gray for measuring the surface curvature of test specimens. My thanks go to Mr. A. Hodgson for his assistance in running the experimental tests.

My thanks go to my friends and colleagues in the Microelectronics Heat Transfer Laboratory, especially Mr. F. Milanez and P. Teertstra for their help and our fruitful discussions.

I would like to thank my parents and my brother their love and support. I also wish to express my appreciation to my wife for her patience and love.

Contents

1 Introduction **1**

1.1 General . . . 1

1.2 Definition of Thermal Contact Resistance . . . 2

1.3 Macro and Micro Thermal Resistances . . . 3

1.4 Problem Statement . . . 4

1.5 Objectives and Overview . . . 6

2 Literature Review **8**

2.1 Introduction . . . 8

2.2 Geometrical Analysis . . . 9

2.2.1 Micro Geometrical Analysis . . . 9

2.2.2 Macro Geometrical Analysis . . . 13

2.2.3 Microhardness . . . 14

2.3 Mechanical Analysis . . . 17

2.3.1 Macrocontact Problem . . . 18

2.3.2 Microcontact Problem . . . 20

2.3.3 Deformation Mode of Asperities . . . 25

2.3.4 Non-Conforming Rough Surface Models . . . 30

2.4 Thermal Analysis . . . 31

2.4.1 Thermal Constriction/Spreading Resistance . . . 32

2.4.2 TCR Models for Conforming Rough Surfaces . . . 35

2.4.3 TCR Models for Non-Conforming Rough Surfaces . . . 36

2.5 Comparison Between TCR Models and Data 40
2.6 Summary and Conclusions 43

3 Mechanical Analysis **46**
3.1 Introduction 46
3.2 Theoretical Background 47
3.2.1 Microcontact Modeling 47
3.2.2 Microhardness 48
3.2.3 Macrocontact Modeling 49
3.3 Present Model 52
3.4 Numerical Results 59
3.5 Approximate Model 60
3.5.1 General Pressure Distribution 64
3.5.2 Compliance 69
3.6 Comparison With Experimental Data 71
3.7 Elastic Compression 74
3.8 Summary and Conclusions 78

4 Thermal Analysis **80**
4.1 Introduction 80
4.2 Theoretical Background 81
4.3 The Present Model 83
4.4 Results 86
4.5 Alternative Approach 90
4.5.1 Macrocontact Boundary Condition 93
4.5.2 Approximate Model For Micro Thermal Resistance 94
4.6 Comparison With Experimental Data 96
4.7 Criterion For Conforming Contacts 100
4.8 Summary and Conclusions 102

5 A Scale Analysis Approach to TCR **104**

5.1 Scope . . . 104

5.2 Introduction . . . 105

5.3 Macro and Micro Thermal Resistances . . . 106

5.4 The Scale Model . . . 108

5.4.1 TCR of the Conforming Rough Limit . . . 109

5.4.2 General Model . . . 117

5.5 Comparison With Experimental Data . . . 119

5.6 Summary and Conclusion . . . 124

6 Experimental Study **126**

6.1 Experimental Apparatus . . . 126

6.2 Preparation of Test Specimens . . . 129

6.3 Assembly and Test Procedure . . . 131

6.4 Test Results . . . 132

6.4.1 Introduction . . . 132

6.4.2 Data Reduction . . . 133

6.5 Experimental Data . . . 134

7 Conclusions and Recommendations **140**

7.1 Conclusions . . . 140

7.2 Recommendations . . . 145

A TCR Data **155**

A.1 Non-Conforming Contacts . . . 157

A.2 Conforming Contacts . . . 171

B Uncertainty Analysis **198**

B.1 Introduction . . . 198

B.2 Differential Error Analysis Method . . . 198

B.3 Thermal Measurements Uncertainty Analysis . . . 199

B.4 Uncertainty in TCR Predictions . . . 200

C Computer Program **203**

C.1 The Code 203

D Radiation Conductance **225**

List of Tables

2.1 Correlations for m, Gaussian surface 10
2.2 Vickers microhardness coefficients, Hegazy 1985 16
2.3 Scale relationships for radius and number of microcontacts, and external force . . 27
2.4 Thermal spreading resistance factor correlations, isothermal contact area 34
2.5 Parameter ranges for experimental data 41
2.6 Physical properties and surface characteristics of comparison base surface 41
2.7 Reseacher and specimen materials 44

3.1 Input parameters for a typical contact 59
3.2 Physical input parameters for spherical rough contacts 64

4.1 Input parameters for a typical contact problem 86
4.2 Range of parameters for the experimental data 96
4.3 Reseacher and specimen materials used in comparisons 97

5.1 Researchers and specimen materials used in comparisons 115
5.2 Range of parameters for experimental data 121

6.1 Surface radius of curvature measurements for spherical samples 130
6.2 Surface measurements for flat sample used in T1 131
6.3 Geometric, mechanical, and thermal properties of tests 133
6.4 Comparison between model and test result T1 135
6.5 Comparison between model and test result T2 136
6.6 Comparison between model and test result T3 137

A.1 Researchers and Specimen materials used in comparisons 156
A.2 Data information, non-conforming rough contacts 158
A.3 Comparison between model and data, Bloom SS17 4PH513 159
A.4 Comparison between model and data, Burde Assembly1 159
A.5 Comparison between model and data, Burde Assembly2 159
A.6 Comparison between model and data, Burde Assembly3 160
A.7 Comparison between model and data, Burde Assembly4 160
A.8 Comparison between model and data, Burde Assembly5 160
A.9 Comparison between model and data, Burde Assembly6 160
A.10 Comparison between model and data, Clausing and Chao 1A 160
A.11 Comparison between model and data, Clausing and Chao 8A 161
A.12 Comparison between model and data, Clausing and Chao 1B 161
A.13 Comparison between model and data, Clausing and Chao 2B 161
A.14 Comparison between model and data, Clausing and Chao 3B 162
A.15 Comparison between model and data, Clausing and Chao 4B 162
A.16 Comparison between model and data, Clausing and Chao 2M 162
A.17 Comparison between model and data, Clausing and Chao 3M 163
A.18 Comparison between model and data, Clausing and Chao 3S 163
A.19 Comparison between model and data, Cassidy and Mark SS303 164
A.20 Comparison between model and data, Fletcher and Gyorog Brass,Test12 Tave52 165
A.21 Comparison between model and data, Fletcher and Gyorog Brass,Test34 Tave-10 165
A.22 Comparison between model and data, Fletcher and Gyorog Brass,Test34 Tave94 165
A.23 Comparison between model and data, Fletcher and Gyorog MgAz31B,Test51 Tave90 165
A.24 Comparison between model and data, Fletcher and Gyorog MgAz31B,Test51 Tave-23 166
A.25 Comparison between model and data, Fletcher and Gyorog SS304,Test34 Tave-33 166
A.26 Comparison between model and data, Fletcher and Gyorog SS304,Test34 Tave89 166
A.27 Comparison between model and data, Fletcher and Gyorog SS304,Test67 Tave160 166
A.28 Comparison between model and data, Fletcher and Gyorog SS304,Test67 Tave73 166

A.29 Comparison between model and data, Fisher 11A, Ni200-CS 167
A.30 Comparison between model and data, Fisher 11B, Ni200-CS 167
A.31 Comparison between model and data, Fisher 13A, Ni200-CS 167
A.32 Comparison between model and data, Gyorog, SS304 168
A.33 Comparison between model and data, Kitscha T1, Steel 1020-CS 168
A.34 Comparison between model and data, Kitscha T2, Steel 1020-CS 168
A.35 Comparison between model and data, McMillan and Mikic P1, SS303 169
A.36 Comparison between model and data, McMillan and Mikic P2, SS303 169
A.37 Comparison between model and data, Mikic and Rohsenow T2, SS305 170
A.38 Comparison between model and data, Smuda and Gyorog, SS304 170
A.39 Data information, conforming rough contacts 172
A.40 Comparison between model and data, Antonetti,P3435, Ni200 173
A.41 Comparison between model and data, Antonetti,P2627, Ni200 173
A.42 Comparison between model and data, Antonetti,P1011, Ni200 173
A.43 Comparison between model and data, Antonetti,P0809, Ni200 174
A.44 Comparison between model and data, Antonetti,P1617, Ni200-Ag 174
A.45 Comparison between model and data, Antonetti,P3233, Ni200-Ag 174
A.46 Comparison between model and data, Hegazy,PNI0102, Ni200 175
A.47 Comparison between model and data, Hegazy,PNI0304, Ni200 176
A.48 Comparison between model and data, Hegazy,PNI0506, Ni200 177
A.49 Comparison between model and data, Hegazy,PNI0708, Ni200 178
A.50 Comparison between model and data, Hegazy,PNI0910, Ni200 179
A.51 Comparison between model and data, Hegazy,PSS0102, SS304 180
A.52 Comparison between model and data, Hegazy,PSS0304, SS304 181
A.53 Comparison between model and data, Hegazy,PSS0506, SS304 182
A.54 Comparison between model and data, Hegazy,PSS0708, SS304 183
A.55 Comparison between model and data, Hegazy,PZ40102, Zircaloy4 184
A.56 Comparison between model and data, Hegazy,PZ40304, Zircaloy4 185
A.57 Comparison between model and data, Hegazy,PZ40506, Zircaloy4 186
A.58 Comparison between model and data, Hegazy,PZ40708, Zircaloy4 187

A.59 Comparison between model and data, Hegazy,PZN0102, Zr2.5Nb 188
A.60 Comparison between model and data, Hegazy,PZN0304, Zr2.5Nb 189
A.61 Comparison between model and data, Hegazy,PZN0506, Zr2.5Nb 190
A.62 Comparison between model and data, Hegazy,PZN0708, Zr2.5Nb 191
A.63 Comparison between model and data, Milanez et al.,T1, SS304 192
A.64 Comparison between model and data, McWaid,T1, SC1SC2 192
A.65 Comparison between model and data, McWaid,T1, SM1SM2 193
A.66 Comparison between model and data, Nho,Al,G-Ni,L 193
A.67 Comparison between model and data, Nho,Al,L-Ni,G 194
A.68 Comparison between model and data, Nho,Al6061T6,G-L 194
A.69 Comparison between model and data, Nho,Al6061T6,L-G 195
A.70 Comparison between model and data, Nho,Ni200,G-Al6061T6,L 195
A.71 Comparison between model and data, Nho,Ni200,L-Al6061T6,G 196
A.72 Comparison between model and data, Nho,Ni200,G-L 196
A.73 Comparison between model and data, Nho,Ni200,L-G 197

B.1 Uncertainty associated with thermal joint resistance measurements, T1 201
B.2 Uncertainty associated with thermal joint resistance measurements, T2 201
B.3 Uncertainty associated with thermal joint resistance measurements, T3 201
B.4 Input parameters uncertainties 201
B.5 Uncertainty associated with thermal joint resistance predictions, T1 202
B.6 Uncertainty associated with thermal joint resistance predictions, T2 202
B.7 Uncertainty associated with thermal joint resistance predictions, T3 202

D.1 Relative importance of radiative conductance as function of joint temperature, upper bound 226

List of Figures

1-1 Non-conforming rough contact in vacuum 2
1-2 Conforming rough, elastoconstriction, and transition regions 4
1-3 Thermal contact resistance modeling flow diagram 5

2-1 Comparison between correlations for m and experimental data 11
2-2 Equivalent contact of conforming rough surfaces 13
2-3 Flow diagram of geometrical modeling 15
2-4 Measured hardness and microhardness, Hegazy 1985 16
2-5 Mechanical problem overview for spherical rough contacts 18
2-6 Greenwood and Williamson 1966 geometrical model 22
2-7 Effect of mean separation on mean size of microcontacts 27
2-8 Effect of mean separation on real contact area 28
2-9 Effect of mean separation on number of microcontacts 28
2-10 Effect of mean separation on external force 29
2-11 Circular heat source on a half-space 33
2-12 Two flux tubes in series 34
2-13 Comparison between thermal spreading resistance correlations, isothermal contact area 35
2-14 Clausing and Chao 1965 geometrical model 37
2-15 Comparison of existing models with data at the elastoconstriction limit 42
2-16 Comparison of existing models with data at the conforming rough limit 43

3-1 Equivalent contact geometry of two spherical rough surfaces 50

3-2 Contact geometry after loading 53
3-3 Discrete point forces and the equivalent pressure distribution on the plastic zone 54
3-4 Numerical algorithm, the main loop 56
3-5 Pressure-displacement iteration procedure, the inner loop 57
3-6 Successive iterative method to estimate $u_{0,new}$ 57
3-7 Pressure distribution 58
3-8 Mean microcontacts radius 59
3-9 Density of microcontacts 60
3-10 Microhardness 61
3-11 Effect of surface roughness on contact pressure distribution 61
3-12 Non-dimensional pressure distribution for spherical rough contacts 62
3-13 Effect of microhardness on non-dimensional maximum contact pressure, $\tau = 5333$ 65
3-14 Effect of microhardness on non-dimensional maximum contact pressure, $\tau = 247$ 66
3-15 Non-dimensional maximum contact pressure 66
3-16 Non-dimensional radius of macrocontact 67
3-17 Comparison between present model and Greenwood and Tripp model, maximum contact pressure 69
3-18 Bulk deformation at center and edge of contact area 71
3-19 Summary of parameter values of experimental data 72
3-20 Comparison between present model and experimental data, contact radius 73
3-21 Comparison between present model and experimental data, compliance 74
3-22 Contact of two finite spherical rough bodies 75
3-23 Elastic foundation, Winkler model 76
3-24 Contact pressure distribution 77

4-1 Thermal resistance network for non-conforming rough contacts in a vacuum . . . 83
4-2 Geometry of contact 84
4-3 Microcontacts distribution in contact area and thermal resistance network for a surface element 85
4-4 Thermal resistance network for surface element 86
4-5 Micro thermal contact resistance 87

4-6 Microcontacts relative radius . . . 88
4-7 Effect of roughness on TCR . . . 89
4-8 Effect of load . . . 89
4-9 Effect of radius of curvature on TCR . . . 90
4-10 Comparison between approximate and full model, conforming rough contacts . . 95
4-11 Comparison of present model with experimental data . . . 98
4-12 Macro thermal resistance . . . 101

5-1 Geometry of spherical rough contact in vacuum, heat source on half-space, and flux tube geometry . . . 106
5-2 Thermal resistance network for conforming rough, transition, and elastoconstriction regions . . . 107
5-3 Proportionalities between microcontact size and surface slope and roughness . . . 109
5-4 Schematic geometry of microcontact . . . 110
5-5 Comparison between half-space and flux tube solutions . . . 112
5-6 Comparison between scale analysis model and data, conforming rough limit . . . 114
5-7 Range of roughness parameter α for experimental data used in comparison . . . 121
5-8 Comparison between general model and non-conforming rough data . . . 122
5-9 Comparison of general model with all data . . . 123

6-1 General view of test apparatus . . . 127
6-2 Schematic view of test column . . . 128
6-3 Comparison between model and test result, T1 . . . 135
6-4 Comparison between model and test result, T2 . . . 136
6-5 Comparison between model and test result, T3 . . . 137
6-6 Comparison between T1-T3 data and present model . . . 139

NOMENCLATURE

A	=	area, m^2
a	=	radius of contact, m
a'_L	=	relative radius of macrocontact, a_L/a_H
a_s	=	radius of microcontacts, m
b	=	flux tube radius, m
B	=	ratio of macrocontact over specimen radius, a_L/b_L
c_0	=	function of τ, $1.8\ \tau^{-0.028}$
c'_0	=	function of τ, $0.31\ \tau^{0.056}$
c_1	=	microhardness coefficients, Pa
c_2	=	microhardness coefficients
CMY	=	Cooper, Mikic, and Yovanovich model
d	=	mean plane separation, GW model
d_v	=	Vickers indentation diagonal, μm
dr	=	increment in radial direction, m
E	=	Young's modulus, Pa
E'	=	equivalent elastic modulus, Pa
F	=	external force, N
F^*	=	relative force error
f_i	=	discrete point forces at microcontacts, N
GW	=	Greenwood and Williamson model
H, H_B	=	bulk hardness, Pa
H'	=	$c_1\left(1.62\sigma'/m\right)^{c_2}$, Pa
H^*	=	$c_1\left(\sigma'/m\right)^{c_2}$, Pa
H_{mic}	=	microhardness, Pa
H_{BGM}	=	geometric mean Brinell hardness, Pa
h	=	thermal contact conductance, W/m^2K
k	=	thermal conductivity, W/mK
k_s	=	harmonic mean thermal conductivity, W/mK
L	=	sampling length, m; conforming rough limit length scale $L = b_L^2/\left(\sigma/m\right)$, m

m	=	effective mean absolute surface slope
m'	=	effective RMS surface slope
n_s	=	number of microcontacts
P	=	pressure, Pa
P_0	=	maximum contact pressure, Pa
P_0'	=	relative maximum contact pressure, $P_0/P_{0,H}$
P^*	=	non-dimensional pressure, $F/\left(\pi b_L^2 H^*\right)$
Q	=	heat flow rate, W
q	=	heat flux, W/m^2
R	=	thermal contact resistance, K/W
R^*	=	non-dimensional thermal resistance
RMS	=	root mean square
R_a	=	arithmetic average surface roughness, μm
R_q	=	RMS surface roughness, μm
r, z	=	cylindrical coordinates
s	=	$0.95/\left(1+0.071c_2\right)$
T	=	temperature, K
TCR	=	Thermal Contact Resistance, K/W
u	=	sphere profile, m
u_0	=	maximum indentation, m
Y	=	mean surface plane separation, m

Greek

α	=	non-dimensional parameter $\equiv \sigma\rho/a_H^2$
β	=	summits radii of curvature, m
γ	=	general pressure distribution exponent
γ_{GW}	=	Greenwood and Williamson plasticity index
γ_{Mikic}	=	Mikic plasticity index
δ	=	surface max out-of-flatness, m
ε	=	flux tube relative radius $\equiv a/b$

η	=	microcontact density
Θ	=	non-dimensional parameter $\equiv R_L/R_s$
θ	=	angle of the surface asperities, rad
κ	=	H_B/H_{BGM}
λ	=	non-dimensional separation $\equiv Y/\sqrt{2}\sigma$
ν	=	Poisson's ratio
ρ	=	radius of curvature, m
σ	=	RMS surface roughness, μm
σ'	=	σ/σ_0, $\sigma_0 = 1$ μm reference value
τ	=	non-dimensional parameter $\equiv \rho/a_H$
ϕ	=	normal probability function
ψ	=	dimensionless spreading resistance
Ω	=	non-dimensional parameter
ω	=	normal deformation, m
ξ	=	non-dimensional radial position,$\equiv r/a_{:L}$
ξ_{hardness}	=	empirical correction factor, $= 0.3$

Subscripts

0	=	value at origin
$1, 2$	=	surface 1,2
a	=	apparent
b	=	bulk
c	=	conduction, contact, critical
e	=	effective
EC	=	elastoconstriction
g	=	gap
GW	=	Greenwood and Williamson
H	=	Hertz
j	=	joint
L	=	large (macro scale)

m	=	mean
mac	=	macro
mic	=	micro
p	=	plastic deformation
r	=	real
s	=	small
v	=	Vickers

Chapter 1

Introduction

1.1 General

Heat transfer through interfaces formed by the mechanical contact of two non-conforming rough solids is an important phenomenon in a wide range of applications: microelectronics cooling, cryogenic insulations, heat exchangers, spacecraft structures, satellite bolted joints, and ball bearings. Real surfaces have roughness and surface curvature/out-of-flatness simultaneously. Because of surface roughness, contact between two surfaces occurs only over microscopic contact spots which are located in the "contact plane". The real area of contact, i.e., the total area of microcontacts, is a small fraction of the nominal contact area, typically a few percent [1, 2]. As illustrated in Fig. 1-1, the macrocontact area, the area where microcontacts are distributed, is formed as a result of surface curvature of contacting bodies. Heat flow is constricted to pass through the macrocontact and then microcontacts. This phenomenon is indirectly observed through a relatively high temperature drop across the interface. Here an example is given to show the magnitude and relative importance of thermal contact resistance (TCR) versus the "bulk resistance". Consider two 3×10^{-4} m^2 flat SS plates with a thickness of 5 mm and surface roughness of 1 μm. The TCR for the bare joint in a vacuum under 0.1 MPa contact pressure, is in the order of 30 K/W as compared to the plate bulk resistance of 0.2 K/W.

Thermal energy can be transferred between contacting bodies by three different modes, i) conduction at the microcontacts, ii) conduction through the interstitial fluid in the gap between the contacting solids, and iii) thermal radiation across the gap. The radiation heat transfer

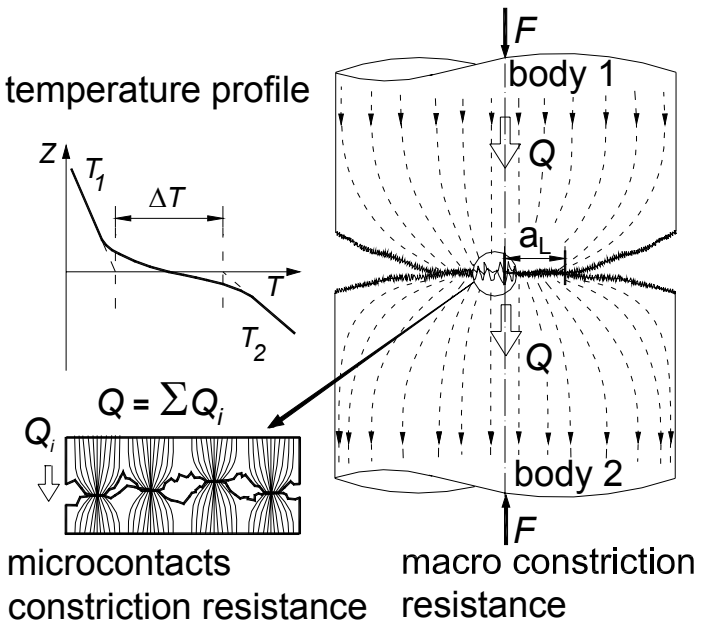

Figure 1-1: Non-conforming rough contact in vacuum

remains small, less than two percent of the conduction through the microcontacts, in the range of interest, i.e., $T_c \leq 100\ ^\circ C$. Therefore it can be neglected for most engineering applications, see Appendix D. Since in this study the interstitial fluid is assumed to be absent, the only remaining heat transfer mode is conduction at the microcontacts.

1.2 Definition of Thermal Contact Resistance

The thermal resistance caused by the interface is called the thermal joint resistance, R_j, and is defined as follows [3]:

$$R_j = \Delta T / Q \tag{1.1}$$

where Q is the steady-state heat flow normal to the interface. The joint temperatures are obtained by extrapolating the steady-state temperature profiles of the contacting bodies to the interface and the temperature drop ΔT is the difference between two joint temperatures.

The thermal joint conductance, h_j, is defined in the manner of the film coefficient in con-

vective heat transfer, i.e.,

$$h_j = Q/\left(\Delta T A_a\right) \tag{1.2}$$

where A_a is the apparent contact area.

1.3 Macro and Micro Thermal Resistances

As illustrated in Fig. 1-1, when the heat flow Q is transferred from a heat source at T_1 to a heat sink at T_2, it experiences a macro thermal constriction $R_{\mathrm{L},1}$ and spreading $R_{\mathrm{L},2}$ resistances as a result of the macrocontact area. Heat is then passed through n_s (parallel) microcontacts in the contact plane, which is called the effective microcontact resistance, R_s. Therefore, TCR of a non-conforming rough joint in a vacuum can be written as

$$R_j = R_L + R_s \tag{1.3}$$

where $R_{\mathrm{L}} = R_{\mathrm{L},1} + R_{\mathrm{L},2}$ and $R_{\mathrm{s}} = R_{\mathrm{s},1} + R_{\mathrm{s},2}$.

Equation (1.3) is a general expression and applicable to all spherical rough contacts. Many researchers including Clausing and Chao [4], Nishino et al. [5], and Lambert and Fletcher [6] used this relationship. A proof of Eq. (1.3) is given in Chapter 5.

Two limiting cases can be distinguished for Eq. (1.3), i) the conforming rough limit, i.e., contact of flat rough surfaces where the surface curvatures are very large thus macro thermal resistance R_L is negligible and micro thermal resistance R_s is the controlling component, ii) the elastoconstriction limit where the radii of curvature of contacting bodies are relatively small and surfaces are smooth, thus the macro thermal resistance R_L is predominant and R_s is negligible, and iii) transition region or general contact in which both R_L and R_s exist and have the same order of magnitude. Figure 1-2 shows the above-mentioned regions and their corresponding thermal resistance. Later in Chapter 5, a non-dimensional parameter will be introduced and a criterion will be proposed to specify these limits.

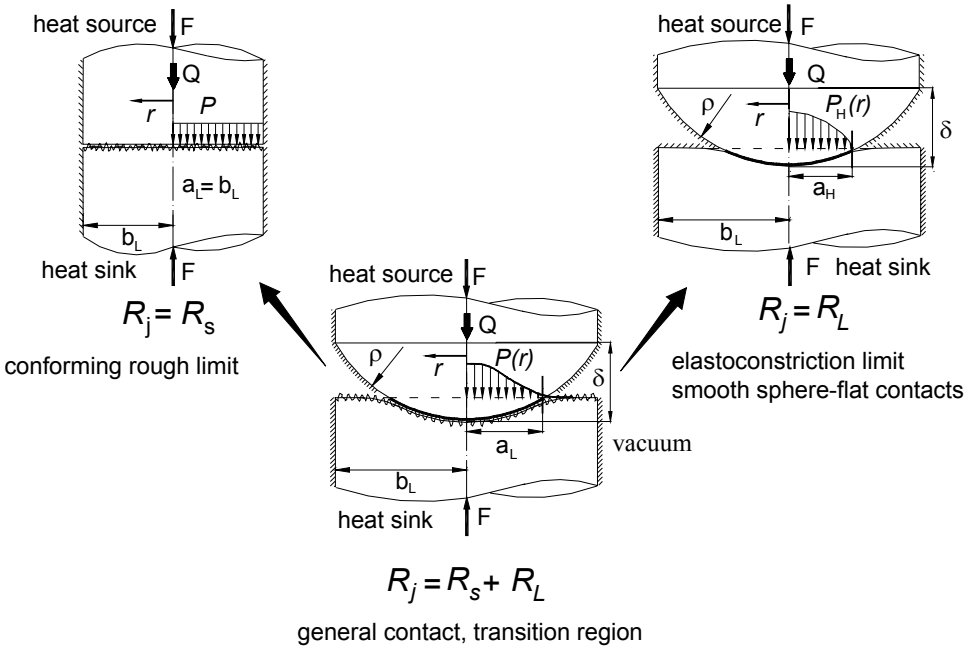

Figure 1-2: Conforming rough, elastoconstriction, and transition regions

1.4 Problem Statement

Thermal contact resistance consists of three different parts: geometrical, mechanical, and thermal. Each problem includes a macro and a micro sub-problem. Figure 1-3 illustrates the TCR analysis and its components. The heart of a TCR analysis is its mechanical part. To solve the mechanical problem, the geometry of the contacting surfaces (macro and micro) must be quantitatively described. The mechanical problem also includes two parts: macro or large-scale contact and micro or small-scale contact. The macroscale mechanical analysis determines the macrocontact radius, a_L, and the pressure distribution; the microscale analysis predicts separation between the mean contacting planes, size and number of microcontacts, and the relative size of microcontacts. The macro and the micro mechanical problems are strongly coupled. The thermal analysis, based on the results of the mechanical analysis, is then used to calculate the microscopic and macroscopic thermal resistances.

The geometrical and mechanical analyses of the TCR can be affected as a result of heat transfer and temperature changes in the vicinity of the contact area. For instance, thermal

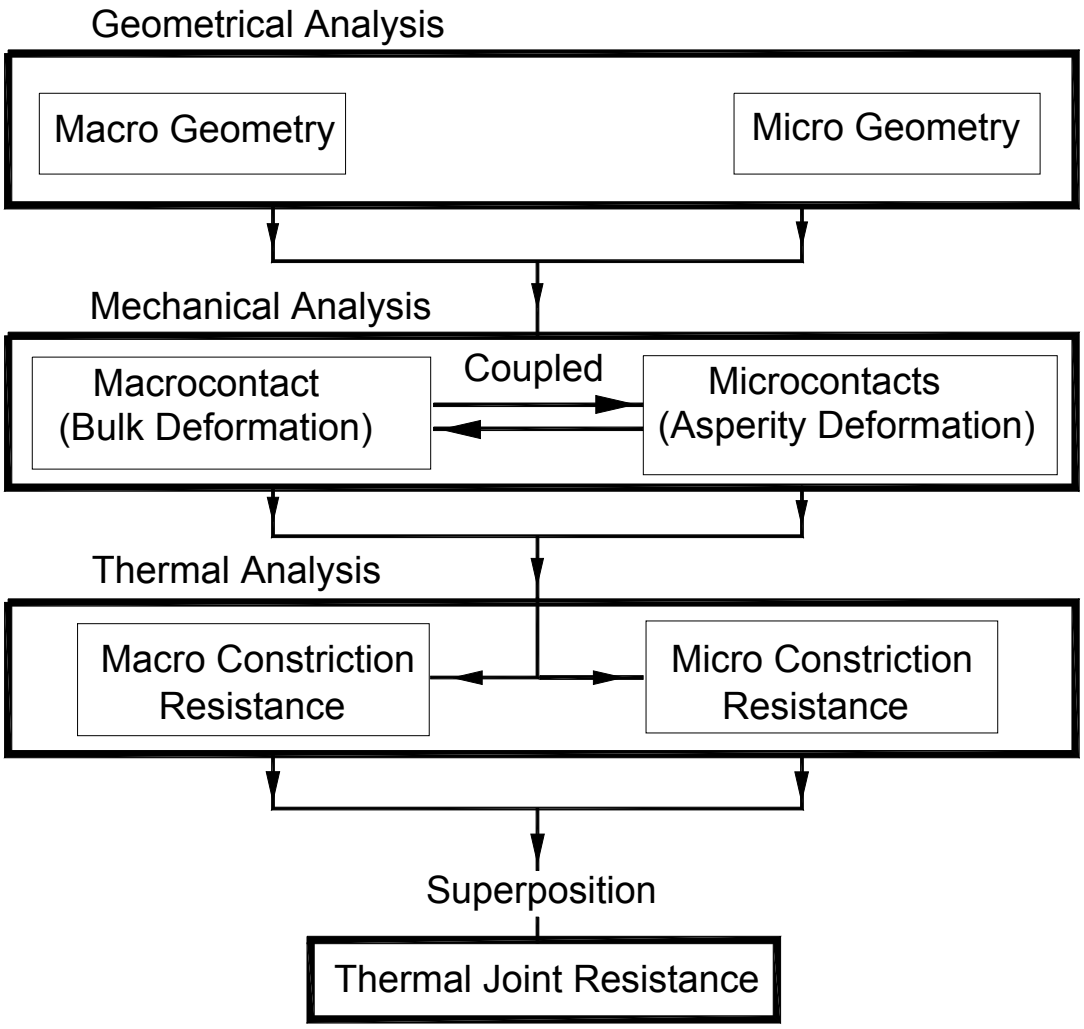

Figure 1-3: Thermal contact resistance modeling flow diagram

stresses and thermal expansions can lead to changes in surface characteristics and the stress field which in turn can affect the geometrical and mechanical analyses, respectively. However, in this study, these influences are assumed to have secondary order effects, and thus are neglected. As a result of this simplification, the three components of the thermal contact resistance problem can be decoupled as shown in Fig. 1-3.

1.5 Objectives and Overview

Existing theoretical geometrical, mechanical, and thermal models are reviewed in Chapter 2. Through comparison with more than 400 experimental data points, collected by many researchers during the last forty years, it can be shown that the existing TCR models are applicable only to the limiting cases namely, conforming rough contacts and smooth sphere-flat (elastoconstriction) contacts and do not cover the entire range of TCR. Therefore, the need for a theoretical model that can predict TCR over the entire range of contacts still exists.

The objective of this study is to develop compact analytical model(s) for predicting TCR for the entire range of non-conforming joints, i.e., from conforming rough to smooth sphere-flat (elastoconstriction) contact. Another purpose of this research is to find a criterion to define a "flat surface" where the effect of surface curvature on TCR is negligible.

In Chapter 3, a new analytical contact mechanics model is developed, which enables the prediction of contact parameters such as pressure distribution, mean size and number of microcontacts, and radius of the macrocontact area. A general pressure distribution is developed which covers the entire range of spherical contacts from the smooth Hertzian to the conforming rough contacts. Compact correlations are developed for determining the radius of the macrocontact area, the maximum contact pressure, and the compliance by using the Buckingham Pi theorem and curve-fitting techniques. These expressions are used in the thermal joint analyses in Chapters 4 and 5. The compliance and the contact radius predicted by the model are compared against more than 220 experimental data points collected by others and showed good agreement.

In Chapter 4, the results of the mechanical model are used to develop an analytical thermal model for determining TCR of non-conforming rough contacts in a vacuum. The thermal model

is constructed on the premise that the mean separation between the contacting surfaces in an infinitesimal surface element can be assumed constant. Therefore, the conforming rough model of Cooper et al. [7] can be implemented to calculate the surface element thermal resistance. The macrocontact resistance is calculated using the flux tube solution. Additionally, simple correlations for determining TCR are derived using the general pressure distribution introduced in Chapter 3 and the Yovanovich [8] correlation for thermal conductance of conforming rough contacts. These correlations cover the entire range of TCR from conforming rough to smooth spherical contacts.

In Chapter 5, a novel approach is taken by employing scale analysis methods to develop an analytical TCR model for conforming rough contacts. Instead of using probability relationships to calculate size and number of microcontacts, scale relationships are derived based on physical observations. The scale relationship shows the trend of the experimental data. The constant of the scale relationship is found through comparison with the data.

To verify the proposed thermal model, an experimental program was conducted to obtain data for non-conforming rough contacts in a vacuum. The contact assembly included a bead-blasted flat specimen placed in contact with a smooth polished spherical sample in series with an ARMCO iron flux meter in a vacuum chamber. The collected data show excellent agreement with the model (maximum relative difference less than 6.8%).

In addition, both thermal models, developed in Chapters 4 and 5 are compared and verified with more than 880 TCR data points collected by many researchers during the past 40 years. The data cover a wide range of surface characteristics, thermal and mechanical properties, mean contact temperature, directional heat transfer, and contact between dissimilar metals.

Chapter 2

Literature Review

2.1 Introduction

Analytical, experimental, and numerical models have been developed to predict TCR since the 1930's. Several hundred papers on thermal contact resistance have been published which illustrates the importance of this topic, and also indicates that the development of a general predictive model is difficult.

In this Chapter, the TCR problem is divided into three different problems: geometrical, mechanical, and thermal. Each problem includes a macro and micro scale sub-problem; existing theories and models for each part are reviewed. Empirical correlations for microhardness, and the equivalent (sum) rough surface approximation are discussed. Suggested correlations for estimating the mean absolute surface slope are summarized and compared with experimental data.

The classical conforming rough contact models, i.e., elastic and plastic, as well as elasto-plastic models are reviewed. A set of dimensionless relationships are derived for the contact parameters, i.e., the mean microcontact size, number of microcontacts, the real contact area, and the external load as functions of the dimensionless separation λ, for the above models. These scale relationships are plotted; it is graphically shown that the trends of these models, in terms of the contact parameters, are similar.

The most common assumptions of existing thermal models are summarized. As basic elements of thermal analysis, spreading resistance of a circular heat source on a half-space and

flux tube are reviewed, also existing flux tube correlations are compared.

More than 400 TCR data points collected by different researchers during last forty years are grouped into two limiting cases: conforming rough, and elastoconstriction. Existing TCR models are reviewed and compared with the experimental data at these two limits. It is shown that the existing theoretical models are limited to a certain range and do not cover both of the above-mentioned limiting cases.

2.2 Geometrical Analysis

It is necessary to consider the effect of both surface roughness and surface curvature/out-of-flatness on the contact of non-conforming rough surfaces. Therefore, the geometrical analysis is divided into micro and macro components.

2.2.1 Micro Geometrical Analysis

All solid surfaces are rough, and this roughness or surface texture can be thought of as the surface deviation from the nominal topography. Surface textures can be created using many different processes. Most man-made surfaces, such as those produced by grinding or machining have a pronounced "lay". Generally, the term "Gaussian surface" is used to refer to a surface where its asperities are isotropic and randomly distributed over the surface. It is not easy to produce a wholly isotropic roughness. The usual procedure for experimental purposes is to air-blast a metal surface with a cloud of fine particles, in the manner of shot peening, which gives rise to a random rough surface.

According to Liu, et al. [9] five types of instruments are currently available for measuring the surface topography: stylus-type surface profilometer, optical (white-light interference) measurements, Scanning Electron Microscope (SEM), Atomic Force Microscope (AFM), and Scanning Tunneling Microscope (STM). Among these, the first two instruments are usually used for macro-to-macro asperity measurements, whereas the others may be used for micro or nanometric measurements. Surface texture is most commonly measured by a profilometer, which draws a stylus over a sample length of the surface. A datum or centerline is established by finding the straight line, or circular arc in the case of round components, from which the mean

Table 2.1: Correlations for m, Gaussian surface

Reference	Correlation
Tanner and Fahoum [11]	$m = 0.152\ \sigma^{0.4}$
Antonetti et al. [12]	$m = 0.124\ \sigma^{0.743}, \quad \sigma \leq 1.6\,(\mu m)$
Lambert and Fletcher [6]	$m = 0.076\ \sigma^{0.52}$

square deviation is a minimum. The arithmetic average of the absolute values of the measured profile height deviations, R_a, taken within a sampling length from the graphical centerline [10]. The value of R_a is

$$R_a = \frac{1}{L}\int_0^L |z\,(x)|\,dx \tag{2.1}$$

where, L is the sampling length in the x direction and z is the measured value of the surface height along this length. When the surface is Gaussian, the standard deviation σ is identical to the RMS value, R_q.

$$\sigma = R_q = \sqrt{\frac{1}{L}\int_0^L z^2\,(x)\,dx} \tag{2.2}$$

For a Gaussian surface, Ling [13] showed that the average and the RMS heights are related as follows:

$$R_q \approx \sqrt{\frac{\pi}{2}} R_a \approx 1.25 R_a \tag{2.3}$$

Similarly, the absolute average and RMS asperity slopes, m and m' respectively, can be determined across the sampling length from the following:

$$m = \frac{1}{L}\int_0^L \left|\frac{dz\,(x)}{dx}\right| dx,\ m' = \sqrt{\frac{1}{L}\int_0^L \left(\frac{dz\,(x)}{dx}\right)^2 dx} \tag{2.4}$$

Mikic and Rohsenow [14] showed that for Gaussian surfaces the relationship between the average and RMS values of the asperity slopes is $m' \approx 1.25m$.

Tanner and Fahoum [11] and Antonetti et al. [12], using published experimental surface data, suggested empirical correlations to relate RMS asperity slope, m', to average roughness, R_a. Lambert and Fletcher [6], also using the same method, correlated the absolute average asperity slopes, m, as a function of RMS roughness in micrometers; correlations for m are summarized in Table 2.1. Figure 2-1 illustrates the comparison between these correlations and experimental data. As shown in Fig. 2-1, the uncertainty of the above correlations is high, and

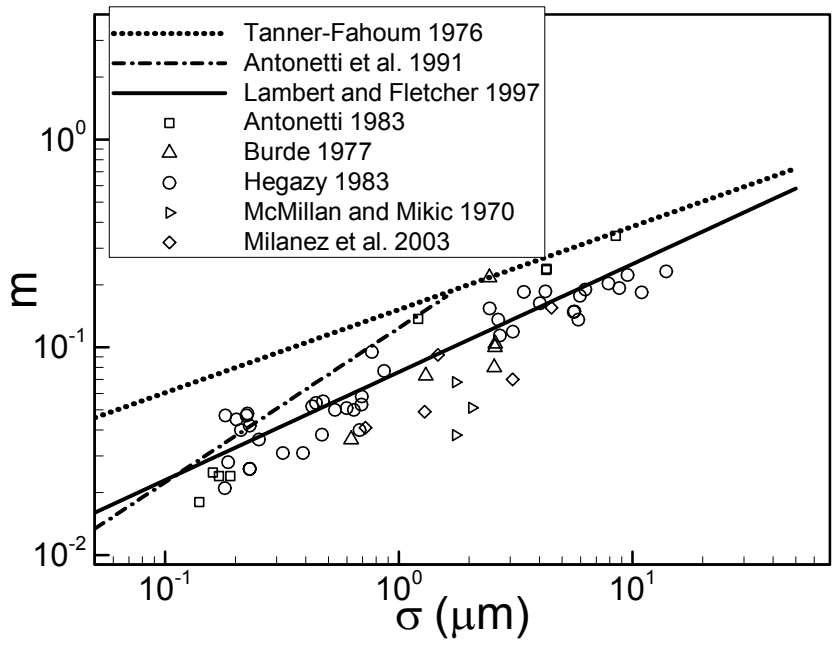

Figure 2-1: Comparison between correlations for m and experimental data

use of these correlations are justifiable only where the surface slope is not reported and/or a rough estimation of m is needed.

Equivalent (Sum) Rough Surface

According to the examination of the microgeometry with equivalent magnitude in the vertical direction and in the traversing direction, asperities seem to have curved shapes at their tops [15]. A common way to model the surface roughness is to represent surface asperities by simple geometrical shapes with a probability distribution for the different asperity parameters involved. One of the first presentations to use this asperity-based model is found in Coulomb's work in 1782. To explain the laws of friction, he assumed that the asperities possessed a spherical shape, all of which had the same radius and the same summit altitude. Greenwood and Williamson [1] assumed that each asperity summit had a hemi-spherical shape whose height above a reference plane had a normal (Gaussian) probability density function. Williamson et al. [16] have shown experimentally that many of the techniques used to produce engineering surfaces give a Gaussian distribution of surface heights.

The solution of any contact mechanics problem requires that the geometry of the intersection and overlap of the two undeformed surfaces be known as a function of their relative position. Greenwood [17] stated that; "*a genuine treatment of two rough surfaces is complicated by the difficulty of describing the unit event, the formation of a single contact spot. For example, if both surfaces are covered by spheres, it is necessary to study the contact of one sphere on the shoulder of another, and then evaluate the probabilities of different degrees of misalignment, in order to get the average unit event. A non-genuine treatment is comparatively simple: both surfaces are taken to be rough with normal distributions. The statistical treatment now concerns the probability of the sum of two heights (which is also normally distributed) exceeding the separation, and this is exactly equivalent to a distribution of a single variable.*" Following the non-genuine approach, one can simplify the contact between Gaussian rough surfaces by the contact between a single Gaussian surface, having the effective (sum) surface characteristics, placed in contact with a perfectly smooth flat surface. Also, since the slope, m, of a profile is proportional to the difference between adjacent equispaced ordinates; m is Gaussian if the profile is Gaussian [18]. This simplification was used by many researchers, such as Clausing and Chao [4], Cooper et al. [7], Francis [19], Johnson [20], and Persson [21]. The equivalent roughness and surface slope can be calculated from

$$\sigma = \sqrt{\sigma_1^2 + \sigma_2^2} \quad \text{and} \quad m = \sqrt{m_1^2 + m_2^2} \tag{2.5}$$

According to Francis [19], a contact model based on the sum (equivalent) surface, circumvents the problem of misalignment of contacting peaks; in addition, the sum surface sees peak to valley and peak to saddle contacts. The sum surface of two Gaussian surfaces is itself Gaussian and if parent surfaces are not exactly Gaussian, the sum (equivalent) surface will be closer to Gaussian than the parent surfaces. Additionally, the sum surface will be in general less anisotropic than the two contacting surfaces, thus the Gaussian sum surface is a reasonable basis for a general contact model [19]. Figure 2-2 shows a normal section through the contact in which the surfaces are imagined to overlap without deforming, and the equivalent rough or sum surface of the contact in the same normal section. The overlap geometry as a function of the mean separation, Y, of the undeformed surfaces is thus given directly and exactly by

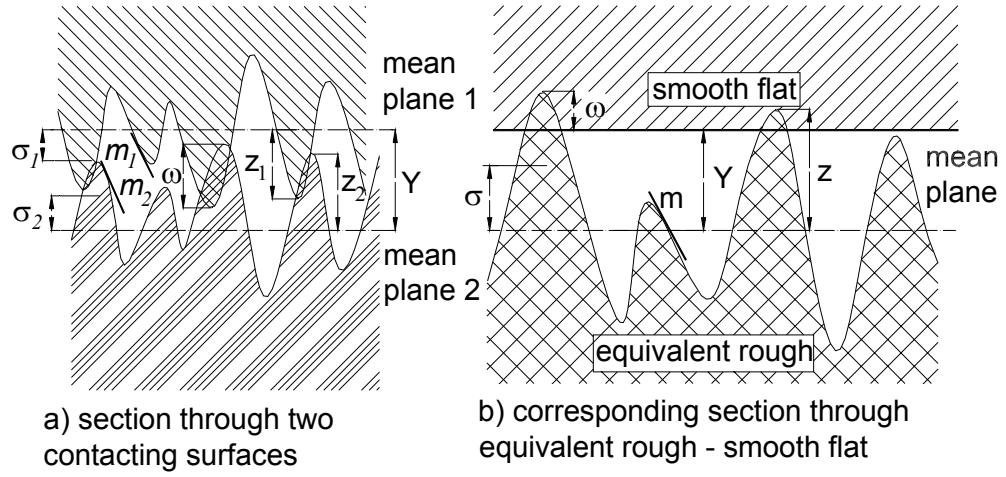

Figure 2-2: Equivalent contact of conforming rough surfaces

the shape of the equivalent rough surface. The number of microcontacts formed is simply the number of equivalent surface peaks that have $Z \geq Y$.

2.2.2 Macro Geometrical Analysis

Many studies on thermal contact resistance assume an ideally uniform distribution of micro contact spots, i.e., conforming rough surface models. Such approaches are successful when the macroscopic nonuniformity of the contact is negligible. However, no real engineering surfaces are perfectly flat, thus the influence of macroscopic nonuniformity can never be ignored. Considering the waviness or out-of-flatness of contacting surfaces in a comprehensive manner is very complex because of the random nature of the waviness. Certain simplifications must be introduced to describe the macroscopic topography of surfaces by a few parameters. A sphere is the simplest example of a macroscopically homogenous surface. Specifically, its profile is described only by its radius. Theoretical approaches by Clausing and Chao [4], Mikic and Rohsenow [14], Yovanovich [22], Nishino et al. [5], and Lambert and Fletcher [6] assume that a spherical profile may approximate the shape of the macroscopic nonuniformity. According to Lambert [23] this assumption is justifiable, because nominally flat engineering surfaces are often spherical, or crowned (convex) with a monotonic curvature in at least one direction.

According to Johnson [20], in static frictionless contact of solids, the contact stresses depend only upon the relative profile of the two surfaces, i.e., upon the shape of the interstitial gap between them before loading. The actual system geometry may be replaced, without loss of generality, by a flat surface and a profile, which results in the same undeformed gap between the surfaces. For convenience, all elastic deformations can be considered to occur in one body which has an effective elastic modulus, and the other body is assumed to be rigid. The effective elastic modulus can be found from

$$\frac{1}{E'} = \frac{1-\upsilon_1^2}{E_1} + \frac{1-\upsilon_2^2}{E_2} \tag{2.6}$$

where E and υ are the Young's modulus and Poisson's ratio, respectively. For the contact of two spheres, the effective radius of curvature is:

$$\frac{1}{\rho} = \frac{1}{\rho_1} + \frac{1}{\rho_2} \tag{2.7}$$

For relatively large radii of curvature, where the contacting surfaces are nearly flat, an approximate geometrical relationship can be found between radius of curvature and the maximum out-of-flatness [4]

$$\rho = \frac{b_L^2}{2\delta} \tag{2.8}$$

where δ is the maximum out-of-flatness of the surface and b_L is the radius of the contacting bodies.

Figure 2-3 details the procedure, which has been used widely for the geometric modeling of the actual contact between two curved rough bodies. As a result of the above, the complex geometry of non-conforming rough contacts can be simplified to the contact of the equivalent truncated spherical surface with the equivalent rough flat.

2.2.3 Microhardness

Hardness is defined as the resistance to permanent deformation; hardness definitions and tests can be found in various standard textbooks e.g. Tabor [2], and Mott [24]. The most common hardness testing method is the static indentation. In a static indentation test, a steady load

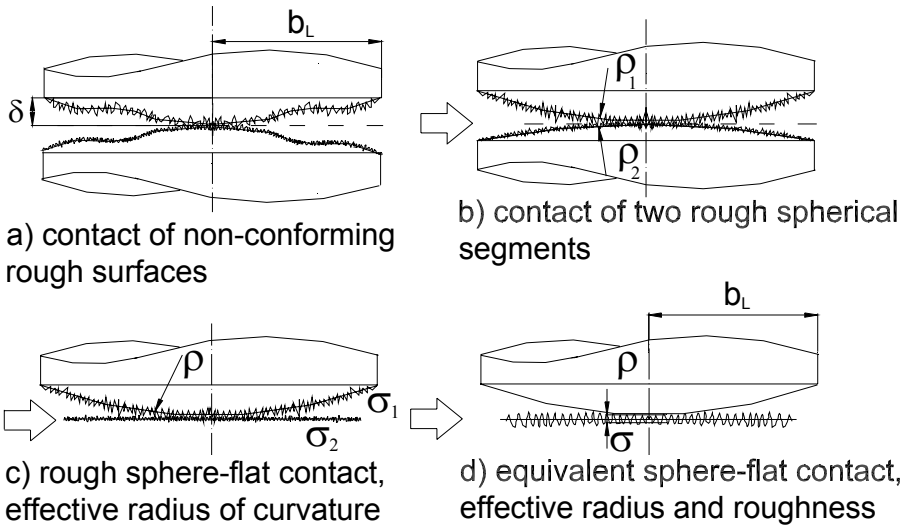

Figure 2-3: Flow diagram of geometrical modeling

is applied to an indenter which may be a ball, cone or pyramid and the hardness is calculated from the area or depth of indentation produced. Hegazy [25] demonstrated through experiments with four alloys, SS 304, nickel 200, zirconium-2.5% niobium, and Zircaloy-4, that the effective microhardness is significantly greater than the bulk hardness. As shown in Fig. 2-4, microhardness decreases with increasing the depth of indenter until bulk hardness is obtained. Hegazy concluded that this increase in the plastic yield stress (microhardness) of the metals near the free surface is a result of local extreme work hardening or some surface strengthening mechanism. He derived empirical correlations to account for the decrease in contact microhardness of the softer surface with increasing depth of penetration of asperities on the harder surface

$$H_v = c_1 \left(d'_v\right)^{c_2} \tag{2.9}$$

where H_v is the Vickers microhardness in GPa, $d'_v = d_v/d_0$ and $d_0 = 1\ \mu m$, d_v is the Vickers indentation diagonal in μm, and c_1, c_2 are correlation coefficients determined from Vickers microhardness measurements. Table 2.2 shows c_1 and c_2 for some materials. Relating the hardness of a microcontact to the mean size of microcontacts, Hegazy [25] suggested a correlation for

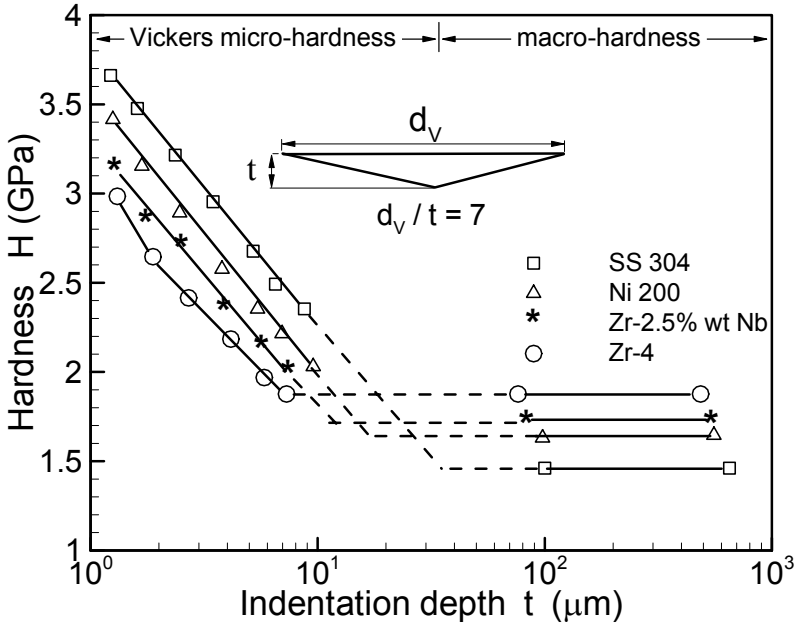

Figure 2-4: Measured hardness and microhardness, Hegazy 1985

Table 2.2: Vickers microhardness coefficients, Hegazy 1985

Material	$c_1(GPa)$	c_2
Zr-4	5.677	-0.278
Zr-2.5wt% Nb	5.884	-0.267
Ni 200	6.304	-0.264
SS 304	6.271	-0.229

effective microhardness (conforming rough surfaces)

$$H_{mic} = c_1 \left(0.95\frac{\sigma'}{m}\right)^{c_2} \tag{2.10}$$

where $\sigma' = \sigma/\sigma_0$ and $\sigma_0 = 1\ \mu m$, σ is surface roughness in micrometers.

Microhardness depends on several parameters, mean surface roughness, mean slope of asperities, method of surface preparation, and applied pressure. Song and Yovanovich [26] related H_{mic} to the surface parameters and nominal pressure (conforming rough surface)

$$\frac{P}{H_{mic}} = \left[\frac{P}{c_1\left(1.62\sigma'/m\right)^{c_2}}\right]^{\frac{1}{(1+0.071c_2)}} \tag{2.11}$$

Sridhar and Yovanovich [27] suggested empirical relations to estimate Vickers microhardness coefficients, using the bulk hardness of the material. Two least-square-cubic fit expressions were reported

$$\begin{aligned} c_1 &= H_{BGM}\left(4.0 - 5.77\kappa + 4.0\kappa^2 - 0.61\kappa^3\right) \\ c_2 &= -0.57 + 0.82\kappa - 0.41\kappa^2 + 0.06\kappa^3 \end{aligned} \tag{2.12}$$

where $\kappa = H_B/H_{BGM}$, H_B is the Brinell hardness of the bulk material, and $H_{BGM} = 3.178(GPa)$. The above correlations are valid for the range $1.3 \leq H_B \leq 7.6\ GPa$, the RMS percent difference between data and calculated values were reported; 5.3% and 20.8% for c_1, and c_2, respectively. Milanez et al. [28] studied the effect of microhardness coefficients on TCR by comparing the TCR's computed from the measured versus the estimated, from Eq. (2.12), microhardness coefficients. They concluded that despite the difference between the measured and estimated values of microhardness coefficients, the TCR's predicted by both methods are in good agreement.

2.3 Mechanical Analysis

Figure 2-5 illustrates the mechanical analysis overview for contact of spherical rough surfaces, which includes; a macro and a micro part. Existing theories/models for each part (macro and micro) are categorized based on the normal deformation mode of the bulk (substrate) and asperities into: elastic, plastic, and elastoplastic groups.

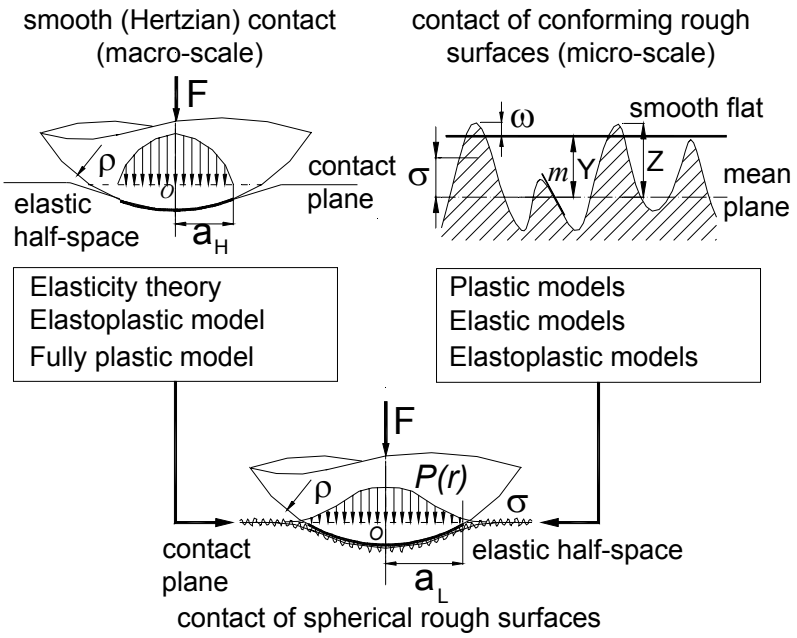

Figure 2-5: Mechanical problem overview for spherical rough contacts

2.3.1 Macrocontact Problem

When two smooth solid spheres, or equivalently a flat and the effective sphere, are pressed against each other, with an increase in external load, the three ranges of loading purely elastic, elastic-plastic (contained), and fully plastic (uncontained) occur in most engineering structures. Hertz [29] developed his elastic contact theory by introducing the simplification that each body can be regarded as an elastic half-space loaded over a small contact region of its plane surface. He also assumed surfaces are continuous and non-conforming, strains are small (to be in the elastic limit), surfaces are frictionless, and the pressure distribution is $P(r) = P_0\sqrt{1-(r/a_H)^2}$.

The Hertzian theory expressions for spheres can be summarized as

$$
\begin{aligned}
a_H &= \left(\frac{3F\rho}{4E'}\right)^{1/3} \\
\omega_0 &= \frac{a_H^2}{\rho} = \left(\frac{9F^2}{16\rho E'^2}\right)^{1/3} \\
P_0 &= \frac{3F}{2\pi a_H^2} = \left(\frac{6FE'^2}{\pi^3\rho^2}\right)^{1/3}
\end{aligned}
\tag{2.13}
$$

where ω_0 is the maximum normal deformation and P_0 is the maximum contact pressure (at the center of the contact).

According to Johnson [20], the load at which plastic yield begins in the contact of two solids is related to the yield point of the softer material. The yield point can be found either from Tresca's maximum shear stress, or Von Mises' shear strain-energy criterion. When the yield point is first exceeded, the plastic zone is small and fully contained by the material which remains elastic, so that the plastic strains are of the same order of magnitude as the surrounding elastic strains. In these circumstances the material displaced by the indenter is accommodated by an elastic expansion of the surrounding solid. As the indentation becomes more severe, the plastic zone (core) expands, and an increasing pressure is required beneath the indenter to produce the necessary expansion. Eventually the plastic zone breaks out to the free surface and displaced material is free to escape by plastic flow to the sides of the indenter. This is the uncontained mode of deformation, which should be analyzed by the theory of rigid-plastic solids [20]. However, the contact load must be increased about 400 times from the point of initial yielding to the state of fully plastic flow, which indicates that the elastoplastic transitional region spans a broad range of loading.

When the plastic deformation is severe so that the plastic strains are large compared with the elastic strains, the elastic deformation may be neglected. Provided the material does not strain-harden significantly, it may be idealized as a perfectly plastic solid which flows plastically at a constant stress (roughly three times the yield stress) [20]. A loaded body of rigid-plastic material consists of regions in which plastic flow takes place, and regions where there is no deformation due to the assumption of rigidity. Hardy et al. [30], using a numerical analysis, showed that the plastic flow leads to a flattening of the pressure distribution, and at high loads

may peak slightly towards the edge of the contact area.

2.3.2 Microcontact Problem

Based on the assumed deformation mode of asperities, existing microcontact mechanical models can be categorized into three main groups: plastic, elastic, and elastoplastic models. The fundamental assumptions, which are common in most of the models can be summarized as

- contacting surfaces are rough, with a Gaussian asperity distribution
- behavior of a given microcontact is independent of all other microcontacts
- interfacial force on any microcontact spot acts normally (no friction)
- the deformation mechanics (i.e. the stress and displacement fields) are uniquely determined by the shape of the equivalent surface.

Plastic Models

Abott and Firestone [31] developed the most widely used model for a fully plastic contact. With the concept of equivalent roughness, the model assumes that the asperities are flattened or equivalently penetrate into the smooth surface without any change in the shape of the part of surfaces not yet in contact. Therefore, bringing the two surfaces together within a distance Y is equivalent to slicing off the top of the asperities at a height Y above the mean plane. Since the real area of contact is much smaller than the apparent contact area, the pressure at the top of the asperities must be sufficiently large that they are comparable with the strength of the materials of the contacting bodies. Bowden and Tabor [32], and Holm [33] suggested that these contact pressures are equal to the flow pressure of the softer of the two contacting materials and the normal load is then supported by plastic flow of its asperities. Therefore, pressure at microcontacts will be equal to the microhardness and effectively independent of load and the contact geometry. The real area of contact is then proportional to the load, $A_r/A_a = P_m/H_{mic}$, where P_m is the mean apparent contact pressure.

Pullen and Williamson [34] experimentally investigated plastic flow under large loads. They assumed that material displaced from the contacting regions must reappear by raising some part

of the non-contacting surface. They assumed that the volume of material remained constant and that the material that is plastically displaced appears as a uniform rise over the entire surface. Since the uniform rise will not affect the shape of the surface outside the contact area, they showed that the contact area due to the interaction of micro contacts is not proportional to the normal load at relatively high loads; and proposed as a good approximation; $A_r/A_a = P_p/(1+P_p)$, where $P_p = P_m/H_{mic}$. Note that this phenomenon is important only at relatively large pressures.

Some authors used conical or curved shapes to describe the morphology of asperities. Tsukizoe and Hisakado [35, 36], assumed a conical shape for surface asperities of equal base angle, which depends on the surface mean absolute slope. They proposed a statistical contact model for predicting the contact spot size and density for an isotropic Gaussian rough surface in contact with an ideal smooth flat surface. On the basis of this assumption and neglecting the asperity interactions, they obtained the following expressions for microcontact size and number

$$\begin{aligned} a_s &= \frac{\sqrt{2}}{\pi}\frac{(\sigma/m)}{\lambda} \\ n_s &= \frac{\sqrt{\pi}}{8}\left(\frac{m}{\sigma}\right)^2 \lambda \exp\left(-\lambda^2\right) A_a \end{aligned} \tag{2.14}$$

where, $\lambda = Y/\sqrt{2}\sigma$ is the dimensionless separation.

Cooper et al. [7], based on the level-crossing theory and using the sum surface approximation, derived relationships for mean microcontact size, and number of microcontacts by assuming hemispherical asperities whose height and surface slopes have Gaussian distributions

$$\begin{aligned} a_s &= \sqrt{\frac{8}{\pi}}\left(\frac{\sigma}{m}\right)\exp\left(\lambda^2\right)\operatorname{erfc}(\lambda) \\ n_s &= \frac{1}{16}A_a\left(\frac{\sigma}{m}\right)^2\frac{\exp\left(-2\lambda^2\right)}{\operatorname{erfc}(\lambda)} \end{aligned} \tag{2.15}$$

Their model was essentially based on the assumption that each microcontact consists of two hemispherical asperities in symmetric plastic contact. They also showed that the ratio of real area of contact to the apparent area, as a function of Y, could be related to the probability function

$$\frac{A_r}{A_a} = \int_Y^\infty \phi(z)\,dz = \frac{1}{2}\operatorname{erfc}(\lambda) \tag{2.16}$$

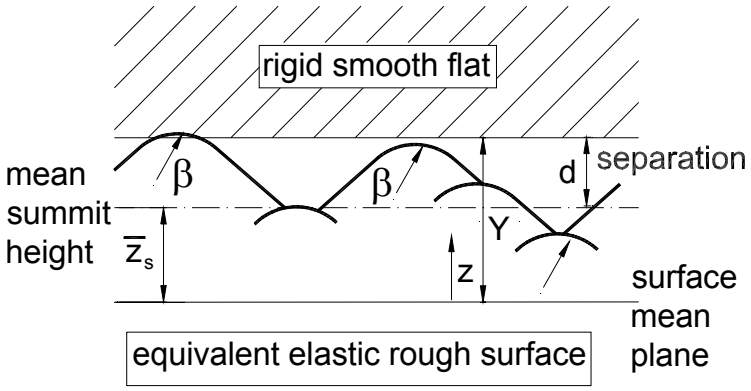

Figure 2-6: Greenwood and Williamson 1966 geometrical model

where $\phi(z)$ is the normal probability function of the asperity heights defined as

$$\phi(z) = \frac{1}{\sqrt{2\pi}\sigma} \exp\left(\frac{-z^2}{2\sigma^2}\right) \tag{2.17}$$

Elastic Models

For applications such as lubrication or moving machine parts in which the contacting surfaces meet many times, Archard [37] pointed out that the asperities may flow plastically at first, but they must reach a steady-state in which the load is supported elastically. He then offered a model in which each asperity is covered with micro asperities, and each micro asperity with micro-micro asperities that gave successive closer approximations to the friction law, $A_r = F$, as more stages were considered.

Greenwood and Williamson [1] (GW) developed an elastic model for contact of flat rough surfaces based on the deformation of an average size summit. As shown in Fig. 2-6, they assumed that all summits have the same radius of curvature at their top, and possess a Gaussian distribution about a mean reference plane, and the distribution of summit heights is the same as the heights standard deviation, i.e., $\sigma_{\text{summit}} = \sigma$. The GW model required three input parameters: the standard deviation of summit height distribution σ_{summit}, the density of summits η_{GW}, and the radius of curvature of the summits β that was assumed to be constant.

Relationships for the GW model, as reported, are

$$\begin{aligned} n_s &= \eta_{GW} A_a I_0\left(d'\right) \\ A_r &= \pi \eta_{GW} A_a \beta \sigma I_1\left(d'\right) \\ F &= \frac{4}{3} \eta_{GW} A_a \beta^{1/2} \sigma^{3/2} E' I_{3/2}\left(d'\right) \end{aligned} \tag{2.18}$$

where $d' = d/\sigma$ and;

$$I_n\left(d'\right) = \frac{1}{\sqrt{2\pi}} \int_{d'}^{\infty} \left(s - d'\right)^n \exp\left(-s^2/2\right) ds \tag{2.19}$$

Unlike other models, the GW model is based on the contact of summits and separation, d, is measured from the mean summit line (not the surface mean line), which is located somewhere above the mean surface plane. Since it was assumed that the summits' standard deviation is the same as the surface roughness, the GW relationships can be re-written as functions of $\lambda = Y/\sqrt{2}\sigma$ (to make the relationships comparable with other models). After evaluating the integrals and simplifying, one can find

$$\begin{aligned} n_s &= \frac{1}{2} \eta_{GW} A_a \ \mathrm{erfc}\left(\lambda\right) \\ A_r &= \frac{\sqrt{\pi}}{2} \eta_{GW} A_a \beta \sigma \left[\exp\left(-\lambda^2\right) - \sqrt{\pi}\lambda \ \mathrm{erfc}\left(\lambda\right)\right] \\ F &= \frac{2^{1/4}}{3\sqrt{\pi}} \eta_{GW} A_a E' \beta^{1/2} \sigma^{3/2} \sqrt{\lambda} \exp\left(-\lambda^2/\ 2\right) \left[\left(1 + 2\lambda^2\right) K_{\frac{1}{4}}\left(\lambda^2/\ 2\right) - 2\lambda^2 K_{\frac{3}{4}}\left(\lambda^2/\ 2\right)\right] \end{aligned} \tag{2.20}$$

where $K_n\left(\cdot\right)$ is the modified Bessel function of the second kind of the nth order.

The GW asperity model has been extended to include other contact geometries, e.g. spherical surfaces [38], more complex geometries, e.g. non-uniform radii of curvature of asperity peaks [39], and anisotropic surfaces [40]. Whitehouse and Archard [39] and Onions and Archard [41] further improved the statistic model by representing the features of the surface topography with two parameters: the standard deviation, σ, and the exponent of an exponential correlation function, which was named the "correlation distance". Bush et al. [42] developed an elastic contact model for isotropic surfaces that treated the asperities as elliptical paraboloids with random principal axis orientation and aspect ratio. O'Callaghan and Cameron [43] developed a model for the isotropic problem addressed by Bush et al. [40]. In their model, both surfaces can be

rough and asperities need not contact at their tops. O'Callaghan and Cameron [43] concluded, as did Francis [19], that the contact of two rough surfaces was negligibly different from the contact of a smooth and an equivalent rough surface. McCool [44] compared the basic GW model with other more general isotropic and anisotropic models and found that the simpler GW model, despite its simple form, gives good results.

Elastoplastic Models

Chang et al. [45], using GW model assumptions, presented a model based on volume conservation of an asperity control volume during plastic deformation. The deformed asperity was modeled as a truncated spherical segment and its radius was assumed to be the same as that of the undeformed asperity. For all plastically deformed asperities the average pressure over the contact area was assumed to be a factor of hardness, which was constant throughout the elastic-plastic deformation. Zhao et al. [46], using the Chang et al. [45] model, developed an elastic-plastic microcontact model for nominally flat rough surfaces. The transition from elastic deformation to fully plastic flow of the contacting asperities was curve-fitted. A cubic polynomial, smoothly joining the expressions for elastic and plastic area of contacts, spans the elastoplastic region based on two extremes of the Chang et al. [45] model.

The advantage of the GW-type models is their relative simplicity and explicitness in expressions. However, assuming a constant summit radius is unrealistic; for a random surface, β is also a random variable [19]. In addition β and η_{GW} cannot be measured directly and must be calculated through statistical relationships, and are sensitive to the sampling length of the surface measurement [20]. According to the GW model, the summits or "peaks" on a surface profile are the points higher than their immediate neighbors over the sampling interval. Recently Greenwood and Wu [47] reviewed the assumptions of the GW model and concluded that "*the GW definition of peaks is wrong and gives a false idea of both number and the radius of curvature of asperities*". Greenwood and Wu proposed to return to the Archard [37] idea that roughness consists of roughness on roughness and that the contact may be plastic at light loads but it becomes elastic at heavier loads.

2.3.3 Deformation Mode of Asperities

When real surfaces are pressed together they make contact at numerous points, which deform, elastically, plastically or elastoplastically to support the load. According to Tabor [2] when two metals are placed in contact "*they will be supported on the tips of their asperities, at first the deformation is elastic, but for asperities of the order of μm radius, the minutest loads will produce plastic deformation. Indeed full plasticity may occur even for the hardest steels at a load of the order of a few milligrams.*" Tabor showed that in most practical cases, the real area of contact is proportional to the applied load. It is also inversely proportional to the effective hardness of the surface asperities. Greenwood [17] described the contact of two surfaces as follows: "*surfaces touch at a large number of contacts, and these contacts will be in all the states from fully elastic, to fully plastic. The fully elastic ones are a negligible fraction of the total; the effective flow pressure will be intermediate between plastic and elastic values.*" Considering that the plastic flow is irreversible and cannot be repeated on subsequent loadings, Archard [37] emphasized the point that the normal contact must be elastic. He showed that any elastic model (based on simple Hertzian theory) in which the number of contacts remains constant will give $A_r \sim F^{2/3}$, which does not satisfy the observed proportionality $A_r \sim F$ reported by Tabor [2]. But, if the average contact size remains constant, and the number of microcontact increases, the area will be proportional to the load.

Greenwood and Williamson [1] introduced a plasticity index as a criterion for plastic flow of microcontacts, $\gamma_{GW} = (E'/H)\sqrt{\sigma/\beta}$. They reported that the load has little effect on the deformation regime. When the index is less than 0.6, plastic contact could be caused only if the surfaces were forced together under very large nominal pressure. When $\gamma_{\mathrm{GW}} \geq 1$ plastic flow will occur even at small nominal pressures. Based on the plasticity index, they concluded that "*most surfaces have plasticity indices larger than 1.0, and thus, except for especially smooth surfaces, the asperities will flow plastically under the lightest loads, as has been frequently postulated.*" Chang et al. [45] with the same assumptions as GW, set the criteria for the deformation mode based on the deformation of an average asperity. For compliances less than the critical compliance ω_c, where ω_c is the inception of plastic deformation based on experimental work of Tabor [2] and Johnson [20], the contact is elastic and Hertzian theory can be applied. For compliances higher than ω_c, a plastic model was used. Mikic [48] proposed an alternative

plasticity index, $\gamma_{\text{Mikic}} = H_{mic}/E'm$. Mikic also reported that the mode of deformation, as stated by GW, depends only on material properties and the shape of the asperities, and it is not sensitive to the pressure level. Mikic performed an analysis to determine the contact pressure over the contact area based on the fact that all contact spots do not have the same contact pressure, although the average contact pressure would remain constant. For surfaces with $\gamma_{Mikic} \geq 3$, 90% of the actual area will have the elastic contact pressure, therefore the contact will be predominantly elastic, and for $\gamma_{Mikic} \leq 0.33$, 90% of the actual area will have the plastic contact pressure, therefore the contact will be predominantly plastic. He concluded that for most engineering surfaces the asperity deformation mode is plastic and the average asperity pressure is the effective microhardness.

To compare elastic and plastic models, Greenwood and Williamson [1] (GW) elastic, Cooper et al. [7] (CMY) plastic, and Tsukizoe and Hisakado [35, 36] (TH) plastic models were chosen, and their trends plotted versus the dimensionless mean separation. GW requires input surface parameters; η, β and σ, while CMY and TH require σ, m, thus a quantitative comparison between these models requires detailed surface information, and would be restricted to a particular case. However, for a contact, surface parameters are constant and do not change as the mean separation varies. Therefore, we derive scale relationships and compare these models qualitatively, by considering constant surface parameters. This comparison only illustrates trend/behavior of surface parameters predicted by each model as the separation changes. Therefore, the absolute values of these parameters can not be inferred from the comparison, i.e., Figs. **??** to **??**.

Table 2.3 shows the scale relationships that were used in the comparison. The real area of microcontacts was calculated from, $A_r = \pi n_s a_s^2$. Additionally, as the fully plastic deformation of asperities was assumed for CMY and TH models, one can write $F = H_{mic}A_r$, where microhardness H_{mic} is considered a constant for a contact.

The range of separation in typical real contacts is roughly $1.5 \leq \lambda \leq 3$. The scale relationships in Table 2.3 are plotted versus the separation, λ, over a wider range in Figs. 2-7 to 2-10. It can be observed that by decreasing the dimensionless separation λ;

- The mean size of microcontacts in all models increases. The size of microcontacts in the TH model increases continuously due to the assumed conical shape of asperities, while

Table 2.3: Scale relationships for radius and number of microcontacts, and external force

Model	a'_s	n'_s	F'
GW [1]	$\sqrt{\frac{\exp\left(-\lambda^2\right)}{\operatorname{erfc}\left(\lambda\right)} - \sqrt{\pi}\lambda}$	$\operatorname{erfc}(\lambda)$	$\sqrt{\lambda}\exp\left(-\frac{\lambda^2}{2}\right)\left[\begin{array}{l}\left(1+2\lambda^2\right) \\ K_{\frac{1}{4}}\left(\frac{\lambda^2}{2}\right) - \\ 2\lambda^2 K_{\frac{3}{4}}\left(\frac{\lambda^2}{2}\right)\end{array}\right]$
TH [35, 36]	$\frac{1}{\lambda}$	$\lambda\exp\left(-\lambda^2\right)$	$\frac{\exp\left(-\lambda^2\right)}{\lambda}$
CMY [7]	$\exp\left(\lambda^2\right)\operatorname{erfc}(\lambda)$	$\frac{\exp\left(-2\lambda^2\right)}{\operatorname{erfc}\left(\lambda\right)}$	$\operatorname{erfc}(\lambda)$

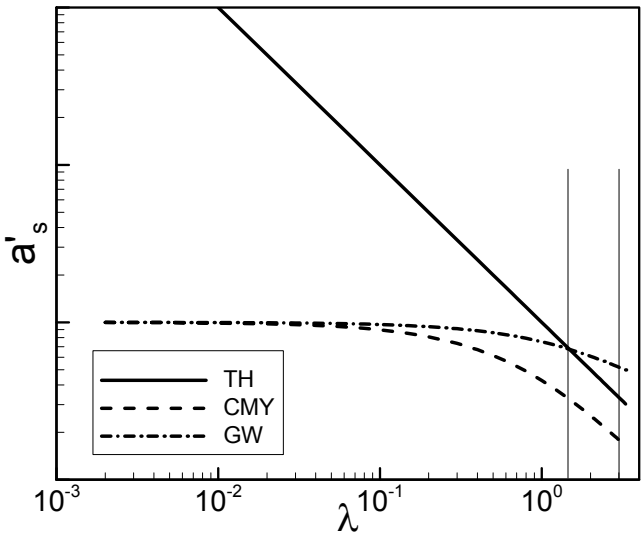

Figure 2-7: Effect of mean separation on mean size of microcontacts

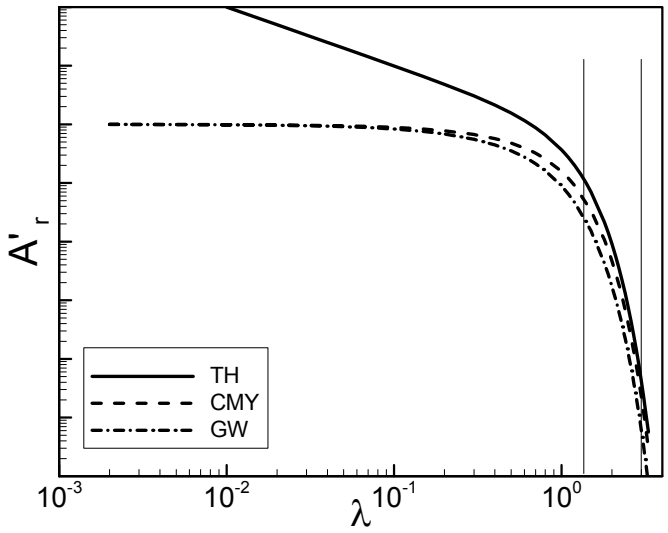

Figure 2-8: Effect of mean separation on real contact area

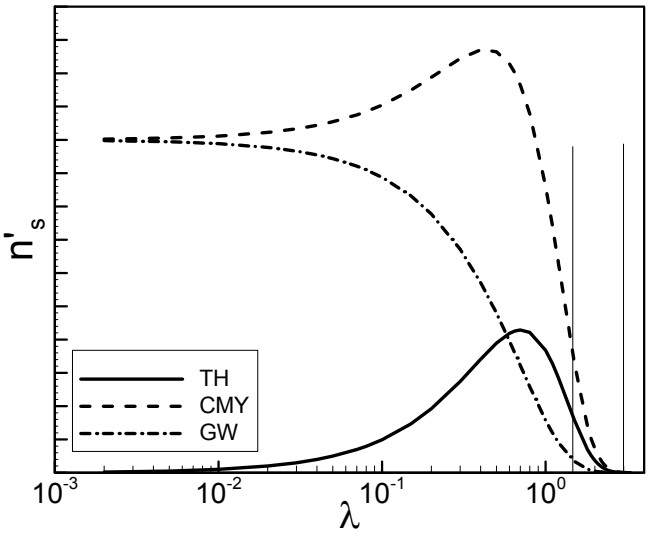

Figure 2-9: Effect of mean separation on number of microcontacts

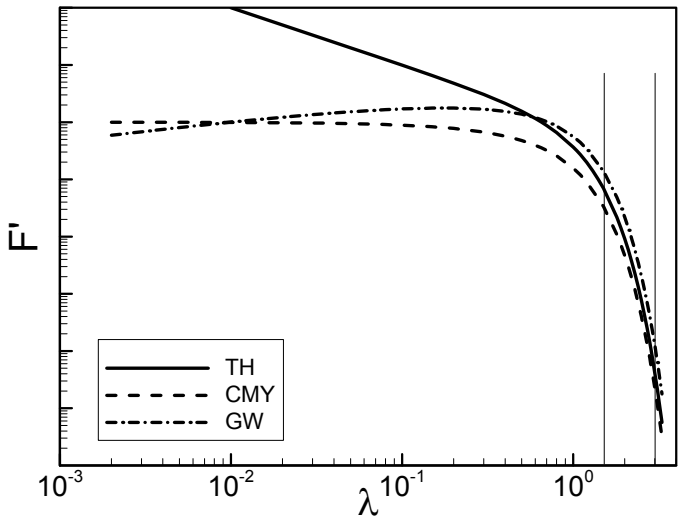

Figure 2-10: Effect of mean separation on external force

the predicted mean microcontact size by GW and CMY approaches some limiting value.

- The real contact area increases and the trends predicted by the three models are very similar, in the applicable range of the separation $1.5 \leq \lambda \leq 3$.

- The external force also increases in a comparable manner in all three models. It is interesting to observe that the external force is nearly proportional to the real contact area in GW model, which indicates that the GW elastic model behaves like plastic models, thus an elastic effective microhardness can be defined.

- The number of microcontacts increases in CMY and TH to a maximum, and falls by further decreasing the separation, while the GW model does not show this phenomenon. As the separation becomes smaller, more contacting spots form, also the mean size of the existing microcontact increases, until they begin to merge and create larger contact spots (clustering), which results in fewer microcontacts. Based on the microgeometry model, a rough surface can be imagined as a collection of peaks and valleys. At the limit when separation approaches zero, CMY and TH predict that all surface peaks (asperities higher than the mean line) are cut off and only the ones under the mean line (valleys) remain.

On the other hand, the GW model predicts that the peaks are elastically compressed to the mean-line, without changing the shape of the rest of the surface profile.

This analysis may not be strictly correct, since these models were not designed to cover a low range of separations and high deformations.

The real contact area plays the most important role in the prediction of the constriction/spreading thermal resistance. The relationship between the applied load and the separation is also important in the case where an interstitial gas is present. From the comparison, it can be concluded that despite the different basic assumptions and input parameters in the GW elastic and CMY and TH plastic models, their behavior in terms of real contact area, size and number of microcontacts, and the relationship between the external force and real contact area are comparable in the applicable range of the separation. In a manner similar to Greenwood and Tripp [38] it therefore follows that the behavior of contacting rough surfaces is determined essentially by surface statistical characteristics, which are the same in the compared models, and the deformation mode of asperities is a second order effect. Additionally, a combination of plastic and elastic modes would introduce no new features.

2.3.4 Non-Conforming Rough Surface Models

There are very few analytical models for the contact of non-conforming rough surfaces in the literature. Greenwood and Tripp [38] performed the first in-depth analytical study of the effect of roughness on the pressure distribution and deformation of contacting elastic spherical bodies. The contacting rough surfaces were modeled as a smooth sphere and a rough flat. With the same assumptions as GW, they derived a geometrical relationship relating the local separation to the bulk deformation and the sphere profile. The elastic deformations produced by a normal pressure distribution over an area of the surface can be calculated by superposition, using the Boussinesq solution for a concentrated load on a half-space, and using the fact that the displacement due to an axisymmetric pressure distribution will also be axisymmetric. The most important trends in their model were that an increase in roughness resulted in a decrease in the maximum axial contact pressure, P_0, compared with the Hertzian pressure, $P_{0,H}$, and enlarges the effective macroscopic contact radius, a_L, beyond the Hertzian contact radius.

Tsukada and Anno [49], with the same assumptions of Greenwood and Tripp [38], developed

a model and offered expressions for pressure distribution as a function of non-dimensional maximum pressure $P_0/P_{0,H}$ and non-dimensional radius of macrocontact area a_L/a_H for rough sphere-flat contact. Tsukada and Anno [49] and Sasajima and Tsukada [50] presented these two parameters in graphical form for relatively small radii of curvature 5, 10, and 15 mm and roughness in the range of 0.1 to 2 μm in discrete curves.

2.4 Thermal Analysis

The complex nature of the TCR problem dictates making simplifying assumptions in order to develop thermophysical models. These complexities include the macro and micro scale thermal constriction/spreading resistances, the random distribution of size, shape, and location of microcontacts. Also the boundary condition of microcontacts, i.e., isothermal or isoflux, is not known. Therefore, in addition to the geometrical and mechanical assumptions, most existing thermal contact resistance models are based on the following common assumptions:

- contacting solids are isotropic, and thermal conductivity and physical parameters are constant
- contacting solids are thick relative to the roughness or waviness
- surfaces are clean, and contact is static
- radiation heat transfer is negligible
- microcontacts are circular
- steady-state heat transfer at microcontacts
- microcontacts are isothermal; Cooper et al. [7] proved that all microcontacts must be at the same temperature, provided the conductivity in each body is independent of direction, position and temperature
- microcontact spots are flat; it is justifiable because surface asperities usually have a very small slope [14].

Thermal contact models have been constructed based on the premise that within the macro-contact area a number of heat channels in the form of cylinders exist. The joint resistance under vacuum conditions can be calculated by superposition of microscopic and macroscopic resistances [4, 14, 22, 51, 5, 6]:

$$R_j = R_s + R_L \tag{2.21}$$

The real shapes of microcontacts can be a wide variety of singly connected areas depending on the local profile of the contacting asperities. Yovanovich et al. [52] studied the steady-state thermal constriction resistance of a singly connected planar contact of arbitrary shape. By using an integral formulation and a semi-numerical integration process applicable to any shape, they proposed a definition for thermal constriction resistance based on the square root of the contact area. The square root of the contact area was found to be the characteristic dimension and a non-dimensional constriction resistance based on the square root of area was proposed, which varied by less than 5% for all shapes considered. Therefore, the real shape of the microcontacts would be a second order effect and an equivalent circular contact, which has the same area, can represent the microcontacts.

2.4.1 Thermal Constriction/Spreading Resistance

As mentioned in Chapter 1, thermal spreading resistance is defined as the difference between the average temperature of the contact area and the average temperature of the heat sink, which is located far from the contact area, divided by the total heat flow rate Q [3]; $R = \Delta T/Q$.

If it is assumed that the micro contacts are very small compared with the distance separating them from each other, the heat source on a half-space solution can be used [4]. Figure 2-11 illustrates the geometry of a circular heat source on a half-space. Classical steady-state solutions are available for the circular source areas of radius a on the surface of a half-space of thermal conductivity k, for two boundary conditions; isothermal and isoflux source. The spreading resistance for isothermal and isoflux boundary conditions are $R_{\text{s, isothermal}} = 1/(4ka)$, and $R_{\text{s, isoflux}} = 8/\left(3\pi^2 ka\right)$, respectively [3]. It can be seen that the difference between the spreading resistance for isoflux and isothermal sources is only 8%, $R_{\text{s, isoflux}} = 1.08 R_{\text{s, isothermal}}$.

As the microcontacts increase in number and grow in size, a constriction parameter, indicated by $\psi(\cdot)$, must be introduced to account for the interference between neighboring mi-

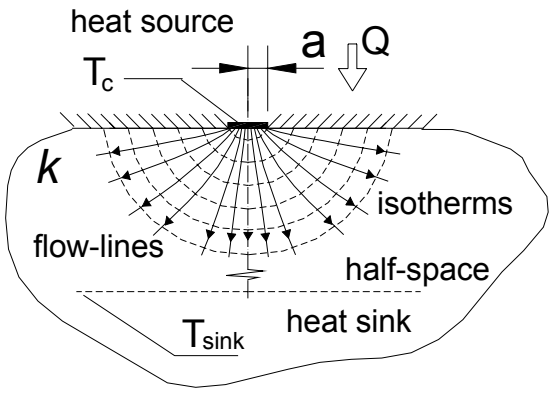

Figure 2-11: Circular heat source on a half-space

crocontacts. Roess [53] analytically determined the constriction parameter for the heat flow through a flux tube. Figure 2-12 illustrates the geometry of two flux tubes in a series. An equivalent long cylinder of radius, b, is associated with each microcontact of radius a. The total area of these flux tubes is equal to the interface apparent area. The constriction and spreading resistances are identical and in series, because of the geometrical symmetry, $\psi_{\text{spreading}} = \psi_{\text{constriction}} = \psi$. Roess [53] suggested an expression in the form of

$$R_{\text{two flux tubes}} = \frac{\psi(\varepsilon)}{4k_1 a} + \frac{\psi(\varepsilon)}{4k_2 a} = \frac{\psi(\varepsilon)}{2k_s a} \tag{2.22}$$

where, $k_s = 2k_1k_2/(k_1 + k_2)$ is the harmonic mean of the thermal conductivities, and $\varepsilon = a/b$. To overcome the mixed boundary value problem, Roess replaced the temperature boundary condition by a heat flux distribution proportional to $\left[1 - (r/a)^2\right]^{-1/2}$ over the source $0 \leq r \leq a$, and adiabatic outside the source $a < r \leq b$. Roess presented his results in the form of a series. Mikic and Rohsenow [14], using a superposition method, derived an expression for the thermal contact resistance for half of an elemental heat channel (semi-infinite cylinder), with isothermal boundary condition. They found another solution for mixed boundary condition of the flux tube, by using a procedure similar to Roess [53]. They also studied thermal contact resistance of the flux tube with a finite length. It was shown that the influence of the finite length of the elemental heat channel on the contact resistance was negligible for all values of $l \geq b$, where l is the length of the flux tube. Later this expression was simplified by Cooper et al.

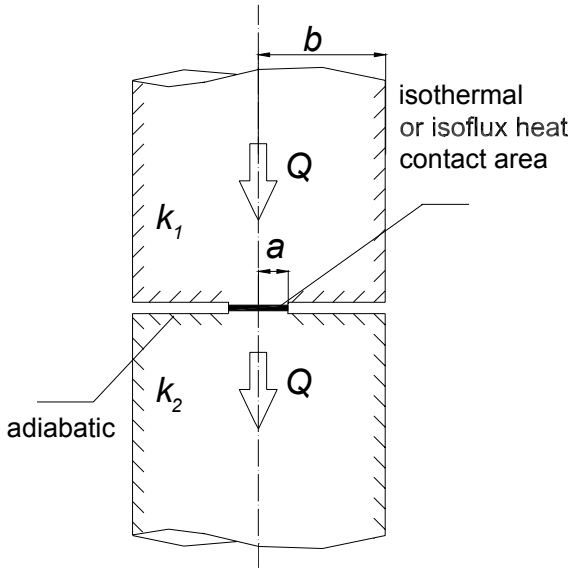

Figure 2-12: Two flux tubes in series

Table 2.4: Thermal spreading resistance factor correlations, isothermal contact area

Reference	Correlation
Roess [53]	$1 - 1.4093\varepsilon + 0.2959\varepsilon^3 + 0.0525\varepsilon^5 + 0.021041\varepsilon^7$ $+0.0111\varepsilon^9 + 0.0063\varepsilon^{11}$
Mikic-Rohsenow [14]	$1 - 4\varepsilon/\pi$
Cooper et al. [7]	$(1-\varepsilon)^{1.5}$
Gibson [55]	$1 - 1.4092\varepsilon + 0.3381\varepsilon^3 + 0.0679\varepsilon^5$
Negus-Yovanovich [56]	$1 - 1.4098\varepsilon + 0.3441\varepsilon^3 + 0.0431\varepsilon^5 + 0.0227\varepsilon^7$

[7], see Table 2.4. Yovanovich [54] generalized the solution to include the case of uniform heat flux, and arbitrary heat flux over the microcontact. A number of correlations for isothermal spreading resistance for the flux tube are listed in Table 2.4. Figure 2-13 shows the comparison between these correlations. It is observed that at the limit when $\varepsilon \to 0$, the flux tube spreading resistance factor approaches one, which is the case of a heat source on a half-space. Also the results from all these various correlations for spreading resistance factor show very good agreement for the range $0 \leq \varepsilon \leq 0.3$, which is typically the range of interest in thermal contact resistance applications.

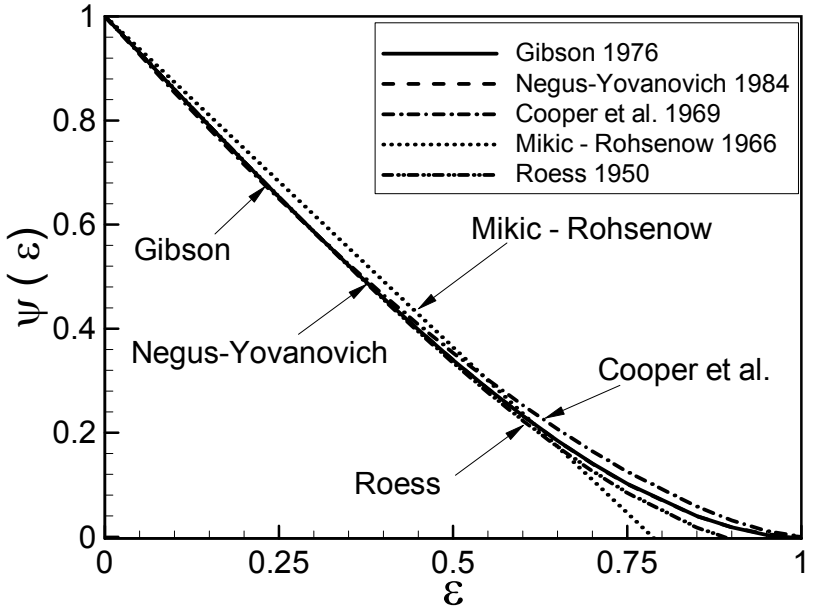

Figure 2-13: Comparison between thermal spreading resistance correlations, isothermal contact area

2.4.2 TCR Models for Conforming Rough Surfaces

During the last four decades, many experiments have been conducted and several correlations proposed for nominally flat rough surfaces. Madhusudana and Fletcher [57], and Sridhar and Yovanovich [58] reviewed existing conforming rough models. Here only a few models will be reviewed, in particular those that are going to be compared with experimental data.

Cooper et al. [7] developed an analytical model, with the same assumptions that were discussed at the beginning of this section, for contact of flat rough surfaces in a vacuum. Eq.(2.15) shows the mean size and number of microcontacts and Eq.(2.16) presents the ratio of real area to the apparent area. The remaining relations of the Cooper et al. [7] model is

$$R_c = \frac{4\sqrt{\pi}}{A_a\sqrt{2}k_s}\left(\frac{\sigma}{m}\right)\frac{\left[1-\sqrt{\frac{1}{2}\mathrm{erfc}\left(\lambda\right)}\right]^{1.5}}{\exp\left(-\lambda^2\right)} \tag{2.23}$$

where R_c, λ =erfc$^{-1}\left(2P_m/H_{mic}\right)$, and k_s are thermal contact resistance, dimensionless separation, and harmonic mean of thermal conductivities, respectively. Yovanovich [8] suggested

a correlation based on the Cooper et al. [7] model, which is quite accurate for optically flat surfaces

$$R_c = \frac{(\sigma/m)}{1.25 A_a k_s \left(P/H_c\right)^{0.95}} \tag{2.24}$$

2.4.3 TCR Models for Non-Conforming Rough Surfaces

Clausing and Chao [4] were the first to experimentally study the contact of rough non-flat surfaces. They also developed a model, with the same assumptions that were discussed at the beginning of this section, for determining the thermal joint (macroscopic and microscopic) resistance for rough, spherical surfaces in contact under vacuum conditions. Their geometrical contact model is shown in Fig. 2-14, the effective radius of curvature of the contacting surfaces was found from Eq.(2.8). Using Roess [53] correlation, see Table 2.4, Clausing and Chao found the total micro thermal resistance of identical, circular, isothermal microcontacts in the macrocontact area

$$R_s = \frac{\psi\left(\varepsilon_s\right)}{2 k_s a_s n_s} \tag{2.25}$$

The microscopic portion of the Clausing and Chao model was based on the plastic deformation of asperities; a measured diamond pyramid hardness was used to consider the asperity hardness of the contacting surfaces. However, material microhardness was multiplied by, ξ_{hardness}, an empirical correction factor introduced by Holm [33], to account for the effects of elastic deformation of asperities. The real contact area A_r, then was calculated

$$A_r = \frac{F}{\xi_{\text{hardness}} H_{mic}} = n_s \pi a_s^2 \tag{2.26}$$

Additionally the following simplifications were made to enable an estimation of the microscopic constriction resistance:

- the microscopic contact spots were assumed to be identical and uniformly distributed, in a triangular array, over the macrocontact area, see Fig. 2-14
- the average size of the microcontacts a_s was independent of load and it was of the same order of magnitude as the surface roughness, i.e. $a_s \equiv \sigma$.

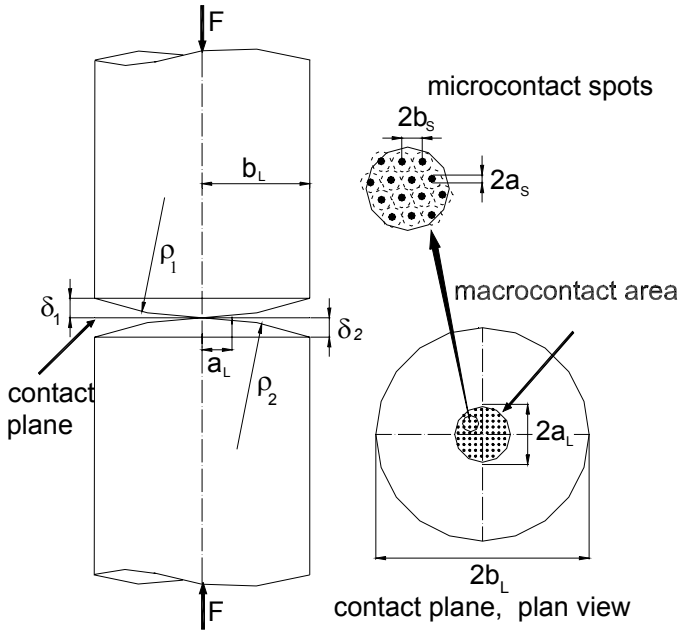

Figure 2-14: Clausing and Chao 1965 geometrical model

They did not report the exact relationship between the microcontact radius and the roughness. In this study, it is assumed, $a_s = \sigma$. They assumed an average value of $\xi_{\text{hardness}} = 0.3$ to take into account both plastic and elastic deformation of microcontacts. Also, a value of $\psi(\varepsilon_s) = 1$ was assumed, which means microcontacts were considered as isothermal circular heat sources on a half-space [59], additionally they assumed, $\xi_{\text{hardness}}\pi = 1$. With the above assumptions the microscopic thermal resistance became

$$R_s = \frac{\sigma H_{mic}}{2k_s F} \tag{2.27}$$

Neglecting the effect of roughness on the macrocontact area, Clausing and Chao determined the radius of the macrocontact area from the Hertzian theory, Eq. (2.13), i.e., $a_L = a_H$. They reported a_L for elastic contact of spheres in the following form:

$$\varepsilon_L = \frac{a_H}{b_L} = 1.285 \left[\left(\frac{P}{E_m} \right) \left(\frac{b_L}{\delta} \right) \right]^{1/3} \tag{2.28}$$

where $E_m = 2E_1E_2/(E_1 + E_2)$, $\delta = \delta_1 + \delta_2$, and it was assumed that $\upsilon_1^2 = \upsilon_2^2 = 0.1$. Therefore, the thermal joint resistance, based on the Clausing and Chao model, became

$$R_j = \frac{\sigma H_{mic}}{2k_s F} + \frac{\psi(\varepsilon_L)}{2k_s a_H} \tag{2.29}$$

where $\psi(\cdot)$ is the Roess [53] spreading factor, see Table 2.4. Clausing and Chao verified their model against experimental data and showed good agreement. Their model was suitable for contacts in which the macroscopic constriction resistance was much greater than the microscopic resistance.

Kitscha [60] and Fisher [61] developed models similar to the Clausing and Chao's model and experimentally verified their models for relatively small radii of curvature and different levels of roughness. Burde [51] derived expressions for size distribution, and number of microcontacts, which described the increase in the macroscopic contact radius for increasing roughness. His model showed good agreement with experimental data for spherical specimens with relatively small radii of curvature with different levels of roughness. Burde did not verify his model or perform experiments for surfaces approaching nominally flat. Also, results of his model were reported in the form of many plots, which are not convenient to use.

Mikic and Rohsenow [14] studied thermal contact resistance for various types of surface waviness and conditions. In particular; nominally flat rough surface in a vacuum, nominally flat rough surfaces in a fluid environment, smooth wavy surfaces in a vacuum environment with either of the following three types of waviness involved: spherical, cylindrical in one direction, and cylindrical in two perpendicular direction, and rough spherical wavy surfaces in a vacuum. Thermal contact resistance for two spherical wavy rough surfaces was considered as the summation of a micro and a macro thermal constriction resistance given by

$$R_j = \frac{\psi(a_{L,\text{eff}}/b_L)}{2k_s a_{L,\text{eff}}} + \frac{\psi(\varepsilon_s)}{2k_s a_s n_s} \tag{2.30}$$

where $\psi(\cdot)$ is the Mikic and Rohsenow [14] spreading factor, see Table 2.4. Similar to Clausing and Chao [4], the effective radius of curvature of the contacting surfaces was found from Eq. (2.8). The macrocontact area for smooth surfaces was determined by the Hertzian theory, Eq. (2.13). Mikic and Rohsenow derived expressions for the mean size and number of microcontacts

by assuming fully plastic deformation of asperities and equivalent surface approximation. These relationships were used later by Cooper et al. [7]. Their model was based on the uniform distribution of identical microcontacts inside the macrocontact area. In the case of rough surface contacts, knowing that the macrocontact area would be larger than the one predicted by the Hertzian theory, they defined an effective macrocontact area. This area contained all the microcontact spots as if they had been uniformly distributed. Using this definition and the assumption that the mean surface would deform elastically, they suggested an iterative procedure for calculating the macrocontact radius. Mikic and Rohsenow verified their model against three sets of experiments. Their computed ratios of macrocontact radius to Hertzian macrocontact radius were 1.6, 1.6, and 1.77 for each experiment and were considered constant throughout the tests, as the external load increased. Mikic and Rohsenow did not derive the actual continuously varying pressure distribution for the contact of spherical rough surfaces. Additionally their expressions for effective macrocontact radius were very complex, and the iterative solution was quite tedious.

Later Mikic [62] derived expressions, based on the Mikic and Rohsenow [14] plastic model, for macroscopic and microscopic thermal resistances in a vacuum, which related the micro and macro thermal resistances to arbitrary pressure distribution and surface properties. The derived relations were general in the sense that they did not require the knowledge of the effective macrocontact area and they could be applied for any symmetrical cylindrical or Cartesian pressure distribution at an interface.

Lambert [23] studied the thermal contact resistance of two rough spheres in a vacuum. He started with the Greenwood and Tripp [38] elastic model for mechanical analysis, and Mikic [62] thermal model as the basis for his thermal analysis. Lambert [23] was not able to solve the set of the mechanical relationships numerically, and mentioned that "*the Greenwood and Tripp model is under-constrained, and convergence may be achieved for the physically impossible cases*". To obtain numerical convergence, Lambert implemented results for the dimensionless axial minimum mean plane, reported by Tsukada and Anno [49], in the mechanical part of his model. The procedure for applying the Lambert [23] model, presented in appendix-A of his thesis, was used to calculate TCR in this study. He suggested two 7th order polynomial expressions for pressure distribution and radius of macrocontact area as a function of a dimensionless load.

Lambert also introduced three dimensionless correction functions in the form of logarithmic polynomials in his thermal model, without specifying the origin and reasons for their presence. His approximate procedure was quite long and required computer-programming skills to apply it. Also, logarithmic expressions for dimensionless macrocontact radius, a_L/a_H , showed a discontinuity, which caused a strange behavior in the predicted thermal joint resistance, see Figs. 2-15 and 2-16. Lambert collected and summarized experimental data reported by many researchers and compared his model with experimental data. He showed a good agreement with experimental data.

Nishino et al. [5] studied the contact resistance of spherical rough surfaces in a vacuum under low applied load. Macroscopic and microscopic thermal contact resistance was calculated based on the Mikic [62] thermal model. Nishino et al. [5] used a pressure measuring colored film that provided information, by means of digital image processing, about the contact pressure distribution. They also verified their method experimentally with aluminum alloy specimens, the experimental data showed good agreement with their technique. They concluded that the macroscopic constriction resistance was predominant under the condition of low applied load. However, the Nishino et al. model required measurements with pressure sensitive film and they did not suggest a general relationship between contact pressure and surface profile and characteristics.

2.5 Comparison Between TCR Models and Data

The developed theoretical models by Clausing and Chao [4] Eq. (2.29), Yovanovich [8] Eq. (2.24), and Lambert [23] are compared with experimental data. References, material and thermophysical properties, and surface characteristics of the experimental data are summarized in Appendix A. As indicated in Table 2.5, the experimental data cover a relatively wide range of the experimental parameters. Table 2.7 indicates the researchers and the specimen materials used in the experiments.

The comparison is done at two extremes; conforming rough surfaces where the macro resistance is negligible and elastoconstriction limit where contacting surfaces have relatively small radii of curvature and the micro resistance is almost negligible.

Table 2.5: Parameter ranges for experimental data

Parameters
$57.3 \leq E' \leq 114.0\ GPa$
$16.6 \leq k_s \leq 75.8\ W/mK$
$0.12 \leq \sigma \leq 13.94\ \mu m$
$0.04 \leq m \leq 0.34$
$0.013 \leq \rho \leq 120\ m$

Table 2.6: Physical properties and surface characteristics of comparison base surface

$\sigma = 1.3\ \mu m$	$m = 0.073$	$H_{mic} = 3.92\ GPa$
$b_L = 7.15\ mm$	$E' = 114\ GPa$	$k_s = 40.7\ W/mK$

TCR for the above models was calculated for a base typical rough surface, the physical properties and surface characteristics are shown in Table 2.6. Surface curvatures $\rho = 14.3$ mm, and $\rho = 100$ m were chosen for elastoconstriction and conforming rough limits, respectively. Experimental data collected by Kitscha [60], Fisher [61], and Burde [51] were compared with the theoretical models in Fig. 2-15. The elastoconstriction approximation introduced by Yovanovich [63], which accounts only for macro resistance predicted by Hertzian theory and neglects the micro thermal resistance completely, was also included in the comparison. The elastoconstriction approximation was included to clearly demonstrate that the macro resistance is the dominating part of thermal joint resistance in the elastoconstriction limit, and the micro thermal resistance is negligible. As can be seen in Fig. 2-15, the elastoconstriction approximation and the Clausing and Chao [4] model are very close and show good agreement with the data. The Lambert [23] model, as a result of its expression for macrocontact radius a_L, showed a strange behavior. As expected, Yovanovich [8] model, which was developed for conforming rough surfaces, does not agree with the data.

Experimental data collected by Antonetti [64], Hegazy [25], and Milanez et al. [65] were compared with the theoretical models in Fig. 2-16. As shown, the Yovanovich [8] model showed good agreement with the data. Lambert [23] was very close to Yovanovich [8] in most of the comparison range, however the strange behavior in the predicted macrocontact area showed up as can be seen in the plot. The Clausing and Chao [4] model under predicted thermal resistance in the conforming rough region.

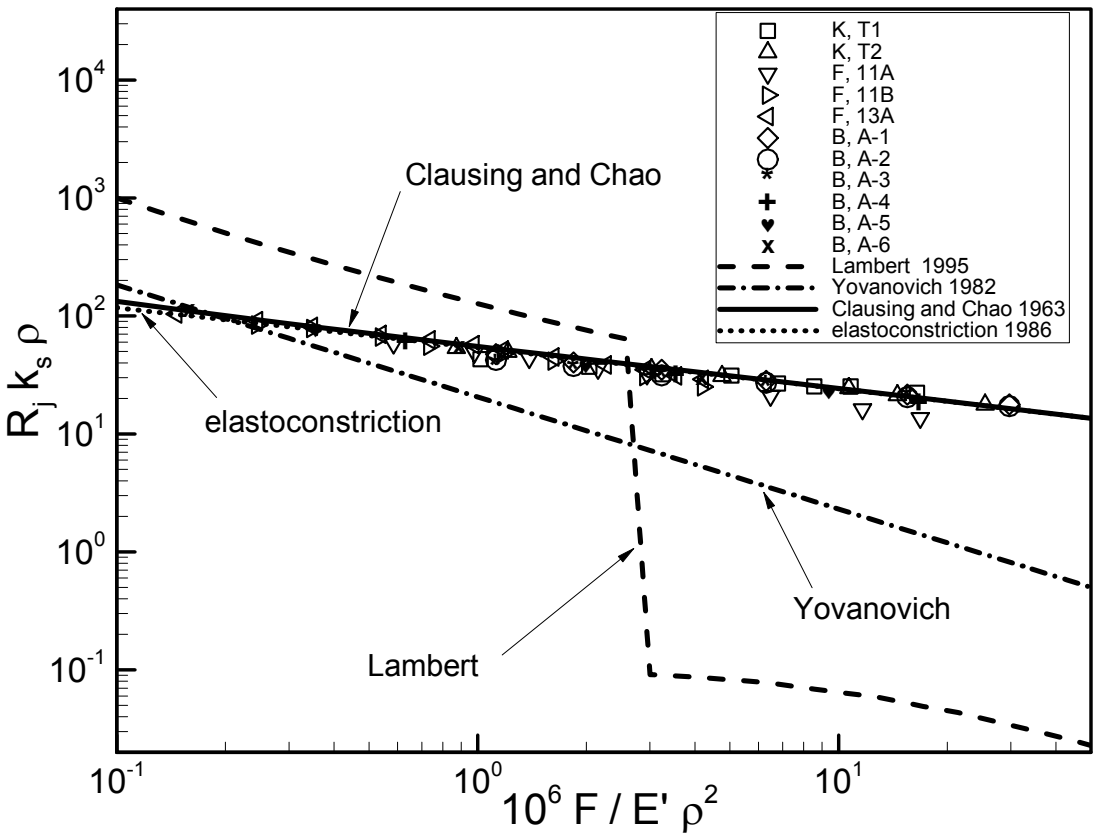

Figure 2-15: Comparison of existing models with data at the elastoconstriction limit

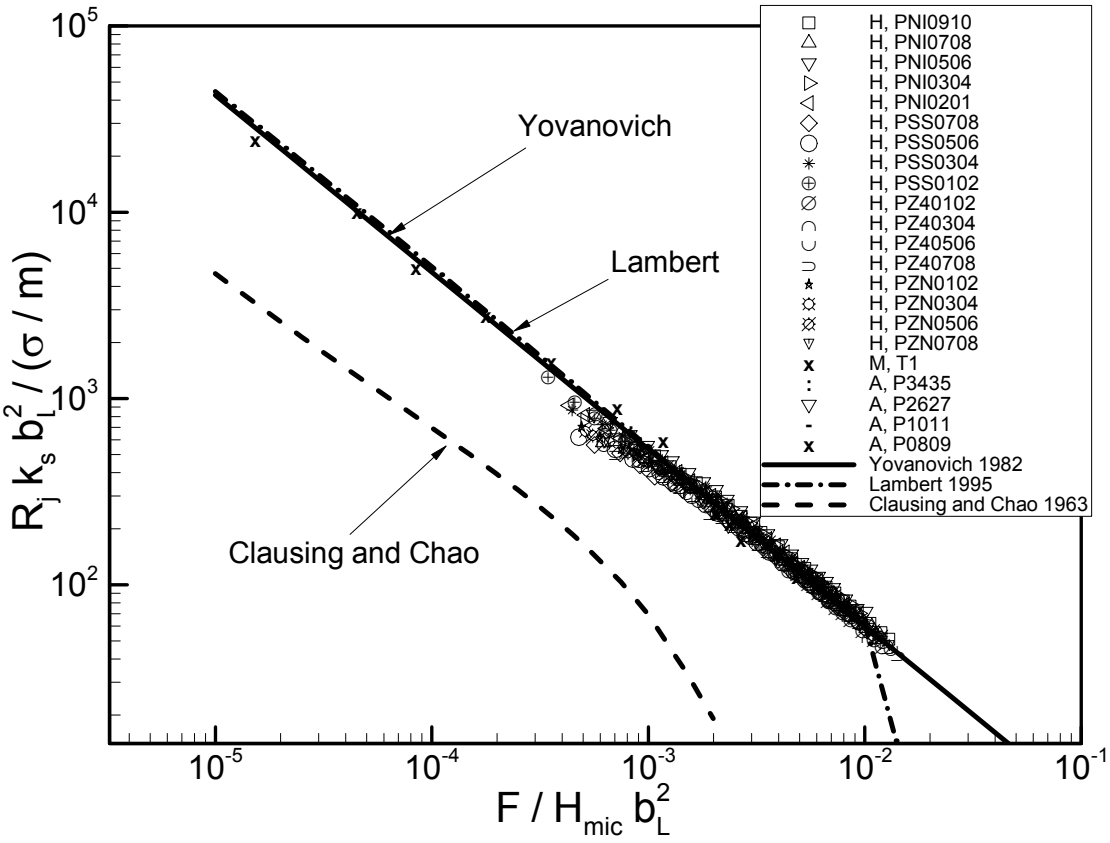

Figure 2-16: Comparison of existing models with data at the conforming rough limit

Kitscha [60], and Fisher [61] did not report the surface slope, m; the Lambert and Fletcher [6] correlation was used to estimate these values, see Table 2.1. The exact values of radii of curvature for conforming rough surfaces were not reported. Since, these surfaces were prepared to be optically flat, radii of curvature in the order of $\rho \approx 100\,(m)$ are considered for these surfaces. Table 2.7 indicates the researchers and the specimen materials used in the experiments.

2.6 Summary and Conclusions

Thermal contact resistance modeling and its components were studied. The modeling process was divided into three analyses: geometrical, mechanical, and thermal where each one included a macro and micro scale part.

Table 2.7: Reseacher and specimen materials

Ref.	Researcher	Specimen Material(s)
A	Antonetti [64]	Ni 200
B	Burde [51]	SPS 245, Carbon Steel
F	Fisher [61]	Ni 200, Carbon Steel
H	Hegazy [25]	Ni 200 SS 304 Zircaloy4 Zr-2.5%wt Nb
K	Kitscha [60]	Steel 1020,Carbon Steel
M	Milanez et al. [65]	SS 304

Proposed empirical correlations to relate surface slopes, m, to surface roughness σ, were summarized and compared with experimental data. The comparison showed that the uncertainty of the correlations was high; use of these correlations is not recommended unless only an estimation of m is required.

GW [1] elastic, CMY [7] and TH [35, 36] plastic conforming rough models were reviewed and a set of scale relationships were derived for the contact parameters, i.e., the mean microcontact size, number of microcontacts, density of the microcontacts, and the external load as functions of dimensionless separation. These scale relationships were compared and it was graphically shown that despite the different assumptions and input parameters, their behaviors in terms of the contact parameters were similar. It can be concluded from the comparison that the behavior of contacting rough surfaces is determined essentially by surface statistical characteristics. Also a combination of plastic and elastic modes would introduce no new features.

The common assumptions of the existing thermal analyses were summarized. Suggested correlations by different researchers for the flux tube spreading resistance were compared. It was observed that, at the limit, the correlations approached the heat source on a half-space solution. Also all the spreading resistance correlations showed good agreement for the applicable range.

Experimental data points obtained for five materials, namely SS 304, carbon steel, nickel 200, zirconium-2.5% niobium, and Zircaloy-4, were summarized and grouped into two limiting cases: conforming rough, and elastoconstriction. These data were non-dimensionalized and compared with TCR models at the two limiting cases. It was shown that none of the existing

theoretical models covers both of the above-mentioned limiting cases.

This clearly shows the need to develop theoretical model(s) which can predict TCR over all cases including the above mentioned limiting cases and the transition range where both roughness and out-of-flatness are present and their effects on contact resistance are of the same order.

Chapter 3

Mechanical Analysis

3.1 Introduction

An accurate knowledge of contact mechanics, i.e., pressure distribution, size of the macrocontact area, and the separation between the mean planes as functions of applied load, geometrical and mechanical characteristics/properties of the contacting bodies, plays an important role in predicting and analyzing thermal and electrical contact resistance and many tribological phenomena.

The contact of two spherical rough surfaces includes two problems with different scales, i) the bulk or macro scale problem, i.e., bulk elastic compression which can be calculated using Hertz [29] theory for ideal *smooth* mean profiles of two surfaces, and ii) the small or micro scale problem, i.e., deformation of surface asperities. The scales of the sub-problems (macro and micro) are very different, yet at the same time, strongly interconnected. Due to surface roughness, contact between two surfaces occurs only at discrete microscopic contacts and the real area of contact, the total area of these microcontacts, is typically a small fraction of the nominal contact area [2, 1].

The macrocontact area is defined as the area in which the microcontacts are distributed, also the contact pressure falls to a negligible value at the edge of the macrocontact. The surface asperities act like a compliant layer on the surface of the contacting bodies, so that the contact is extended over a larger apparent area than it would be if the surfaces were smooth, and consequently, the contact pressure for a given load will be reduced [20].

In this Chapter, an analytical model is developed that enables one to predict the contact parameters such as pressure distribution and size of the macrocontact area. It is required to find simple correlations for determining the above contact parameters that can be used in analytical thermal contact models. Also a criterion is proposed to specify a *flat surface* where the surface curvature can be neglected.

3.2 Theoretical Background

As previously mentioned, the spherical rough contact mechanics problem is divided into macro and micro sub-problems. The macro problem is the contact of two spherical bodies, which is assumed to be within the elastic limit, while the micro or the deformation of the surface asperities is assumed to be plastic.

3.2.1 Microcontact Modeling

The solution of any contact mechanics problem requires that the geometry of the intersection and overlap of the two undeformed surfaces be known as a function of their relative position. If the asperities of a surface are isotropic and randomly distributed over the surface, the surface is called Gaussian. Williamson et al. [16] have shown experimentally that many of the techniques used to produce engineering surfaces give a Gaussian distribution of surface heights. Many researchers, including Greenwood and Williamson [1] assumed that the contact between two Gaussian rough surfaces can be simplified to the contact between a single Gaussian surface, having the effective (sum) surface characteristics, placed in contact with a perfectly smooth surface, as shown in Fig. 2-2. The equivalent roughness, σ, and surface slope, m, can be found from

$$\sigma = \sqrt{\sigma_1^2 + \sigma_2^2} \quad \text{and} \quad m = \sqrt{m_1^2 + m_2^2} \tag{3.1}$$

As discussed in Chapter 2, existing microcontact mechanical models can be categorized into three main groups: elastic, plastic, and elastoplastic based on the deformation mode of asperities. By comparing the elastic model of Greenwood and Williamson [1] and the plastic model of Cooper et al. [7] for nominal flat contacts, it was shown in Chapter 2 that the behavior of the above models are similar, despite the different assumed deformation mode of asperities. It

was also concluded that in most real contacts, asperities deform plastically except for special cases where the surfaces are extremely smooth, see section 2.3.3 for more detail.

The present model is developed assuming the asperities deform plastically. Plastic models assume that the asperities are flattened during contact. This is the same as assuming that the asperities penetrate into the smooth surface in the equivalent model, without any change in shape of the parts of the equivalent rough surface not yet in contact. Therefore, bringing two rough surfaces together within a distance, Y, is equivalent to removing the top of the asperities at a height Y above the mean plane. The assumption of pure plastic microcontacts enables the micro mechanics to be specified completely by the mean slope m and the surfaces roughness σ, without having to assume some deterministic peak shapes, as with elastic microcontact models. Cooper et al. [7] derived the following relationships for contact of nominal flat rough surfaces, assuming plastically deformed asperities, whose height and surface slopes have Gaussian distributions, where the mean separation Y is constant throughout the contact plane

$$\left.\begin{aligned} a_s &= \sqrt{\frac{8}{\pi}}\left(\frac{\sigma}{m}\right)\exp\left(\lambda^2\right)\operatorname{erfc}\,\lambda \\ n_s &= \frac{1}{16}\left(\frac{m}{\sigma}\right)^2\frac{\exp\left(-2\lambda^2\right)}{\operatorname{erfc}\,\lambda}A_a \\ \frac{A_r}{A_a} &= \frac{1}{2}\operatorname{erfc}\,\lambda \end{aligned}\right\} \tag{3.2}$$

where $\lambda = Y/\sqrt{2}\sigma$, n_s, a_s, A_r and A_a are the dimensionless mean plane separation, number and average size of microcontacts, the real and the apparent contact area, respectively.

3.2.2 Microhardness

As mentioned in Chapter 2, microhardness is not a constant of materials. Hegazy [25] demonstrated through experiments with four alloys that the effective microhardness is significantly greater than the bulk hardness. Microhardness decreases with increasing depth of the indenter until bulk hardness is obtained. He derived empirical correlations to account for the decrease in contact microhardness of the softer surface with increasing depth of penetration of asperities on the harder surface:

$$H_v = c_1\left(d'_v\right)^{c_2} \tag{3.3}$$

where H_v is the Vickers microhardness in GPa, $d'_v = d_v/d_0$ and $d_0 = 1\ \mu m$, d_v is the Vickers indentation diagonal in μm, and c_1 and c_2 are correlation coefficients determined from the Vickers microhardness measurements.

3.2.3 Macrocontact Modeling

According to Johnson [20] in static frictionless contact of solids, the contact stresses depend only on the relative profile of the two surfaces, i.e., upon the shape of the interstitial gap before loading. Hertz [29] replaced the two spheres contact geometry by a flat surface and a profile which results in the same undeformed gap between the surfaces. Additionally, all elastic deformations can be considered to occur in one body, which has an effective elastic modulus, E', and the other body is assumed to be rigid. The effective elastic modulus can be found from

$$\frac{1}{E'} = \frac{1-\upsilon_1^2}{E_1} + \frac{1-\upsilon_2^2}{E_2} \tag{3.4}$$

where E and υ are the Young's modulus and Poisson's ratio, respectively. For the contact of two spheres, the effective radius of curvature is

$$\frac{1}{\rho} = \frac{1}{\rho_1} + \frac{1}{\rho_2} \tag{3.5}$$

As a result of these assumptions and by considering axisymmetric loading, we can simplify the complex geometry of two spherical rough surfaces to a rigid smooth sphere having the equivalent radius of curvature in contact with a rough flat surface which has the equivalent surface characteristics, Fig. 3-1.

The open literature contains very few analytical mechanical models for the contact of spherical rough surfaces, see Chapter 2. The first in-depth analytical study to investigate the effect of roughness on the pressure distribution and deformation of contacting elastic spherical bodies was performed by Greenwood and Tripp (GT) [38]. Greenwood and Tripp model was developed based on the same assumptions as the Greenwood and Williamson [1] nominal flat rough contact model. Their assumptions can be summarized as follows:

- contact is axisymmetric and the bulk deformation is elastic

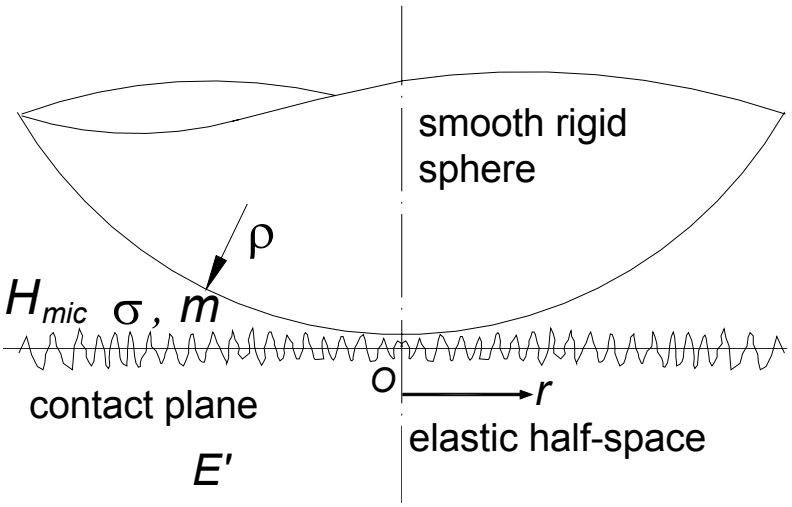

Figure 3-1: Equivalent contact geometry of two spherical rough surfaces

- rough surfaces are isotropic with Gaussian height distribution and a standard deviation, σ
- the distribution of summit heights is the same as the surface heights standard deviation, i.e., $\sigma_s = \sigma$
- the deformation of each asperity is independent of its neighbors
- the asperity summits have a spherical shape all with a constant radius, β, the asperities entirely deform within the elastic limit and Hertz [29] theory can be applied for each individual summit.

They derived a geometrical relationship relating the local separation to the bulk deformation and the sphere profile. The elastic deformations produced by a pressure distribution over an area of the surface can be calculated by superposition, using the Boussinesq solution for a concentrated load on a half-space, and the fact that the displacement due to an axisymmetric pressure distribution is also axisymmetric. It can be shown that the normal displacement in a

half-space due to an arbitrary pressure distribution can be found from [66]

$$\omega_b(r) = \begin{cases} \dfrac{2}{E'}\displaystyle\int_0^{\infty} P(s)\,ds & r = 0 \\ \dfrac{4}{\pi E' r}\displaystyle\int_0^{r} sP(s)\,K\left(\dfrac{s}{r}\right)ds & r > s \\ \dfrac{4}{\pi E'}\displaystyle\int_r^{\infty} P(s)\,K\left(\dfrac{r}{s}\right)ds & r < s \end{cases} \tag{3.6}$$

where $\omega_b(r)$ is the local bulk deformation, $K(\cdot)$ is the complete elliptic integral of the first kind, and s is a dummy variable. Greenwood and Tripp [38] used Eq. (3.6), which gave a complementary relation between local separation and the pressure. They reported a complete set of relationships and solved it numerically.

The results of the GT analysis were found to be primarily a function of a non-dimensional parameter $T = 2F/\sigma E'\sqrt{2\rho\sigma}$ and a weak function of $\mu = 8\sigma\eta\sqrt{2\rho\beta}/3$. The most important trends in the GT model were that an increase in roughness resulted in a decrease in the pressure and an increase in the contact area. The GT model was a significant achievement, however its limitations are

- the GT model was presented as a set of relationships; applying the model is complex and requires numerically intensive solutions
- two of its input parameters, i.e., summits radius β and density η cannot be measured directly and must be estimated through statistical calculations. Additionally, these parameters are sensitive to the surface measurements [20, 47].

Roca and Mikic [67] developed an alternative numerical model by assuming plastic deformation of asperities and that the height of the surface roughness has a Gaussian distribution. Similar trends to those of the GT model were presented. The modeling results of [67] were also mainly a function of a non-dimensional parameter $\overline{\sigma} = \pi\sigma E'/a_H P_{0,H}$ and a weak function of $H/P_{0,H}$, where $P_{0,H}$ is the maximum pressure in the Hertzian limit. Mikic and Roca did not report general relations to calculate the contact parameters.

Greenwood et al. [68] introduced a non-dimensional parameter α called roughness parameter

that governs primarily the rough spherical contact as

$$\alpha = \frac{\sigma}{\omega_{0,H}} \equiv \frac{\sigma\rho}{a_H^2} = \sigma \left(\frac{16\rho E'^2}{9F^2} \right)^{1/3} \tag{3.7}$$

Greenwood et al. [68] showed that the controlling non-dimensional parameters in both [38] and [67] models can be written in terms of α, i.e., $T = 4\sqrt{2}/3\sqrt{\alpha^3}$ and $\overline{\sigma} = 3\pi^2\alpha/4$, respectively. They concluded that it is unimportant whether the asperities deform elastically or plastically; the contact pressure is predominantly governed by α. Further, if the value of α is less than 0.05, the effect of roughness is negligible and the Hertzian theory can be used.

3.3 Present Model

The micro mechanical analysis of the present model is developed on the basis of the Cooper et al. [7] plastic model. The macrocontact area is divided into infinitesimal conforming surface elements where the conforming rough surface relationships, i.e., Eqs. (3.2) can be applied. Bulk deformations are related to the local separation of the contacting surfaces, through a geometrical relationship similar to Greenwood and Tripp [38]. The assumptions of the present model can be summarized as:

- contacting surfaces are macroscopically spherical, which are considered as a sphere-flat contact, Fig. 3-1
- microscopically, contacting surfaces are rough and isotropic with a Gaussian asperity distribution. Only one surface is taken to be rough while the equivalent roughness is assumed to be on the flat plane and the sphere is assumed to be smooth
- microcontacts deform plastically and the asperity pressure is the local microhardness of the softer material in contact. Reasons supporting this assumption are discussed in section 2.3.3
- deformation of each asperity is independent of its neighbors
- only the first loading cycle is considered

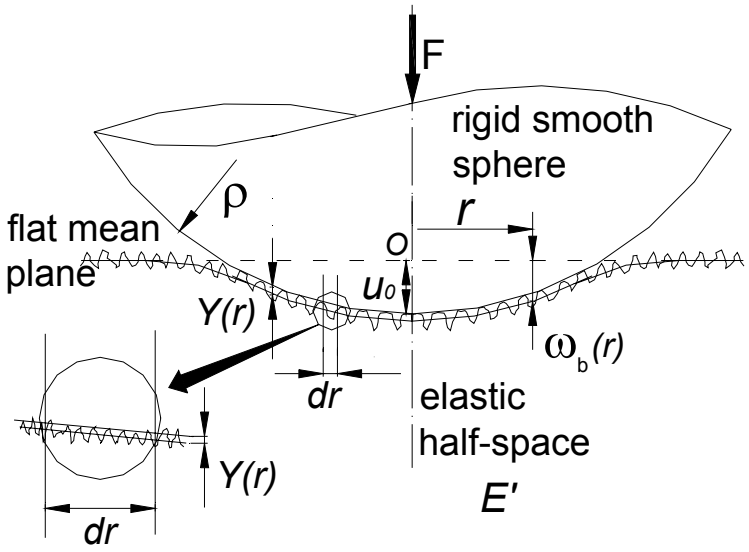

Figure 3-2: Contact geometry after loading

- the load is axisymmetric and the contact is frictionless, i.e., there are no tangential forces in the contact area
- the macrocontact is elastic where the elasticity theory given in Eq. (3.6) is employed to determine the substrate deformation
- the contact is static, i.e., there is no relative motion or vibration effect.

In the vicinity of the contact region the profile of the sphere can be written as

$$u(r) = u_0 - r^2/2\rho \tag{3.8}$$

Figure 3-2 shows the contact geometry after applying the load. The local separation, $Y(r)$, is defined as the distance between two mean planes of the contacting surfaces and can be written as

$$Y(r) = \omega_b(r) - u(r) = \omega_b(r) - u_0 + r^2/2\rho \tag{3.9}$$

At each microcontact a discrete point force is created as illustrated in Fig. 3-3. The sum of these discrete point forces must be equal to the external force, F. It is assumed that the asperities of

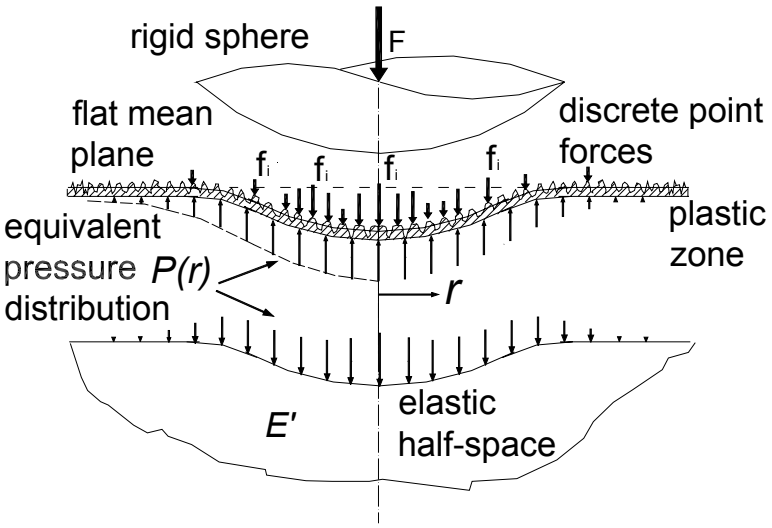

Figure 3-3: Discrete point forces and the equivalent pressure distribution on the plastic zone

the rough surface behave like a plastic zone on an elastic half-space, in the sense that the effect of the discrete point forces on the elastic half-space is considered as an equivalent continuous pressure distribution, $P(r)$. It should be noted that all bulk deformations are assumed to occur in the elastic half space which has an effective elasticity modulus E' and the sphere is assumed to be rigid. Consider an infinitesimal surface element, $dr \to 0$ where Fig. 3-2 shows a magnified element in which the local separation, $Y(r)$, is uniform. The ratio of real to apparent area for a surface element can be found from Eq. (3.2)

$$\frac{dA_r(r)}{dA_a(r)} = \frac{1}{2}\text{erfc } \lambda(r) \tag{3.10}$$

where $dA_a(r) = 2\pi r dr$. As a result of surface curvature, the mean local separation and consequently the mean size of the microcontacts vary with radial position. The local microhardness can be determined from the Vickers microhardness correlation, Eq. (3.3) as a function of the local mean microcontact radius. The relation between the Vickers diagonal d_v and the microcontact radius a_s, based on equal areas, is: $d_v = \sqrt{2\pi}a_s$. Therefore, the local microhardness is

$$H_{mic}(r) = c_1\left[\sqrt{2\pi}a_s(r)\right]^{c_2} \tag{3.11}$$

where the local radius of the microcontacts can be found from Eq. (3.2)

$$a_s(r) = \sqrt{\frac{8}{\pi}} \left(\frac{\sigma}{m}\right) \exp\left[\lambda^2(r)\right] \ \text{erfc}\ \lambda(r) \tag{3.12}$$

The external load F is the summation of the point forces at the microcontacts

$$F = \sum_{i}^{n_s} \mathrm{f}_i = \iint\limits_{contact\ area} H_{mic}(r)\ dA_r(r) \tag{3.13}$$

Substituting Eq. (3.10) into Eq. (3.13)

$$F = \pi \int_0^\infty H_{mic}(r)\, \text{erfc}\ \lambda(r)\ \ r dr \tag{3.14}$$

Instead of a_L, the upper limit of the integral is set to infinity, since the macrocontact radius is not known and the effective pressure distribution rapidly approaches zero. On the bulk side, the equivalent pressure must satisfy the force balance

$$F = 2\pi \int_0^\infty P(r)\, r dr \tag{3.15}$$

The equivalent pressure distribution on the elastic half-space can be found from Eqs. (3.14) and (4.14)

$$P(r) = \frac{1}{2} H_{mic}(r)\, \text{erfc}\ \lambda(r) \tag{3.16}$$

With the pressure distribution, one can find the normal displacement of the bulk from Eq. (3.6). Equations (3.6), (3.9), (3.11), (3.12), (3.15), and (3.16) form a closed set of governing relationships. A computer program was developed to solve the set numerically.

No exact definition exists for the macrocontact radius in the literature. In this study, it is assumed to be the radius where the normalized pressure is negligible, i.e., $P(r = a_L)/P_0 < 0.01$.

Numerical Solution

The following procedure, Fig. 3-4, is used to solve the above-mentioned governing relationships. A value of $u_{0,1}$ is assumed, thus pressure distribution can be computed. $P(r)$ is then used to

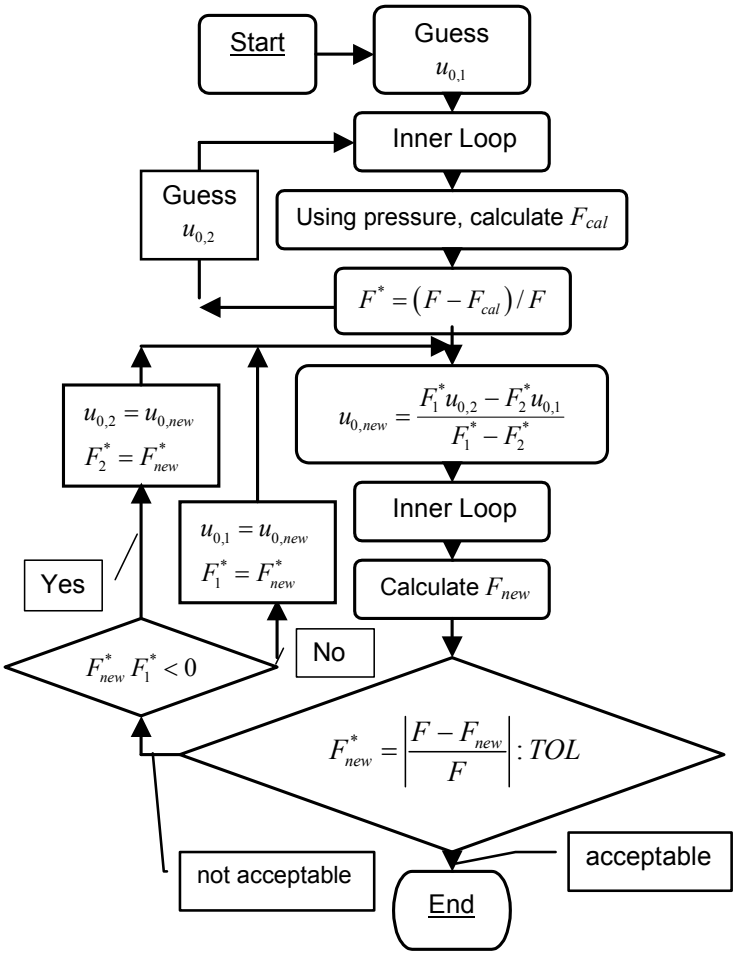

Figure 3-4: Numerical algorithm, the main loop

calculate an improved $\omega_b(r)$.

This improved $\omega_b(r)$ now is used to calculate a new pressure distribution $P_{new}(r)$ and so on until $P(r)$ converges. The algorithm of the above procedure is shown in Fig. 3-5, the inner loop flow chart.

The pressure distribution $P(r)$ is integrated over the macrocontact area and F_{cal} is calculated. The calculated force F_{cal} is compared with the actual external load F and the relative force error F_1^* is determined

$$F^* = \frac{F - F_{cal}}{F} \tag{3.17}$$

Another u_0, $u_{0,2}$, is guessed and all the above-mentioned steps are repeated for $u_{0,2}$ to compute

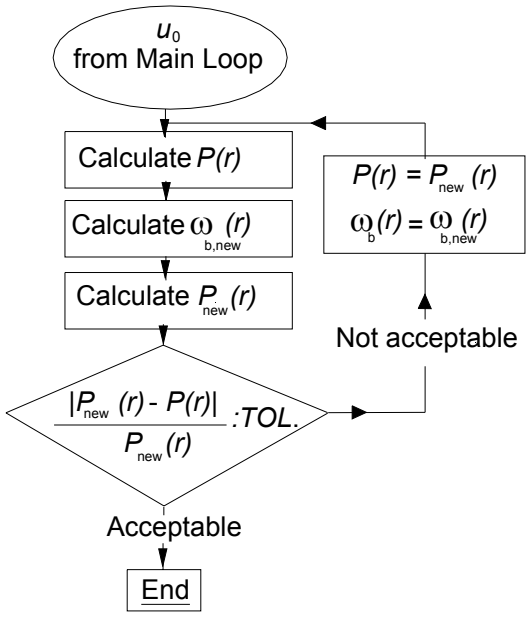

Figure 3-5: Pressure-displacement iteration procedure, the inner loop

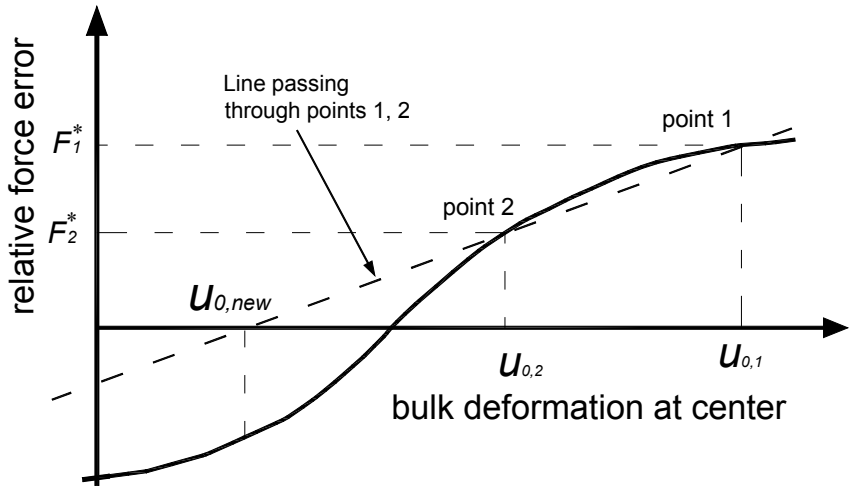

Figure 3-6: Successive iterative method to estimate $u_{0,new}$

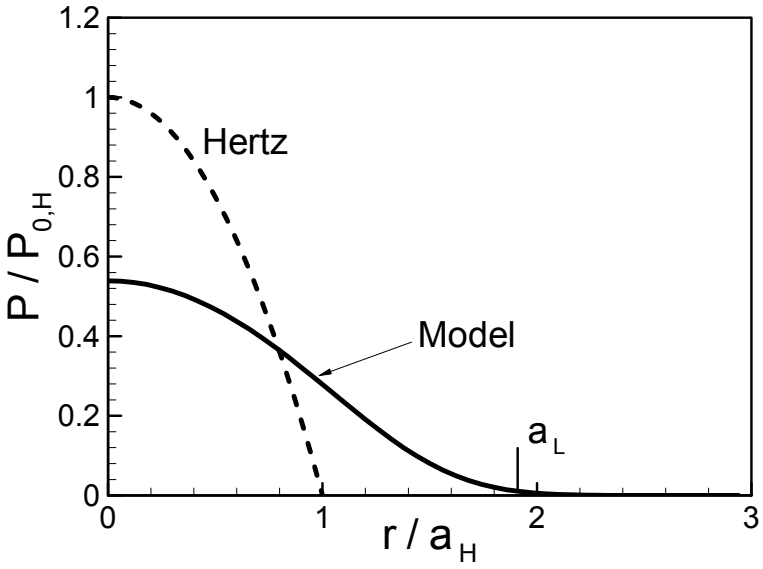

Figure 3-7: Pressure distribution

F_2^*. A line can be fitted to these two points $(u_{0,1}, F_1^*)$ and $(u_{0,2}, F_2^*)$

$$F^* = \frac{F_2^* - F_1^*}{u_{0,2} - u_{0,1}} u_0 + \frac{u_{0,2}F_1^* - u_{0,1}F_2^*}{u_{0,2} - u_{0,1}} \tag{3.18}$$

It should be noted that when the convergence is achieved the relative force error is zero (a negligible value), i.e., $F_{cal} = F$. we can calculate $u_{0,new}$ by setting $F^* = 0$ in Eq. (3.18)

$$u_{0,new} = \frac{F_1^* u_{0,2} - F_2^* u_{0,1}}{F_1^* - F_2^*} \tag{3.19}$$

Then the relative force error F_{new}^* can be calculated through the inner loop procedure. Figure 3-6 shows the linear interpolation method used to determine a new value for $u_{0,new}$. If F_{new}^* is not within the acceptable tolerance, u_0 and F^* are updated and the iterative pressure-displacement calculation procedure is repeated until the convergence is achieved. To make the numerical convergence faster, we used a secant method to update u_0 and F^*, see Fig. 3-4. The loop is continued until the integrated pressure and external load are within an acceptable tolerance.

Table 3.1: Input parameters for a typical contact

$\rho = 25\ mm$	$F = 50\ N$
$\sigma = 1.41\ \mu m$	$E' = 112.1\ GPa$
$m = 0.107$	$c_1/c_2 = 6.27\ GPa/-0.15$

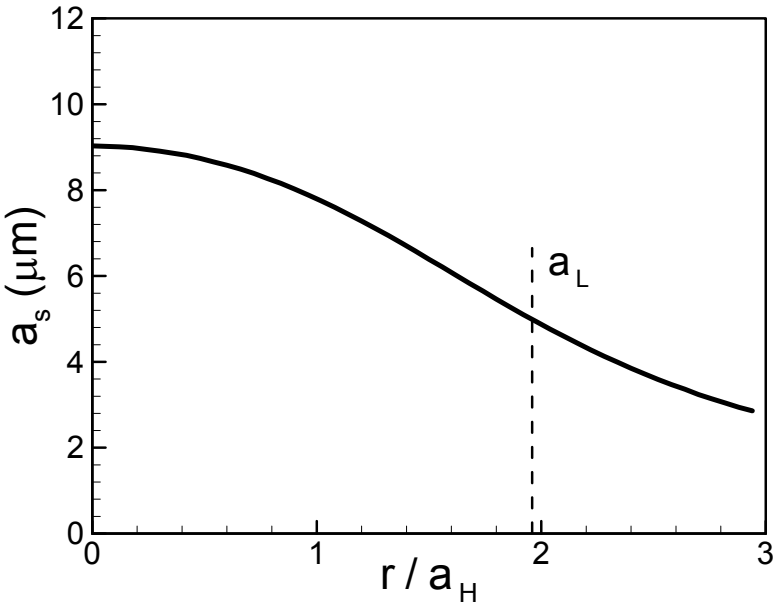

Figure 3-8: Mean microcontacts radius

3.4 Numerical Results

A simulation procedure was run to construct the results shown in Figs. 3-7 to 3-10, based on the algorithms described in the previous section and by using input data shown in Table 3.1. Contact of a SS sphere-flat with an equivalent radius of curvature of 25 mm, equivalent surface roughness of 1.41 μm, and an applied load of 50 N was chosen as an example.

Figure 3-7 shows the pressure distribution predicted by the present model and the Hertzian pressure. It can be seen that due to the presence of roughness the maximum contact pressure compared to the Hertzian contact pressure, is reduced and the load is spread over a greater area. Figure 3-7 also shows the predicted macrocontact radius a_L and that the effective pressure distribution, unlike the Hertzian pressure distribution, falls asymptotically to zero. As expected, the mean radius of microcontacts a_s, and microcontacts density η_s, decrease as the

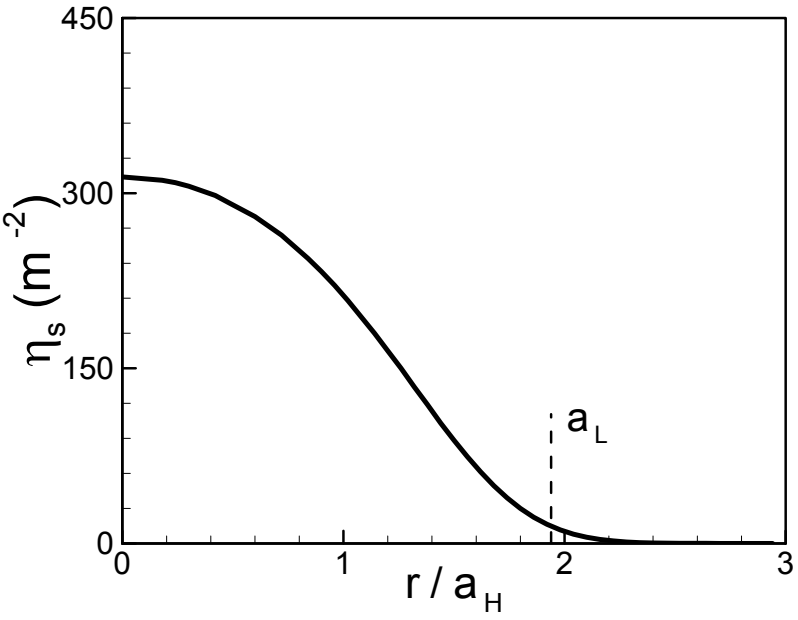

Figure 3-9: Density of microcontacts

radial position r increases. It can be seen in Fig. 3.8 that the mean size of the microcontacts is not zero beyond the predicted macrocontact radius a_L. However as shown in Fig. 3.9 the density of microcontacts is very small for $r > a_L$, thus the real contact is very small. Therefore, the contribution of the microcontacts beyond a_L to the force balance is negligible. The microhardness profile is shown in Fig. 3-10.

To investigate the effect of roughness on the pressure distribution, the program was run for a wide range of roughness from 0.02 to 14.4 μm while all other parameters in Table 3.1 were held constant. Figure 3-11 illustrates the effect of roughness on the pressure distribution. It can be seen that the effective pressure distribution approaches the Hertzian pressure distribution as the roughness decreases.

3.5 Approximate Model

The main goal of this study is to develop simple correlations for determining the effective pressure distribution and the macrocontact radius as functions of non-dimensional parameters that

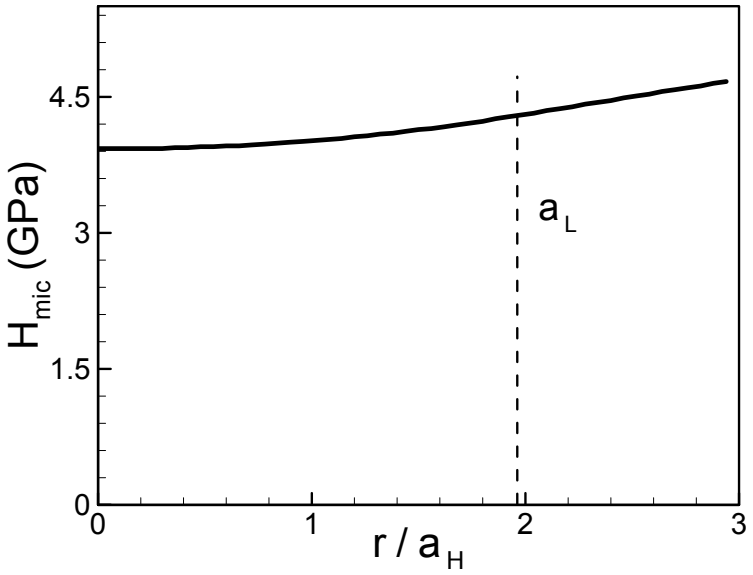

Figure 3-10: Microhardness

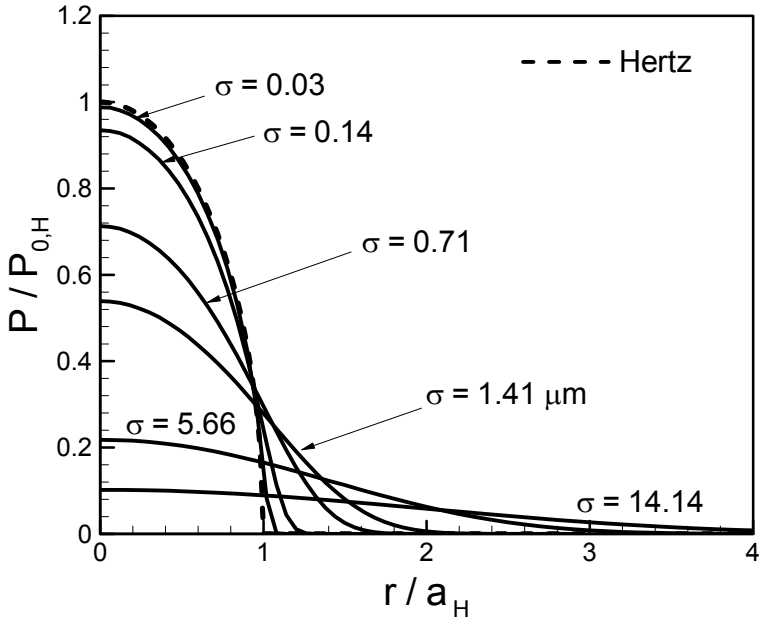

Figure 3-11: Effect of surface roughness on contact pressure distribution

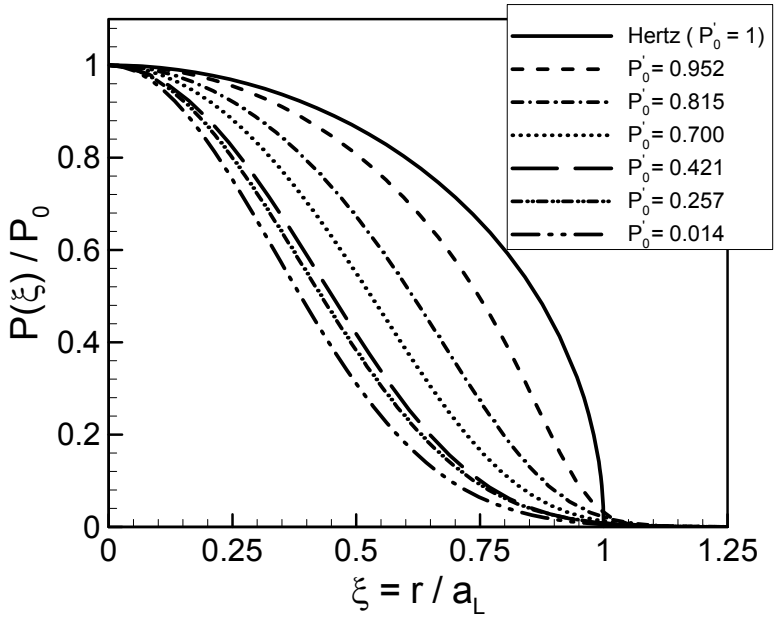

Figure 3-12: Non-dimensional pressure distribution for spherical rough contacts

describe the contact problem. To develop an approximate solution, the following simplifications are made:

- an effective microhardness H_{mic} that is constant throughout the contact region is considered
- the surface slope m is assumed to be a function of surface roughness, σ.

In this section, it is demonstrated that a general pressure distribution as a function of the maximum contact pressure exists. Then, the number of governing non-dimensional parameters is determined using a dimensional analysis. Finally simple correlations for the maximum contact pressure and the macro contact radius are proposed.

Figure 3-12 illustrates non-dimensional pressure distributions for some values of $P_0' = P_0/P_{0,H}$ as a function of non-dimensional radial location $\xi = r/a_L$. It was observed that the non-dimensional pressure distribution can be specified as a function of the dimensionless maximum pressure P_0', and the radial position, ξ. In other words, a general profile exists that presents all possible pressure distributions.

The Hertzian pressure distribution [29] where the contacting surfaces are perfectly smooth is

$$P_H\left(r/a_H\right) = P_{0,H}\sqrt{1-\left(r/a_H\right)^2} \tag{3.20}$$

where

$$P_{0,H} = \frac{3F}{2\pi a_H^2} \quad \text{and} \quad a_H = \left(\frac{3F\rho}{4E'}\right)^{1/3}$$

The profile of the pressure distribution, especially in the contacts where the non-dimensional maximum pressure is less than 0.6, is very similar to a normal (Gaussian) distribution. However, as the non-dimensional maximum pressure approaches one (the Hertzian contact) the pressure distribution begins to deviate from the normal distribution profile.

After considerable investigation, the general profile for the pressure distribution for spherical rough surface contact was found to be

$$P\left(\xi\right) = P_0\left(1-\xi^2\right)^{\gamma} \tag{3.21}$$

where $\xi = r/a_L$, and γ can be calculated through a force balance

$$F = 2\pi\int_0^{a_L} P\left(r\right) r dr \tag{3.22}$$

Substituting Eq. (3.21) into (3.22), after evaluating the integral, one finds

$$\gamma = 1.5P_0'\ \left(a_L'\right)^2 - 1 \tag{3.23}$$

where $P_0' = P_0/P_{0,H}$, and $a_L' = a_L/a_H$.

Using a force balance and Eq. (3.21), one can find a relationship between the maximum contact pressure P_0 and the applied force F as

$$P_0 = \left(1+\gamma\right)\frac{F}{\pi a_L^2} \tag{3.24}$$

At the limit, where roughness approaches zero, P_0' and a_L' both approach one and $\gamma = 0.5$ and Eqs. (3.21) and (3.24) yield the Hertzian pressure distribution, Eq. (3.20).

Table 3.2: Physical input parameters for spherical rough contacts

Parameter	Dimension
Effective elastic modulus, E'	$ML^{-1}T^{-2}$
Force, F	MLT^{-2}
Microhardness, H_{mic}	$ML^{-1}T^{-2}$
Radius of curvature, ρ	L
Roughness, σ	L
Max. contact pressure, P_0	$ML^{-1}T^{-2}$

With the general pressure distribution profile, i.e., Eq. (3.21), the problem is reduced to find relationships for P_0 and a_L. Additionally, the radius of the macrocontact area a_L, based on its definition, can be determined if P_0 and the pressure distribution are known; therefore the key parameter is the maximum contact pressure, P_0.

3.5.1 General Pressure Distribution

Dimensional analysis or the Buckingham Π theorem has been applied to many physical phenomena such as fluid flow, heat transfer and stress and strain problems. The Buckingham Π theorem proves that in a physical problem including n quantities in which there are m dimensions, the quantities can be arranged into $n - m$ independent dimensionless parameters [69]. Table 3.2 summarizes the independent input parameters and their dimensions for spherical rough contacts. H_{mic} is an effective (mean) value for the microhardness of the softer material in contact.

Lambert and Fletcher [6] using published experimental surface data, proposed a correlation for the absolute average asperity slopes, m, as a function of RMS roughness σ

$$m = 0.076\ \sigma^{0.52} \tag{3.25}$$

where σ is the surface RMS roughness in μm, see section 2.2.1 for more detail.

Since the surface slope m can be estimated using Eq. (3.25), it is not considered as an independent input parameter and is not included in Table 3.2.

All quantities in Table 3.2 are known to be essential to the maximum contact pressure and

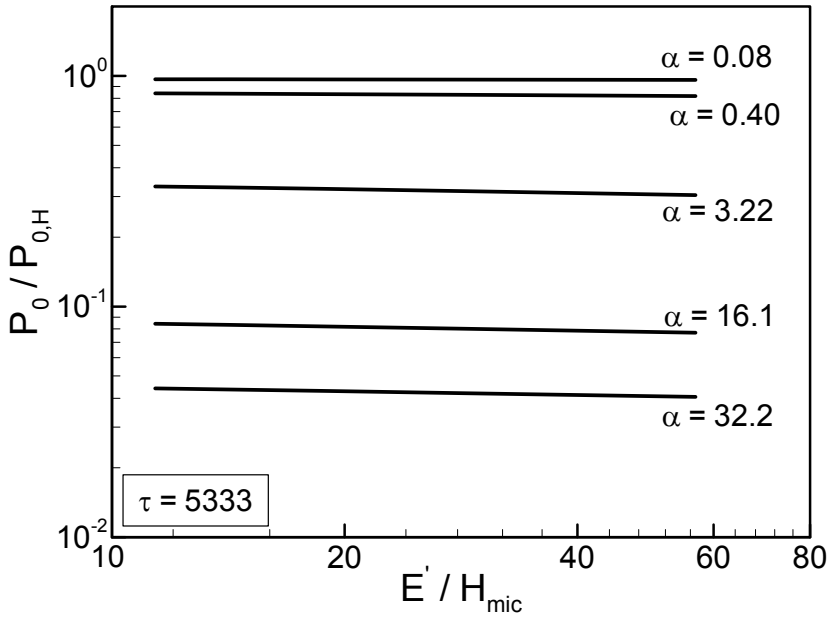

Figure 3-13: Effect of microhardness on non-dimensional maximum contact pressure, $\tau = 5333$

hence some functional relation must exist in the form of

$$P_0 = P_0\left(\rho, \sigma, E', F, H_{mic}\right) \tag{3.26}$$

Applying the Buckingham Π theorem, we find that there are three Π groups so the maximum pressure can be more compactly stated as a function of these three non-dimensional parameters. Following Greenwood et al. [68], we choose α the roughness parameter, Eq. (3.7), as one of the non-dimensional parameters. The other non-dimensional parameters were chosen to be τ the *geometric* parameter, and E'/H_{mic} the *microhardness* parameter. The geometric parameter τ is chosen as

$$\tau = \frac{\rho}{a_H} = \left(\frac{4E'\rho^2}{3F}\right)^{1/3} \tag{3.27}$$

The computer program explained in the previous section was run for a wide range of non-dimensional input parameters, i.e. $0.005 \leq \alpha \leq 100$ and $50 \leq \tau \leq 80\ 000$, to construct Figs. 3-13 - 3-16. These values of α and τ are chosen to span a wide range applicable to most thermal contact resistance problems. Values of α include the entire range of spherical rough contacts

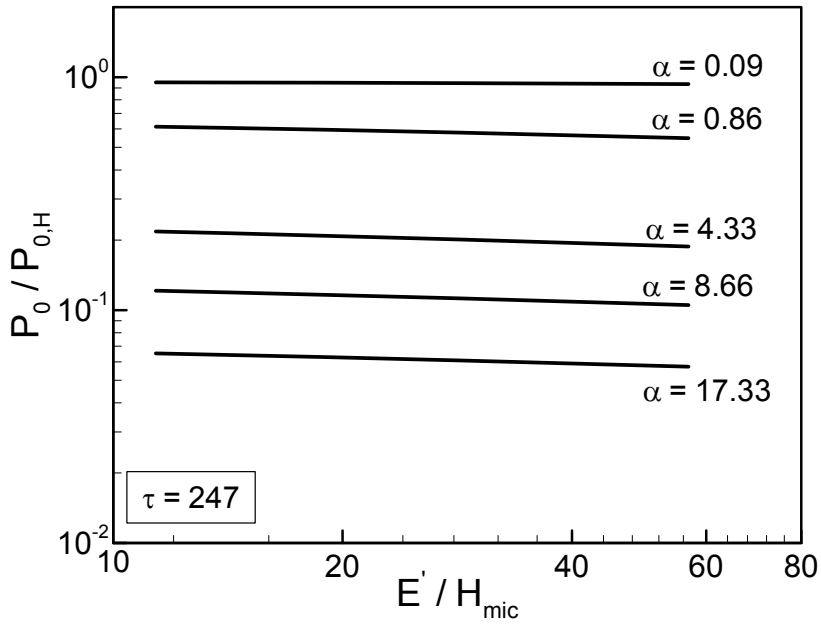

Figure 3-14: Effect of microhardness on non-dimensional maximum contact pressure, $\tau = 247$

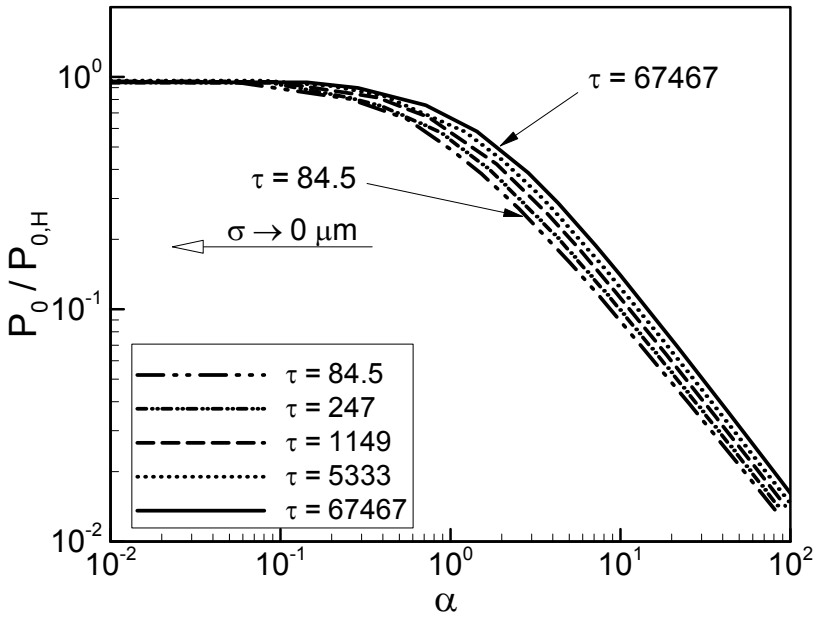

Figure 3-15: Non-dimensional maximum contact pressure

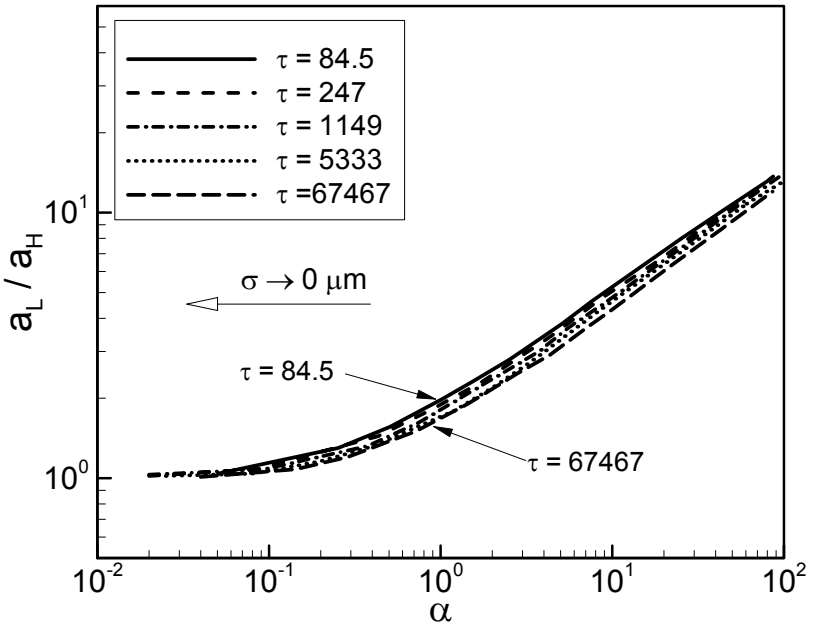

Figure 3-16: Non-dimensional radius of macrocontact

from very smooth (Hertzian $\alpha = 0$) to extremely rough contacts. The geometric parameter τ may be interpreted as a measure of the bulk strain. Since the bulk deformation is assumed "elastic" and also to justify the half-space assumption [29] the radius of curvature must be much larger than the contact area, $\rho \gg a_H$. Thus the lower bound of τ was set arbitrarily at $\tau = 50$ and the upper bound was selected to cover a relatively large radii of curvature and light loads.

The effect of microhardness parameter E'/H_{mic}, on the maximum contact pressure P_0' was observed to be small and may be ignored, see Figs. 3-13 and 3-14. Figure 3-15 illustrates the dimensionless maximum contact pressure in the form of a family of curves for a wide range of α and τ. As α decreases, which is equivalent to a decrease in roughness or an increase in the applied load, the dimensionless maximum pressure approaches unity, the Hertzian pressure. Figure 3-16 illustrates the macrocontact radius as a function of α and τ. As can be seen, by decreasing α, the dimensionless radius of contact approaches one or the Hertzian contact.

The dimensionless maximum contact pressure and the macrocontact radius plots were curve fitted. The following expressions can be used to estimate the maximum dimensionless contact

pressure and the dimensionless radius of contact, respectively

$$P_0' = \frac{P_0}{P_{0,H}} = \frac{1}{1 + 1.37\alpha\ \tau^{-0.075}} \tag{3.28}$$

$$a_L' = \frac{a_L}{a_H} = \begin{cases} 1.605/\sqrt{P_0'} & 0.01 \leq P_0' \leq 0.47 \\ 3.51 - 2.51P_0' & 0.47 \leq P_0' \leq 1 \end{cases} \tag{3.29}$$

The maximum difference between Eqs. (3.28) and (3.29) and the full model is estimated to be less than 4.5 percent in the range of $0.01 \leq P_0' \leq 1$. An expression for the non-dimensional radius of the macrocontact, a_L', was developed as a function of α and τ in the form of

$$a_L' = \frac{a_L}{a_H} = 1.80\frac{\sqrt{\alpha + 0.31\tau^{0.056}}}{\tau^{0.028}} \tag{3.30}$$

The following approximate expression for a_L is proposed for contacts where the effective radius of curvature is relatively large, i.e., approaching flat surface

$$a_L' = 1.5\sqrt{\alpha + 0.45} \tag{3.31}$$

It is clear from Eqs. (3.28) and (3.30) that the effect of surface roughness on the contact pressure and the macrocontact area is governed primarily by the roughness parameter α and parameter τ has a second order effect.

The maximum contact pressure P_0 from Eq. (3.28), is compared with the GT [38] model in Fig. 3-17 over a range of α, for two values of μ which bracket a wide range of contacts [68]. As shown, both models demonstrate the same trend over the comparison range; the two values of τ were chosen to best fit the GT curves shown, they also cover a wide range of contacts.

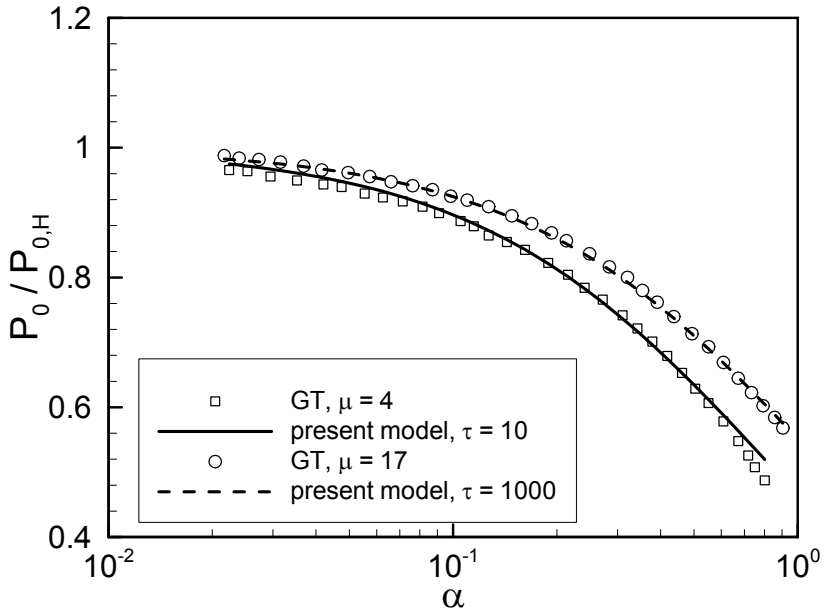

Figure 3-17: Comparison between present model and Greenwood and Tripp model, maximum contact pressure

3.5.2 Compliance

The elastic deformation of the half-space can be calculated by substituting the general pressure distribution Eq. (3.21) into Eq. (3.6), where the radius of the contact area is a_L as:

$$\omega_b'(\xi) = \begin{cases} \dfrac{\pi}{4} B(0.5, \gamma+1) & \xi = 0 \\ \displaystyle\int_0^{\xi} s\left(1-s^2\right)^{\gamma} K\left(\frac{s}{\xi}\right) ds & s < \xi \\ \displaystyle\int_{\xi}^{1} \left(1-s^2\right)^{\gamma} K\left(\frac{\xi}{s}\right) ds & s > \xi \end{cases} \tag{3.32}$$

where $B(x,y)$ and $\omega_b' = \pi E' \omega_b / (4P_0\, a_L)$ are the beta function and the non-dimensional bulk deformation, respectively. A general analytical solution for the integrals in Eq. (3.32) does not exist and they must be solved numerically for different values of γ. Since, the deformation at the edge of the contact area is required to calculate the compliance, Eq. (3.32) was solved numerically for a wide range of γ at $\xi = 1$. The solution was correlated and the following

relationship is proposed:

$$\omega_b\left(a_L\right)=\frac{4P_0\ a_L}{\pi E'\left[4.79-3.17\left(P_0'\right)^{3.13}\right]} \tag{3.33}$$

where $0<P_0'\leq 1$. The maximum relative difference between Eq. (3.33) and the numerical solution is approximately 4.6 percent. In the Hertzian limit, elastic deformations of the half-space at the center and the edge of the contact area are

$$\omega_{b,H}\left(0\right)=\frac{a_H^2}{\rho}=\frac{\pi P_{0,H}\ a_H}{2E'} \tag{3.34}$$

$$\omega_{b,H}\left(a_H\right)=\frac{a_H^2}{2\rho}=\frac{\pi P_{0,H}\ a_H}{4E'} \tag{3.35}$$

It can be seen that in the Hertzian limit, Eqs. (3.32) and (3.33) yield the Hertzian values, i.e., Eqs. (3.34) and (3.35), respectively. Figure 3-18 shows non-dimensional deformations at the center $\omega_b'\left(0\right)$ and at the edge of the contact area $\omega_b'\left(a_L\right)$; in addition, the ratio of these deformations is shown in the plot over a wide range of P_0'. As the non-dimensional maximum pressure decreases, i.e., the effect of roughness becomes more significant, bulk deformations at both the center and the edge of the contact decrease. As seen in Fig. 3-18, the ratio of deformations, $\omega_b\left(0\right)/\omega_b\left(a_L\right)$, increases as the non-dimensional maximum pressure P_0' decreases. In other words, the ratio of $\omega_b\left(0\right)/\omega_b\left(a_L\right)$ is larger for "rougher" contacts which is a direct result of the general pressure distribution profile, i.e., the general pressure falls off faster than the Hertzian pressure, see Fig. 3-12.

The mutual approach of distant points in the two solids is called compliance. Compliance between rough spherical bodies is a function of asperity deformation $\omega_a\left(r\right)$, the bulk deformation $\omega_b\left(r\right)$, and the sphere profile and is given by [70]

$$\kappa=r^2/2\rho+\omega_a\left(r\right)+\omega_b\left(r\right)$$

Assuming the deformation of asperities at the edge of the contact area is zero $\omega_a\left(a_L\right)=0$, one can find the compliance from

$$\kappa=a_L^2/2\rho+\omega_b\left(a_L\right) \tag{3.36}$$

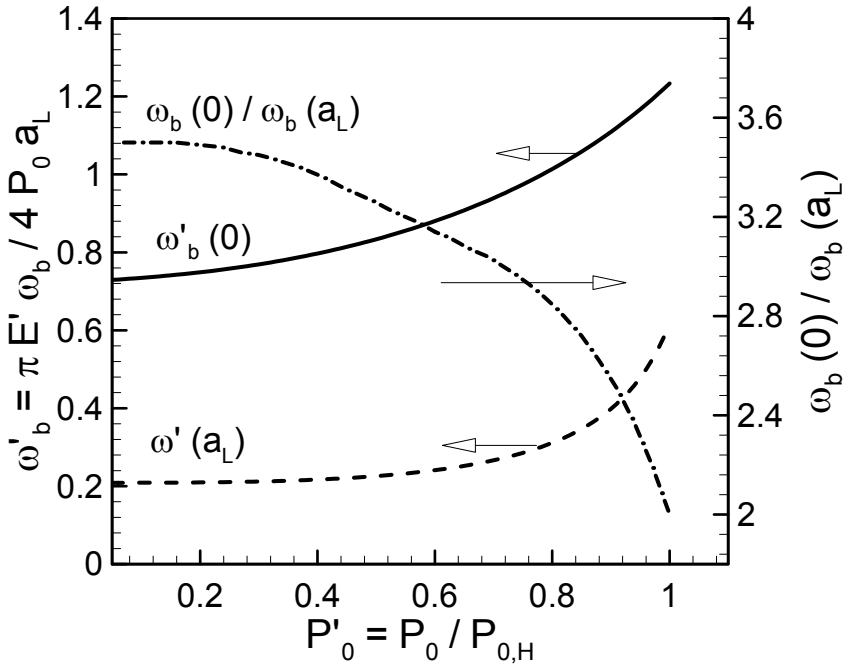

Figure 3-18: Bulk deformation at center and edge of contact area

Combining Eqs. (3.29), (3.33), and (3.36), one obtains

$$\kappa' = \frac{\kappa}{\kappa_H} = 0.5\left(a'_L\right)^2 + \frac{8P'_0\ a'_L}{\pi^2\left[4.79 - 3.17\left(P'_0\right)^{3.13}\right]} \tag{3.37}$$

where $\kappa_H = a_H^2/\rho$ is the Hertzian compliance. Equation (3.37) is plotted in Fig. 3-21 for a range of P'_0.

3.6 Comparison With Experimental Data

To verify the proposed model, the radius of the contact area and the compliance predicted by the model are compared with experimental data collected by Tsukada and Anno (TA) [49], Greenwood et al. (GJM) [68], and Kagami et al. (KYH) [70]. The experimental arrangement contains a smooth sphere placed in contact with a rough plane. The contact area was made visible by depositing a thin layer of copper [68] or an evaporated carbon film and a lamp black film [70]. The contact radii were measured using a metallurgical microscope. Due to

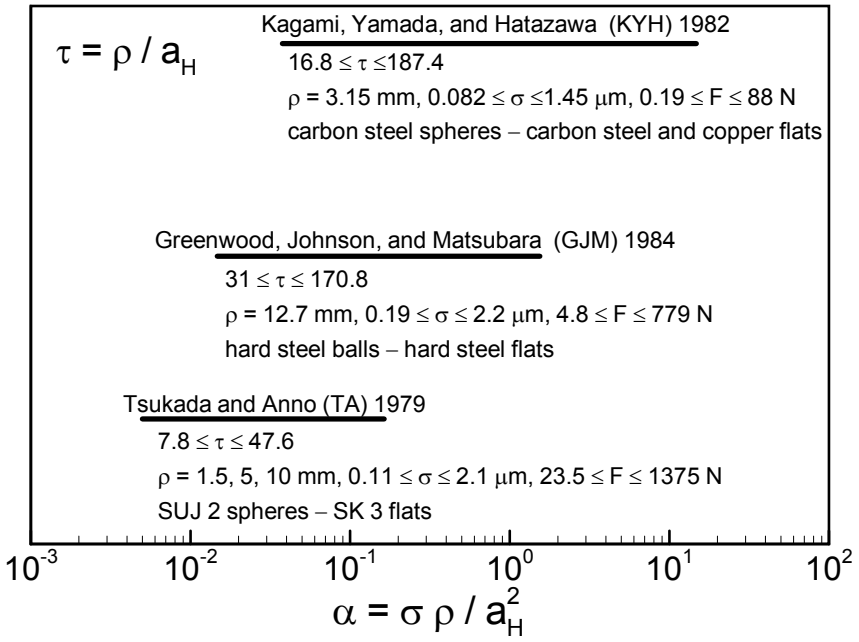

Figure 3-19: Summary of parameter values of experimental data

the measurement method, the experimental data may contain a relatively high uncertainty particularly at light loads or very rough surfaces since it involved some degree of judgment. Ranges of non-dimensional parameters α and τ covered by the experimental data are shown in Fig. 3-19. The experimental data include contact between similar (steel-steel) and dissimilar (steel-copper) materials and cover a relatively wide range of load, roughness, and radius of curvature. The proposed relationship for a_L, Eq. (3.29) is compared with the data in Fig. 3-20 and good agreement is observed. The present model shows the data trend over the entire range of the comparison. More than 160 data points, 26 sets, were compared with the present model in Fig. 3-20. Specimen materials, roughness, and radius of curvature for data sets are listed in Fig. 3-20. The RMS difference between the proposed expression and the data is approximately 6.2 percent.

Greenwood et al. [68] compared their data and Kagami et al. [70] data with the GT model. Their comparison showed a relatively high discrepancy especially with the Kagami et al. data. Greenwood et al. attributed the observed discrepancy to the experimental difficulties

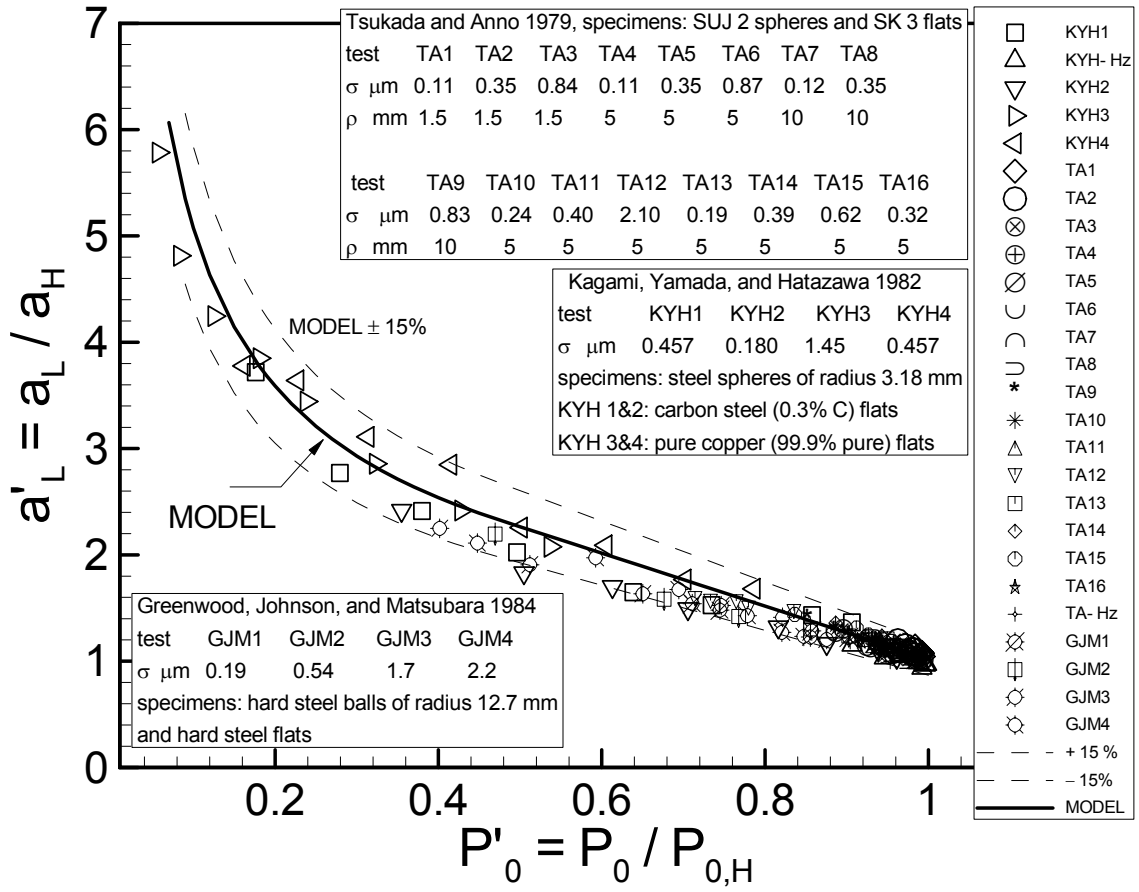

Figure 3-20: Comparison between present model and experimental data, contact radius

of measuring the contact radius. They also stated that the Kagami et al. data did not correlate particularly well with the roughness parameter α. However, as can be seen in Fig. 3-20, this discrepancy has not been encountered in this study. Additionally, our comparison shows that the Kagami et al. data (except for a few points for very rough surfaces at light loads) follow the correlation very well.

Kagami et al. [70] also measured the compliance between a smooth steel sphere and rough steel and copper plates. They collected more than 40 data points, two steel-steel and two steel-copper sets. Compliances were measured under various loads and with different roughness using differential transformers [70]. Figure 3-21 shows the comparison between the present model, Eq. (3.37) and the KYH compliance data. The present model shows good agreement with the

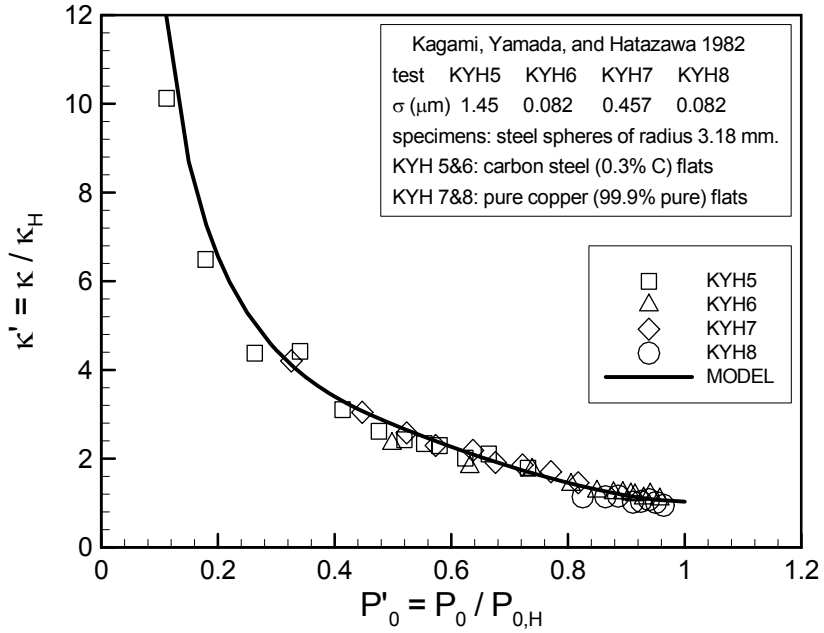

Figure 3-21: Comparison between present model and experimental data, compliance

RMS difference approximately 7.7 percent.

3.7 Elastic Compression

In most engineering applications the size of the contacting bodies is finite and/or the radius of curvature is large, especially in the contacts where the surfaces are almost flat or slightly curved. The macrocontact area extends to the boundaries of the contacting bodies, i.e., $a_L = b_L$, as a result of applying a specific force that we call the *critical force*, F_c, see Fig. 3-22. The size of the macrocontact area remains constant as the force is increased beyond the critical force, but the contact pressure increases. Since the bulk deformation is assumed to be elastic, we refer to the above contact problems as *elastic compression*. Elastic compression cannot be treated as a half-space contact problem, since the half-space assumption cannot be justified especially in the regions close to the edge of the contacting bodies. The critical force and the critical pressure distribution, the pressure distribution associated with the critical force for a specified spherical rough contact assembly are unique.

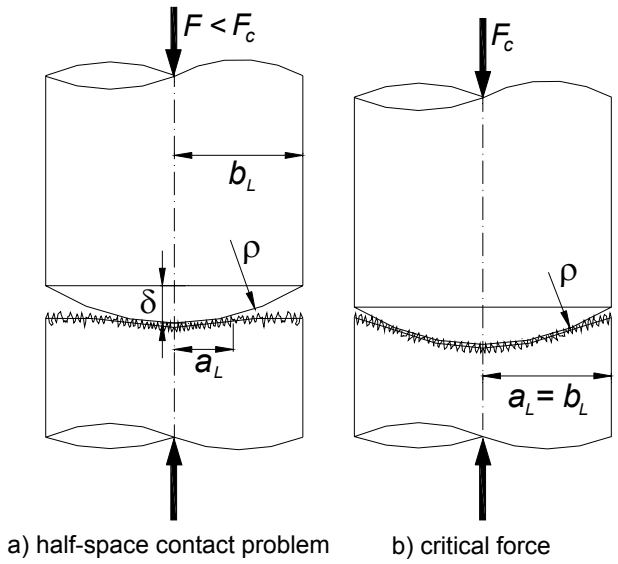

Figure 3-22: Contact of two finite spherical rough bodies

In contact stress theory the displacement at any point in the contact surface depends on the distribution of pressure throughout the whole contact. According to Johnson [20] the above interconnection may be avoided if the solids are modeled by a simple Winkler elastic foundation rather than a half-space. As illustrated in Fig. 3-23, the elastic compression approximation implies that as load passes the critical load the elastic foundation, which rests on a rigid base, is compressed by the rigid spherical indenter. There is no interaction between the springs of the model, i.e., shear between adjacent elements of the foundation is ignored. Therefore, contact pressure at any point depends only on the displacement at that point. Equation (3.21) can be used to calculate the contact pressure distribution, where the external force is less than or equal to the critical load. Beyond the critical load where $F > F_c$, the size of the macrocontact remains constant and the elastic foundation approximation may be used to determine the pressure distribution. A uniform increase will be added to the critical pressure distribution at each point in the contact area by assuming the elastic foundation approximation. Therefore,

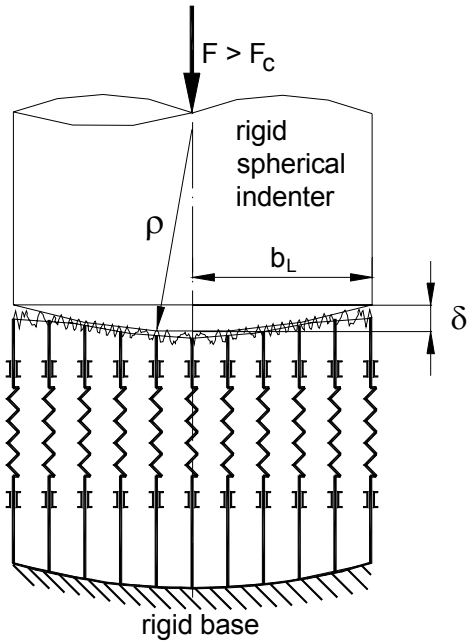

Figure 3-23: Elastic foundation, Winkler model

the general pressure distribution can be summarized as

$$P(\xi) = \begin{cases} P_0 \left(1-\xi^2\right)^{\gamma} & F \leq F_c \\ P_{0,c} \left(1-\xi^2\right)^{\gamma_c} + \dfrac{F-F_c}{\pi b_L^2} & F \geq F_c \end{cases} \tag{3.38}$$

where $a_L = b_L$ for $F \geq F_c$, $P_{0,c}$, and γ_c are the maximum pressure and the exponent of the critical pressure distribution, respectively. Figure 3-24 shows the predicted pressure distributions for some values of the external load as an example. The parameters of the contact are: $\rho = 10\ m$, $E' = 112\ GPa$, $\sigma = 2\ \mu m$, and $b_L = 12\ mm$.

To find a relationship for the critical force, Eqs. (3.28) and (3.31) should be solved simultaneously where $a_L = b_L$. Equation (3.31) is a function of α only and it was developed for relatively large radii of curvature, i.e., the situations where the elastic compression more likely occurs. The critical force can be estimated from,

$$F_c = \frac{4E'}{3\rho} \left[\max\left\{0, \left(b_L^2 - 2.25\sigma\rho\right)\right\}\right]^{3/2} \tag{3.39}$$

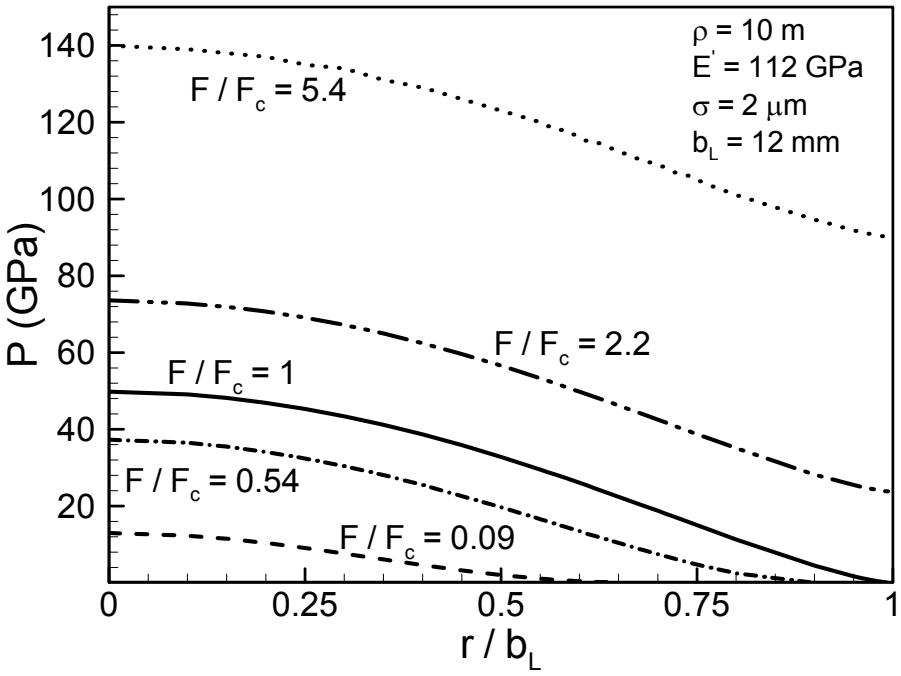

Figure 3-24: Contact pressure distribution

where $\max\{x, y\}$ returns the maximum value between x and y.

A criterion for defining the flat surface, where the surface curvature has a negligible effect on the pressure distribution can be derived by setting $F_c = 0$. Setting F_c equal to zero means that if no load is applied $a_L = b_L$, thus the contacting surfaces are *ideally* flat, which leads to

$$\frac{b_L^2}{\sigma\rho} \leq 2.25 \tag{3.40}$$

For spherical surfaces with large radii of curvature, Clausing and Chao [4] used a geometrical approximation that relates the maximum out-of-flatness, δ (see Fig. 3-23) to the radius of curvature

$$\rho = \frac{b_L^2}{2\delta} \tag{3.41}$$

Combining Eqs. (3.40) and (3.41), we obtain a criterion for out-of-flatness of a flat surface

$$\frac{\delta}{\sigma} \leq 1.12 \tag{3.42}$$

In other words, if the out-of-flatness and the roughness of a surface are in the same order of magnitude, the surface is flat, i.e., surface curvature has no effect on the contact pressure distribution. This criterion is derived based on the concept that the effect of surface curvature on the contact pressure is negligible in flat or conforming contacts. In the next Chapter another criterion will be defined based on a thermal contact resistance perspective.

3.8 Summary and Conclusions

The mechanical contact of spherical rough surfaces was studied and a new analytical model was developed. The deformations of surface asperities were considered to be plastic while the bulk deformation was assumed to remain within the elastic limit.

A closed set of governing relationships was derived and solved numerically. A computer code was developed to solve the governing relationships. The pressure distributions predicted by the model were plotted for different values of surface roughness and it was shown that as the surface roughness approaches zero the predicted pressure distribution approaches the Hertzian pressure.

Additionally, it was shown that a general pressure distribution profile exists that encompasses all spherical rough contacts. The maximum contact pressure was observed to be the key parameter that specifies the contact pressure distribution. The suggested general pressure distribution expression yields the Hertzian contact pressure at the limit, where roughness is set to zero.

Using dimensional analysis, we obtained the number of independent non-dimensional parameters that describe the maximum contact pressure to be three, the roughness α, the geometric τ, and the microhardness E'/H_{mic} parameters. The effect of the microhardness parameter E'/H_{mic} on the maximum contact pressure was observed to be small and therefore ignored. Simple correlations were suggested for calculating the maximum contact pressure distribution and the radius of the macrocontact area, as functions of roughness α, and geometric parameters τ. The present model was also compared with the existing model of Greenwood and Tripp [38] and showed good agreement. Elastic deformation produced on the half-space as a result of applying the general pressure distribution was found. Compact relationships for the deforma-

tion at the center and at the edge of the contact area were proposed. Additionally, a simple expression for the compliance of spherical rough contacts was proposed. The compliance and the contact radius predicted by the model were compared against more than 200 experimental data points collected by others and showed good agreement.

An expression for estimating the critical load was derived, where $a_L = b_L$. The Winkler approximation was used to derive a relationship for the contact pressure distributions, where the loads are higher than the critical load. This expression along with the above correlation formed a general pressure distribution that encompasses all possible contact cases ranging from the smooth Hertzian to the conforming rough contact.

Also a criterion was offered to identify the flat surface, where the effect of surface curvature on the contact pressure can be neglected. Based on this criterion, the surface can be considered flat if the surface out-of-flatness and roughness are in the same order of magnitude.

The advantages of the present model over the Greenwood and Tripp [38] (GT) model can be summarized as,

- the present model requires two input surface parameters, roughness σ, and surface slope m. The GT model needs three input parameters, i.e., σ_s, β, and η_s
- unlike the summit radius β and the microcontact density η_s in the GT model, the present model input parameters can be measured directly and they are not sensitive to the surface measurements
- for the present model, a general pressure distribution profile was proposed that covers all possible spherical contact cases
- simple correlations are proposed for determining the maximum contact pressure and the radius of macrocontact as functions of two non-dimensional parameters, i.e., the roughness parameter α and the geometric parameter τ. While the GT model requires computer programing and tedious iteration methods.

Chapter 4

Thermal Analysis

4.1 Introduction

As mentioned in Chapter 1, thermal energy can be transferred between rough contacting bodies in a vacuum via conduction through the microcontacts and radiation. Radiation heat transfer across the interface is small and therefore is ignored. As illustrated in Fig. 1-1, heat flow is constrained to pass through the macrocontact, and then, in turn through the microcontacts. Two sets of resistances in series can be used to represent the thermal contact resistance (TCR) for a joint in a vacuum: the large-scale or macroscopic constriction resistance, R_L, and the small-scale or microscopic constriction resistance, R_s [59, 22, 14]

$$R_j = R_s + R_L \tag{4.1}$$

Many theoretical models for determining TCR have been developed for two limiting cases, i) conforming rough, where contacting surfaces are assumed to be perfectly flat, and ii) elasto-constriction, where the effect of roughness is neglected, i.e., contact of two smooth spherical surfaces. The above limiting cases are simplified cases of real contacts since engineering surfaces have both out-of-flatness and roughness simultaneously. As discussed in Chapter 1, TCR problems basically consist of three separate problems: 1) geometrical, 2) mechanical, and 3) thermal, each sub-problem also includes a micro and macro scale component. A mechanical model was developed and presented in Chapter 3 of this study. The mechanical analysis determines the

macrocontact radius and the effective pressure distribution for the large-scale contact problem. The microcontact analysis gives the local separation between the mean planes of the contacting bodies, the local mean size and the number of microcontacts. The results of the mechanical analysis are used in the thermal analysis to calculate the microscopic and macroscopic thermal constriction resistances.

Few analytical models for contact of two non-conforming rough surfaces exist in the literature. In Chapter 2, existing analytical non-conforming rough TCR models are reviewed and it was showed through comparison with experimental data that none of the existing models covers the above mentioned limiting cases and the transition region in which both roughness and out-of-flatness are present and their effects on TCR are of the same importance.

4.2 Theoretical Background

Considering the curvature or out-of-flatness of contacting surfaces in a comprehensive manner is very complex because of its random nature. Certain simplifications must be introduced to describe the macroscopic topography of surfaces using a few parameters. Theoretical approaches by Clausing and Chao [59], Mikic and Rohsenow [14], Yovanovich [22], Nishino et al. [5], and Lambert and Fletcher [6] assumed that a spherical profile might approximate the shape of the macroscopic nonuniformity. According to Lambert [23] this assumption is justifiable, because nominally flat engineering surfaces are often spherical, or crowned (convex) with a monotonic curvature in at least one direction. The approximate relationship between the radius of curvature and the maximum out-of-flatness, for relatively large radii of curvature (approaching flat), is [4]

$$\rho = \frac{b_L^2}{2\delta} \tag{4.2}$$

where δ is the maximum out-of-flatness of the surface.

When two non-conforming random rough surfaces are placed in mechanical contact, many microcontacts are formed within the macrocontact area. Microcontacts are small and located far from each other. Thermal contact models are constructed based on the premise that inside the macrocontact area a number of parallel cylindrical heat channels exist. The real shapes of microcontacts can be a wide variety of singly connected areas depending on the local profile

of the contacting asperities. Yovanovich et al. [52] studied the steady-state thermal constriction resistance of singly connected planar contacts of arbitrary shape. By using an integral formulation and a semi-numerical integration process applicable to any shape, they proposed a definition for thermal constriction resistance based on the square root of the contact area. A non-dimensional constriction resistance based on the square root of area was proposed, which varied by less than 5% for all shapes considered. Yovanovich et al. [52] concluded that the real shape of the contact was a second order effect, and an equivalent circular contact, where surface area is preserved, can be used to represent the contact.

As the basic element for macro and micro thermal analysis, thermal constriction of the flux tube was employed by many researchers. Cooper et al. [7] proposed a simple accurate correlation for calculating the thermal spreading resistance of the isothermal flux tube, (see section 2.4.1 for more detail):

$$R_{\text{flux tube 1}} + R_{\text{flux tube 2}} = \frac{\psi(\varepsilon)}{2k_s a} = \frac{(1-\varepsilon)^{1.5}}{2k_s a} \tag{4.3}$$

where $\varepsilon = a/b$, $k_s = 2k_1k_2/(k_1+k_2)$, and $\psi(\cdot)$ is the spreading resistance factor. In Eq. (4.3), it is assumed that the radii of two contacting bodies are the same, i.e., $b_1 = b_2 = b$. For the general case where $b_1 \neq b_2$, thermal spreading resistance will be, $R_{\text{flux tube}} = \psi(a/b)/4ka$.

Figure 4-1 illustrates the thermal resistance network for non-conforming rough contacts. The total or joint resistance can be written as

$$R_j = R_{L,1} + R_{s,1} + R_{s,2} + R_{L,2} \tag{4.4}$$

where

$$\left(\frac{1}{R_s}\right)_{1,2} = \left(\sum_{i=1}^{n_s} \frac{1}{R_{s,i}}\right)_{1,2} \tag{4.5}$$

where n_s, $R_{s,i}$ are the number of microcontacts and the resistance of each microcontact, respectively. Subscripts 1, 2 signify bodies 1, 2.

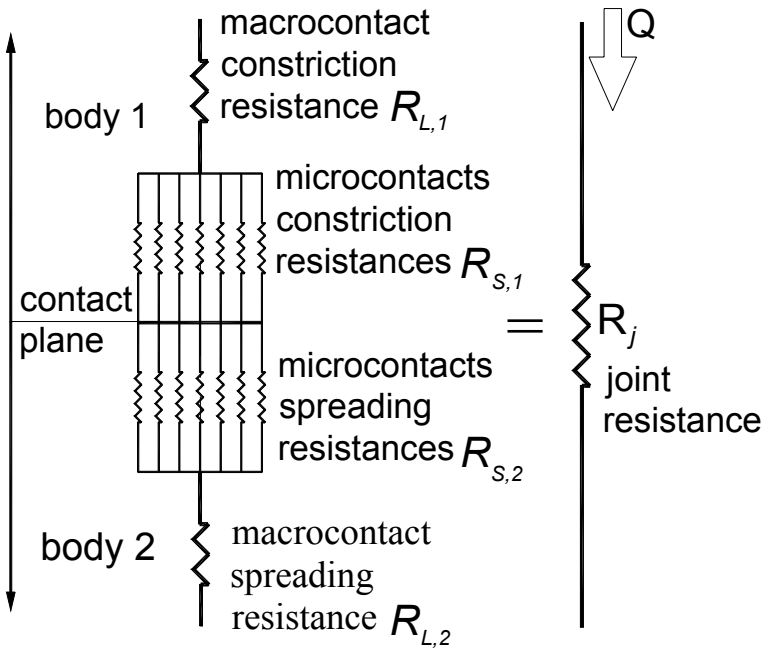

Figure 4-1: Thermal resistance network for non-conforming rough contacts in a vacuum

4.3 The Present Model

In addition to the geometrical and mechanical assumptions, which were discussed in Chapter 3, the remaining assumptions of the present model are:

- contacting solids are isotropic and thick relative to the roughness
- radiation heat transfer is negligible
- microcontacts are circular and steady-state heat transfer at microcontacts
- microcontacts are isothermal, Cooper et al. [7] showed that all microcontacts must be at the same temperature, provided the conductivity in each body is independent of direction, position and temperature.
- surfaces are clean and the contact is static.

Figure 4-2 shows the geometry of the contact with equivalent radius of curvature and roughness where a_L is the radius of the macrocontact area and b_L is the radius of the contacting

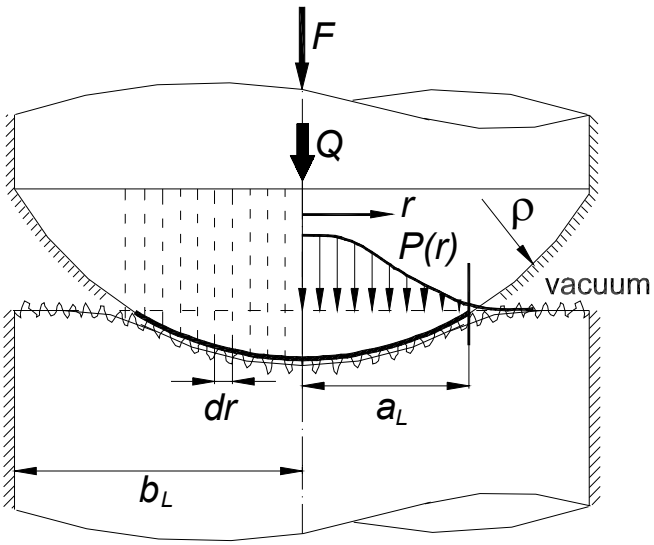

Figure 4-2: Geometry of contact

bodies.

The flux tube solution is employed to determine the macrocontact thermal resistance, i.e.,

$$R_L = \frac{(1 - a_L/b_L)^{1.5}}{2k_s a_L} \tag{4.6}$$

Separation between the mean planes of contacting bodies and pressure distribution are not uniform in the contact area, consequently, the number and the average size of microcontacts decrease as the radial position r increases. Figure 4-3 illustrates the modeled geometry of the microcontact distribution, macrocontact area the circle with radius a_L, is divided into surface elements, dashed rings with increment dr. Figure 4-3 shows the mean average size of microcontacts as small filled-circles. Around each microcontact a dashed circle illustrates the flux tube associated with the microcontact. While microcontacts can vary in both size and shape, a circular contact of equivalent area can be used to approximate the actual microcontacts, since the local separation is uniform in each surface element.

Local spreading resistance for microcontacts can be calculated by applying the flux tube expression

$$R_s(r) = \frac{\psi[\varepsilon(r)]}{2k_s a_s(r)} \tag{4.7}$$

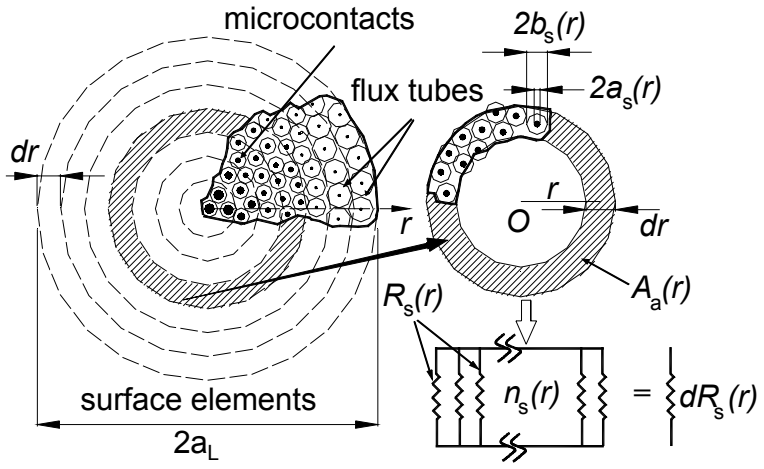

Figure 4-3: Microcontacts distribution in contact area and thermal resistance network for a surface element

where $\varepsilon(r) = a_s(r)/b_s(r)$ is the local microcontacts relative radius, $a_s(r)$, $\psi(\cdot)$ are the local mean average microcontact radius and the spreading resistance factor given by Eq. (4.3).

The microcontacts local density and relative radius can be calculated from, see Chapter 3,

$$\varepsilon(r) = \sqrt{\frac{A_r(r)}{A_a(r)}} = \sqrt{\frac{1}{2}\text{erfc }\lambda(r)} \tag{4.8}$$

$$n_s(r) = \frac{1}{16}\left(\frac{m}{\sigma}\right)^2 \frac{\exp\left[-2\lambda^2(r)\right]}{\text{erfc }\lambda(r)} A_a \tag{4.9}$$

where $\lambda(r) = Y(r)/\sqrt{2}\sigma$, A_r and A_a are non-dimensional separation, and real and apparent contact area, respectively.

Thermal resistance network for a surface elements dr is shown in Fig. 4-3. In each element $n_s(r)$ microcontacts exist which provide identical parallel paths for transferring thermal energy. Therefore, microcontact thermal resistance for a surface element $dR_s(r)$ is

$$dR_s(r) = \frac{R_s(r)}{n_s(r)} \tag{4.10}$$

As shown in Fig. 4-4, surface elements form another set of parallel paths for transferring thermal energy in the macrocontact area. Therefore, the effective micro thermal resistance for the joint

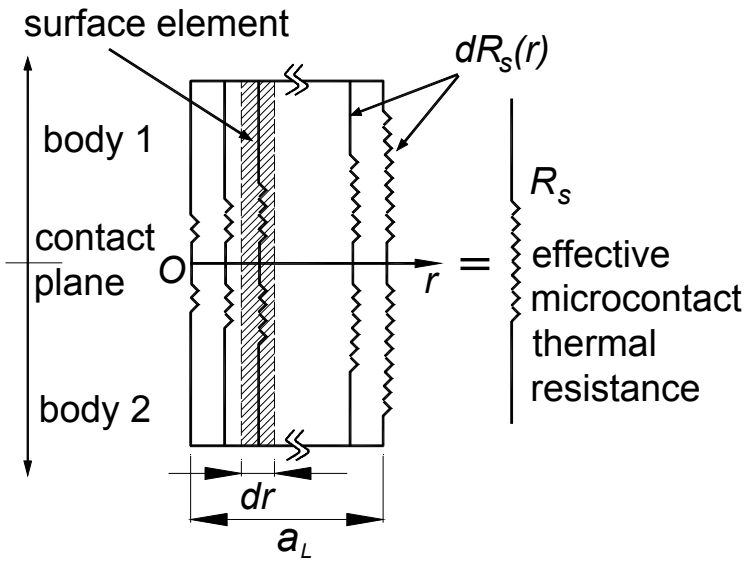

Figure 4-4: Thermal resistance network for surface element

Table 4.1: Input parameters for a typical contact problem

$\rho = 25\ mm$	$F = 50\ N$
$\sigma = 1.41\ \mu m$	$E' = 112.1\ GPa$
$m = 0.107$	$c_1/c_2 = 6.27\ GPa/-0.15$
$b_L = 25\ mm$	$k_s = 16\ W/mK$

is

$$R_s = \frac{1}{\sum 1/dR_s\,(r)} \tag{4.11}$$

The joint resistance is the sum of the macro and micro thermal resistances, i.e., Eq. (4.1).

4.4 Results

As explained in Chapter 3, a simulation routine was developed to calculate the thermal joint resistance. As an example, contact of a 25 mm sphere with a flat surface was considered and solved with the routine. The contacting bodies are stainless steel and have a 1.41 μm equivalent roughness, Table 4.1 lists the contact parameters. The mechanical results were presented in Chapter 3 and Figs. 4-5 and 4-6 present thermal outputs. As expected, the thermal resistance of the microcontacts (resistance of the local mean microcontact) increases as r increases. The

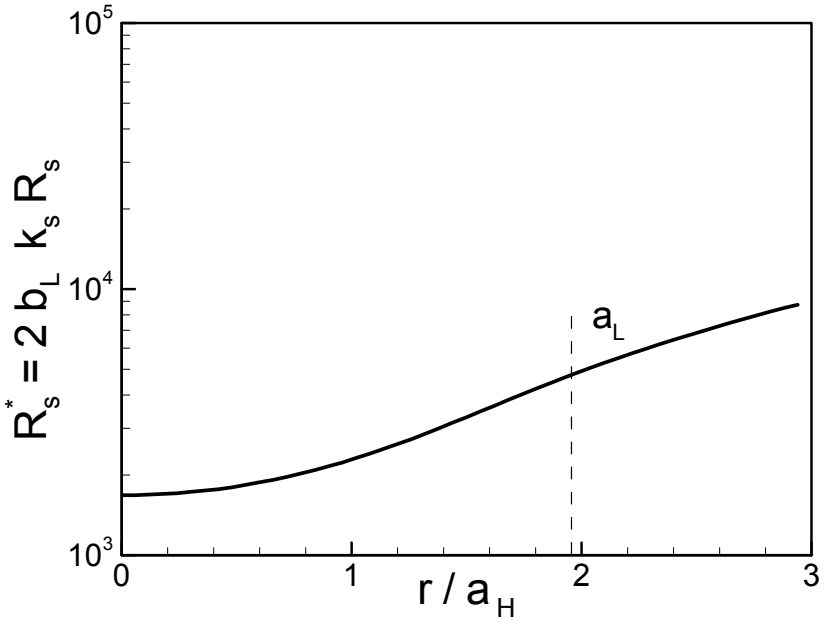

Figure 4-5: Micro thermal contact resistance

microcontact relative radius ε has its maximum value at the center of the contact and decreases with increasing radial position r.

To investigate the effect of input parameters on thermal joint resistance R_j and its components, i.e., the macro R_L and the micro R_s thermal resistances, the simulation routine was run for a range of each input parameter, while the remaining parameters in Table 4.1 were held constant. Additionally, elastoconstriction thermal resistance introduced by Yovanovich [63] indicated by R_H, was also included in the study. Elastoconstriction is a limiting case in which the surfaces are assumed to be perfectly smooth, i.e., $a_L = a_H$ and $R_s = 0$.

The effect of roughness on macro, micro, and joint resistances are shown in Fig. 4-7. Recall that the joint resistance is the summation of the macro and micro contact resistances. With relatively small roughness, the macro thermal resistance dominates the joint resistance and the micro thermal resistance is negligible, also the joint resistance is close to the elastoconstriction thermal resistance. By increasing roughness, a_L becomes larger thus, the macro thermal resistance decreases, while the micro thermal resistance increases and at some point they become comparable in size. An additional increase in the surface roughness leads to a situation where

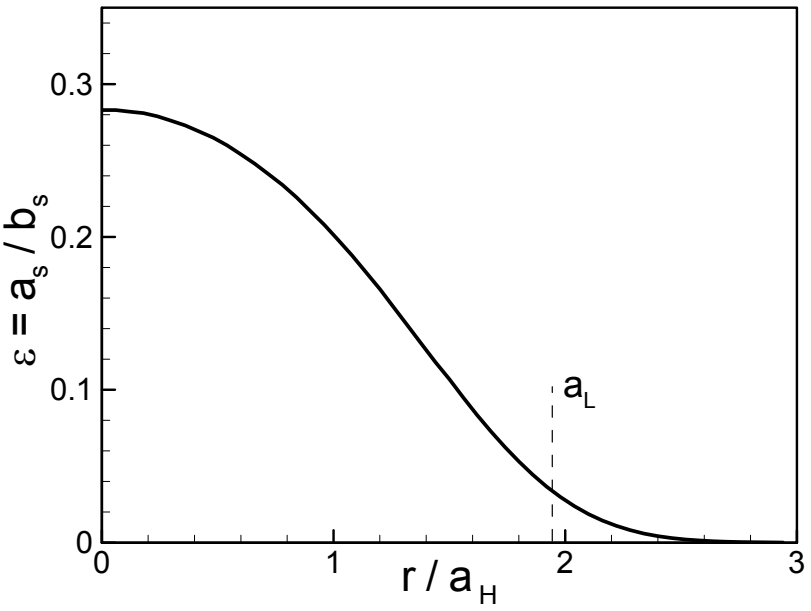

Figure 4-6: Microcontacts relative radius

the micro thermal resistance controls the joint resistance. Figure 4-7 shows that for a fixed geometry and load, there is a roughness that minimizes the thermal joint resistance.

The effect of load on micro, macro and joint thermal resistance is shown in Fig. 4-8. The micro thermal resistance controls the joint resistance at light loads due to the small number and size of the microcontacts. As the load increases the joint resistance decreases continuously, micro and macro thermal resistances become comparable in size and at larger loads the macro thermal resistance becomes the controlling component of the joint resistance. At higher loads the joint resistance approaches the elastoconstriction resistance as if no roughness exists.

Figure 4-9 shows the effect of radius of curvature. At very small radii, the macro thermal resistance dominates due to the small size of the macrocontact. As the radius of curvature increases, approaching a flat surface, the micro thermal resistance becomes more important and the macro resistance becomes smaller and eventually when $a_L = b_L$ the macro resistance falls to zero. Note that the micro thermal resistance does not change as the surface curvature ρ varies over a wide range, this is a very important trend and will be discussed later.

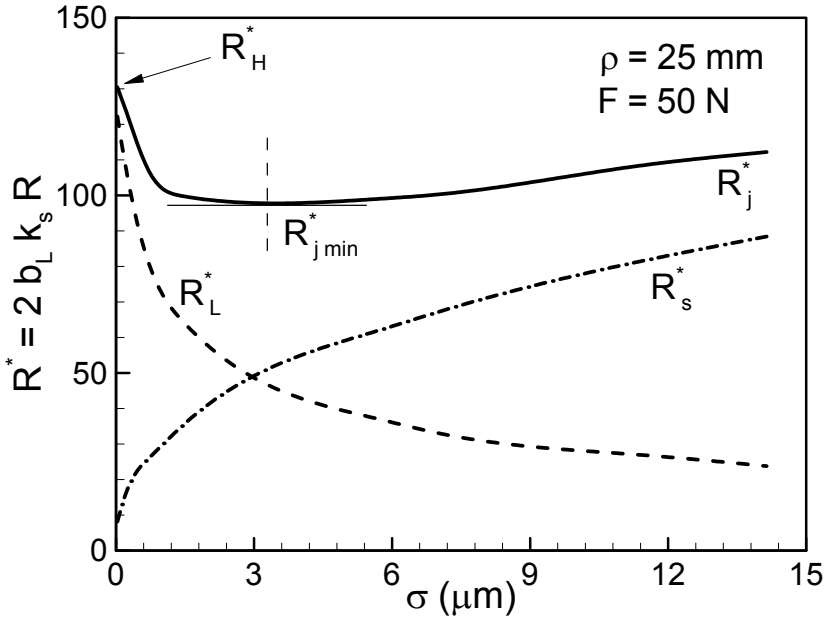

Figure 4-7: Effect of roughness on TCR

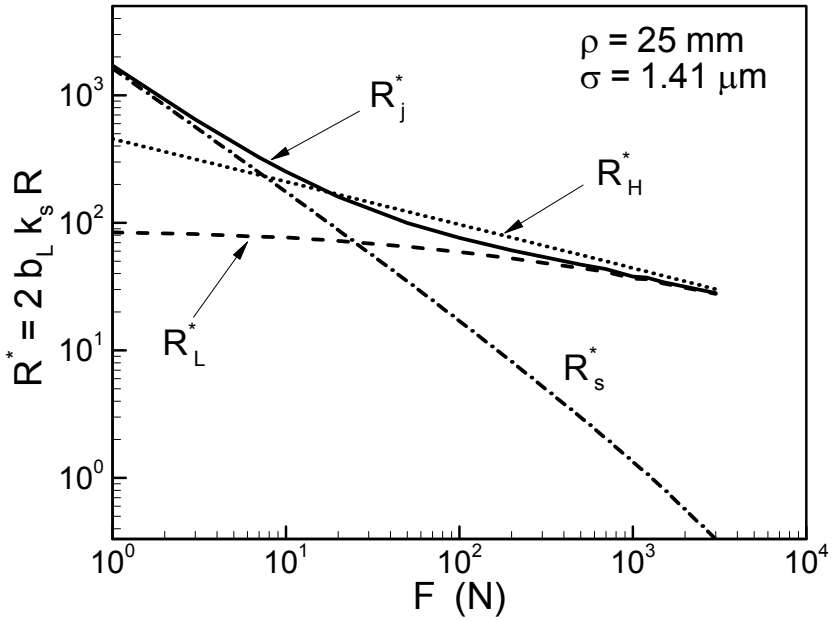

Figure 4-8: Effect of load

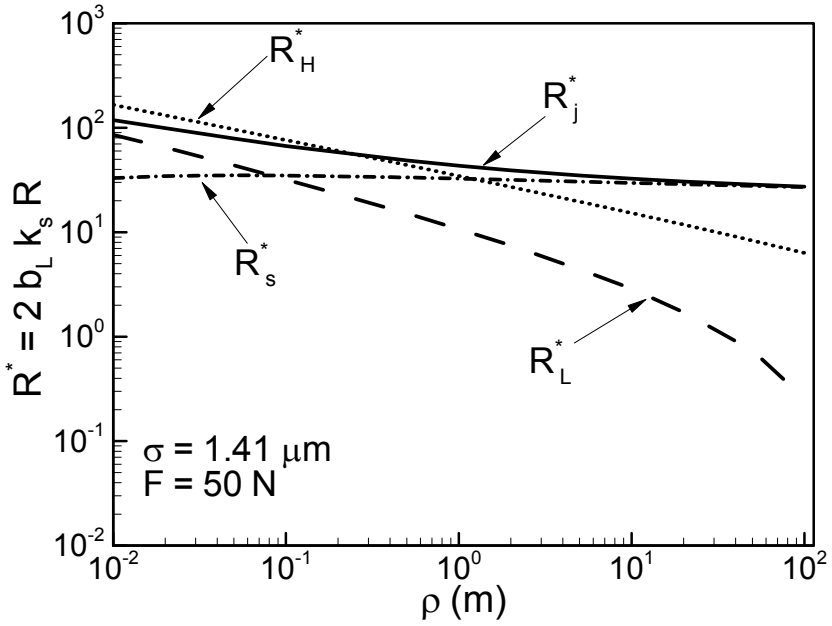

Figure 4-9: Effect of radius of curvature on TCR

4.5 Alternative Approach

The goal of this study is to develop simple correlations for determining TCR. In this section, a general expression for the micro thermal spreading resistance is derived, which in conjunction with the macro thermal resistance, Eq. (4.6), gives a correlation to calculate the thermal joint resistance in a vacuum environment.

The amount of heat transferred in a non-conforming rough contact is

$$Q = \sum dQ = \iint_{contact\ plane} dQ \tag{4.12}$$

where dQ is the heat transferred in a surface element. The local thermal joint conductance is a function of r

$$Q = \iint_{contact\ plane} h_s\left(r\right) \Delta T_s dA_a \tag{4.13}$$

where dA_a and ΔT_s = constant, are the area of a surface element and the temperature drop,

respectively. Since the macrocontact area is approximated as a circle

$$Q = 2\pi\Delta T_s \int_0^{a_L} h_s(r)\, r dr \tag{4.14}$$

The effective thermal micro conductance for a joint can be defined as: $h_s = Q/A_a\Delta T_s$. Therefore, the effective microcontact conductance can be found from

$$h_s = \frac{2\pi}{A_a} \int_0^{a_L} h_s(r)\, r dr \tag{4.15}$$

or in terms of thermal resistance where $R = 1/(hA_a)$,

$$R_s = \frac{1}{2\pi} \left(\int_0^{a_L} h_s(r)\, r dr \right)^{-1} \tag{4.16}$$

Yovanovich [8] proposed an accurate expression for determining the thermal conductance of conforming rough contacts,

$$h_s = 1.25 k_s \left(\frac{m}{\sigma}\right) \left(\frac{P}{H_{mic}}\right)^{0.95} \tag{4.17}$$

where H_{mic} is the microhardness of the softer material in contact. Combining Eqs. (4.16) and (4.17), a relationship between thermal micro resistance and pressure distribution can be found

$$R_s = \frac{\sigma}{2.5\pi m k_s} \left[\int_0^{a_L} \left[\frac{P(r)}{H_{mic}(r)} \right]^{0.95} r dr \right]^{-1} \tag{4.18}$$

Microhardness depends on several parameters: mean surface roughness σ, mean absolute slope of asperities, m, type of material, method of surface preparation, and applied pressure. According to Hegazy [25], surface microhardness can be introduced into the calculation of relative contact pressure in the form of the Vickers microhardness

$$H_v = c_1 \left(d_v'\right)^{c_2} \tag{4.19}$$

where H_v is the Vickers microhardness in (GPa), $d_v' = d_v/d_0$ and $d_0 = 1\,(\mu m)$, d_v is the Vickers indentation diagonal in μm and c_1 and c_2 are correlation coefficients determined from Vickers microhardness measurements. Song and Yovanovich [26] developed an explicit expression

relating microhardness to the applied pressure

$$\frac{P}{H_{mic}} = \left(\frac{P}{H'}\right)^{\frac{1}{1+0.071c_2}} \tag{4.20}$$

where $H' = c_1 \left(1.62\sigma'/m\right)^{c_2}$, $\sigma' = \sigma/\sigma_0$ and $\sigma_0 = 1\ \mu m$.

Sridhar and Yovanovich [27] developed empirical relations to estimate the Vickers microhardness coefficients, see Chapter 2. However, in situations where an effective value for microhardness $H_{mic,e}$ is known the microhardness coefficients can be calculated from $c_1 = H_{mic,e}$ and $c_2 = 0$.

Combining Eqs.(4.18), and (4.20) gives

$$R_s = \frac{\sigma H'^s}{2.5\pi k_s m} \left(\int_0^{a_L} \left[P\left(r\right)\right]^s r dr\right)^{-1} \tag{4.21}$$

where $s = 0.95/\left(1 + 0.071c_2\right)$. A general pressure distribution was proposed in Chapter 3, which covers the entire spherical rough contacts including flat contacts

$$P\left(\xi\right) = \begin{cases} F/\pi b_L^2 & F_c = 0 \\ P_0\left(1-\xi^2\right)^{\gamma} & F \le F_c \\ P_{0,c}\left(1-\xi^2\right)^{\gamma_c} + \dfrac{F-F_c}{\pi b_L^2} & F \ge F_c \end{cases} \tag{4.22}$$

where $\xi = r/a_L$, $\gamma = 1.5\left(P_0/P_{0,H}\right)\left(a_L/a_H\right)^2 - 1$. F_c is the critical force where $a_L = b_L$ and it is given by

$$F_c = \frac{4E'}{3\rho}\left[\max\left\{0, \left(b_L^2 - 2.25\sigma\rho\right)\right\}\right]^{3/2} \tag{4.23}$$

where $\max\{x, y\}$ returns the maximum value between x and y. Substituting the pressure distribution, for $F \le F_c$ into Eq. (4.21) one obtains

$$R_s = \frac{\sigma\left(H'/P_0\right)^s}{2.5\pi\ m\ k_s\ a_L^2}\left[\int_0^1 \left(1-\xi^2\right)^{s\gamma}\xi\ d\xi\right]^{-1} \tag{4.24}$$

After evaluating and simplifying the integral, we obtain

$$R_s = \frac{\sigma\,(1+s\gamma)}{1.25\pi\ m\ k_s\ a_L^2}\left(\frac{H'}{P_0}\right)^s \tag{4.25}$$

For $F \geq F_c$, the effective microcontact thermal resistance, following the same method, becomes

$$R_s = \frac{\sigma}{1.25\pi m k_s\ b_L^2}\left[\left(\frac{H'}{P_{0,c}}\right)^s (1+s\gamma_c) + \left(\frac{\pi H' b_L^2}{F-F_c}\right)^s\right] \tag{4.26}$$

where $P_{0,c}$ and γ_c are the values at the critical force. The general relationship for micro thermal resistance can be summarized as

$$R_s^* = \begin{cases} \left(\dfrac{\pi H' b_L^2}{F}\right)^s & F_c = 0 \\ \left(\dfrac{b_L}{a_L}\right)^2 \left(\dfrac{H'}{P_0}\right)^s (1+s\gamma) & F \leq F_c \\ \left(\dfrac{H'}{P_{0,c}}\right)^s (1+s\gamma_c) + \left(\dfrac{\pi H' b_L^2}{F-F_c}\right)^s & F \geq F_c \end{cases} \tag{4.27}$$

where $R_s^* = 1.25\pi b_L^2 k_s\,(m/\sigma)\,R_s$.

4.5.1 Macrocontact Boundary Condition

Equation (4.17) shows that the micro conductance, h_s, is (almost) proportional to the contact pressure. From the general pressure distribution profile Eq. (3.21), we know that the contact pressure has its maximum value at the center of the contact where $r = 0$, which in turn means that the micro conductance, and consequently the heat flux, must have their maximum at the center. However, assuming an isothermal boundary condition for the macrocontact area implies that the heat flux has its minimum at the center and approaches infinity at the edge of the macrocontact area $r = a_L$.

To resolve this problem, we start with investigating the trend of the micro thermal resistance R_s shown in Fig 4-9. In this plot, all input parameters of the contact are kept constant and the surface radius of curvature has been varied from a small to a relatively large value, i.e., conforming rough surface. For plotting Fig 4-9, the full thermal model has been used which

employs the local number and radius of the microcontacts and calculates the effective micro thermal resistance directly from the flux tube solution, see section 4.3. As shown in Fig. 4-9, the micro thermal resistance remains unchanged as the surface radius of curvature is varied, thus it can be concluded that the micro thermal resistance is a very weak function of the radius of curvature or the pressure distribution profile. In fact it is determined by the external load. In section 4.5.2, a correlation for micro thermal resistance is derived that shows the micro thermal resistance is inversely proportional to the external load, Eq. (4.29). One way to avoid this problem is to calculate a mean contact pressure over the macrocontact area, i.e., $\overline{P} = F/\pi a_L^2$ then use Eq. (4.17) to find the effective micro thermal resistance R_s.

The isothermal boundary condition assumption of the macrocontact area can be proven independently. The present thermal model is constructed based on the premise that the microcontacts are isothermal. The microcontacts are also more or less at the same temperature, i.e., the contact temperature. If these assumptions are granted, it can be shown that an isothermal surface exists at a distance beneath the contact plane, see section 5.3. This isothermal plane can be used for calculating the macro thermal resistance R_L.

4.5.2 Approximate Model For Micro Thermal Resistance

Equation (4.27) can be simplified by introducing an approximation. Since the Vickers coefficient c_2 is negative and in the range of $-0.35 \leq c_2 \leq 0$, the parameter $s = 0.95/\left(1 + 0.071 c_2\right)$ is close to one, i.e., $0.95 \leq s \leq 0.97$ and can be approximated as, $s = 1$. Introducing this simplification, the micro thermal resistance R_s, i.e., Eq. (4.21) simplifies to,

$$R_s = \frac{\sigma H'}{2.5\pi k_s m} \left(\int_0^{a_L} P\left(r\right) r dr \right)^{-1} \tag{4.28}$$

From a force balance one can write, $F = 2\pi \int_0^{a_L} P\left(r\right) r dr$, and Eq. (4.28) becomes,

$$R_s = \frac{H'}{1.57 k_s F} \left(\frac{\sigma}{m} \right) \tag{4.29}$$

where, the leading constant in Eq. (4.17) has been changed from 1.25 to 1.57 to compensate for introducing the approximation, where the exponent s is set one. The approximate model, Eq. (4.29), is compared with the full model for conforming rough contacts, Eq. (4.27)-a, in

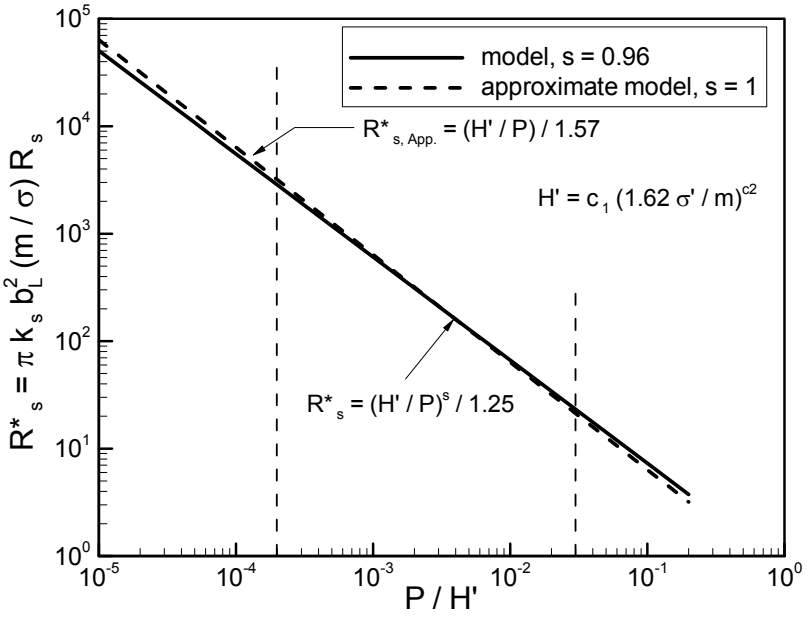

Figure 4-10: Comparison between approximate and full model, conforming rough contacts

Fig. 4-10, where an average value of $s = 0.96$ was chosen. It can be seen that the approximate model shows good agreement with the full model in the range of $2 \times 10^{-4} \leq P/H' \leq 5 \times 10^{-2}$, which includes a wide range of loading, i.e., moderate and high loads. The difference between the approximate and the full model increases in light loads, $P/H' < 10^{-4}$.

Equation (4.29) is general and applicable to all contact geometries, i.e., conforming and non-conforming rough contacts. The approximate model provides a simpler relationship to determine the micro thermal resistance R_s. In addition the approximate effective micro thermal resistance is independent of the surface curvature. This trend can also be observed in Fig. 4-9, where it should be noted that the full model (computer program) with no simplifications was used to construct the plot. Also from the approximate relationship, it can be concluded that the profile of the pressure distribution does not affect the effective micro thermal resistance.

The joint resistance can be found using the approximate R_s and by superimposing Eqs. (4.6) and (4.29)

$$R_j = \frac{H'}{1.57 k_s F} \left(\frac{\sigma}{m}\right) + \frac{(1 - a_L/b_L)^{1.5}}{2 k_s a_L} \tag{4.30}$$

From Eq. (4.30) one can conclude that i) the effective micro thermal resistance, except for the

Table 4.2: Range of parameters for the experimental data

Parameter
$7.15 \leq b_L \leq 14.28\ mm$
$25.64 \leq E' \leq 114.0\ GPa$
$7.72 \leq F \leq 16763.9\ N$
$16.6 \leq k_s \leq 227.2\ W/mK$
$0.04 \leq m \leq 0.34$
$0.12 \leq \sigma \leq 13.94\ \mu m$
$0.013 \leq \rho \lessapprox 120\ m$

thermal conductivity, is only a function of the contact micro-scale characteristics, i.e., surface roughness σ, slope m, microhardness H', and the load F, ii) on the other hand, the macro thermal resistance is a function of the macro-scale contact parameters, i.e., the macrocontact radius a_L, and size of the contacting bodies b_L. These conclusions are in agreement with the TCR analysis described in Fig. 1-3. From Chapter 3, we know that the macrocontact radius is a function of the effective elasticity modulus E', radius of curvature ρ, surface roughness σ, and the load F.

The applied load and the surface roughness appear to play important roles in both macro and micro thermal resistances. The effect of surface roughness on the macro resistance is limited to the macrocontact radius, a_L. The applied load is the connecting bridge between the macro and micro mechanical analyses, since the force balance must be satisfied in both analyses.

4.6 Comparison With Experimental Data

During the last four decades a large number of experimental data have been collected for a wide variety of materials such as aluminium, brass, magnesium, nickel 200, silver and stainless steel in a vacuum. About 600 data points were collected from an extensive review of the literature, summarized and compared with the present model. As summarized in Table 4.2, the experimental data form a complete set of the materials with a wide range of mechanical, thermal, and surfaces characteristics used in applications where TCR is of concern. The data also include the contact between dissimilar metals such as Ni200-Ag and SS-CS.

Generally, TCR experimental procedures include two cylindrical specimens of the same diameter b_L which are pressed coaxially together by applying an external load in a vacuum

Table 4.3: Reseacher and specimen materials used in comparisons

Ref.	Researcher	Material(s)
A	Antonetti [64]	Ni200 Ni200-Ag
B	Burde [51]	SPS 245, CS
CC	Clausing-Chao [59]	Al2024 T4 Brass Anaconda Mg AZ 31B SS303
F	Fisher [61]	Ni 200-Carbon Steel
H	Hegazy [25]	Ni200 SS304 Zircaloy4 Zr-2.5%wt Nb
K	Kitscha [60]	Steel 1020-CS
MM	McMillan-Mikic [71]	SS303
MR	Mikic-Rohsenow [14]	SS305
M	Milanez et al. [65]	SS304

chamber. After reaching steady-state conditions, TCR is measured at each load, see Chapter 6 for more detail. These experiments have been conducted by many researchers such as Burde [51] and Clausing and Chao [59]. Table 4.3 indicates the researchers, reference publications, specimen designation, and the material type used in the experiments.

The comparison includes all three regions of TCR, i.e., the conforming rough, the elastoconstriction and the transition. Appendix A summarizes the experiment number, i.e., the number which was originally assigned to a particular experimental data set by the researchers and geometrical, mechanical and thermal properties of the experimental data, as reported. Clausing and Chao [59], Fisher [61], Kitscha [60], and Mikic and Rohsenow [14] did not report the surface slope m; the Lambert and Fletcher [6] correlation was used to estimate these values, see Table 2.1. Additionally, the exact values of radii of curvature for conforming rough surfaces were not reported. Since these surfaces were prepared to be optically flat, radii of curvature in the order of $\rho \approx 100\ m$ are considered for these surfaces.

Figure 4-11 illustrates the comparison between the present model and the experimental

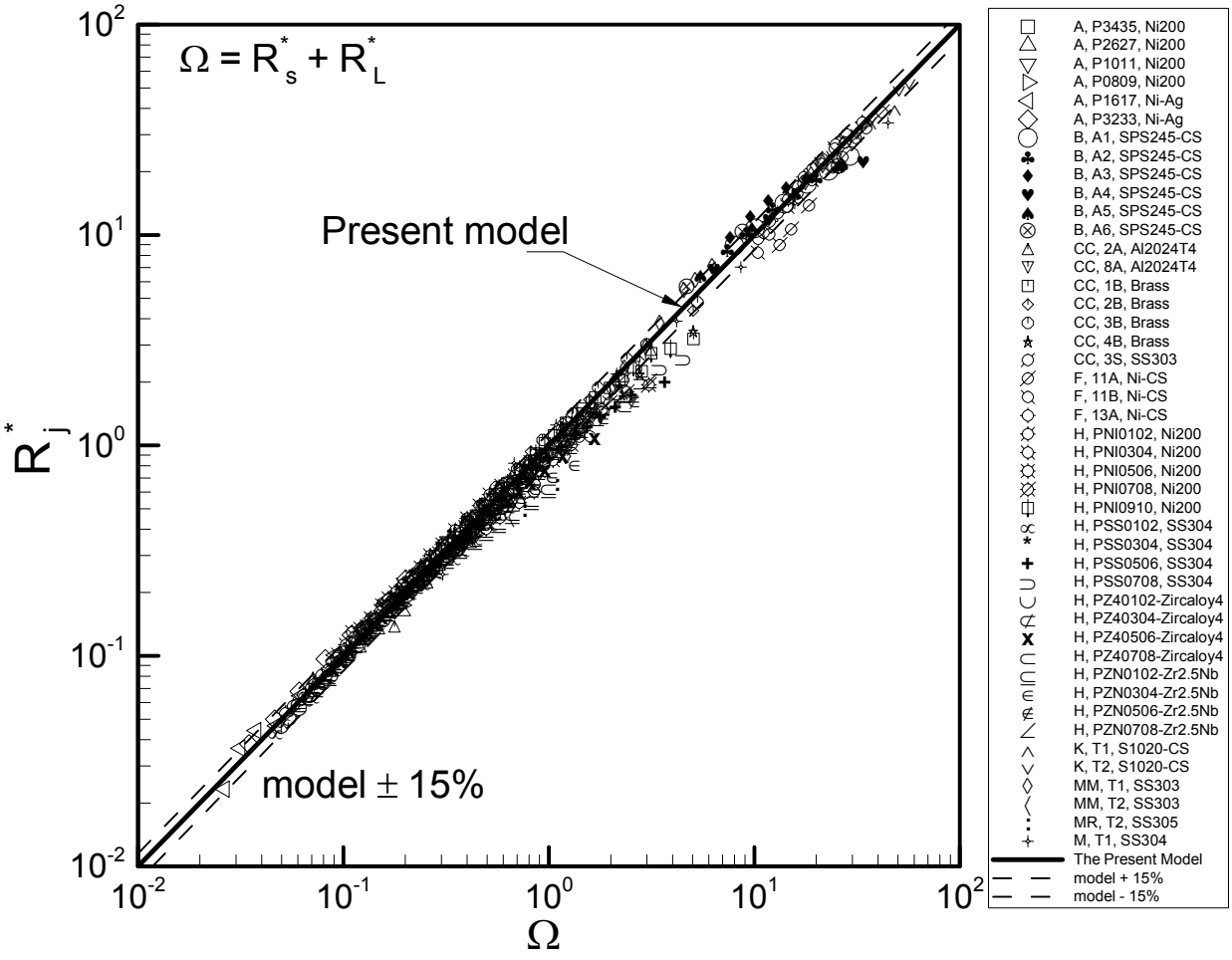

Figure 4-11: Comparison of present model with experimental data

data, with Eqs. (4.6) and (4.27), where

$$R_j^* = k_s b_L R_j$$

$$\Omega = \frac{(1-B)^{1.5}}{2B} + \begin{cases} \dfrac{(\sigma/m)}{1.25\pi b_L}\left(\dfrac{H'}{P}\right)^s & F_c = 0 \\ \dfrac{(\sigma/m)\,(1+s\gamma)}{1.25\pi b_L B^2}\left(\dfrac{H'}{P_0}\right)^s & F \le F_c \\ \dfrac{(\sigma/m)}{1.25\pi b_L}\left\{\left(\dfrac{H'}{P_{0,c}}\right)^s (1+s\gamma_c) + \left(\dfrac{\pi H' b_L^2}{F-F_c}\right)^s\right\} & F \ge F_c \end{cases} \quad (4.31)$$

where $B = a_L/b_L \le 1$, and $P_0 = P_{0,H}/\left(1 + 1.37\alpha\tau^{-0.075}\right)$ is the maximum contact pressure. The parameter Ω is the non-dimensional TCR predicted by the (full) model, i.e., $\Omega = R_s^* + R_j^*$ or $R_j^* = \Omega$. Therefore the model is shown by a 45-degree line in Fig. 4-11. The macrocontact radius a_L can be determined from Eq. (3.30),

$$a_L = a_H \frac{1.80\sqrt{\alpha + 0.31\ \tau^{0.056}}}{\tau^{0.028}} \quad (4.32)$$

Using Eq. (4.32) a relationship for B can be found as a function of non-dimensional and geometrical parameters, i.e.,

$$B = \frac{a_L}{b_L} = \max\left\{1,\ 1.80\left(\frac{a_H}{b_L}\right)\frac{\sqrt{\alpha + 0.31\ \tau^{0.056}}}{\tau^{0.028}}\right\} \quad (4.33)$$

Experimental data are distributed over four decades of Ω from approximately 0.03 up to 70. The model shows good agreement with the data over the entire range of comparison with the exception of a few points. The approximate model, Eq. (4.30), was also compared with the experimental data using the same method and showed good agreement; since the plots are almost identical a direct comparison of the approximate model with data is not presented.

In most of the conforming rough data sets, such as Hegazy [25], experimental data show a lower resistance at relatively light loads in comparison with the model and the data approach the model as the load increases. This trend can be observed in almost all conforming rough data sets (see Fig. 4-11). This phenomenon which is called the *truncation effect* [65] is important at light loads when surfaces are relatively rough. A possible reason for this behavior is the Gaussian

assumption of the surface asperities which implies that asperities with "infinite" heights exist. Milanez et al. [65] experimentally studied the truncation effect and proposed correlations for maximum asperities heights as functions of surface roughness.

If the external load increases beyond the elastic limit of the contacting bodies, elastoplastic and plastic deformations occur. The plastic macrocontact radius, a_P, is larger than the elastic radius a_L, i.e., $a_P > a_L$. Consequently, lower TCR will be measured; this trend can be clearly seen in the Fisher [61] data sets "F,11A,Ni-CS", see Fig. 4-11.

The accuracy of experimental data were reported by Antonetti [64], Fisher [61], and Hegazy [25] to be 8.1, 5, and 7 percent, respectively. Unfortunately, the uncertainty of other researchers data are not available. Because of the above-mentioned approximations to account for unreported data, the accuracy of the full model is difficult to assess. However, the RMS and the average absolute difference between the model and data are approximately 13.6% and 9.3%, respectively. The RMS and the average absolute difference between the approximate model and data are approximately 14.8% and 10.9%, respectively, as a result of choosing the constant in Eq. (4.30) to be 1.57.

4.7 Criterion For Conforming Contacts

A criterion for determining a "flat surface" was derived in Chapter 3, implying that when the effect of surface curvature on contact pressure distribution is negligible the surface is *ideally* flat. It was shown that if the surface roughness and curvature are in the same order of magnitude, i.e., $\delta/\sigma \sim 1$ with no load applied the macrocontact reaches the edge of the contacting bodies and $a_L = b_L$.

From the TCR point of view, the conforming or flat contact can be defined as a contact in which the macro thermal resistance R_L is negligible. As discussed previously, surface curvature has no effect on the micro thermal resistance (the approximate model). Thus, the effect of surface curvature is limited to the macro thermal resistance, R_L.

The macro thermal resistance is determined from Eq. (4.6), which can be re-written in the non-dimensional form as,

$$R_L^* = k_s R_L b_L = \frac{(1-B)^{1.5}}{2B} \tag{4.34}$$

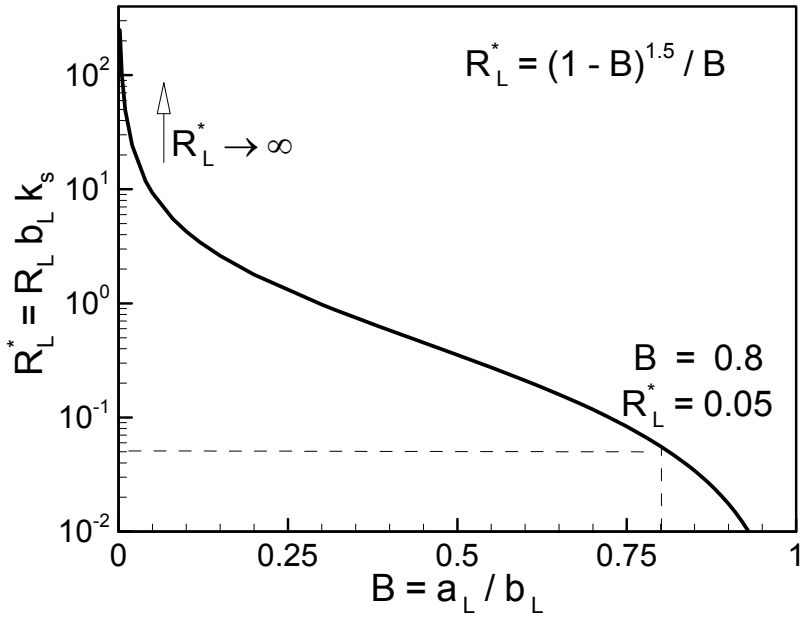

Figure 4-12: Macro thermal resistance

where $B = a_L/b_L \leq 1$. As shown in Fig. 4-12 the macro thermal resistance is zero at $B = 1$, i.e. $a_L = b_L$ (perfectly flat contacts), as B decreases from 1 to 0.8 the macro thermal resistance increases from 0 to 0.05, this increase is relatively small and considered negligible. Therefore, a criterion for the flat joint is proposed arbitrarily by setting $B = 0.8$, where the macro thermal resistance is *almost* negligible. It should also be noted that for $0.8 \leq B \leq 1$ (large radii of curvature) the micro thermal resistance controls the joint resistance, see Fig 4-9.

A correlation for determining the macrocontact radius, a_L, was proposed in Chapter 3 for surfaces with relatively large radii of curvature, $a_L = 1.5\, a_H\, \sqrt{\alpha + 0.45}$. Using this relationship, one can write, $B = 0.8 = 1.5\,(a_H/b_L)\,\sqrt{\alpha + 0.45}$. Substituting the non-dimensional parameter, $\alpha = \sigma\rho/a_H^2$ and Eq. (4.2), we obtain,

$$\frac{\sigma}{\delta} = 2\left[0.28 - 0.45\left(\frac{a_H}{b_L}\right)^2\right] \tag{4.35}$$

As can be seen from Eq. (4.35), the relative out-of-flatness is a function of a_H/b_L which contains the applied load, the elastic properties, and the geometry of the contacting bodies. As shown

in Fig. 3-11, an increase in surface roughness results in an increase in the macrocontact radius. Setting $B = a_L/b_L = 0.8$, depending on the level of surface roughness a range for a_H/b_L can be estimated, approximately $0.7 \leq a_H/a_L \leq 0.96$, which results in, $0.56 \leq a_H/b_L \leq 0.77$. This range means that the increase in the macrocontact radius (compared to the smooth Hertzian radius) is within a 5 to 30 percent increase. It is a reasonable estimate, noting that we are investigating the contact of surfaces with relatively large radii of curvature under light loads. Combining Eq. (4.35) and the above-mentioned range for a_H/b_L, a range for δ/σ can be found for flat contacts, approximately $3 \leq \delta/\sigma \leq 30$ from very rough to very smooth surfaces, respectively.

4.8 Summary and Conclusions

TCR of non-conforming rough surfaces was considered as the superposition of macro and micro thermal resistance components accounting for the effects of surface curvature and roughness, respectively.

The results of the mechanical model presented in Chapter 3, i.e., the local mean separation, the local mean radius and the number of microcontacts, were used to develop an analytical thermal model for determining TCR of non-conforming rough contacts in a vacuum. The thermal model was constructed based on the premise that the mean separation between the contacting surfaces in an infinitesimal surface element can be assumed constant. Therefore, the conforming rough model of Cooper et al. [7] could be implemented to calculate the surface element thermal resistance. The surface element thermal resistances were integrated over the macrocontact area to calculate the effective micro thermal resistance of the contact. The macrocontact resistance was calculated using the flux tube solution.

The effects of the major contact parameters, i.e., roughness, load, and radius of curvature on TCR were investigated. It was shown that there is a value of surface roughness that minimizes TCR. Additionally, at large loads the effect of roughness on the TCR becomes negligible.

By using the general pressure distribution introduced in Chapter 3 and the Yovanovich [8] correlation for thermal conductance of conforming rough contacts, we derived simple correlations for determining TCR which cover the entire range of TCR from conforming rough to

smooth spherical contacts. The input parameters to utilize the proposed correlations are: load F, the effective elasticity modulus E', Vickers microhardness correlation coefficients c_1 and c_2, effective surface roughness σ and surface slope m, the effective surface out-of-flatness δ or radius of curvature ρ, radius of the contacting surfaces b_L, and the harmonic mean of the thermal conductivities k_s.

It was shown that the micro thermal resistance R_s is independent of the surface curvature and the profile of the contact pressure by introducing an approximate model for the micro thermal resistance. Additionally, the micro and the macro thermal resistances are functions of the micro and macro scale contact parameters, respectively. The applied load appears directly in both resistances; the surface roughness influences the macro thermal resistance implicitly through the macrocontact radius.

The thermal model was compared with more than 600 experimental data points and showed good agreement over the entire range of TCR. The RMS difference between the model and the data was estimated to be approximately 13.6%. The list of materials in the comparison formed a complete set of the metals used in applications, where TCR is of concern. It was also shown that the present model is applicable to dissimilar metals.

A criterion for specifying the conforming rough contact was developed. A contact is conforming where the equivalent surface out-of-flatness is approximately between 3 to 30 times of the equivalent surface roughness for very rough to very smooth surfaces, respectively.

Chapter 5

A Scale Analysis Approach to TCR

5.1 Scope

In this Chapter, a new model is developed for predicting thermal contact resistance (TCR) of non-conforming rough joints of bare solids in a vacuum. Instead of using probability relationships that are used in Chapter 4 to calculate the mean size and number of microcontacts, Cooper et al. model [7], a novel approach is taken by employing the "scale analysis method". The main objective of this approach is to develop a simplified model that is easy to use and does not sacrifice accuracy. Based on the known characteristics and deformation mechanisms of rough surfaces, a scale relationship is developed. The scale relationship satisfies the observed physical proportionality and shows the trend of the experimental data. The constant of the scale relationship is then determined through comparison with experimental data. This is an example to demonstrate the power of scale analysis methods. In other words, TCR is determined without knowing the "exact" size and number of microcontacts.

It is shown that the geometry of heat sources on a half-space for microcontacts is justifiable for an applicable range of contact pressure. Also, it is shown that the surface curvature and contact pressure distribution have no effect on the effective micro thermal resistance. The present model allows one to predict TCR over the entire range of non-conforming joints from conforming rough to smooth Hertzian. A new non-dimensional parameter, i.e., ratio of the macro over micro thermal resistances, is introduced as a criterion to identify three regions of TCR.

The proposed model shows excellent agreement with the collected TCR data for SS 304. Additionally more than 880 experimental data points, collected by many researchers, are summarized and compared with the present model and good agreement is observed.

5.2 Introduction

According to the examination of the microgeometry of rough surfaces, surface asperities have small slopes and curved shapes at their summits [20, 15]. It is a common methodology to simplify the contact of two Gaussian rough surfaces by the contact of a smooth plane with a random rough surface which has equivalent surface characteristics.

Cooper et al. [7] proved that the microcontacts can be assumed isothermal provided the thermal conductivity in each body is independent of direction, position and temperature.

As discussed in Chapter 4, the real shapes of microcontacts can be a wide variety of singly connected areas depending on the local profile of the contacting asperities. Yovanovich et al. [52] showed that the real shape of the microcontacts is a second order effect and an equivalent circular contact, which has the same area, can represent the microcontacts.

As shown in Fig. 5-1, there are two geometries that can be used as basic elements to model the thermal constriction/spreading resistance of the microcontacts, i) heat source on a half-space in which microcontacts are assumed to be located far from each other, where thermal constriction/spreading resistance can be found from [3]

$$R_{mic,\text{ half-space}} = \frac{1}{2k_s a_s} \tag{5.1}$$

where a_s and k_s are the radius of the microcontact spot and the harmonic mean of thermal conductivities of contacting bodies and ii) the flux tube geometry, considering the effect of neighboring microcontacts. Cooper et al. [7] proposed a simple accurate correlation for determining the flux tube constriction/spreading resistance,

$$R_{mic,\text{ flux tube}} = \frac{\psi(\varepsilon_s)}{2k_s a_s} \tag{5.2}$$

where $\psi(\varepsilon_s) = (1-\varepsilon_s)^{1.5}$ and $\varepsilon_s = a_s/b_s$.

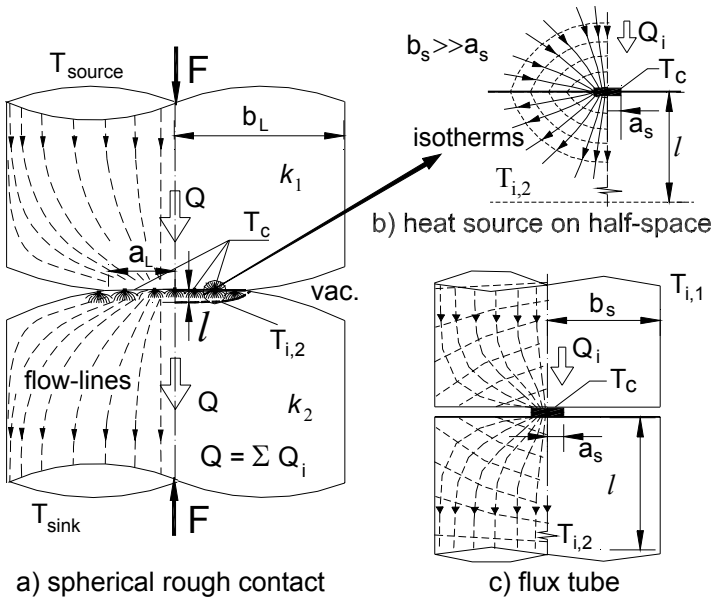

Figure 5-1: Geometry of spherical rough contact in vacuum, heat source on half-space, and flux tube geometry

Using the flux tube correlation, Eq. (5.2), and neglecting the effect of surface roughness, the joint resistance for the smooth sphere-flat contact, i.e., elastoconstriction limit [63] can be determined from

$$R_{\mathrm{j,\,EC}} = \frac{(1 - a_H/b_L)^{1.5}}{2k_s a_H} \tag{5.3}$$

Comparison between the elastoconstriction model, i.e., Eq. (5.3) and the smooth sphere-flat experimental data shows good agreement, see Chapter 2, thus the flux tube solution can be employed for determining the macro thermal resistance.

5.3 Macro and Micro Thermal Resistances

As illustrated in Fig. 5-2, when the heat flow rate Q is transferred from a heat source at T_{source} to a heat sink at T_{sink}, it experiences the macro thermal constrictions $R_{\mathrm{L},1}$ and $R_{\mathrm{L},2}$ that arose due to the macrocontact area. Then, heat passes through n_s microcontacts in the contact plane, which is called the effective microcontact resistance, R_s. The total thermal joint resistance of

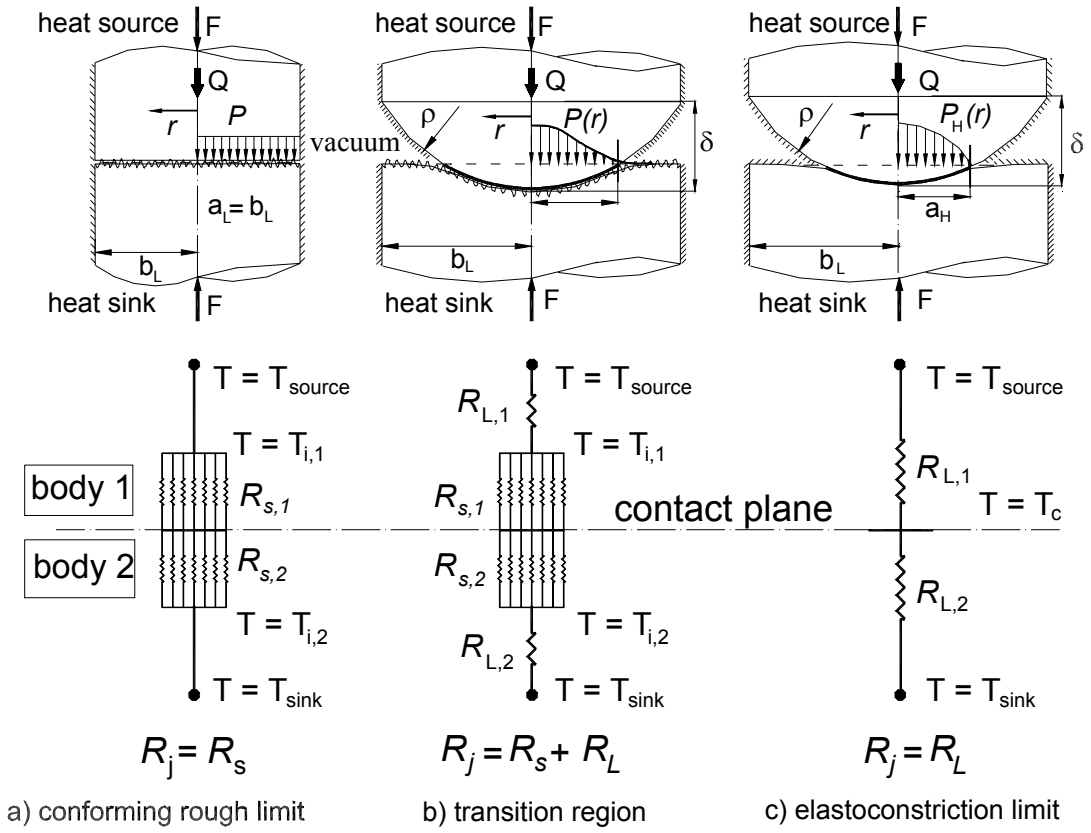

Figure 5-2: Thermal resistance network for conforming rough, transition, and elastoconstriction regions

a non-conforming rough joint in a vacuum can be written as

$$R_j = R_L + R_s \tag{5.4}$$

where $R_{\mathrm{L}} = R_{\mathrm{L},1} + R_{\mathrm{L},2}$, $R_{\mathrm{s}} = R_{\mathrm{s},1} + R_{\mathrm{s},2}$, and

$$\frac{1}{R_{\mathrm{s,\ 1\ or\ 2}}} = \sum^{n_s} \frac{1}{R_{\mathrm{mic,\ 1\ or\ 2}}}$$

where $R_{\mathrm{mic,\ 1\ or\ 2}}$ is the sum of thermal constriction and spreading resistances of a single micro-contact in body 1 or 2.

Equation (5.4) is a general expression and applicable to all spherical rough contacts and it

was used by many researchers such as Clausing and Chao [4], Nishino et al. [5], and Lambert and Fletcher [6]. A proof of Eq. (5.4) is given as follows. Assuming circular isothermal microcontacts, at T_c, that have a mean radius (in the order of $a_s \sim \mu m$), isothermal planes must exist at intermediate temperatures $T_{\mathrm{i},1}$ and $T_{\mathrm{i},2}$, i.e., $T_{\mathrm{source}} < T_{\mathrm{i},1} < T_c < T_{\mathrm{i},2} < T_{\mathrm{sink}}$ at some location l above/below the contact plane in body 1 and 2, respectively. If the microcontacts are considered as heat sources on a half-space the distance between these intermediate isothermal planes and the contact plane $l = 40a_s \sim 40\ \mu m$ [72]. As microcontacts grow in size and number, they start to affect each other (the flux tube geometry) and l decreases, $l \sim b_s$ [14]. Consequently, macro thermal constriction/spreading resistances $R_{\mathrm{L},1}$ and $R_{\mathrm{L},2}$ are in series between the heat source and the isothermal plane $T_{\mathrm{i},1}$ and the isothermal plane $T_{\mathrm{i},2}$ and the heat sink, respectively. Also microcontacts provide n_s parallel paths for transferring heat between two isothermal planes $T_{\mathrm{i},1}$ and $T_{\mathrm{i},2}$.

Two limiting cases can be distinguished for Eq. (5.4), i) the conforming rough limit, i.e., contact of flat rough surfaces where the surface curvatures are very large thus macro thermal resistance R_L is negligible and micro thermal resistance R_s is the controlling part, ii) the elastoconstriction limit where the radii of curvature of contacting bodies are small and surfaces are smooth, thus the macro thermal resistance R_L is predominant and R_s is negligible, and iii) transition region or general contact in which both R_L and R_s exist and have the same order of magnitude. Figure 5-2 shows the above-mentioned regions and their corresponding thermal resistance networks. Later, a non-dimensional parameter will be introduced and a criteria will be proposed to specify these limits.

5.4 The Scale Model

Due to the random nature of the surface roughness, studying the deformation and heat transfer of each single asperity is impossible, as a result a representative (modeled) asperity is chosen and studied. Surface roughness is modeled by assuming a Gaussian distribution of asperities. The RMS surface roughness σ is a measure for the mean surface asperity heights.

In this section, using scale analysis, first an expression is derived for TCR of conforming rough contacts, R_s. Then, the non-conforming macrocontact area is divided into infinitesimal

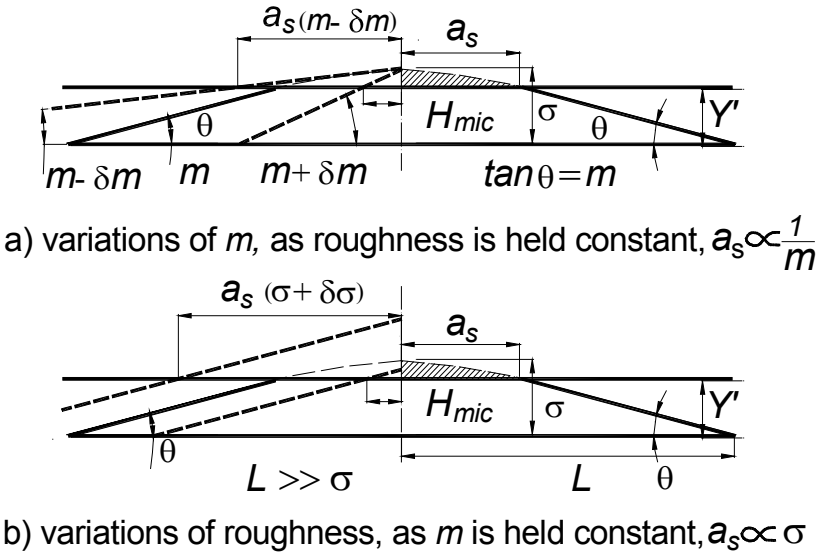

Figure 5-3: Proportionalities between microcontact size and surface slope and roughness

surface elements where the conforming rough model relation can be applied. By integrating the local conductance over the macrocontact, an effective microcontact resistance R_s is found. Using the flux tube correlation, the macrocontact resistance R_L is computed. Finally, superimposing the macro and micro thermal resistances using Eq. (5.4), the joint resistance is determined.

5.4.1 TCR of the Conforming Rough Limit

Surface roughness can be visualized as shallow valleys and hills with small slopes where asperities have spherical shapes at their summits. Figure 5-3 illustrates a model asperity, which represents the equivalent rough surface characteristics σ and m, placed in contact with a smooth plate at a mean separation Y'. Using the equivalent rough surface simplification and considering the fact that the mean surface slope, m, is small, the microcontacts are flat and in the same contact plane. As discussed previously, the shape of microcontacts can be assumed circular. Figure 5-3 also illustrates proportionalities between the mean microcontact radius a_s and the surface roughness σ and slope m. As surface slope slightly decreases from m to $m - \delta m$, while the roughness σ and Y' are held constant, the mean radius of microcontacts increases and vice versa, thus one can write $a_s \propto 1/m$. Following the same method for surface roughness, we obtain $a_s \propto$

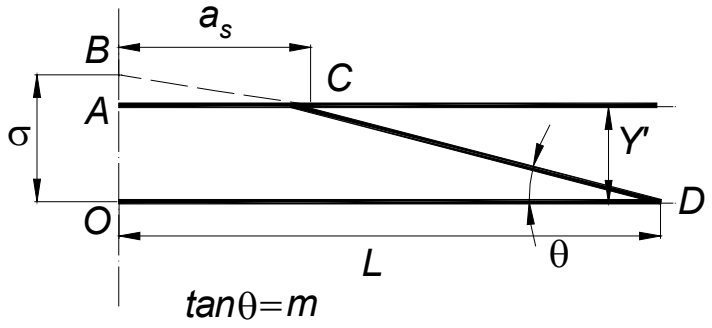

Figure 5-4: Schematic geometry of microcontact

σ. Combining the above proportionalities, the mean radius of the microcontacts is proportional to the surface roughness and inversely proportional to the surface slope, i.e., $a_s \propto \sigma/m$. This relationship can also be derived from the geometry of a representative microcontact. Figure 5-4 shows half of a microcontact. In triangles $\triangle OBD$ and $\triangle ABC$, one can write $AC \propto OD$ from similar triangles. But we know that $AC = a_s$ and $OD = L = \sigma/m$ which leads to $a_s \propto \sigma/m$. Considering n_s circular microcontacts with the mean radius of a_s within the macrocontact area, the real contact area is, $A_r \propto \pi n_s a_s^2 \propto \pi n_s \left(\sigma/m\right)^2$.

The microcontacts are assumed to deform plastically, i.e., each microcontact can be visualized as a small microhardness indenter. The empirical correlation proposed by Yovanovich and Hegazy [73], is used to estimate the microhardness. Preserving the microcontact area, i.e., $A_v = \pi a_s^2$, where A_v is the projected area of the Vickers microhardness test, the Vickers indentation diagonal d_v can be related to the mean radius of microcontacts a_s, $d_v = \sqrt{2\pi} a_s$, microhardness becomes,

$$H_{mic} \propto H^* \equiv c_1 \left(\frac{\sigma}{m\sigma_0}\right)^{c_2} \tag{5.5}$$

Assuming plastic deformation of microcontacts, the external force can be related to the real contact area and surface microhardness through a force balance,

$$F = A_r H_{mic} \propto \pi n_s \left(\frac{\sigma}{m}\right)^2 H^* \tag{5.6}$$

where H_{mic} is the microhardness of the softer material in contact. From Eq. (5.6) the number

of microcontacts can be determined

$$n_s \propto \frac{F}{\pi \left(\sigma/m\right)^2 H^*} \tag{5.7}$$

It can be seen from Eq. (5.7) that an increase in load creates new microcontacts while the mean size of microcontacts remains constant, i.e., $a_s \propto \sigma/m$. This is in agreement with Greenwood and Williamson [1] and also satisfies the proportionality $A_r \propto F$ reported by Tabor [2].

The thermal model is based on the premise that n_s heat channels, covering the nominal contact area, form a set of parallel paths for transferring heat flow. If the half-space assumption is considered, see Fig. 5-1-b, TCR can be found from,

$$R_{\text{s, half-space}} = \frac{1}{2k_s n_s a_s} \propto \frac{1}{2k_s n_s \left(\sigma/m\right)} \tag{5.8}$$

Many researchers including Cooper et al. [7] modeled the micro thermal constriction/spreading resistance using the flux tube geometry, thus TCR is,

$$R_{\text{s, flux tube}} = \frac{\psi\left(\varepsilon_s\right)}{2k_s n_s a_s} \propto \frac{\psi\left(\varepsilon_s\right)}{2k_s n_s \left(\sigma/m\right)} \tag{5.9}$$

where $\psi\left(\cdot\right)$ is the constriction alleviation factor given in Eq. (5.2). The apparent contact area is covered by flux tubes with a mean radius b_s, the relative size of microcontacts can be found from, $\varepsilon_s = a_s/b_s = \sqrt{A_r/A_a}$, where $A_a = \pi b_L^2$. Substituting A_r and A_a one obtains

$$\varepsilon_s \propto \sqrt{\frac{F/\pi b_L^2}{H^*}} \equiv \sqrt{P^*} \tag{5.10}$$

where P^* is a non-dimensional parameter that can be interpreted as the ratio of the nominal contact pressure to the pressure at the microcontacts. The number of microcontacts can be written in terms of P^* by re-arranging Eq.(5.7)

$$n_s \propto \frac{b_L^2}{\left(\sigma/m\right)^2} P^* \tag{5.11}$$

We find the TCR for conforming rough surfaces by using the non-dimensional parameter P^*

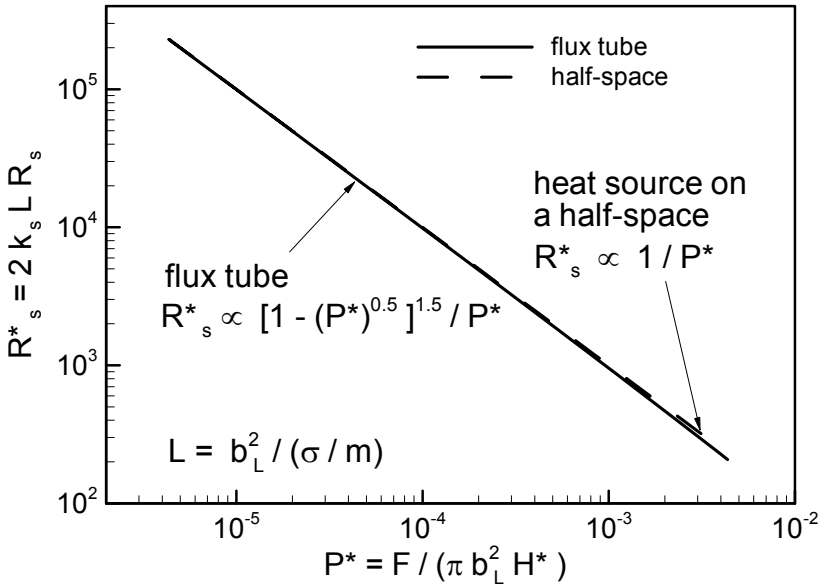

Figure 5-5: Comparison between half-space and flux tube solutions

and the flux tube solution

$$R_{\text{s, flux tube}} \propto \frac{(\sigma/m)\left(1-\sqrt{P^*}\right)^{1.5}}{2k_s\ b_L^2\ P^*} \tag{5.12}$$

or in the non-dimensional form

$$R^*_{\text{s, flux tube}} = 2k_sLR_s \propto \frac{\left(1-\sqrt{P^*}\right)^{1.5}}{P^*} \tag{5.13}$$

where $L = b_L^2/(\sigma/m)$ is the conforming rough limit length scale. The TCR for conforming rough surfaces, using the heat source on a half-space solution, can be found by substituting Eq. (5.11) into Eq. (5.8)

$$R^*_{\text{s, half-space}} \propto \frac{1}{P^*} \tag{5.14}$$

Figure 5-5 shows the comparison between Eqs. (5.13) and (5.14). It can be seen that over a wide range of P^* they are almost identical and show very good agreement. However, as expected, at relatively large values of P^* the half-space relationship, Eq. (5.14), shows slightly higher

resistances than the flux tube. The RMS relative difference between two relationships is less than 4 percent. Therefore, the microcontacts can be modeled as heat sources on a half-space and Eq. (5.14) is chosen for thermal analysis of microcontacts.

Using these powerful scale analysis techniques, we derived Eq. (5.14) which illustrates that the TCR of microcontacts is inversely proportional to the dimensionless pressure (or external load). To find the equality or exact relationship, Eq. (5.14) must be multiplied by the scale analysis constant, c, which can be found through comparison with experimental data, i.e.,

$$R_s^* = \frac{c}{P^*} \tag{5.15}$$

The dimensional forms of thermal resistance and conductance using $h_s = 1/\left(R_s A_a\right)$, are

$$\begin{aligned} R_s &= \frac{\pi c \left(\sigma/m\right) H^*}{2 k_s F} \\ h_s &= \frac{2}{\pi c} k_s \left(\frac{m}{\sigma}\right) \frac{P}{H^*} \end{aligned} \tag{5.16}$$

where c and $P = F/\left(\pi b_L^2\right)$ are the scale analysis constant, and nominal contact pressure, respectively. From Eqs. (5.16) and (5.6), it can be seen that the effective micro thermal resistance is inversely proportional to the real contact area, i.e., $R_s \propto \left(\sigma/m\right)/\left(k_s A_r\right)$.

Approximately 610 experimental data points collected by Antonetti [64], Hegazy [25], Milanez et al. [65], McWaid [74], and Nho [75] are summarized, non-dimensionalized, and plotted along with Eq. (5.15) in Fig. 5-6 with $c = 0.36$. Minimizing the RMS difference between the model, Eq. (5.15), and the experimental data, the constant of the scale analysis c was found to be $c = 0.36$. The relative RMS and the mean absolute difference between the data and the relationship are 14.1% and 10.9%, respectively. Table 5.1 indicates the researchers and the specimen materials used in the experiments. Appendix A lists the data set number, the number which was originally assigned to the experimental data set by the researchers, geometrical, mechanical, average contact temperature, and thermophysical properties of the experimental data, as reported.

Nho [75] studied the contact of ground with lapped surfaces. He showed that the grinding process generates near-Gaussian surface heights distributions. The surface slope was estimated

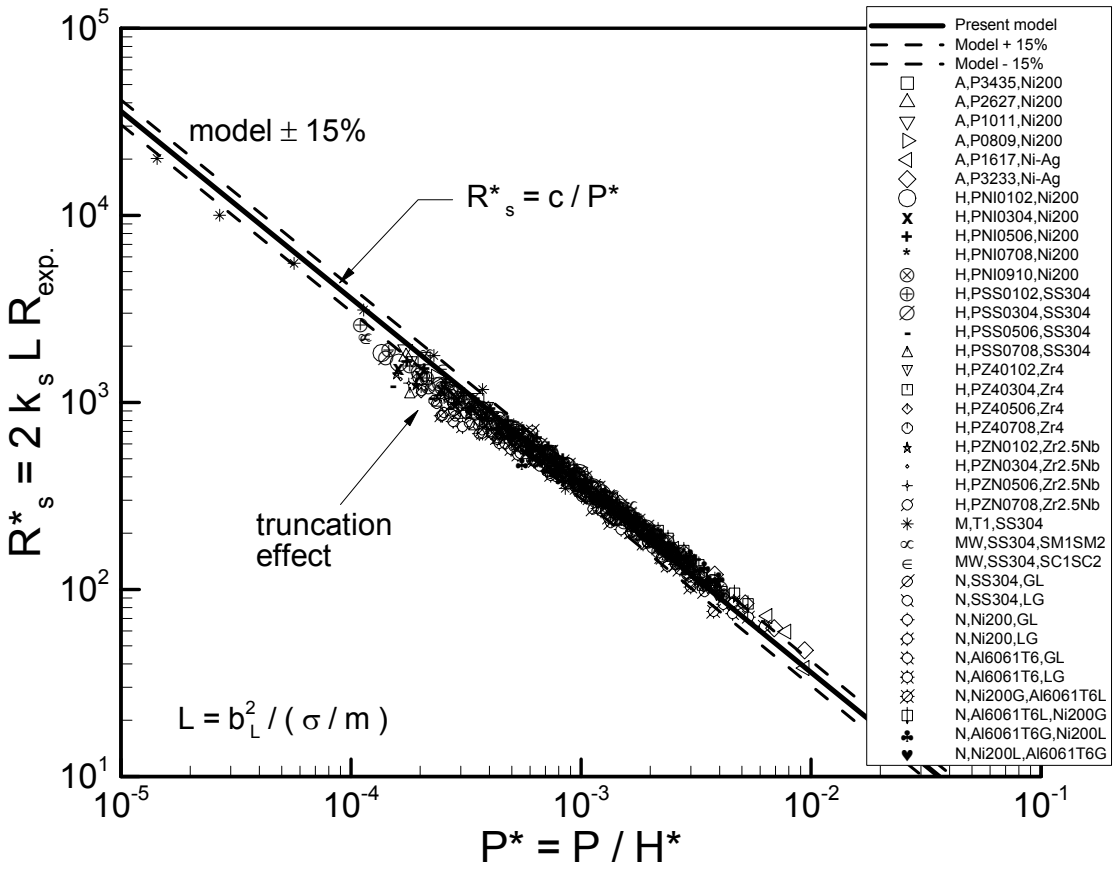

Figure 5-6: Comparison between scale analysis model and data, conforming rough limit

Table 5.1: Researchers and specimen materials used in comparisons

Ref.	Researcher	Material(s)
A	Antonetti [64]	Ni 200 Ni 200-Ag
Blo	Bloom [76]	SS 17-4 PH
B	Burde [26]	SPS 245, CS
CC	Clausing and Chao [59]	Al 2024 T4 Brass Anaconda Mg AZ 31B SS303
CM	Cassidy and Mark [77]	SS 416
F	Fisher [61]	Ni 200-Carbon Steel
FG	Fletcher and Gyorog [78]	Brass 360 Mg Az 31B SS 304
G	Gyorog [79]	SS 304
H	Hegazy [25]	Ni 200 SS 304 Zircaloy 4 Zr-2.5%wt Nb
K	Kitscha [60]	Steel 1020-CS
MM	McMillan and Mikic [71]	SS 303
MR	Mikic and Rohsenow [14]	SS 305
M	Milanez et al. [65]	SS 304
MW	McWaid [74]	SS 304
N	Nho [75]	Al 6061 T6 Ni 200 SS 304 Ni $\leftrightarrows$ Al
SG	Smuda and Gyorog [80]	SS 304

from the geometric mean $m = \sqrt{m_{\min} m_{\max}}$, where $m_{\min}$ and $m_{\max}$ are the minimum and maximum surface slopes measured by the profilometer. Nho carried out an extensive experimental program on the heat flow directional effect on similar and dissimilar metal, i.e., aluminum alloy 6061-T6, nickel 200, and SS 304 pairs over a broad range of thermophysical properties and contact pressure. Nho's data are named to show the heat flow direction and the surface preparation method, for example "N, Ni200-G,Al6061T6-L" means that the experiment was conducted between ground nickel 200 and lapped aluminium 6061T6 and the heat flow direction was from nickel to aluminium specimen. As can be seen in Fig. 5-6, data show a negligible directional effect for similar metals. Additionally, the directional effect is not observed in dissimilar metals whenever the thermal conductivities of the pair are close, for example nickel 200 and aluminium 6061T6, but for pairs with significantly different thermal conductivities such as nickel 200 and SS 304 a large deviation from the predicted TCR is observed; those data are not included in the comparison.

As can be observed in Fig. 5-6, a common trend can be recognized in most of the conforming rough data sets. Experimental data show a lower resistance at relatively light loads compared with the model; the data approach the model as the load increases. As previously mentioned in Chapter 4, this phenomenon which is called the truncation effect [65], and it is important at light loads when surfaces are relatively rough. A possible explanation for this trend is the Gaussian assumption of the surface asperities which implies that asperities with "infinite" heights exist.

Yovanovich [8] proposed an accurate correlation for determining the thermal conductance of conforming rough contacts based on the analytical model of Cooper et al. [7]

$$h_c = 1.25 k_s \left(\frac{m}{\sigma}\right) \left(\frac{P}{H_{mic}}\right)^{0.95} \tag{5.17}$$

Comparison of Eq. (5.16) with $c = 0.36$ and Eq. (5.17) reveals that the present model and Yovanovich [8] correlation are in good agreement over moderate and high loads, $1 \times 10^{-4} \leq P/H_{mic} \leq 2 \times 10^{-2}$; for relatively light loads, $P/H_{mic} \leq 1 \times 10^{-4}$, Eq. (5.16) predicts higher resistances.

5.4.2 General Model

In Chapter 3, a simple correlation was proposed for calculating the radius of the macrocontact as a function of two non-dimensional parameters, Eq. (3.30)

$$a_L = 1.80\ a_H\ \frac{\sqrt{\alpha + 0.31\tau^{0.056}}}{\tau^{0.028}} \tag{5.18}$$

where $\alpha = \sigma\rho/a_H^2$ and $\tau = \rho/a_H$ are the roughness parameter introduced by Johnson [20] and the geometric parameter, respectively.

The thermal macro resistance can be found by using the flux tube correlation, Eq. (5.2), and the radius of the macrocontact area given by Eq. (5.18)

$$R_L = \frac{(1 - a_L/b_L)^{1.5}}{2k_s a_L} \tag{5.19}$$

In Eq. (5.19), it is assumed that the radii of two contacting bodies are the same, i.e., $b_{\mathrm{L},1} = b_{\mathrm{L},2} = b_{\mathrm{L}}$. In the general case where $b_{\mathrm{L},1} \neq b_{\mathrm{L},2}$, thermal spreading resistance will be, $R = \psi\,(a/b)\,/4ka$.

The macrocontact area is a circle, thus the heat transferred in a non-conforming rough contact under vacuum conditions can be calculated from,

$$Q = 2\pi\Delta T_s \int_0^{a_L} h_s\,(r)\,r dr \tag{5.20}$$

where $h_s\,(r)$, $\Delta T_s = T_{\mathrm{i},1} - T_{\mathrm{i},2}$ are the local thermal conductance, and the effective temperature difference for microcontacts, respectively. The effective micro thermal conductance for a joint can be defined as $h_s = Q/\,(A_a \Delta T_s)$. Therefore, the effective microcontact thermal resistance, where $R = 1/\,(hA_a)$ is,

$$R_s = \frac{1}{2\pi}\left[\int_0^{a_L} h_s\,(r)\,r dr\right]^{-1} \tag{5.21}$$

Assuming constant pressure in the surface elements dr, one can calculate the local thermal conductance at r from Eq. (5.16)

$$h_s\,(r) = \frac{2}{c\pi} k_s \left(\frac{m}{\sigma}\right) \frac{P\,(r)}{H^*} \tag{5.22}$$

where $P(r)$ is the local contact pressure at r. Substituting Eq. (5.22) into Eq. (5.21), one obtains

$$R_s = \frac{cH^*(\sigma/m)}{4k_s}\left[\int_0^{a_L} P(r)\, r dr\right]^{-1} \tag{5.23}$$

From a force balance, we know that $F = 2\pi \int_0^{a_L} P(r)\, r dr$, therefore Eq. (5.23) simplifies to

$$R_s = \frac{c\pi H^*(\sigma/m)}{2k_s F} \tag{5.24}$$

Equations (5.16) and (5.24) are identical which implies that the effective thermal micro resistance R_s is not a function of the surface curvature. Additionally, the pressure distribution profile does not affect the thermal micro resistance. Through experiments, it can be observed that the joint resistance R_j increases as surface curvature decreases from the conforming ($\rho \to \infty$) toward non-conforming contacts. This increase arises due to the formation of the macrocontact area and consequently the macro resistance R_L. It should be noted that the effective micro thermal resistance R_s remains unchanged as surface curvature varies, Eq. (5.24).

By superimposing the macro and the micro resistances, Eq. (5.4), the thermal joint resistance for a general contact is obtained

$$R_j = \frac{0.565H^*(\sigma/m)}{k_s F} + \frac{(1 - a_L/b_L)^{1.5}}{2k_s a_L} \tag{5.25}$$

From Eq. (5.25) one can conclude that i) the effective micro thermal resistance, except for the thermal conductivity, is only a function of the contact micro-scale characteristics, i.e., surface roughness σ, slope m, microhardness H^*, and the load F, ii) on the other hand, the macro thermal resistance is a function of the macro-scale contact parameters, the macrocontact radius a_L, and size of the contacting bodies b_L. The macrocontact radius is a function of the effective elasticity modulus E', radius of curvature ρ, surface roughness σ, and the load F, Eq. (5.18).

The applied load and the surface roughness appear to play important roles in both macro and micro thermal resistances. The effect of surface roughness on the macro resistance is limited to the macrocontact radius, a_L. The applied load is the connecting bridge between the macro and micro mechanical analyses, since the force balance must be satisfied in both analyses.

Equation (5.25) is a general relationship that covers both limiting cases and the transition

region. It can be easily seen that in the conforming rough limit, where $a_L \to b_L$ the macro resistance $R_L \to 0$ and Eq. (5.25) yields Eq. (5.16). Also, in the elastoconstriction limit, where $\sigma \to 0$ the micro resistance $R_s \to 0$ and $a_L \to a_H$ and Eq. (5.25) is reduced to Eq. (5.3).

Dividing both sides of Eq. (5.25) by R_s, one obtains

$$\frac{1.77 k_s F}{H^* (\sigma/m)} R_j = 1 + \Theta \tag{5.26}$$

where Θ is the ratio of the macro to micro thermal resistances

$$\Theta = \frac{F (1 - a_L/b_L)^{1.5}}{1.13 H^* (\sigma/m) a_L} \tag{5.27}$$

Θ is a non-dimensional parameter which includes the applied load, macro and micro geometrical parameters, i.e., σ, m, ρ, and b_L as well as the elastic and plastic mechanical properties of the contacting bodies, E' and H^*. Based on this non-dimensional parameter, a criterion can be defined for the elastoconstriction and conforming rough limits

$$\begin{cases} \Theta \ll 1 & \text{conforming rough} \\ \Theta \gg 1 & \text{elastoconstriction} \end{cases} \tag{5.28}$$

As expected, Θ is independent of the thermal conductivity.

Equation (5.25) can be non-dimensionalized with respect to the conforming rough limit length scale L and re-written,

$$R_j^* = 2 k_s L R_j = \frac{0.36}{P^*} + \frac{L (1 - a_L/b_L)^{1.5}}{a_L} \tag{5.29}$$

where $L = b_L^2 / (\sigma/m)$ and $P^* = F / \left(\pi b_L^2 H^*\right)$.

5.5 Comparison With Experimental Data

To verify the general model developed in this Chapter, an experimental program was designed and conducted to obtain data for non-conforming rough contacts in a vacuum. Test procedure and experimental results are shown in Chapter 6. Three sets of experimental data are collected

that cover the transition region. The collected data show excellent agreement with the model, Eq. (5.29).

Additionally, approximately 260 experimental data points collected by Burde [51], Bloom [76], Cassidy and Mark [77], Clausing and Chao [59], Fisher [61], Fletcher and Gyorog [78], Gyorog [79], Kitscha [60], McMillan and Mikic [71], Mikic and Rohsenow [14], and Smuda and Gyorog [80] are summarized through a comprehensive literature review. The non-dimensional roughness parameter, $\alpha = \sigma\rho/a_H^2$, is an important mechanical parameter for the spherical rough contacts. As the roughness parameter approaches zero the contact pressure and the macrocontact radius approaches the Hertzian values. The roughness parameter may be reduced by i) increasing load ii) decreasing surface roughness, and iii) decreasing the radius of curvature. Figure 5-7 summarizes the range of the roughness parameter for the experimental data used in the comparison. As shown, the above data sets cover a wide range of the roughness parameter.

The collected data were non-dimensionalized and compared with the model, Eq. (5.26), in Fig. 5-8. The three regions of TCR are also shown in the plot. The present model illustrates good agreement with the data; the RMS and mean absolute relative difference between the model and data are approximately 11.7% and 9.4%, respectively. Table 5.1 lists the researchers and the specimen materials used in the experiments. Appendix A lists the data set number, the number which was originally assigned to the experimental data set by the researchers, geometrical, mechanical, average contact temperature, and thermophysical properties of the experimental data, as reported.

As the external load increases beyond the elastic limit of the contacting bodies, elastoplastic and plastic deformations may occur. The plastic macrocontact radius, a_P, is larger than the radius a_L (elastic), i.e., $a_P > a_L$. Consequently, lower TCR will be measured; this trend can be clearly seen in the Fisher [61] data set "F,11A,Ni200-CS", see Figs. 5-8 and 5-9.

More than 880 experimental data points, data sets used in comparisons in Figs. 5-6 to 5-8, are combined, non-dimensionalized, and compared with the present model, Eq. (5.29), in Fig. 5-9. The present model shows good agreement over the entire range of the comparison with the experimental data, which cover a wide range of the input parameters, see Table 5.2.

The data include the contact between dissimilar metals such as Ni 200-Al 6061T6, Ni 200-Ag and SS-CS. Additionally, the comparison includes the directional heat flow.

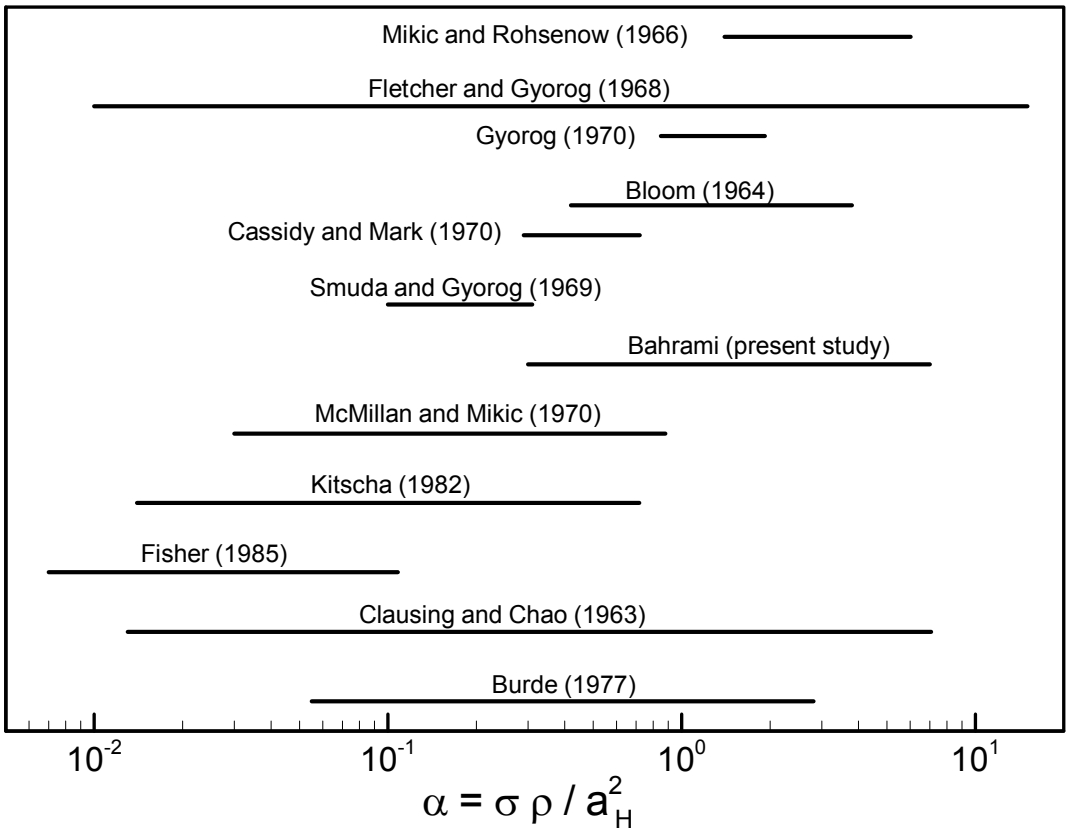

Figure 5-7: Range of roughness parameter α for experimental data used in comparison

Table 5.2: Range of parameters for experimental data

Parameter
$7.15 \leq b_L \leq 14.28\ mm$
$25.64 \leq E' \leq 114.0\ GPa$
$7.72 \leq F \leq 16763.9\ N$
$16.6 \leq k_s \leq 227.2\ W/mK$
$0.04 \leq m \leq 0.34$
$0.12 \leq \sigma \leq 13.94\ \mu m$
$-60 \leq \overline{T_c} \leq 195\ ^\circ C$
$0.0127 \leq \rho \leq 120\ m$

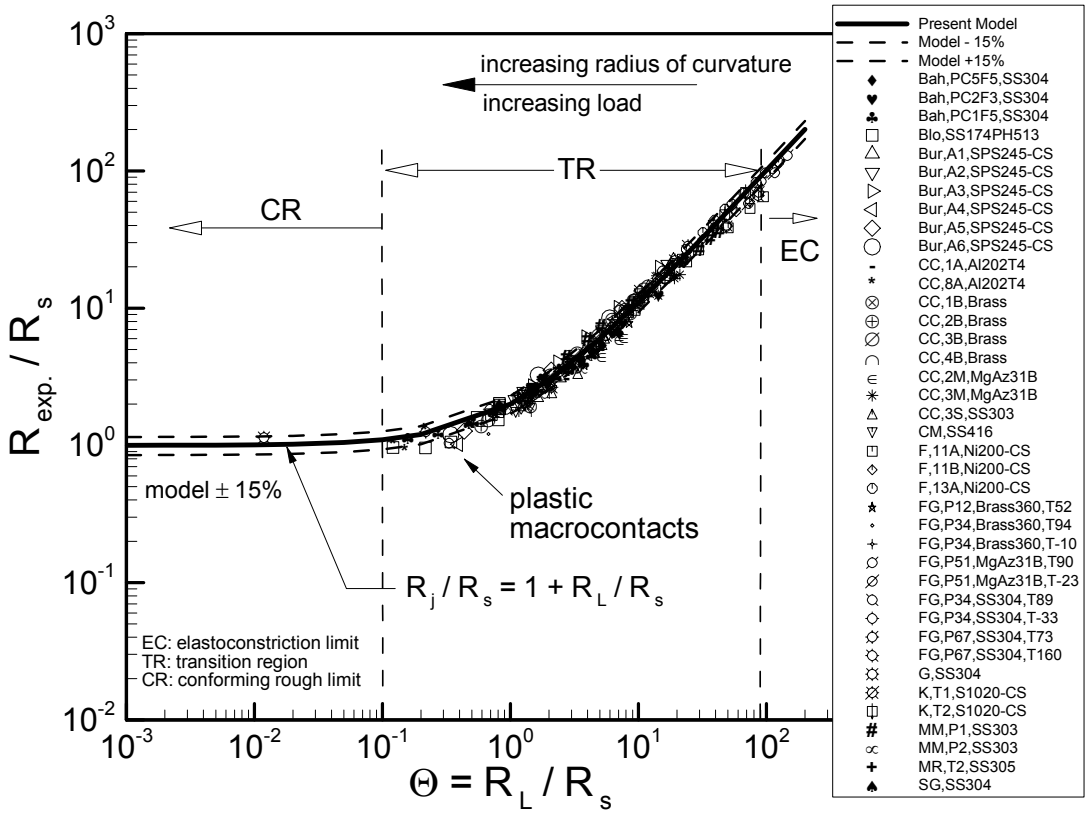

Figure 5-8: Comparison between general model and non-conforming rough data

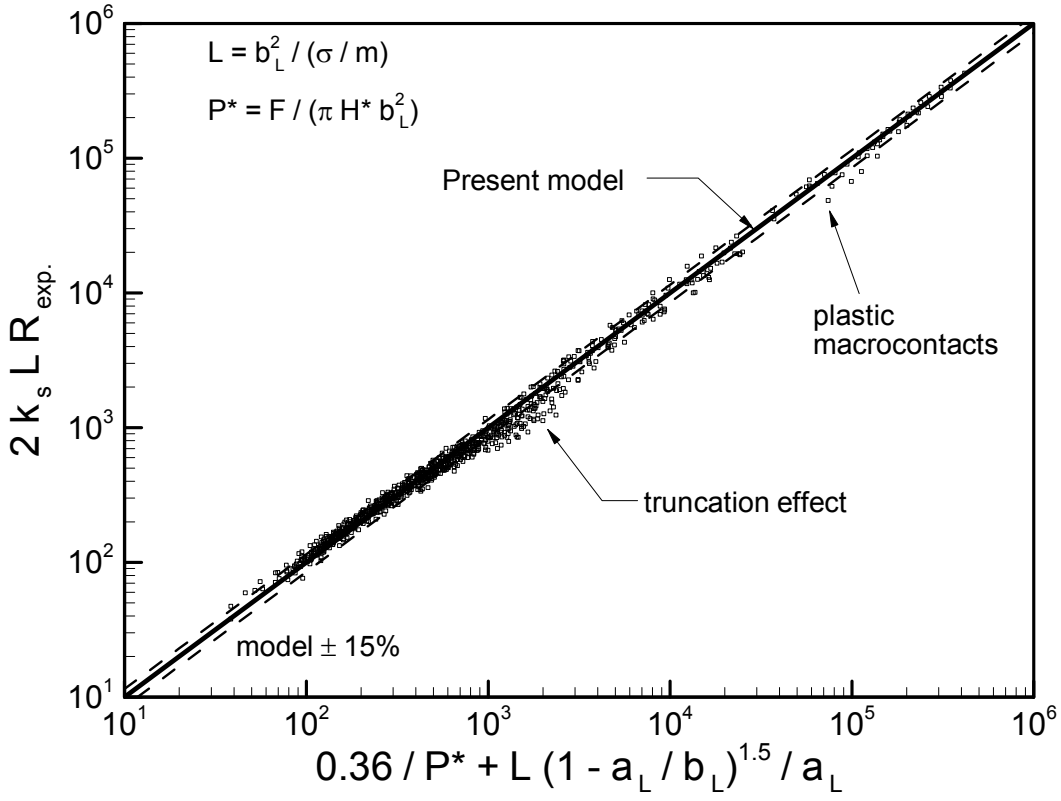

Figure 5-9: Comparison of general model with all data

The surface slope m has not been reported by Clausing and Chao [59], Kitscha [60], Fisher [60], and Mikic and Rohsenow [14] and were estimated using a correlation proposed by Lambert and Fletcher [6], $m = 0.076\sigma^{0.52}$, where σ is in micrometer, see Table 2.1. Because of the above-mentioned approximation to account for unreported data, the accuracy of the model is difficult to assess. However, the RMS and the mean absolute difference between the model and data for the entire set of data are approximately 13.8% and 10.4%, respectively. A ±15 percent bound is included in Fig. 5-9; 730 out of 880 data points fall into the ±15 percent bound. The accuracy of experimental data were reported by some of researchers, such as Antonetti [64], Fisher [61], and Hegazy [25] to be 8.1, 5, and 7 percent, respectively.

5.6 Summary and Conclusion

It was shown that the joint resistance was the superposition of the macro and micro thermal resistances in a vacuum. Comparing the heat source on a half-space with the flux tube solutions over a wide range of applicable load range, it was shown that the heat source on a half-space assumption for the geometry of microcontacts was justifiable. In other words, microcontacts were located far enough from each other that they did not interfere and could be considered as heat sources on a half-space. In this Chapter, instead of using probability relationships, scale analysis methods were used and a novel TCR model was developed for the conforming rough contacts. The effective micro thermal resistance was observed to be inversely proportional to the real contact area and directly proportional to the parameter (σ/m).

The scale analysis relationship derived for the conforming rough contacts was integrated over the macrocontact area to extend the scale analysis model to cover the general contact or the transition region. It was shown that the effective micro thermal resistance component of the joint resistance, R_s, was not a function of the surface curvature/out-of-flatness. Additionally, the profile of the effective contact pressure distribution did not affect the effective micro thermal resistance, R_s. Using the proposed correlation for the radius of the macrocontact in Chapter 3 and the flux tube correlation the macro thermal resistance was determined. Superimposing the macro and the micro thermal resistances a general relationship for TCR was derived. This expression covered the entire TCR ranging from the conforming rough to the spherical smooth

bare joints in a vacuum.

A new non-dimensional parameter was introduced which represents the ratio of the macro over the micro thermal resistances. Based on this non-dimensional parameter a criteria was proposed for specifying the three regions of TCR, i.e., the conforming rough limit, the elasto-constriction limit and the transition region.

The scale analysis model was compared with 75 data sets, more than 880 TCR data points collected by many researchers during last 40 years, which cover a wide range of surface characteristics, thermal and mechanical properties, mean contact temperature, directional heat transfer, and contact between dissimilar metals. The RMS difference between the model and data was approximately 13.8% over the entire range of the comparison.

Chapter 6

Experimental Study

6.1 Experimental Apparatus

The experimental apparatus used in this study is the same as that used and described by Mantelli [81]. The experimental apparatus was developed to fit inside the vacuum chamber. Figure 6-1 shows a general view of the experimental apparatus. A brief description of each component of the test apparatus is given below.

The test chamber consisted of a stainless steel base plate and a stainless steel bell jar enclosing the test column. The test column consisted of, from top to bottom: the loading mechanism, the heater block, the load cell, the smooth spherical sample, the flat rough specimen, the Armco iron flux meter, and the heat sink (cold plate). A schematic sketch of test column is shown in Fig. 6-2.

Two cylindrical specimens, 25 mm in diameter by 45 mm long, were held coaxially between the heating block and the flux meter. The spherical sample was fitted into a 25 mm diameter recess in a cylindrical brass heating block.

A Lebow 300 lbs load cell model 3397 was used to measure the applied load to the joint. The load was applied over a load button placed in the center of the load cell. A DC excitation voltage of 12 V was applied to the load cell and resulting sensitivity was 0.0397 mV/N.

The heater block consisted of circular flat copper in which two cylindrical Watlow 120V, 500 W pencil-type electrical heaters were installed. The power to the heaters could be adjusted through an auto transformer.

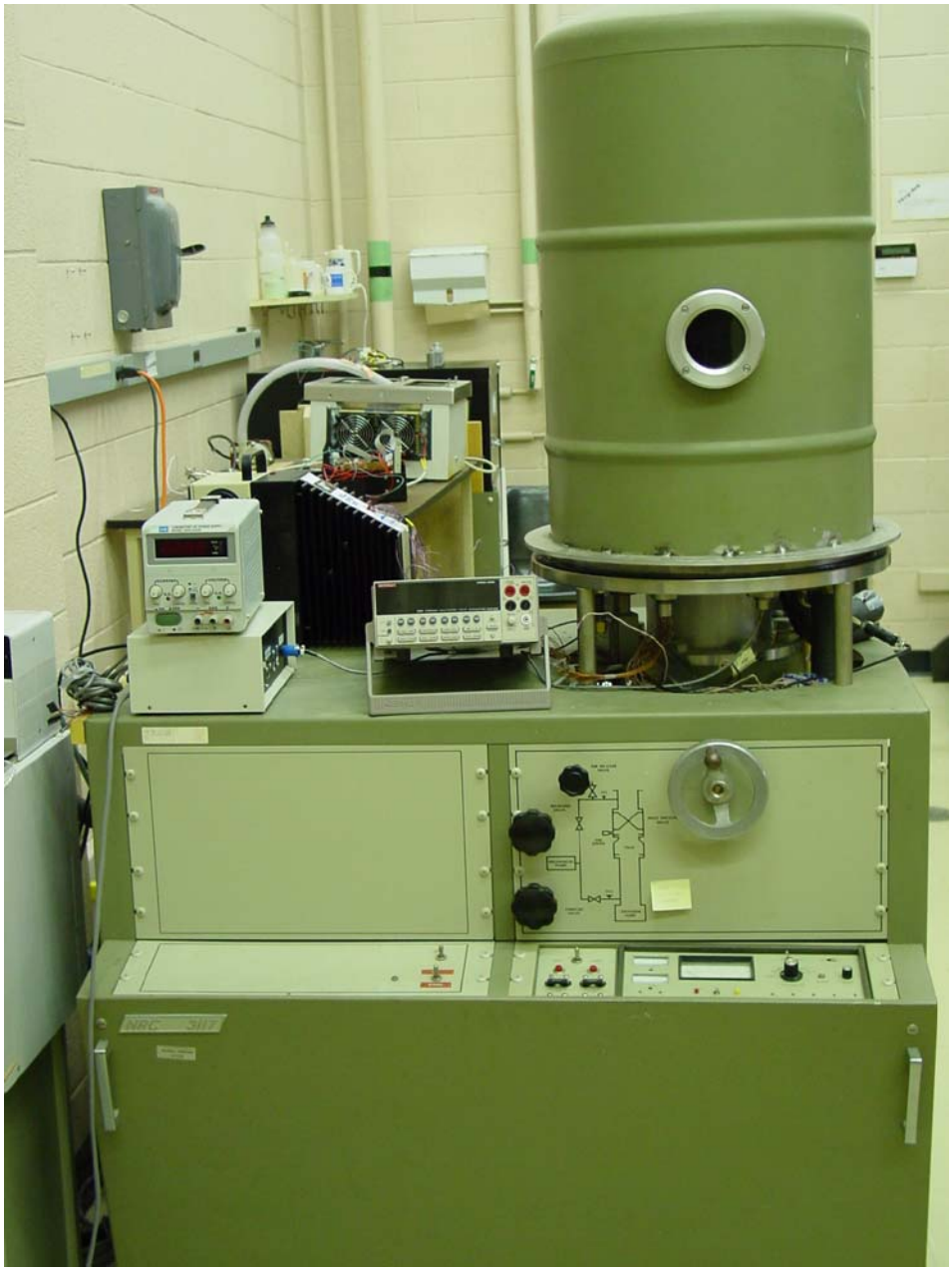

Figure 6-1: General view of test apparatus

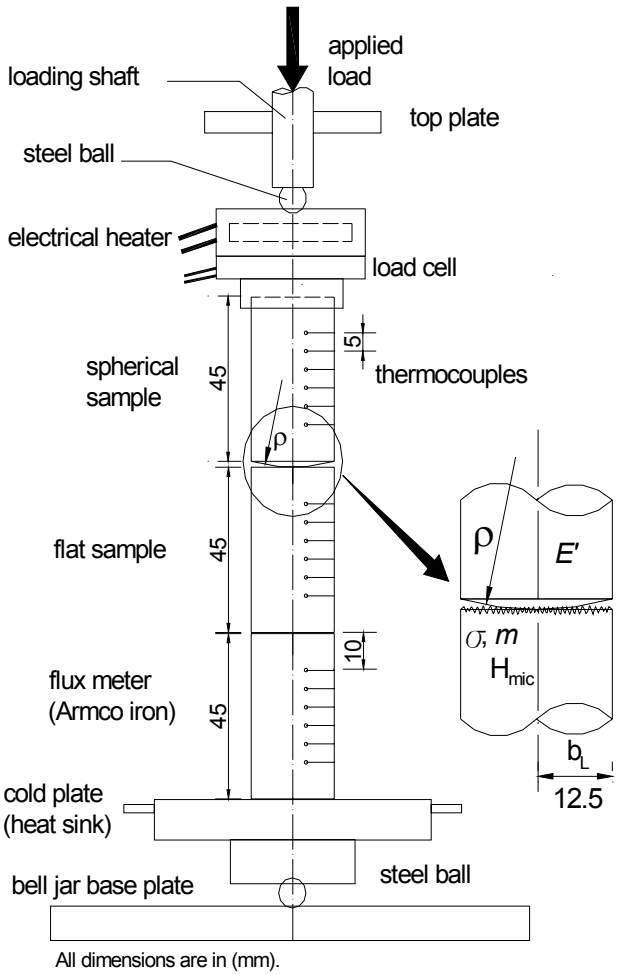

Figure 6-2: Schematic view of test column

The cold plate consisted of a hollow copper cylinder, 5.08 cm high and 17.78 cm diameter, cooling was accomplished using a closed loop water-glycol bath in which the coolant temperature could be set. Flexible bellows were incorporated in the cooling flow lines inside the chamber to facilitate the movement of the cold plate under loading.

6.2 Preparation of Test Specimens

Contact surfaces were prepared on the faces of 25 mm diameter by 45 mm long cylindrical specimens. Both flat and spherical specimens were made of SS304, $E = 207\ GPa$ and $\nu = 0.3$. Samples were machined into cylindrical shapes of 25 mm diameter and 45 mm length. The contact assembly included a bead-blasted flat specimen placed in contact with a smooth polished spherical sample in series with an Armco iron flux meter in a vacuum chamber.

The experimental program was designed to study/cover the transition region where the magnitude of the micro and the macro thermal resistances are comparable. As shown in Chapters 4 and 5, a large number of reliable TCR data are available for the conforming rough and the elastoconstriction limits, therefore no tests were conducted in these limiting regions. Two radii of curvature were chosen for spherical samples, 0.45 and 0.95 m. Radii of curvature of spherical samples were measured using a Mitutoyo BHN 305 coordinate measuring machine (CMM) that was connected to a PC. The CMM machine has a probe, which enables one to measure the coordinate and the surface curvature at any point on a spherical body. To find a radius of curvature, 30 points were measured randomly over each spherical sample, the software of the equipment then curve-fitted these points and calculated the radius of curvature that best fitted the surface curvature. For each spherical sample, five separate radii of curvature were measured and averaged to find a realistic radius of curvature. The maximum relative difference between the average radii and the measurements is less than 3.5 percent. Table 6.1 shows the radius of curvature measurements for spherical samples used in T1 to T3.

Flat specimens were first machined on a lathe and then finely ground to the required dimensions. Next, flat samples were mechanically lapped. After mechanical lapping, the specimens were carefully hand-lapped and cleaned. Some of the flat specimens (prepared by mechanical and then hand lapping) were found to have out-of-flatness, approximately spherical, and

Table 6.1: Surface radius of curvature measurements for spherical samples

Measurement #	Surface radius of curvature, ρ (m) T1	T2	T3
1	0.995	0.458	0.946
2	0.943	0.439	0.948
3	0.938	0.461	0.953
4	0.949	0.448	0.954
5	0.979	0.453	0.945
	$\overline{\rho} = 0.946$	$\overline{\rho} = 0.452$	$\overline{\rho} = 0.961$

were discarded. The flatness deviation of the flat specimens was checked using an optical flat instrument. In general, the out-of-flatness deviations were less than 0.3 μm. The random (Gaussian) roughness was created on the flat specimens by bead-blasting with two different grades of glass beads. After this process, the roughened specimens were cleaned, and using a Taylor-Hobson ST3Plus Talysurf profilometer, the surface roughness and slope of the flat samples were measured. Eight randomly selected traces of surface height profile were taken from each bead-blasted specimen. Each trace was approximately 10 mm long. The RMS difference between the mean values and the surface roughness and slope measurements is approximately 6 percent. Table 6.2 lists surface measurements for the flat surface that used in test T1 as an example to show the procedure, the average surface roughness and asperity angle were $\overline{\sigma} = 2.04$ μm and $\overline{\theta} = 6.25$ degree. The mean absolute surface slope m were calculated using,

$$m = \sqrt{\frac{2}{\pi}} \tan\left(\overline{\theta}\right)$$

Both contact specimens and the flux meter were prepared for placement of six thermocouples by drilling holes of 0.64 mm diameter and 2.5 mm deep. Copper-constantan thermocouples were installed in the holes along the specimens, spot welded to the surface. Thermocouple wires were wound once around the sample to reduce thermal conduction down the thermocouples leads as a result of the thermal gradient between samples and the leads. Thermocouples were placed along the samples length so that the temperature distribution within each section could be determined. These thermocouples were located 5 mm apart with the first one 10 mm from the contact surface, see Fig. 6-2. The thermal conductivity of Armco iron flux meter was known and was used to measure the heat flow rate transferred through the contact.

Table 6.2: Surface measurements for flat sample used in T1

θ asperity angle degree	σ roughness μm	% diff. roughness $100 \times (\overline{\sigma} - \sigma) / \overline{\sigma}$
6.21	1.91	-6.20
6.54	2.07	1.66
6.94	2.15	5.59
6.05	1.93	-5.22
5.54	1.86	-8.66
6.45	1.99	-2.27
6.29	2.12	4.11
5.98	2.26	10.99
$\overline{\theta} = 6.25$	$\overline{\sigma} = 2.04$	RMS diff. $= 6\%$

Also, separate tests were conducted to correlate thermal conductivity of SS 304 specimens as a function of temperature. The temperature distributions within the flat and spherical specimens were used to determine the contact temperature drop by extrapolating to the contact plane.

6.3 Assembly and Test Procedure

The parts of test column were assembled as shown in Fig. 6-2. The load could be applied to the test column via a lever system by adjusting a nut.

The overall thermal resistance measurements were made under steady-state conditions, which were consider achieved when all temperatures had a variation less than 0.05 K in 3 minutes. At this condition, the variation of thermal resistance is negligible. The temperatures were measured using type T (copper-constantan) thermocouples. The heater power was controlled manually and kept constant for each data point. A Keithley Integra series 2701 Ethernet multimeter/data acquisition system was used to acquire temperature and load readings and transfer the data to a PC.

The following procedure was employed for all thermal resistance measurements. The data acquisition system, computer, electrical heater, cooling system, and vacuum pump were powered on and the computer program were executed. All test column interfaces were cleaned and greased (except the test joint) with thermal grease to minimize the contact resistance at these interfaces. Then, test specimens were positioned coaxially between the heater and the flux

meter, and the test column was aligned visually to ensure that the column interfaces remained aligned during the test. The first load was applied.

The test column was insulated with fiberglass insulation. The column was then covered with an aluminum cylindrical shell to minimize the radiative heat loss. The input power to electrical power adjusted. The ball jar was carefully lowered, and the test chamber was evacuated using the mechanical pump. After reaching vacuum pressures to approximately 10^{-5} torr, the diffusion pump was powered on and connected in series with the mechanical pump. The vacuum process took approximately 8 to 10 hours. The temperature and pressure readings were updated by the data acquisition system and displayed on the monitor every 3 minutes. When the steady-state conditions were satisfied, the last experimental data were stored in a file. The applied load and the electrical power were increased manually and after approximately 4 hours a new steady-state condition was attained and another reading was obtained. The heater power input was increased by increasing the applied load to maintain a relatively high temperature drop across the joint. For experimental uncertainty analysis see Appendix B.

6.4 Test Results

6.4.1 Introduction

An experimental program was carried out under strictly controlled conditions using carefully prepared and specified spherical flat specimens. Three sets of data were collected as indicated by T1 to T3. The values chosen for radii of curvature, load, and surface roughness provides TCR data over a relatively wide range of the transition region. The surface roughness and slope, radius of curvature, microhardness coefficients, and average thermal conductivity for each test are listed in Table 6.3. To verify the reproducibility of experiments, Test T3 was conducted with the same radius of curvature and surface roughness of T1; new specimens were used over a wider range of applied load compared to T1.

Table 6.3: Geometric, mechanical, and thermal properties of tests

Parameter	T1	T2	T3
σ (μm)	2.04	2.78	2.04
m	0.087	0.199	0.087
ρ (m)	0.95	0.45	0.95
c_1 (GPa)	6.23	6.55	6.23
c_2	-0.23	-0.12	-0.23
$\overline{k_s}$ (W/mK)	18.23	18.82	18.46

6.4.2 Data Reduction

Thermal joint resistance under steady-state condition can be determined from

$$R_j = \frac{\Delta T}{Q} \qquad K/W \tag{6.1}$$

where ΔT and Q are temperature drop across the joint and heat flow rate, respectively. The temperature drop was determined by extrapolating the temperature distributions to the interface, and compute the temperature difference between the extrapolated values. Since the heat loss from the samples was negligible under vacuum conditions, the heat flow through the joint was assumed to be identical to the Armco iron flux meter. The heat transferred through Armco iron flux meter was determined using Fourier's equation

$$Q = -kAdT/dz \qquad \text{W} \tag{6.2}$$

where dT/dz is the temperature gradient along the flux meter and k is the thermal conductivity of the Armco iron flux meter computed at the mean temperature using the following expression

$$k\ \ (W/mK) = -0.0677\ T\,(^{\circ}C) + 79.832 \tag{6.3}$$

where, the maximum relative difference between this expression and tabulated values [82] in the range 30 to 100 $^{\circ}C$ was less than 3%.

Thermal conductivity of test samples was determined by correlating the conductivity data obtained from separate tests. Thermal conductivities were determined from the temperature gradient along the sample and was assigned to the mean specimen temperature. Having a series

of thermal conductivities as a function of temperature, the SS 304 thermal conductivity were curve fitted as,

$$k_{\text{SS 304}}\ \ (W/mK) = 0.0168\ T\,(^{\circ}C) + 17.346$$

with the maximum relative error of 2.29 percent in the range of 15 to 140$^{\circ}C$.

6.5 Experimental Data

Three experiment sets indicated by T1, T2, and T3 were obtained using 25 mm by 45 mm cylindrical samples. Both spherical and flat samples are made from SS 304. Geometrical, mechanical, and thermal properties of the tests are summarized in Table 6.3.

Tables 6.4 to 6.6 show the applied load, the roughness parameter α, the geometry parameter τ, the relative macrocontact radius $B = a_L/b_L$, micro, macro, and the joint thermal resistance predicted by the model, the non-dimensional parameter $\Theta = R_L/R_s$, the experimental data R_{exp}, and the relative difference between the model and data for each data points of tests T1 to T3. The scale analysis model developed in Chapter 5, i.e., Eq. (5.25) was employed for predicting the joint resistance R_j.

Figures 6-3 to 6-5 shows the comparison between the experimental data and the thermal joint resistances predicted by the general model, Eq. (5.25), for tests T1 to T3.

Table 6.4: Comparison between model and test result T1

F	α	τ	B	R_s	R_L	R_j	Θ	$R_{\exp}$	$\frac{R_j - R_{\exp}}{R_j}\%$
N	$(-)$	$(-)$	$(-)$	K/W	K/W	K/W	$(-)$	K/W	$(-)$
373.15	1.10	715.1	0.198	5.84	7.83	13.67	1.34	14.08	-3.0
495.33	0.91	650.7	0.204	4.41	7.53	11.94	1.71	12.19	-2.1
869.38	0.62	539.4	0.219	2.52	6.81	9.33	2.70	9.42	-1.0
1381.5	0.46	462.3	0.236	1.57	6.07	7.64	3.87	7.62	0.3
1740.9	0.39	427.9	0.245	1.22	5.60	6.82	4.60	6.71	1.6
2656.1	0.36	371.7	0.266	0.77	4.80	5.57	6.21	5.53	3.9

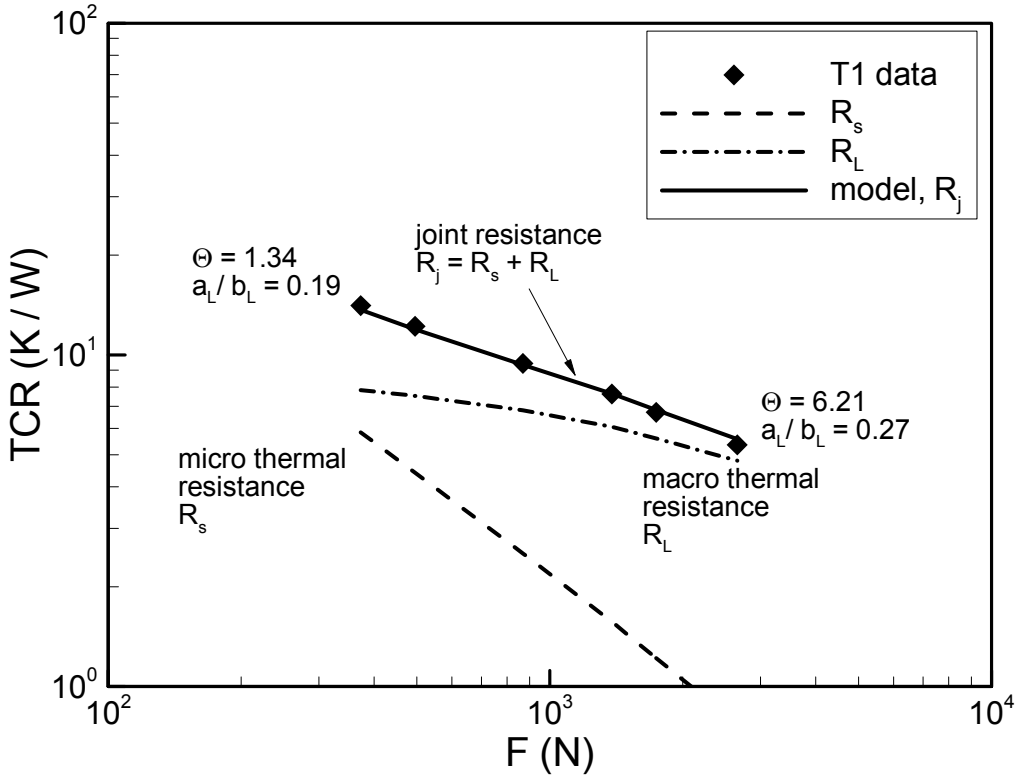

Figure 6-3: Comparison between model and test result, T1

Table 6.5: Comparison between model and test result T2

F	α	τ	B	R_s	R_L	R_j	Θ	$R_{\exp}$	$\frac{R_j - R_{\exp}}{R_j}\%$
N	$(-)$	$(-)$	$(-)$	K/W	K/W	K/W	$(-)$	K/W	$(-)$
210.9	1.71	527.1	0.152	9.34	11.12	20.46	1.19	21.50	-5.1
303.6	1.34	466.8	0.157	6.44	10.61	17.05	1.65	17.50	-2.6
445.7	1.04	410.8	0.162	4.41	10.17	14.58	2.31	13.80	5.3
883.6	0.66	326.9	0.176	2.20	9.04	11.25	4.11	10.90	3.1
1116.9	0.56	302.4	0.182	1.72	8.52	10.24	4.96	10.10	1.3
2577.4	0.32	228.9	0.210	0.73	6.86	7.59	9.42	7.10	6.5

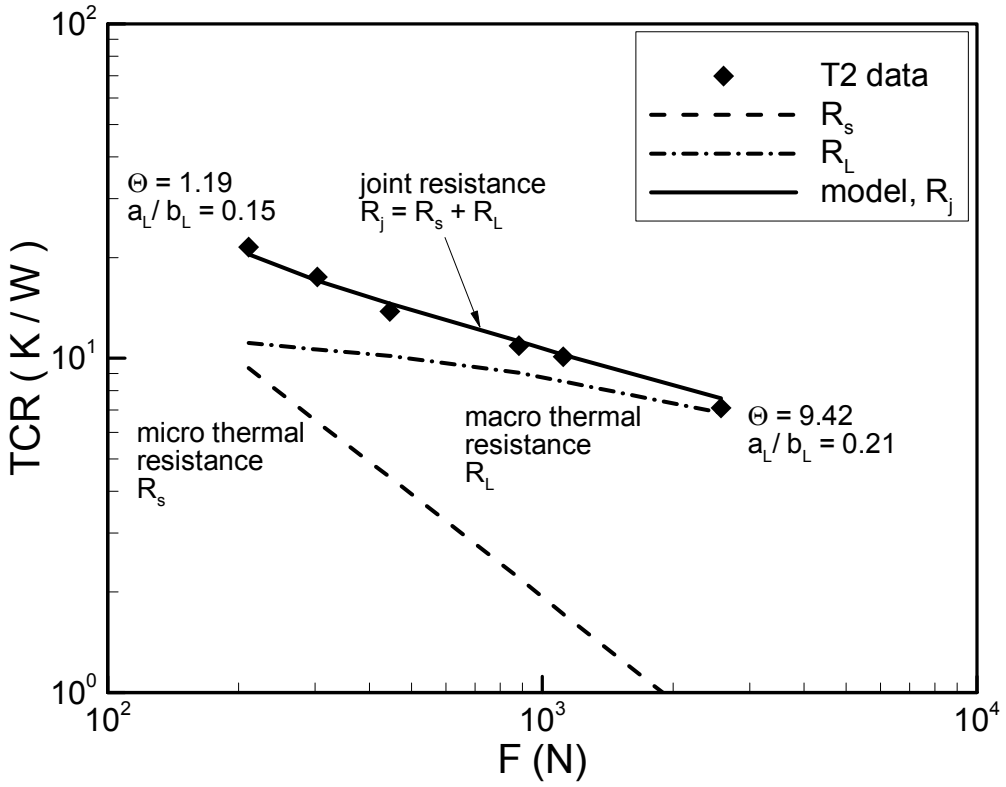

Figure 6-4: Comparison between model and test result, T2

Table 6.6: Comparison between model and test result T3

F	α	τ	B	R_s	R_L	R_j	Θ	$R_{\exp}$	$\frac{R_j - R_{\exp}}{R_j}\%$
N	$(-)$	$(-)$	$(-)$	K/W	K/W	K/W	$(-)$	K/W	$(-)$
31.3	5.73	1634.4	0.169	71.85	9.89	81.74	0.14	79.90	2.3
55.6	3.90	1349.1	0.173	40.16	9.55	49.71	0.24	48.50	2.4
110.1	2.47	1074.2	0.179	20.15	9.06	29.21	0.45	29.60	-1.3
189.2	1.72	896.7	0.186	11.91	8.77	20.68	0.74	21.80	-5.4
409.3	1.03	693.4	0.200	5.36	7.76	13.12	1.45	13.80	-5.2
600.5	0.80	610.2	0.209	3.64	7.26	10.90	2.00	11.50	-5.5
795.8	0.66	555.6	0.217	2.74	6.88	9.63	2.51	9.70	-0.7
1110.2	0.53	497.2	0.227	1.97	6.42	8.38	3.26	7.90	5.8
1338.6	0.47	467.1	0.234	1.61	6.07	7.69	3.77	7.50	2.4
2561.5	0.30	376.3	0.264	0.84	5.05	5.89	6.04	5.80	1.5

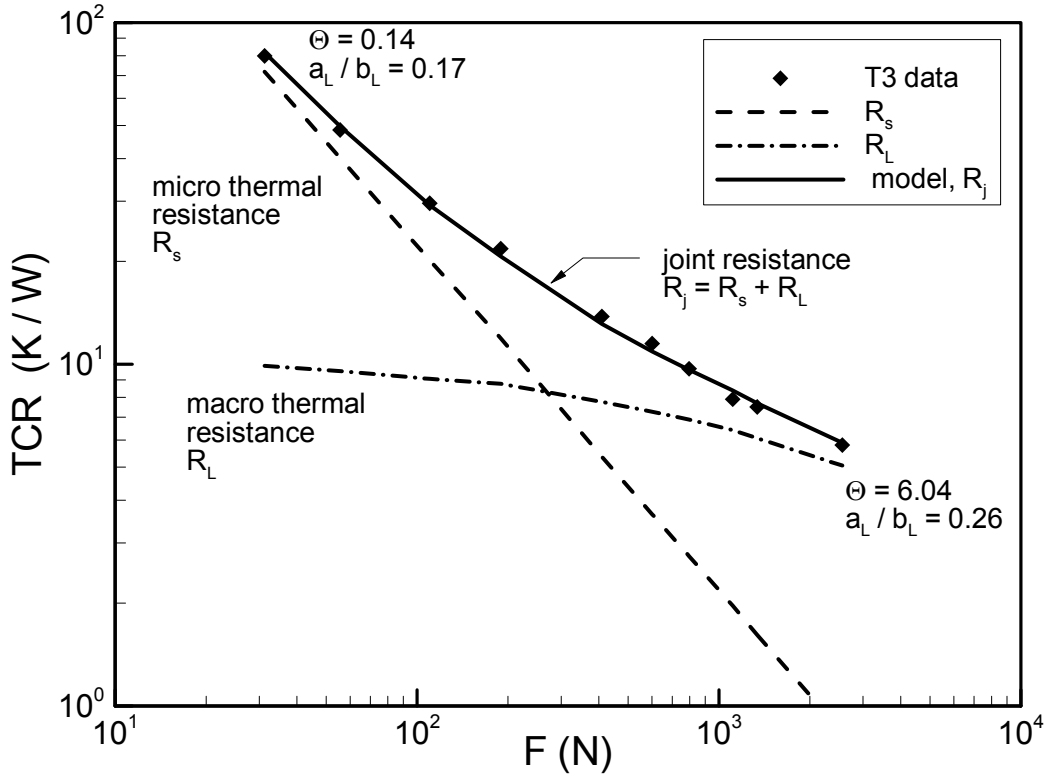

Figure 6-5: Comparison between model and test result, T3

Experimental data T1 to T3 were non-dimensionalized and compared with the model, Eq. (5.29) in Fig. 6-6. The maximum relative difference between the model and the data is 6.84%; the RMS difference between the model and data sets T1, T2, and T3 are 2.43, 4.13, and 3.84 percent, respectively.

The relative importance of the micro and macro thermal resistances (Θ) is also shown in Fig. 6-6. For the data set T3, the ratio of a_L/b_L varies from 0.17 to 0.26 as the load increases from 28 to 2561.5 N. The micro resistance becomes smaller and the macro resistance dominates the joint resistance by increasing the load. Note that even at a relatively large load of 2561.5 N, the radius of the macrocontact area covers only 26 percent of samples radius b_L. The spherical specimen have large radii of curvature, e.g. $\rho = 0.95\ m$ or equivalently the maximum out-of-flatness of 82 μm for T3. These samples seems flat and their surface curvatures can not be detected by naked eye, yet surface curvatures cause a relatively large thermal resistance even at high loads. This clearly shows the significance and impact of the surface curvature/out-of-flatness on TCR.

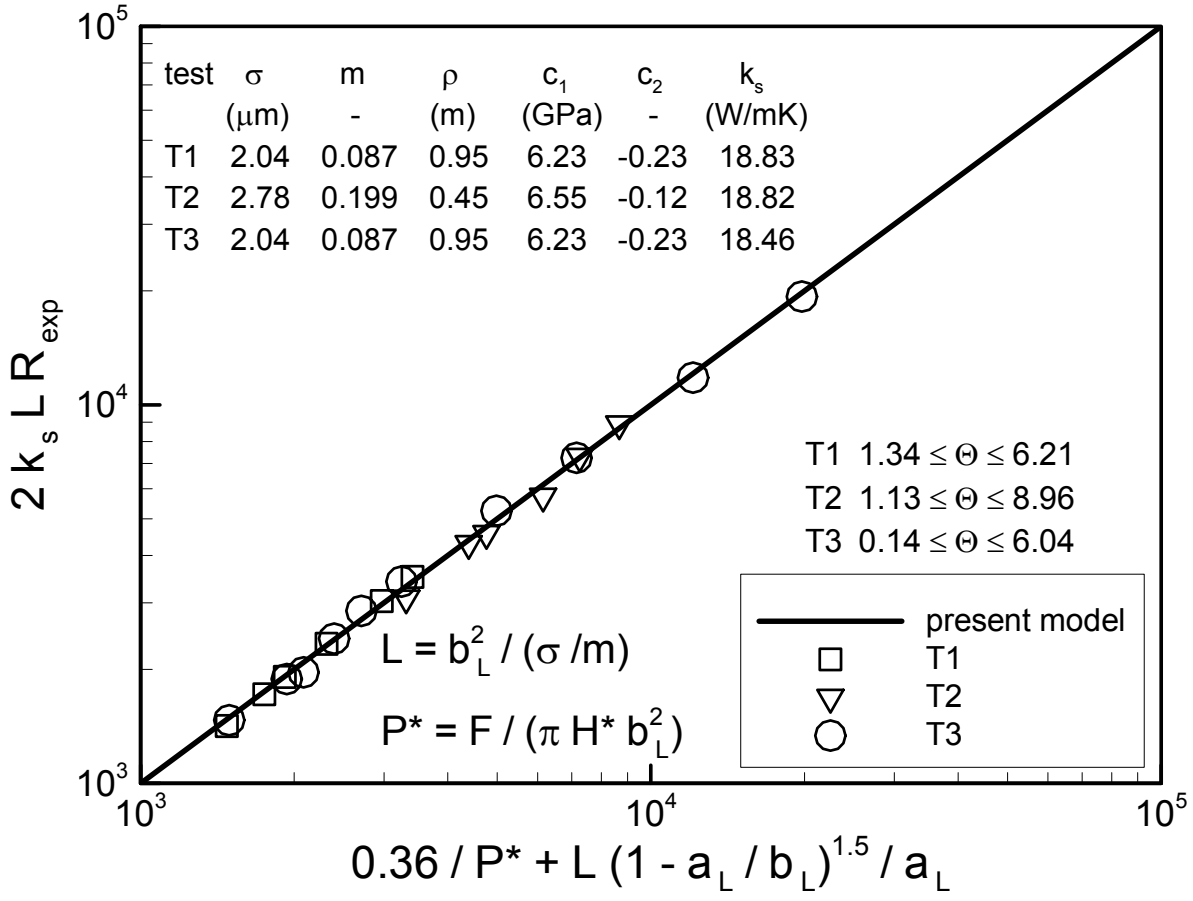

Figure 6-6: Comparison between T1-T3 data and present model

Chapter 7

Conclusions and Recommendations

7.1 Conclusions

Thermal contact resistance (TCR) of bare joints in a vacuum environment is studied analytically. A contact mechanics and two thermal models are proposed. The mechanical and thermal models were verified through comparison with experimental data. The following conclusions can be drawn:

1. The TCR modeling and its components are studied. The modeling process is divided into three analyses: geometrical, mechanical, and thermal where each one includes a macro and micro scale component.

2. Proposed empirical correlations to relate surface slopes, m, to surface roughness σ, are summarized and compared with surface measurement data. The comparison shows that the uncertainty of the correlations is high; use of these correlations is not recommended unless only an estimation of m is required.

3. Greenwood and Williamson [1] elastic, Cooper et al. [7] and Tsukizoe and Kisakado [35, 36] plastic conforming rough models are reviewed and a set of scale relationships are derived for the contact parameters, i.e., the mean microcontact size, number of microcontacts, density of the microcontacts, and the external load as functions of dimensionless separation. These scale relationships are compared and it is graphically shown that despite the different assumptions and input parameters, their behaviors in terms of the contact

parameters are similar. It can be concluded from the comparison that the behavior of contacting rough surfaces is determined essentially by surface statistical characteristics. Also a combination of plastic and elastic modes would introduce no new features.

4. The common assumptions of the existing TCR analyses are summarized. Proposed correlations by different researchers for the flux tube spreading resistance are compared. It is observed that, at the limit, the correlations approach the heat source on a half-space solution. Also all the spreading resistance correlations show good agreement for the applicable range.

5. More than 400 experimental data points collected by many researchers, are summarized and grouped into two limiting cases: conforming rough, and elastoconstriction. These data are non-dimensionalized and compared with existing TCR models at the two limiting cases. It is shown that none of the existing theoretical models covers both of the preceding limiting cases. This clearly shows the need to develop theoretical model(s) which can predict TCR over all cases including the above mentioned limiting cases and the transition range where both roughness and out-of-flatness are present and their effects on contact resistance are of the same order.

6. The mechanical contact of spherical rough surfaces is studied and a new analytical model is developed. The deformations of surface asperities are considered to be plastic and, the bulk deformation is assumed to remain within the elastic limit.

7. A closed set of governing relationships is derived and solved numerically. A computer code is developed to solve the governing relationships. The pressure distributions predicted by the model are plotted for different values of surface roughness and it is shown that as the surface roughness approaches zero the predicted pressure distribution approaches the Hertzian pressure distribution.

8. Additionally, it is shown that a general pressure distribution profile exists that encompasses all spherical rough contacts. The maximum contact pressure is observed to be the key parameter that specifies the contact pressure distribution. The proposed general pressure distribution expression yields the Hertzian contact pressure at the limit, where

surface roughness is set to zero.

9. The number of independent non-dimensional parameters that describe the maximum contact pressure is determined to be three: the roughness α, the geometric τ, and the microhardness E'/H_{mic} parameters. The effect of the microhardness parameter E'/H_{mic} on the maximum contact pressure is observed to be small and ignored. Compact correlations are suggested for calculating the maximum contact pressure, compliance, and the radius of the macrocontact area, as functions of roughness α, and geometric parameters τ. The present model is compared with the existing model of Greenwood and Tripp [38] and the same trend is observed. Also the macrocontact radius and compliance predicted by the model are compared against experimental data collected by others and good agreement is seen.

10. An expression for estimating the critical load is derived, where $a_L = b_L$. The Winkler approximation is used to derive a relationship for the contact pressure distributions, where the loads are higher than the critical load. This expression along with the above correlation form a general pressure distribution that encompasses all possible contact cases ranging from the smooth Hertzian to the conforming rough joints.

11. A criterion is offered to identify the flat surface, where the effect of surface curvature on the contact pressure can be neglected. Based on this criterion, the surface can be considered flat if the surface out-of-flatness and roughness are in the same order of magnitude.

12. The advantages of the present mechanical model over the Greenwood and Tripp [38] (GT) model can be summarized as

    - the present model requires two input surface parameters, roughness σ, and surface slope m,
    - the GT model needs three input parameters, i.e., σ_s, β, and η_s,
    - unlike the summit radius β and the summit density η_s in the GT model, the present model input parameters can be measured directly and they are not sensitive to the surface measurements,

- in the present model, a general pressure distribution profile is proposed that covers all possible contact cases simple correlations are proposed for determining the maximum contact pressure and radius of the macrocontact area as functions of two non-dimensional parameters, i.e., the roughness parameter α and the geometric parameter τ. But the GT model was proposed in the form of a set of governing relationships that required computer programing and tedious iteration methods.

13. TCR of non-conforming rough surfaces is considered as the superposition of macro and micro thermal resistance components accounting for the effects of surface curvature and roughness, respectively.

14. The results of the mechanical model, i.e., the local mean separation, the local mean radius and the number of the microcontacts, are used to develop an analytical thermal model for determining TCR of non-conforming rough contacts in a vacuum. The thermal model is constructed based on the premise that the mean separation between the contacting surfaces in an infinitesimal surface element can be assumed constant. Therefore, the conforming rough model of Cooper et al. [7] is implemented to calculate the surface element thermal resistance. The surface element thermal resistances are integrated over the macrocontact area to calculate the effective micro thermal resistance of the contact. The macrocontact resistance is calculated using the flux tube solution.

15. The effects of the major contact parameters, i.e., roughness, load, and radius of curvature on TCR are investigated. It is shown that there is a value of surface roughness that minimizes TCR. Additionally, at large loads the effect of roughness on the TCR becomes negligible.

16. By using the general pressure distribution and the Yovanovich [8] correlation for thermal conductance of conforming rough contacts, simple correlations for determining TCR are derived which cover the entire range of TCR from conforming rough to smooth spherical contacts. The input parameters to utilize the proposed correlations are: load F, the effective elasticity modulus E', Vickers microhardness correlation coefficients c_1 and c_2, effective surface roughness σ and surface slope m, the effective surface out-of-flatness δ

or radius of curvature ρ, radius of the contacting surfaces b_L, and the harmonic mean of the thermal conductivities k_s.

17. By introducing an approximate model for the micro thermal resistance, it is shown that the micro thermal resistance R_s is independent of the surface curvature and the profile of the contact pressure. Additionally, the micro and the macro thermal resistances are functions of the micro and macro scale contact parameters, respectively. The applied load appears directly in both resistances; the surface roughness influences the macro thermal resistance implicitly through the macrocontact radius.

18. The thermal model is compared with more than 600 experimental data points, collected by many researchers, and showed good agreement over the entire range of TCR. The RMS difference between the model and the data is estimated to be approximately 13.6%. The list of materials in the comparison forms a complete set of the metals used in applications, where TCR is of concern. It is also shown that the model is applicable to dissimilar metals.

19. A criterion for specifying the conforming rough contact is developed. A contact is conforming where the equivalent surface out-of-flatness is approximately 3 to 30 times of the equivalent surface roughness for very rough to very smooth surfaces, respectively.

20. It is shown that the heat source on a half-space assumption for the geometry of microcontacts is justifiable for a wide range of applicable loads. In other words, microcontacts are located far enough from each other that they do not interfere and can be considered as heat sources on a half-space. A novel TCR model was developed for the conforming rough contacts using scale analysis methods instead of using probability relationships. The scale relationship satisfied the observed physical proportionality and showed the trends of the experimental data. The constant of the scale relationship was determined through comparison with experimental data. Based on the model, the effective micro thermal resistance is inversely proportional to the real contact area and directly proportional to the parameter (σ/m).

21. It is shown that the effective micro thermal resistance component of the joint resistance, R_s, is not a function of the surface curvature/out-of-flatness. Additionally, the profile

of the effective contact pressure distribution does not affect the effective micro thermal resistance, R_s. Using the proposed correlation for the radius of the macrocontact and the flux tube correlation, the macro thermal resistance is determined. Superimposing the macro and the micro thermal resistances a general relationship for TCR is derived. This expression covers the entire TCR ranging from the conforming rough to the spherical smooth bare joints in a vacuum.

22. A new non-dimensional parameter is introduced which represents the ratio of the macro over the micro thermal resistances. Based on this non-dimensional parameter a criteria proposed for specifying the three regions of TCR, i.e., the conforming rough limit, the elastoconstriction limit and the transition region.

23. An experimental program is designed and three sets of data for SS 304 are collected. The collected data are compared with the scale analysis model and excellent agreement is observed. In addition, the scale analysis model is compared with 75 data sets, more than 880 TCR data points collected by many researchers during last 40 years, which cover a wide range of surface characteristics, thermal and mechanical properties, mean contact temperature, directional heat transfer, and contact between dissimilar metals. The RMS difference between the model and data is approximately 13.8% over the entire range of the comparison.

7.2 Recommendations

1. Thermal models developed in this study predict TCR of conforming rough joints under moderate and high pressures with a reasonable accuracy. However, as discussed in Chapters 4 and 5, existing analytical TCR models including this work, over-predict joint resistance of conforming rough contacts under light loads, i.e., the "truncation effect". It is recommended that further experimental and analytical work be done on the conforming rough joints under light pressures.

2. The surface out-of-flatness of contacting bodies is considered to be spherical (convex) only in this work. It is recommended to undertake more analytical and experimental study on

the mechanical contact of surfaces that have other out-of-flatness shapes, such as wavy surfaces.

3. A large group of engineering surfaces are cylindrical rough bodies; to the knowledge of author no compact analytical contact mechanics model exists for cylindrical rough contacts. The approach taken in developing of the mechanical model in this study can be employed to develop compact analytical contact model(s) for cylindrical rough joints.

4. The mechanical model developed assumes that the contacting bodies are elastic half-spaces, i.e., Boussinesq solution for a point load on a half-space is employed. This assumptions is not valid for finite contacting bodies, where radius of the macrocontact area approaches the edges of contacting bodies. In this study an approximate model is proposed for this problem, which is called the elastic compression. It is recommended to study this contact problem analytically and verify the accuracy of the proposed approximate model.

5. There are a limited number of experimental TCR data for copper and silicon in the open literature. Since these materials are very important in many thermal contact applications, it is recommended to perform more tests with these materials and compare them with the proposed model.

Bibliography

[1] J. A. Greenwood and B. P. Williamson, "Contact of nominally flat surfaces," *Proc., Roy. Soc., London, A295*, pp. 300–319, 1966.

[2] D. Tabor, *The Hardness of Metals*, Oxford University Press, Amen House, London E.C.4, UK, 1951.

[3] H. S. Carslaw and J. C. Jaeger, *Conduction of Heat in Solids, 2nd. Edition*, Oxford University Press, London, UK, 1959.

[4] A. M. Clausing and B. T. Chao, "Thermal contact resistance in a vacuum environment," *Paper No.64-HT-16, Transactions of ASME: Journal of Heat Transfer*, vol. 87, pp. 243–251, 1965.

[5] K. Nishino, S. Yamashita, and K. Torii, "Thermal contact conductance under low applied load in a vacuum environment," *Experimental Thermal and Fluid Science, Elsevier*, vol. 10, pp. 258–271, 1995.

[6] M. A. Lambert and L. S. Fletcher, "Thermal contact conductance of spherical rough metals," *Journal of Heat Transfer, ASME*, vol. 119, no. 4, pp. 684–690, 1997.

[7] M. G. Cooper, B. B. Mikic, and M. M. Yovanovich, "Thermal contact conductance," *International Journal of Heat and Mass Transfer*, vol. 12, pp. 279–300, 1969.

[8] M. M. Yovanovich, "Thermal contact correlations," *AIAA Paper No. 81-1164, also Progress in Aeronautics and Aerodynamics: Spacecraft Radiative Transfer and Temperature Control,edited by T. E., Horton*, vol. 83, pp. 83–95, 1982.

[9] G. Liu, Q. Wang, and C. Ling, "A survey of current models for simulating contact between rough surfaces," *Tribology Trans.*, vol. 42, no. 3, pp. 581–591, 1999.

[10] ," in *Surface Texture: surface Roughness, Waviness and Lay.* ANSI B46.1, American Society of Mechanical Engineers, 1985.

[11] L. H. Tanner and M. Fahoum, "A study of the surface parameters of ground and lapped metal surfaces, using specular and diffuse reflection of laser light," *Wear*, vol. 36, pp. 299–316, 1976.

[12] V. W. Antonetti, T. D. White, and R. E. Simons, "An approximate thermal contact conductance correlation," *ASME 28th National Heat Transfer Conference, Minneapolis, Minnesota, HTD-Vol. 170*, pp. 35–42, 1991.

[13] F. F. Ling, "On asperity distributions of metalic surfaces," *Journal of Applied Physics*, vol. 29, no. 8, 1958.

[14] B. B. Mikic and W. M. Rohsenow, "Thermal contact conductance," Tech. Rep., Dept. of Mech. Eng. MIT, Cambridge, Massachusetts, NASA Contract No. NGR 22-009-065, September, 1966.

[15] R. V. Francois, "Statistical analysis of asperities on a rough surface," *Wear*, vol. 249, pp. 401–408, 2001.

[16] J. B. Williamson, J. Pullen, and R. T. Hunt, "The shape of solid surfaces," *Surface Mechanics, ASME, New York*, pp. 24–35, 1969.

[17] J. A. Greenwood, "The area of contact between rough surfaces and flats," *Journal of Lubrication Tech., Jan.*, pp. 81–91, 1967.

[18] J. S. Bendat, *Principles and Applications of Random Noise Theory*, Wiley, New York, USA, 1958.

[19] H. A. Francis, "Application of spherical indentation mechanics to reversible and irreversible contact between rough surfaces," *Wear*, vol. 45, pp. 221–269, 1976.

[20] K. L. Johnson, *Contact Mechanics*, Cambridge University Press, Cambridge, UK., 1985.

[21] B. N. J. Persson, *Sliding Friction Physical Principles and Applications*, Springer, Berlin, Germany, 2000.

[22] M. M. Yovanovich, "Thermal constriction resistance of contacts on a half-space: Integral formulation," *AIAA Progress in Astronautics and Aeronautics, Radiative and Thermal Control, Vol. 49, AIAA, NY*, pp. 397–418, 1976.

[23] M. A. Lambert, *Thermal Contact Conductance of Spherical Rough Metals*, Ph.D. thesis, Texas A & M University, Dept. of Mech. Eng., College Station, TX, USA, 1995.

[24] M. A. Mott, *Micro-Indentation Hardness Testing*, Butterworths Scientific Publications, London, UK, 1956.

[25] A. A. Hegazy, *Thermal Joint Conductance of Conforming Rough Surfaces: Effect of Surface Micro-Hardness Variation*, Ph.D. thesis, University of Waterloo, Dept. of Mech. Eng., Waterloo, Canada, 1985.

[26] S. Song and M. M. Yovanovich, "Relative contact pressure: Dependence on surface roughness and vickers microhardness," *AIAA Journal of Thermophysics and Heat Transfer*, vol. 2, no. 1, pp. 43–47, 1988.

[27] M. R. Sridhar and M.M. Yovanovich, "Empirical methods to predict vickers microhardness," *Wear*, vol. 193, pp. 91–98, 1996.

[28] F. H. Milanez, J. R. Culham, and M. M. Yovanovich, "Comparisons between plastic contact hradness models and experiments," *AIAA Paper No. 2003-0160, 41th AIAA Aerospace Meeting and Exhibit, Jan. 6-9, Reno, Nevada.*, 2003.

[29] H. Hertz, "On the contact of elastic bodies," *Journal fur die reine und angewandie Mathematic, (in German)*, vol. 92, pp. 156–171, 1881.

[30] C. Hardy, C. N. Baronet, and G. V. Tordion, "Elastoplastic indentation of a half-space by a rigid sphere," *Journal of Numerical Methods in Engineering*, vol. 3, pp. 451–459, 1971.

[31] E. J. Abott and F. A. Firestone, "Specifying surface quality," *Mechanical Engineering (ASME)*, vol. 55, pp. 569–578, 1933.

[32] F. P. Bowden and D. Tabor, *Friction and Lubrication of Solids*, Oxford University Press, London, UK, 1951.

[33] R. Holm, *Electrical Contacts 3rd Ed.*, Springer Verlag, Berlin, 1958.

[34] J. Pullen and B. P. Williamson, "On the plastic contact of rough surfaces," *Proc., Roy. Soc., London, A327*, pp. 159–173, 1972.

[35] T. Tsukizoe and T. Hisakado, "On the mechanism of contact between metal surfaces-the penterating depth and the average clearance," *Journal of Basic Engineering*, vol. 87, no. 3, pp. 666–674, 1965.

[36] T. Tsukizoe and T. Hisakado, "On the mechanism of contact between metal surfaces: Part2-the real area and number of contact points," *Journal of Lubrication Tech.*, vol. 40, no. 1, pp. 81–88, 1968.

[37] J. F. Archard, "Contact and rubbing of flat surface," *Journal of Applied Physics*, vol. 24, pp. 981–988, 1953.

[38] J. A. Greenwood and J. H. Tripp, "The elastic contact of rough spheres," *Transactions of the ASME: Journal of Applied Mechanics*, vol. 89, no. 1, pp. 153–159, 1967.

[39] D. J. Whitehouse and J. F. Archard, "The properties of random surfaces of significance in their contact," *Proc., Roy. Soc., London, A316*, pp. 97–121, 1970.

[40] A. W. Bush, R. D. Gibson, and G. P. Keogh, "Strongly anisotropic rough surfaces," *ASME Journal of Lubrication Tech.*, vol. 101, no. 1, pp. 15–20, 1979.

[41] R. A. Onions and J. F. Archard, "The contact of surfaces having a random structure," *Journal of Physics D.*, vol. 6, pp. 289–304, 1973.

[42] A. W. Bush, R. D. Gibson, and T. R. Thomas, "The elastic contact of a rough surface," *Wear*, vol. 35, no. 1, pp. 87–111, 1975.

[43] M. O'Callaaghan and M. A. Cameron, "Static contact under load between nominal flat surface in which deformation is purely elastic," *Wear*, vol. 36, pp. 79–97, 1976.

[44] J. I. McCool, "Comparison of rough surfaces," *Wear*, vol. 107, pp. 37–60, 1986.

[45] W. R. Chang, I. Etison, and D. B. Bogy, "An elastic-plastic model for the contact of rough surfaces," *Journal of Tribology*, vol. 109, pp. 257–253, 1987.

[46] Y. Zhao, D. M. Maietta, and L. Chang, "An asperity model incorporating the transition from elastic deformation to fully plastic flow," *Journal of Tribology, Trans. of ASME*, vol. 122, pp. 86–93, 2000.

[47] J. A. Greenwood and J. J. Wu, "Surface roughness and contact: An apology," *Meccanica, Kluwer Academic Publishers*, vol. 36, pp. 617–630, 2001.

[48] B. B. Mikic, "Thermal contact conductance; theoritical considerations," *International Journal of Heat and Mass Transfer*, vol. 17, pp. 205–214, 1974.

[49] T. Tsukada and Y. Anno, "On the approach between a sphere and a rough surface (1st. report- analysis of contact radius and interface pressure," *Journal of the Japanese Society of Precision Engineering (in Japanese)*, vol. 45, no. 4, pp. 473–479, 1979.

[50] K. Sasajima and T. Tsukada, "On the approach between a sphere and a rough surface (2nd. report- critical condition to yield plastic deformation in contacting bodies," *Journal of the Japanese Society of Precision Engineering (in Japanese)*, vol. 47, no. 6, pp. 694–699, 1981.

[51] S. S. Burde, *Thermal Contact Resistance Between Smooth Spheres and Rough Flats*, Ph.D. thesis, University of Waterloo, Dept. of Mech. Eng., Waterloo, Canada, 1977.

[52] M. M. Yovanovich, S. S. Burde, and C. C. Thompson, "Thermal constriction resistance of arbitrary planar contacts with constant flux," *AIAA, Paper No. 76-440*, vol. 56, pp. 126–139, 1976.

[53] L. C. Roess, "Theory of spreading conductance," *Beacon Laboratories of Texas, Beacon, NY, Appendix A (Unpublished paper)*, 1950.

[54] M. M. Yovanovich, "Overall constriction resistance between contacting rough, wavy surfaces," *International Journal of Heat and Mass Transfer*, vol. 12, pp. 1517–1520, 1969.

[55] R. D. Gibson, "The contact resistance of a semi-infinite cylinder in a vacuum," *Applied Energy*, vol. 2, pp. 57–65, 1976.

[56] K. J. Negus and M. M. Yovanovich, "Application of the method of optimized images to the steady three dimensional conduction problems," *ASME, 84-WA/HT-110*, 1984.

[57] C. V. Madhusudana and L. S. Fletcher, "Thermal contact conductance: A review of recent literature," Tech. Rep., Texas A & M University, College Station, TX, USA, September, 1981.

[58] M. R. Sridhar and M.M. Yovanovich, "Critical review of elastic and plastic thermal conductance models and comparison with experiment," *Paper No. 93-2776, 28th. AIAA Thermophysics Conference, Orlando, Florida, July 6-9*, 1993.

[59] A. M. Clausing and B. T. Chao, "Thermal contact resistance in a vacuum environment," Tech. Rep., University of Illinois, Urbana, Illinois, Report ME-TN-242-1, August, 1963.

[60] W. Kitscha, "Thermal resistance of the sphere-flat contact," M.S. thesis, University of Waterloo, Dept. of Mech. Eng., Waterloo, Canada, 1982.

[61] N. F. Fisher, "Thermal constriction resistance of sphere/layered flat contacts: Theory and experiment," M.S. thesis, University of Waterloo, Dept. of Mech. Eng., Waterloo, Canada, 1987.

[62] B. B. Mikic, "Thermal constriction resistance due to non-uniform surface conditions: Contact resistance at non-uniform interface pressure," *International Journal of Heat and Mass Transfer*, vol. 13, pp. 1497–1500, 1970.

[63] M. M. Yovanovich, "Recent developments in thermal contact, gap and joint conductance theories and experiment," *ASME, Keynote Paper Delivered at Eighth International Heat Transfer Conference, San Francisco, CA, August 17- 22*, pp. 35–45, 1986.

[64] V. W. Antonetti, *On the Use of Metallic Coatings to Enhance Thermal Conductance*, Ph.D. thesis, University of Waterloo, Dept. of Mech. Eng., Waterloo, Canada, 1983.

[65] Fernando H. Milanez, M. M. Yovanovich, and M. B. H. Mantelli, "Thermal contact conductance at low contact pressures," *Journal of Thermophysics and Heat Transfer*, vol. 18, pp. 37–44, 2003.

[66] G. M. L. Gladwell, *Contact Problems in the Classical Theory of Elasticity*, Alphen aan den Rijn: Sijthoff and Noordhoff, The Netherlands, Germantown, Maryland, USA, 1980.

[67] B. B. Mikic and R. T. Roca, "A solution to the contact of two rough spherical surfaces," *Journal of Applied Mechanics, ASME*, vol. 96, pp. 801–803, 1974.

[68] J. A. Greenwood, K. L. Johnson, and M. Matsubara, "A surface roughness parameter in hertz contact," *Wear*, vol. 100, pp. 47–57, 1984.

[69] V. L. Streeter and E. B. Wylie, *Fluid Mechanics*, McGraw-Hill Book Company, New York, 1975.

[70] J. Kagami, K. Yamada, and T. Hatazawa, "Contact between a sphere and rough plates," *Wear*, vol. 87, no. 1, pp. 93–105, May 1982.

[71] R. McMillan and B. B. Mikic, "Thermal contact resistance with non-uniform interface pressures," Tech. Rep., Dept. of Mech. Eng. MIT, Cambridge, Massachusetts, NASA Contract No. NGR 22-009-(477), November, 1970.

[72] M. M. Yovanovch and E. E. Marotta, *Thermal Spreading and Contact Resistances*, chapter 4, Heat Transfer Handbook, Editors: A. Bejan and D. Kraus, John Wiley and Sons Inc., Hoboken, New York, USA, 2003.

[73] M. M. Yovanovich and A. Hegazy, "An accurate universal contact conductance correlation for conforming rough surfaces with different micro-hardness profiles," *AIAA, Paper No. 83-1434*, 1983.

[74] T. H. McWaid, *Thermal Contact Resistance Across Pressed Metal Contact in a Vacuum Environment*, Ph.D. thesis, University of California Santa Barbara, Dept. of Mech. Eng., California, USA, 1990.

[75] K. M. Nho, *Experimental Investigation of Heat Flow Rate and Directional Effect on Contact Conductance of Anistropic Ground/Lapped Interfaces*, Ph.D. thesis, University of Waterloo, Dept. of Mech. Eng., Waterloo, Canada, 1990.

[76] M. F. Bloom, "Thermal contact conductance in a vacuum environment," *Douglas Aircraft Company Report SM-47700, December*, 1964.

[77] J. F. Cassidy and H. Mark, "Thermal contact resistance measurements at ambient pressure of one atmosphere to 3x10 e-12 mm hg and comparison with theoretical predictions," *Progress in Aeronautics-Themophysics: Applications to Thermal Design Aircraft, Edited by, J. T. Bevans*, vol. 23, pp. 23–37, 1970.

[78] L. S. Fletcher and D. A. Gyorog, "Heat transfer between surfaces in contact; an analytical and experimental study of thermal contact resistance of metallic interfaces," *AIAA, Paper No. 70-852*, 1970.

[79] D. A. Gyorog, "Investigation of thermal isolation materials for contacting surfaces," *AIAA 8th. Aerospace Science Meeting, Jan. 19-21, New York*, 1970.

[80] P. A. Smuda and D. A. Gyorog, "Thermal isolation with low-conductance interstitial materials under compressive loads," *AIAA, Paper No. 69-25, AIAA 7th Aerospace Science Meeting, New York, Jan. 20-22*, 1969.

[81] M. B. H. Mantelli, *Overall Thermal Resistance of Bolted Joints: Models with Experimental Verification*, Ph.D. thesis, University of Waterloo, Dept. of Mech. Eng., Waterloo, Canada, 1995.

[82] J. G. Hust and A. B. Lankford, *Report of Investigation Research Material 8420 and 8421 Electrolytic Iron, Certificate 8421*, Department of Commerece, National Bureau of Standards, Maryland, USA, May 1984.

[83] J. P. Holman and W. J. Gajda, *Experimental Methods for Engineers*, McGraw-Hill Book Company, New York, USA, 1994.

Appendix A

TCR Data

This appendix contains the comparison between the present model, i.e., Eq. 5.25 and experimental data collected by other researchers. Table A.1 lists the researchers name and the materials used in the experiments. The data are divided into two groups, non-conforming and conforming contacts.

Geometrical, mechanical, and thermal properties of the data sets are summarized in Tables A.2 and A.39. These Tables in conjunction with Table A.1 provide the following information:

1. test number, the number assigned to the experimental results for a particular specimen pair
2. investigator(s) and publication reference
3. equivalent RMS surface roughness σ, mean absolute asperity slope m, and the effective radius of curvature ρ
4. specimen designation, material type or alloy number, and specimen radius b_L
5. mechanical and thermophysical properties, effective elasticity modulus E', harmonic mean of thermal conductivities k_s, microhardness coefficients c_1 and c_2
6. mean joint (contact) temperature, $\overline{T_c}$

Table A.1: Researchers and Specimen materials used in comparisons

Ref.	Researcher	Material(s)
A	Antonetti [64]	Ni 200 Ni 200-Ag
Blo	Bloom [76]	SS 17-4 PH
B	Burde [51]	SPS 245, CS
CC	Clausing and Chao [59]	Al 2024 T4 Brass Anaconda Mg AZ 31B SS303
CM	Cassidy and Mark [77]	SS 416
F	Fisher [61]	Ni 200-Carbon Steel
FG	Fletcher and Gyorog [78]	Brass 360 Mg Az 31B SS 304
G	Gyorog [79]	SS 304
H	Hegazy [25]	Ni 200 SS 304 Zircaloy 4 Zr-2.5%wt Nb
K	Kitscha [60]	Steel 1020-CS
MM	McMillan and Mikic [71]	SS 303
MR	Mikic and Rohsenow [14]	SS 305
M	Milanez et al. [65]	SS 304
MW	McWaid [74]	SS 304
N	Nho [75]	Al 6061 T6 Ni 200 SS 304 Ni $\leftrightarrows$ Al
SG	Smuda and Gyorog [80]	SS 304

A.1 Non-Conforming Contacts

Tables A.3 through A.38 provide the following information for TCR data points for the data sets listed in Table A.2:

1. applied force, F
2. measured thermal contact resistance, R_{exp}
3. the non-dimensional roughness parameter, $\alpha = \sigma\rho/a_H^2$
4. the non-dimensional geometric parameter, $\tau = \rho/a_H$
5. ratio of macrocontact radius over the radius of specimen, $B = a_L/b_L$
6. micro thermal resistance predicted by the model, R_s

$$R_s = \frac{0.565\,(\sigma/m)\,H^*}{k_s F}$$

   where $H^* \equiv c_1\,(\sigma/m\sigma_0)^{c_2}$.

7. macro thermal resistance predicted by the model, R_L

$$R_L = \frac{(1 - a_L/b_L)^{1.5}}{2k_s a_L}$$

   where,

$$a_L = 1.80\ a_H\ \frac{\sqrt{\alpha + 0.31\tau^{0.056}}}{\tau^{0.028}}$$

   where, $a_H = (0.75F\rho/E')^{1/3}$.

8. relative difference between the model and data.

Table A.2: Data information, non-conforming rough contacts

Reference, test # and material	E'	σ / m	ρ	c_1 / c_2	k_s	b_L	$\overline{T_c}$
	GPa	μm	m	GPa	W/mK	mm	$°C$
Blo,SS17,4PH,513	107.69	2.71/.15	31.63	4.33/0	15.2	25.4	-60
Bur,A1,SPS245,CS	113.74	0.63/.04	0.0143	3.93/0	40.7	7.15	70
Bur,A2,SPS245-CS	113.74	1.31/.07	0.0143	3.92/0	40.7	7.15	70
Bur,A3,SPS245-CS	113.74	2.44/.22	0.0143	3.92/0	40.7	7.15	70
Bur,A4,SPS245-CS	113.74	2.56/.08	0.0191	4.44/0	40.7	7.15	70
Bur,A5,SPS245-CS	113.74	2.59/.10	0.0254	4.44/0	40.7	7.15	70
Bur,A6,SPS245-CS	113.74	2.58/.10	0.0381	4.44/0	40.7	7.15	70
CC,1A,Al2024T4	37.86	0.43/.06	13.80	1.72/-.04	136.8	12.7	104
CC,8A,Al2024T4	38.66	2.26/.14	14.66	1.73/-.04	141.4	12.7	110
CC,1B,Brass	49.62	0.47/.06	3.87	3.02/-.17	125.0	12.7	171
CC,2B,Brass	49.62	0.50/.06	4.07	3.02/-.17	125.0	12.7	129
CC,3B,Brass	51.92	0.50/.06	3.34	3.02/-.17	101.5	12.7	71
CC,4B,Brass	49.62	0.50/.06	4.07	3.02/-.17	125.0	12.7	127
CC,2M,MgAz31B	25.64	0.11/.03	30.32	0.41/0	96.0	12.7	100
CC,3M,MgAz31B	25.64	0.11-.03	12.41	0.41/0	96.0	12.7	100
CC,3S,SS303	113.74	0.11/.03	21.17	4.59/-.13	17.8	12.7	118
CM,SS416	106.04	1.26/	13.44	2.62/0	24.9	12.7	
F,11A,Ni200-CS	112.62	0.12/.04	0.0191	4.00/0	57.9	12.5	40
F,11B,Ni200-CS	112.62	0.12/.04	0.0381	4.00/0	57.9	12.5	40
F,13A,Ni200-CS	112.62	0.06/.03	0.0381	4.00/0	58.1	12.5	40
FG,P12,Brass360,T52	54.13	0.07/.02	28.91	1.08/0	107.0	12.7	52
FG,P34,Brass360,T94	53.56	2.21/.14	2.56	1.13/0	112.0	12.7	94
FG,P34,Brass360,T-10	55.84	2.21/.14	2.56	1.13/0	98.0	12.7	-10
FG,P51,MgAz31B,T90	23.36	0.16/.03	0.8077	0.47/0	88.0	12.7	90
FG,P51,MgAz31B,T-23	26.21	0.16/.03	0.8077	0.62/0	70.0	12.7	-23
FG,P34,SS304,T89	106.04	1.17/.10	9.62	2.06/0	15.9	12.7	89
FG,P34,SS304,T-33	106.04	1.17/.10	9.62	2.85/0	13.5	12.7	-33
FG,P67,SS304,T73	106.04	0.11/.03	0.4019	2.85/0	15.6	12.7	73
FG,P67,SS304,T160	106.04	0.11/.03	0.4019	2.85/0	16.6	12.7	160
G,SS304	106.04	0.79/.08	72.00	4.00/0	16.2	12.7	155
K,T1,Steel1020-CS	113.74	0.76/.08	0.0130	4.00/0	48.0	12.7	
K,T2,Steel1020-CS	113.74	0.13/.03	0.0130	4.00/0	51.4	12.7	
MM,P1,SS303	113.74	2.70/.07	0.1180	4.00/0	17.3	12.7	
MM,P2,SS303	113.74	1.75/.07	2.44	4.00/0	22.0	12.7	
MR,T2,SS305	107.14	3.87/.21	39.69	4.2/0	19.9	12.7	
SG,SS304	106.04	0.14/.03	70.74	4.00/0	16.2	12.7	143

Table A.3: Comparison between model and data, Bloom SS17 4PH513

F	$R_{\exp}$	α	τ	B	R_s	R_L	R_j	Θ	$\frac{R_j - R_{\exp}}{R_j}\%$
N	K/W	$(-)$	$(-)$	$(-)$	K/W	K/W	K/W	$(-)$	$(-)$
9167.35	0.49	0.54	2502.2	0.726	0.32	0.26	0.57	0.81	14.53
12590.67	0.43	0.44	2251.0	0.766	0.23	0.19	0.42	0.83	-1.82
13079.13	0.42	0.42	2222.7	0.772	0.22	0.18	0.40	0.83	-4.91
1775.50	1.74	1.61	4324.7	0.594	1.63	0.56	2.19	0.35	20.70
978.96	2.86	2.39	5274.1	0.568	2.95	0.65	3.60	0.22	20.62
488.47	5.76	3.80	6649.5	0.547	5.92	0.72	6.64	0.12	13.30
3648.29	1.28	0.99	3401.8	0.639	0.79	0.44	1.23	0.55	-3.76
6135.21	0.80	0.70	2860.6	0.683	0.47	0.34	0.81	0.72	1.50
8804.55	0.58	0.55	2536.1	0.721	0.33	0.26	0.59	0.80	1.54
12142.74	0.47	0.45	2278.4	0.762	0.24	0.20	0.44	0.83	-8.27
13121.70	0.45	0.42	2220.3	0.772	0.22	0.18	0.40	0.83	-11.80

Table A.4: Comparison between model and data, Burde Assembly1

F	$R_{\exp}$	α	τ	B	R_s	R_L	R_j	Θ	$\frac{R_j - R_{\exp}}{R_j}\%$
N	K/W	$(-)$	$(-)$	$(-)$	K/W	K/W	K/W	$(-)$	$(-)$
26.1	81.61	0.49	105.9	0.028	36.20	58.40	94.60	1.61	13.73
42.8	69.37	0.35	89.8	0.031	22.07	53.53	75.61	2.43	8.25
75.1	60.14	0.24	74.5	0.034	12.58	47.69	60.27	3.79	0.21
146.3	48.44	0.16	59.6	0.040	6.46	40.67	47.12	6.30	-2.79
360	37.00	0.09	44.2	0.050	2.62	31.70	34.32	12.08	-7.81
690.4	30.57	0.06	35.5	0.060	1.37	25.93	27.30	18.95	-11.99

Table A.5: Comparison between model and data, Burde Assembly2

F	$R_{\exp}$	α	τ	B	R_s	R_L	R_j	Θ	$\frac{R_j - R_{\exp}}{R_j}\%$
N	K/W	$(-)$	$(-)$	$(-)$	K/W	K/W	K/W	$(-)$	$(-)$
26.1	72.81	1.02	105.9	0.036	37.27	45.68	82.95	1.23	12.22
42.8	64.68	0.74	89.8	0.038	22.73	43.08	65.81	1.90	1.72
75.1	53.93	0.51	74.5	0.041	12.95	39.70	52.66	3.06	-2.42
146.3	46.63	0.32	59.6	0.046	6.65	35.21	41.86	5.30	-11.40
360	35.20	0.18	44.2	0.055	2.70	28.74	31.44	10.64	-11.94
690.4	29.54	0.12	35.5	0.064	1.41	24.14	25.55	17.13	-15.61

Table A.6: Comparison between model and data, Burde Assembly3

F	$R_{\exp}$	α	τ	B	R_s	R_L	R_j	Θ	$\frac{R_j - R_{\exp}}{R_j}\%$
N	K/W	$(-)$	$(-)$	$(-)$	K/W	K/W	K/W	$(-)$	$(-)$
26.1	64.36	1.92	105.9	0.045	23.48	35.27	58.75	1.50	-9.54
42.8	58.55	1.38	89.8	0.047	14.32	33.92	48.24	2.37	-21.37
75.1	50.84	0.95	74.5	0.050	8.16	32.07	40.23	3.93	-26.38
146.3	42.70	0.61	59.6	0.054	4.19	29.41	33.60	7.02	-27.09
360	34.05	0.33	44.2	0.062	1.70	25.15	26.85	14.77	-26.81

Table A.7: Comparison between model and data, Burde Assembly4

F	$R_{\exp}$	α	τ	B	R_s	R_L	R_j	Θ	$\frac{R_j - R_{\exp}}{R_j}\%$
N	K/W	$(-)$	$(-)$	$(-)$	K/W	K/W	K/W	$(-)$	$(-)$
26.1	77.72	2.21	128.5	0.053	75.63	29.94	105.57	0.40	26.38
146.3	41.04	0.70	72.3	0.062	13.49	25.30	38.79	1.87	-5.81
690.4	24.02	0.25	43.1	0.080	2.86	19.01	21.87	6.65	-9.86

Table A.8: Comparison between model and data, Burde Assembly5

F	$R_{\exp}$	α	τ	B	R_s	R_L	R_j	Θ	$\frac{R_j - R_{\exp}}{R_j}\%$
N	K/W	$(-)$	$(-)$	$(-)$	K/W	K/W	K/W	$(-)$	$(-)$
26.1	75.44	2.46	155.3	0.061	58.77	25.84	84.61	0.44	10.83
146.3	37.31	0.78	87.4	0.070	10.48	22.01	32.50	2.10	-14.82
690.4	22.27	0.28	52.1	0.089	2.22	16.69	18.91	7.51	-17.77

Table A.9: Comparison between model and data, Burde Assembly6

F	$R_{\exp}$	α	τ	B	R_s	R_L	R_j	Θ	$\frac{R_j - R_{\exp}}{R_j}\%$
N	K/W	$(-)$	$(-)$	$(-)$	K/W	K/W	K/W	$(-)$	$(-)$
26.1	73.56	2.81	203.6	0.073	60.93	21.04	81.97	0.35	10.26
146.3	35.68	0.89	114.6	0.083	10.87	18.09	28.96	1.66	-23.21
690.4	19.70	0.32	68.3	0.105	2.30	13.85	16.16	6.01	-21.93

Table A.10: Comparison between model and data, Clausing and Chao 1A

F	$R_{\exp}$	α	τ	B	R_s	R_L	R_j	Θ	$\frac{R_j - R_{\exp}}{R_j}\%$
N	K/W	$(-)$	$(-)$	$(-)$	K/W	K/W	K/W	$(-)$	$(-)$
301.1505	0.53	0.31	3172.2	0.440	0.16	0.27	0.44	1.69	-20.87
548.4991	0.34	0.21	2597.6	0.503	0.09	0.20	0.29	2.26	-16.43
1083.024	0.17	0.13	2070.5	0.595	0.05	0.12	0.17	2.76	1.40
1809.698	0.08	0.10	1744.8	0.684	0.03	0.07	0.10	2.77	16.37
2651.661	0.07	0.07	1536.2	0.763	0.02	0.04	0.06	2.37	-5.52
3444.714	0.04	0.06	1407.9	0.823	0.01	0.03	0.04	1.84	-8.82

Table A.11: Comparison between model and data, Clausing and Chao 8A

F	$R_{\exp}$	α	τ	B	R_s	R_L	R_j	Θ	$\frac{R_j - R_{\exp}}{R_j}\%$
N	K/W	$(-)$	$(-)$	$(-)$	K/W	K/W	K/W	$(-)$	$(-)$
305.8486	0.30	1.69	3309.1	0.738	0.33	0.05	0.38	0.15	20.77
986.5595	0.13	0.77	2239.6	0.836	0.10	0.02	0.13	0.21	-7.04
1892.552	0.06	0.50	1802.5	0.922	0.05	0.01	0.06	0.12	8.53

Table A.12: Comparison between model and data, Clausing and Chao 1B

F	$R_{\exp}$	α	τ	B	R_s	R_L	R_j	Θ	$\frac{R_j - R_{\exp}}{R_j}\%$
N	K/W	$(-)$	$(-)$	$(-)$	K/W	K/W	K/W	$(-)$	$(-)$
102.01	1.42	0.55	2134.4	0.210	0.73	1.05	1.78	1.45	20.24
155.82	1.34	0.42	1853.3	0.226	0.48	0.95	1.42	2.00	5.83
303.95	1.00	0.27	1483.3	0.258	0.24	0.78	1.02	3.20	1.89
548.5	0.75	0.18	1218.3	0.296	0.14	0.63	0.77	4.66	2.35
1086.52	0.53	0.11	970.1	0.352	0.07	0.47	0.53	6.84	0.33
1813.19	0.38	0.08	817.9	0.406	0.04	0.36	0.40	8.70	4.56
2655.15	0.31	0.06	720.2	0.453	0.03	0.28	0.31	10.08	0.22
3332.92	0.26	0.05	667.6	0.484	0.02	0.24	0.26	10.82	0.38

Table A.13: Comparison between model and data, Clausing and Chao 2B

F	$R_{\exp}$	α	τ	B	R_s	R_L	R_j	Θ	$\frac{R_j - R_{\exp}}{R_j}\%$
N	K/W	$(-)$	$(-)$	$(-)$	K/W	K/W	K/W	$(-)$	$(-)$
38.8	2.76	1.15	3045.4	0.193	1.97	1.18	3.15	0.60	12.58
102.01	1.58	0.60	2206.6	0.219	0.75	0.99	1.74	1.32	9.45
155.82	1.35	0.45	1916.0	0.235	0.49	0.90	1.39	1.83	2.77
303.95	1.04	0.29	1533.4	0.267	0.25	0.74	0.99	2.94	-4.71
548.5	0.80	0.20	1259.5	0.304	0.14	0.60	0.74	4.30	-8.65
1086.52	0.59	0.12	1002.9	0.361	0.07	0.45	0.52	6.32	-14.21
1813.19	0.42	0.09	845.5	0.415	0.04	0.34	0.38	8.03	-9.80
2655.15	0.33	0.07	744.6	0.463	0.03	0.27	0.30	9.28	-12.18
3332.92	0.28	0.06	690.2	0.495	0.02	0.23	0.25	9.94	-9.73

Table A.14: Comparison between model and data, Clausing and Chao 3B

F	$R_{\exp}$	α	τ	B	R_s	R_L	R_j	Θ	$\frac{R_j - R_{\exp}}{R_j}\%$
N	K/W	$(-)$	$(-)$	$(-)$	K/W	K/W	K/W	$(-)$	$(-)$
38.8	3.72	1.11	2710.1	0.176	2.43	1.64	4.07	0.68	8.78
102.01	2.35	0.58	1963.5	0.200	0.92	1.39	2.31	1.50	-1.62
155.82	2.00	0.44	1705.0	0.215	0.61	1.26	1.86	2.08	-7.27
303.95	1.46	0.28	1364.5	0.245	0.31	1.04	1.35	3.36	-8.03
548.5	1.10	0.19	1120.8	0.279	0.17	0.85	1.02	4.94	-7.69
1086.52	0.82	0.12	892.4	0.332	0.09	0.64	0.72	7.34	-13.67
1813.19	0.60	0.09	752.4	0.382	0.05	0.49	0.55	9.48	-10.10
2655.15	0.49	0.07	662.6	0.426	0.04	0.40	0.43	11.13	-14.20
3332.92	0.41	0.06	614.2	0.456	0.03	0.34	0.37	12.08	-10.60

Table A.15: Comparison between model and data, Clausing and Chao 4B

F	$R_{\exp}$	α	τ	B	R_s	R_L	R_j	Θ	$\frac{R_j - R_{\exp}}{R_j}\%$
N	K/W	$(-)$	$(-)$	$(-)$	K/W	K/W	K/W	$(-)$	$(-)$
102.01	1.37	0.60	2206.6	0.219	0.75	0.99	1.74	1.32	21.26
155.82	1.20	0.45	1916.0	0.235	0.49	0.90	1.39	1.83	13.54
303.95	0.94	0.29	1533.4	0.267	0.25	0.74	0.99	2.94	5.47
548.50	0.74	0.20	1259.5	0.304	0.14	0.60	0.74	4.30	0.55
1086.52	0.54	0.12	1002.9	0.361	0.07	0.45	0.52	6.32	-4.15
1813.19	0.39	0.09	845.5	0.415	0.04	0.34	0.38	8.03	-3.44
2655.15	0.29	0.07	744.6	0.463	0.03	0.27	0.30	9.28	0.82
3332.92	0.25	0.06	690.2	0.495	0.02	0.23	0.25	9.94	0.53

Table A.16: Comparison between model and data, Clausing and Chao 2M

F	$R_{\exp}$	α	τ	B	R_s	R_L	R_j	Θ	$\frac{R_j - R_{\exp}}{R_j}\%$
N	K/W	$(-)$	$(-)$	$(-)$	K/W	K/W	K/W	$(-)$	$(-)$
35.62154	1.23	0.32	9590.7	0.318	0.26	0.73	0.98	2.83	-24.69
99.31467	0.51	0.16	6814.2	0.403	0.09	0.47	0.56	5.08	9.80
234.0989	0.24	0.09	5120.2	0.508	0.04	0.28	0.32	7.11	24.45
548.7642	0.10	0.05	3854.4	0.653	0.02	0.13	0.15	7.71	28.09
1086.381	0.04	0.03	3069.7	0.805	0.01	0.04	0.05	5.19	26.76

Table A.17: Comparison between model and data, Clausing and Chao 3M

F	R_{exp}	α	τ	B	R_s	R_L	R_j	Θ	$\frac{R_j - R_{\text{exp}}}{R_j}\%$
N	K/W	$(-)$	$(-)$	$(-)$	K/W	K/W	K/W	$(-)$	$(-)$
234.0989	0.68	0.07	2822.3	0.371	0.04	0.55	0.59	14.13	-14.93
548.7642	0.28	0.04	2124.6	0.479	0.02	0.32	0.34	19.28	17.83
1082.834	0.15	0.02	1693.9	0.593	0.01	0.18	0.19	21.25	20.36
1809.452	0.09	0.02	1427.4	0.699	0.01	0.10	0.10	19.19	13.63
2651.6	0.04	0.01	1256.7	0.790	0.00	0.05	0.05	14.42	19.34

Table A.18: Comparison between model and data, Clausing and Chao 3S

F	R_{exp}	α	τ	B	R_s	R_L	R_j	Θ	$\frac{R_j - R_{\text{exp}}}{R_j}\%$
N	K/W	$(-)$	$(-)$	$(-)$	K/W	K/W	K/W	$(-)$	$(-)$
102.0138	9.05	0.39	8733.1	0.253	4.62	5.63	10.25	1.22	11.75
236.5184	4.87	0.22	6598.3	0.304	1.99	4.23	6.23	2.12	21.87
548.4991	2.90	0.13	4985.0	0.375	0.86	2.91	3.77	3.39	23.22
1086.517	2.07	0.08	3969.3	0.454	0.43	1.97	2.40	4.53	13.87
1813.191	1.42	0.06	3346.4	0.528	0.26	1.36	1.62	5.24	12.19
2655.155	1.08	0.04	2946.9	0.592	0.18	0.97	1.15	5.48	5.91
3448.208	0.88	0.04	2701.0	0.642	0.14	0.74	0.88	5.40	-0.23

Table A.19: Comparison between model and data, Cassidy and Mark SS303

F	$R_{\exp}$	α	τ	B	R_s	R_L	R_j	Θ	$\frac{R_j - R_{\exp}}{R_j}\%$
N	K/W	$(-)$	$(-)$	$(-)$	K/W	K/W	K/W	$(-)$	$(-)$
1194.82	1.33	0.72	2775.4	0.603	0.62	0.65	1.27	1.06	-4.13
1306.80	0.99	0.68	2693.7	0.611	0.57	0.63	1.19	1.11	16.79
1428.92	1.16	0.64	2614.7	0.619	0.52	0.60	1.12	1.16	-3.95
1428.92	1.14	0.64	2614.7	0.619	0.52	0.60	1.12	1.16	-1.62
1635.15	1.11	0.59	2499.8	0.632	0.45	0.56	1.01	1.24	-9.83
1708.62	1.02	0.57	2463.5	0.636	0.43	0.55	0.98	1.26	-3.90
1827.19	0.80	0.54	2409.0	0.643	0.40	0.52	0.93	1.29	14.38
2138.31	0.71	0.49	2286.0	0.660	0.35	0.47	0.82	1.37	13.41
2232.55	0.70	0.48	2253.3	0.665	0.33	0.46	0.79	1.39	12.29
2232.55	0.73	0.48	2253.3	0.665	0.33	0.46	0.79	1.39	8.25
2284.74	0.76	0.47	2236.0	0.668	0.32	0.45	0.78	1.40	2.21
2498.07	0.65	0.44	2170.5	0.678	0.30	0.43	0.72	1.44	10.02
2498.07	0.56	0.44	2170.5	0.678	0.30	0.43	0.72	1.44	22.98
2613.09	0.66	0.43	2138.2	0.684	0.28	0.41	0.69	1.45	4.36
2672.38	0.71	0.42	2122.2	0.686	0.28	0.40	0.68	1.46	-4.29
2857.83	0.64	0.40	2075.3	0.695	0.26	0.38	0.64	1.48	1.10
3266.74	0.51	0.37	1984.8	0.713	0.23	0.34	0.57	1.51	10.61
3266.74	0.58	0.37	1984.8	0.713	0.23	0.34	0.57	1.51	-2.26
3416.73	0.53	0.36	1955.3	0.719	0.22	0.33	0.54	1.52	2.42
3573.81	0.53	0.35	1926.3	0.725	0.21	0.31	0.52	1.52	-1.94
3573.81	0.54	0.35	1926.3	0.725	0.21	0.31	0.52	1.52	-4.33
4178.31	0.42	0.31	1828.5	0.748	0.18	0.27	0.44	1.51	4.36
4272.56	0.42	0.31	1814.9	0.752	0.17	0.26	0.43	1.51	4.15
4370.35	0.42	0.30	1801.3	0.755	0.17	0.25	0.42	1.50	-0.40
4569.49	0.42	0.29	1774.7	0.762	0.16	0.24	0.40	1.49	-5.50
4670.83	0.42	0.29	1761.8	0.766	0.16	0.23	0.39	1.48	-5.83

Table A.20: Comparison between model and data, Fletcher and Gyorog Brass,Test12 Tave52

F	$R_{\exp}$	α	τ	B	R_s	R_L	R_j	Θ	$\frac{R_j - R_{\exp}}{R_j}\%$
N	K/W	$(-)$	$(-)$	$(-)$	K/W	K/W	K/W	$(-)$	$(-)$
101.34	0.69	0.17	8411.0	0.314	0.18	0.67	0.84	3.80	18.37
335.44	0.35	0.08	5643.8	0.434	0.05	0.36	0.41	6.79	14.22
1047.87	0.13	0.04	3860.8	0.612	0.02	0.15	0.16	8.53	16.78
2756.49	0.03	0.02	2796.8	0.832	0.01	0.03	0.04	4.73	15.25

Table A.21: Comparison between model and data, Fletcher and Gyorog Brass,Test34 Tave-10

F	$R_{\exp}$	α	τ	B	R_s	R_L	R_j	Θ	$\frac{R_j - R_{\exp}}{R_j}\%$
N	K/W	$(-)$	$(-)$	$(-)$	K/W	K/W	K/W	$(-)$	$(-)$
101.34	1.71	2.46	1688.7	0.299	1.05	0.79	1.84	0.75	6.86
335.44	0.87	1.11	1133.1	0.329	0.32	0.67	0.99	2.12	11.77
1047.87	0.56	0.52	775.1	0.382	0.10	0.51	0.61	5.04	8.03
2756.49	0.37	0.27	561.5	0.457	0.04	0.35	0.39	9.12	4.22

Table A.22: Comparison between model and data, Fletcher and Gyorog Brass,Test34 Tave94

F	$R_{\exp}$	α	τ	B	R_s	R_L	R_j	Θ	$\frac{R_j - R_{\exp}}{R_j}\%$
N	K/W	$(-)$	$(-)$	$(-)$	K/W	K/W	K/W	$(-)$	$(-)$
90.70	1.25	2.57	1728.1	0.297	1.02	0.70	1.72	0.68	27.29
356.22	0.69	1.03	1095.3	0.333	0.26	0.58	0.84	2.21	17.08
1065.61	0.47	0.50	760.2	0.386	0.09	0.44	0.53	5.03	11.10
2808.68	0.30	0.26	550.3	0.463	0.03	0.30	0.33	9.03	8.15

Table A.23: Comparison between model and data, Fletcher and Gyorog MgAz31B,Test51 Tave90

F	$R_{\exp}$	α	τ	B	R_s	R_L	R_j	Θ	$\frac{R_j - R_{\exp}}{R_j}\%$
N	K/W	$(-)$	$(-)$	$(-)$	K/W	K/W	K/W	$(-)$	$(-)$
87.15	3.51	0.08	615.5	0.112	0.16	3.34	3.50	20.82	-0.21
352.67	1.91	0.03	386.2	0.171	0.04	1.98	2.02	49.93	5.47
1047.87	1.13	0.01	268.7	0.241	0.01	1.23	1.24	91.79	8.64
2784.36	0.66	0.01	194.0	0.332	0.01	0.74	0.74	146.73	11.53

Table A.24: Comparison between model and data, Fletcher and Gyorog MgAz31B,Test51 Tave-23

F	$R_{\exp}$	α	τ	B	R_s	R_L	R_j	Θ	$\frac{R_j - R_{\exp}}{R_j}\%$
N	K/W	$(-)$	$(-)$	$(-)$	K/W	K/W	K/W	$(-)$	$(-)$
80.57	5.44	0.09	656.5	0.106	0.29	4.49	4.77	15.57	-13.87
349.12	2.57	0.03	402.7	0.164	0.07	2.62	2.69	39.42	4.25
1034.19	1.31	0.02	280.4	0.231	0.02	1.64	1.66	72.96	21.00
2693.66	0.84	0.01	203.8	0.316	0.01	1.01	1.02	116.96	16.99

Table A.25: Comparison between model and data, Fletcher and Gyorog SS304,Test34 Tave-33

F	$R_{\exp}$	α	τ	B	R_s	R_L	R_j	Θ	$\frac{R_j - R_{\exp}}{R_j}\%$
N	K/W	$(-)$	$(-)$	$(-)$	K/W	K/W	K/W	$(-)$	$(-)$
94.33	19.31	3.26	5177.9	0.402	15.23	3.35	18.58	0.22	-3.92
366.83	7.24	1.32	3292.6	0.444	3.92	2.72	6.64	0.70	-9.06
1100.48	3.05	0.63	2283.0	0.507	1.31	1.99	3.29	1.52	7.39
2840.29	1.76	0.34	1664.3	0.598	0.51	1.24	1.75	2.46	-0.91

Table A.26: Comparison between model and data, Fletcher and Gyorog SS304,Test34 Tave89

F	$R_{\exp}$	α	τ	B	R_s	R_L	R_j	Θ	$\frac{R_j - R_{\exp}}{R_j}\%$
N	K/W	$(-)$	$(-)$	$(-)$	K/W	K/W	K/W	$(-)$	$(-)$
104.81	8.82	3.04	4999.2	0.405	8.41	2.81	11.23	0.33	21.47
356.35	4.57	1.35	3324.6	0.443	2.47	2.33	4.80	0.94	4.74
1055.07	2.29	0.65	2315.3	0.504	0.84	1.71	2.55	2.05	10.29
2840.29	1.24	0.34	1664.3	0.598	0.31	1.05	1.37	3.40	9.08

Table A.27: Comparison between model and data, Fletcher and Gyorog SS304,Test67 Tave160

F	$R_{\exp}$	α	τ	B	R_s	R_L	R_j	Θ	$\frac{R_j - R_{\exp}}{R_j}\%$
N	K/W	$(-)$	$(-)$	$(-)$	K/W	K/W	K/W	$(-)$	$(-)$
101.31	48.97	0.10	608.6	0.058	3.63	37.69	41.33	10.37	-18.50
363.33	28.98	0.04	397.6	0.084	1.01	24.91	25.93	24.59	-11.77
1072.53	13.91	0.02	277.2	0.117	0.34	16.80	17.14	48.94	18.86
2759.94	8.90	0.01	202.3	0.159	0.13	11.52	11.65	86.37	23.63

Table A.28: Comparison between model and data, Fletcher and Gyorog SS304,Test67 Tave73

F	$R_{\exp}$	α	τ	B	R_s	R_L	R_j	Θ	$\frac{R_j - R_{\exp}}{R_j}\%$
N	K/W	$(-)$	$(-)$	$(-)$	K/W	K/W	K/W	$(-)$	$(-)$
101.31	46.99	0.10	608.6	0.058	3.87	40.11	43.98	10.37	-6.85
345.87	26.74	0.04	404.2	0.082	1.13	26.97	28.10	23.81	4.83
1072.53	14.48	0.02	277.2	0.117	0.37	17.87	18.24	48.94	20.62
2815.84	9.82	0.01	200.9	0.160	0.14	12.16	12.30	87.39	20.17

Table A.29: Comparison between model and data, Fisher 11A, Ni200-CS

F	$R_{\exp}$	α	τ	B	R_s	R_L	R_j	Θ	$\frac{R_j - R_{\exp}}{R_j}\%$
N	K/W	$(-)$	$(-)$	$(-)$	K/W	K/W	K/W	$(-)$	$(-)$
23.90	53.00	0.11	131.8	0.013	5.45	51.83	57.28	9.51	7.48
40.03	44.50	0.08	111.0	0.015	3.25	44.88	48.14	13.80	7.56
56.78	40.00	0.06	98.8	0.017	2.29	40.52	42.81	17.67	6.57
88.05	32.40	0.05	85.4	0.019	1.48	35.47	36.95	23.98	12.31
120.37	29.00	0.04	76.9	0.021	1.08	32.17	33.25	29.74	12.79
264.72	19.10	0.02	59.1	0.027	0.49	24.95	25.45	50.73	24.94
475.72	14.70	0.01	48.7	0.032	0.27	20.53	20.80	74.99	29.33
687.92	12.40	0.01	43.0	0.036	0.19	18.11	18.30	95.67	32.24

Table A.30: Comparison between model and data, Fisher 11B, Ni200-CS

F	$R_{\exp}$	α	τ	B	R_s	R_L	R_j	Θ	$\frac{R_j - R_{\exp}}{R_j}\%$
N	K/W	$(-)$	$(-)$	$(-)$	K/W	K/W	K/W	$(-)$	$(-)$
40.00	38.00	0.10	176.0	0.019	3.25	34.77	38.03	10.69	0.07
56.80	35.60	0.08	156.6	0.021	2.29	31.46	33.75	13.73	-5.48
88.10	30.10	0.06	135.3	0.024	1.48	27.60	29.08	18.69	-3.51
120.00	25.20	0.05	122.0	0.026	1.08	25.10	26.18	23.15	3.75
192.00	21.70	0.03	104.3	0.031	0.68	21.62	22.30	31.90	2.68
265.00	18.80	0.03	93.7	0.034	0.49	19.47	19.96	39.65	5.80
476.00	13.90	0.02	77.1	0.041	0.27	16.01	16.28	58.56	14.63
688.00	11.40	0.01	68.2	0.046	0.19	14.11	14.30	74.63	20.30

Table A.31: Comparison between model and data, Fisher 13A, Ni200-CS

F	$R_{\exp}$	α	τ	B	R_s	R_L	R_j	Θ	$\frac{R_j - R_{\exp}}{R_j}\%$
N	K/W	$(-)$	$(-)$	$(-)$	K/W	K/W	K/W	$(-)$	$(-)$
23.90	47.20	0.07	208.9	0.016	3.25	42.59	45.85	13.09	-2.95
40.03	41.48	0.05	175.9	0.018	1.94	36.46	38.41	18.77	-8.00
56.78	37.07	0.04	156.6	0.020	1.37	32.70	34.07	23.88	-8.79
88.05	31.68	0.03	135.3	0.023	0.88	28.43	29.31	32.19	-8.09
120.37	28.50	0.02	121.9	0.026	0.65	25.68	26.32	39.74	-8.25
159.20	25.97	0.02	111.0	0.028	0.49	23.41	23.90	47.93	-8.65
192.00	23.38	0.02	104.3	0.030	0.41	21.99	22.40	54.30	-4.39
265.00	20.40	0.01	93.7	0.033	0.29	19.73	20.02	67.23	-1.86
370.00	17.44	0.01	83.8	0.037	0.21	17.61	17.82	83.77	2.10
476.00	15.94	0.01	77.1	0.040	0.16	16.14	16.31	98.80	2.24
580.02	14.09	0.01	72.2	0.043	0.13	15.07	15.20	112.40	7.31
688.00	13.20	0.01	68.2	0.045	0.11	14.20	14.31	125.60	7.76

Table A.32: Comparison between model and data, Gyorog, SS304

F	$R_{\exp}$	α	τ	B	R_s	R_L	R_j	Θ	$\frac{R_j - R_{\exp}}{R_j}\%$
N	K/W	$(-)$	$(-)$	$(-)$	K/W	K/W	K/W	$(-)$	$(-)$
317.71	5.02	1.92	13214.2	0.926	4.37	0.05	4.43	0.01	-13.45
1074.73	1.19	0.85	8802.7	1.000	1.29	0.00	1.29	0.00	8.12
730.17	1.61	1.10	10013.2	1.000	1.90	0.00	1.90	0.00	15.42

Table A.33: Comparison between model and data, Kitscha T1, Steel 1020-CS

F	$R_{\exp}$	α	τ	B	R_s	R_L	R_j	Θ	$\frac{R_j - R_{\exp}}{R_j}\%$
N	K/W	$(-)$	$(-)$	$(-)$	K/W	K/W	K/W	$(-)$	$(-)$
18.68	65.84	0.72	111.1	0.015	24.62	51.93	76.55	2.11	14.00
37.37	56.92	0.46	88.2	0.017	12.31	46.93	59.24	3.81	3.91
59.61	49.14	0.33	75.5	0.018	7.72	43.20	50.91	5.60	3.48
92.53	47.81	0.25	65.2	0.020	4.97	39.52	44.50	7.95	-7.45
124.55	40.98	0.20	59.0	0.021	3.69	37.01	40.70	10.02	-0.70
157.03	38.71	0.18	54.6	0.023	2.93	35.05	37.97	11.96	-1.92
197.96	38.71	0.15	50.6	0.024	2.32	33.10	35.43	14.25	-9.25
302.45	34.15	0.11	43.9	0.027	1.52	29.64	31.16	19.49	-9.61

Table A.34: Comparison between model and data, Kitscha T2, Steel 1020-CS

F	$R_{\exp}$	α	τ	B	R_s	R_L	R_j	Θ	$\frac{R_j - R_{\exp}}{R_j}\%$
N	K/W	$(-)$	$(-)$	$(-)$	K/W	K/W	K/W	$(-)$	$(-)$
16.01	81.96	0.13	117.0	0.010	11.26	74.62	85.88	6.63	4.56
22.24	76.08	0.11	104.8	0.011	8.10	68.44	76.55	8.45	0.61
55.60	54.26	0.06	77.2	0.014	3.24	52.73	55.97	16.27	3.06
87.19	47.43	0.04	66.5	0.016	2.07	46.00	48.07	22.25	1.33
195.72	37.38	0.03	50.8	0.021	0.92	35.62	36.54	38.67	-2.30
266.89	32.63	0.02	45.8	0.023	0.68	32.19	32.87	47.67	0.71
467.06	27.13	0.01	38.0	0.027	0.39	26.74	27.12	69.28	-0.04

Table A.35: Comparison between model and data, McMillan and Mikic P1, SS303

F	$R_{\exp}$	α	τ	B	R_s	R_L	R_j	Θ	$\frac{R_j - R_{\exp}}{R_j}\%$
N	K/W	$(-)$	$(-)$	$(-)$	K/W	K/W	K/W	$(-)$	$(-)$
733.96	32.47	0.46	142.2	0.096	7.39	20.48	27.87	2.77	-16.50
1178.78	27.80	0.34	121.4	0.104	4.60	18.60	23.21	4.04	-19.77
1623.60	25.00	0.27	109.2	0.110	3.34	17.29	20.63	5.17	-21.17
3402.89	17.37	0.17	85.3	0.130	1.59	14.20	15.80	8.91	-9.98
5182.18	13.36	0.13	74.1	0.144	1.05	12.49	13.54	11.93	1.28
9630.40	10.59	0.08	60.3	0.170	0.56	10.11	10.68	17.95	0.80
14078.62	8.47	0.06	53.1	0.189	0.39	8.77	9.16	22.77	7.48
22975.06	6.35	0.05	45.1	0.219	0.24	7.20	7.43	30.46	14.52
31871.50	5.56	0.04	40.5	0.241	0.17	6.24	6.41	36.64	13.25
43436.87	4.54	0.03	36.5	0.265	0.12	5.41	5.53	43.27	17.85

Table A.36: Comparison between model and data, McMillan and Mikic P2, SS303

F	$R_{\exp}$	α	τ	B	R_s	R_L	R_j	Θ	$\frac{R_j - R_{\exp}}{R_j}\%$
N	K/W	$(-)$	$(-)$	$(-)$	K/W	K/W	K/W	$(-)$	$(-)$
733.96	7.09	0.82	1071.5	0.301	3.61	3.48	7.09	0.96	-0.04
1178.78	4.89	0.60	915.0	0.321	2.25	3.12	5.37	1.39	8.84
1623.60	3.95	0.49	822.3	0.337	1.63	2.86	4.49	1.75	12.11
2513.24	3.44	0.36	710.9	0.364	1.05	2.49	3.54	2.36	2.85
3402.89	2.80	0.30	642.6	0.387	0.78	2.22	3.00	2.85	6.59
5182.18	1.87	0.22	558.5	0.423	0.51	1.85	2.36	3.62	20.84

Table A.37: Comparison between model and data, Mikic and Rohsenow T2, SS305

F	$R_{\exp}$	α	τ	B	R_s	R_L	R_j	Θ	$\frac{R_j - R_{\exp}}{R_j}\%$
N	K/W	$(-)$	$(-)$	$(-)$	K/W	K/W	K/W	$(-)$	$(-)$
463.64	2.63	6.02	7858.6	1.000	4.67	0.00	4.67	0.00	43.75
681.99	1.98	4.65	6910.0	1.000	3.18	0.00	3.18	0.00	37.62
919.76	1.91	3.81	6254.3	1.000	2.36	0.00	2.36	0.00	19.08
1405.97	1.38	2.87	5429.3	1.000	1.54	0.00	1.54	0.00	10.33
2212.97	1.01	2.12	4667.4	1.000	0.98	0.00	0.98	0.00	-3.33
4102.76	0.55	1.41	3799.4	1.000	0.53	0.00	0.53	0.00	-4.72

Table A.38: Comparison between model and data, Smuda and Gyorog, SS304

F	$R_{\exp}$	α	τ	B	R_s	R_L	R_j	Θ	$\frac{R_j - R_{\exp}}{R_j}\%$
N	K/W	$(-)$	$(-)$	$(-)$	K/W	K/W	K/W	$(-)$	$(-)$
359.76	3.02	0.31	12529.0	0.563	1.69	1.25	2.94	0.74	-2.93
1082.83	1.15	0.15	8677.7	0.731	0.56	0.46	1.02	0.82	-12.35
1977.17	0.45	0.10	7099.7	0.861	0.31	0.15	0.45	0.48	0.11
1079.29	1.09	0.15	8687.2	0.731	0.56	0.46	1.03	0.83	-6.00

A.2 Conforming Contacts

Tables A.40 through A.73 provide the following information for TCR data points for the data sets listed in Table A.39:

1. applied force, F
2. measured thermal contact resistance, R_{exp}
3. joint resistance predicted by the model, which is equal to micro thermal resistance $R_j = R_s$

$$R_s = \frac{0.565\,(\sigma/m)\,H^*}{k_s F}$$

   where $H^* \equiv c_1\,(\sigma/m\sigma_0)^{c_2}$.

4. relative difference between the model and data.

Since, the specimens were designed to be flat and radius of curvatures were relatively high, macro thermal resistance for the these data were zero. Therefore, the radius of curvature, macrocontact radius, the roughness parameter α, and the geometric parameter τ were not included in Tables.

Table A.39: Data information, conforming rough contacts

Reference, test # and material	E' GPa	σ/m μm	c_1/c_2 GPa	k_s W/mK	b_L mm	$\overline{T_c}$ $^\circ C$
A,P3435,Ni200	112.09	8.48/.344	6.3/-.26	67.1	14.3	110
A,P2627,Ni200	112.09	1.23/.139	6.3/-.26	64.5	14.3	150
A,P1011,Ni200	112.09	4.27/.237	6.3/-.26	67.7	14.3	100
A,P0809,Ni200	112.09	4.29/.240	6.3/-.26	67.3	14.3	108
A,P1617,Ni-Ag	63.90	4.45/.255	0.39/0	100.0	14.3	195
A,P3233,Ni-Ag	63.90	8.03/.349	0.39/0	100.0	14.3	190
H,PNI0102,Ni200	112.08	0.90/.110	6.3/-.26	75.3	12.5	120
H,PNI0304,Ni200	112.08	3.43/.190	6.3/-.26	76.0	12.5	115
H,PNI0506,Ni200	112.08	4.24/.188	6.3/-.26	75.9	12.5	110
H,PNI0708,Ni200	112.08	9.53/.228	6.3/-.26	75.7	12.5	115
H,PNI0910,Ni200	112.08	13.94/.233	6.3/-.26	75.8	12.5	115
H,PSS0102,SS304	113.74	0.48/.072	6.3/-.26	19.2	12.5	140
H,PSS0304,SS304	113.74	2.71/.116	6.3/-.26	19.1	12.5	145
H,PSS0506,SS304	113.74	5.88/.146	6.3/-.26	18.9	12.5	130
H,PSS0708,SS304	113.74	10.95/.19	6.3/-.26	18.9	12.5	125
H,PZ40102,Zircaloy4	57.26	0.61/.049	3.32/-.15	16.6	12.5	130
H,PZ40304,Zircaloy4	57.26	2.75/.148	3.32/-.15	17.5	12.5	155
H,PZ40506,Zircaloy4	57.26	3.14/.129	3.32/-.15	18.6	12.5	155
H,PZ40708,Zircaloy4	57.26	7.92/.207	3.32/-.15	18.6	12.5	160
H,PZN0102,Zr2.5Nb	57.26	0.92/.083	5.88/-.27	21.3	12.5	165
H,PZN0304,Zr2.5Nb	57.26	2.50/.162	5.88/-.27	21.2	12.5	170
H,PZN0506,Zr2.5Nb	57.26	5.99/.184	5.88/-.27	21.2	12.5	165
H,PZN0708,Zr2.5Nb	57.26	8.81/.200	5.88/-.27	21.2	12.5	160
M,T1,SS304	113.74	0.72/.041	6.27/-.23	18.8	12.5	39
MW,SS304,SM1SM2	113.74	1.34/.105	4.8/0	16.0	12.7	52
MW,SS304,SC1SC2	113.74	1.44/.089	4.5/0	16.0	12.7	52
N,SS304,GL	113.74	0.97/.061	5.12/-.29	19.5	12.5	175
N,SS304,LG	113.74	0.97/.061	5.12/-.29	19.5	12.5	185
N,Ni200,GL	112.08	0.87/.050	4.6/-.21	68.9	12.5	195
N,Ni200,LG	112.08	0.87/.050	4.6/-.21	69.4	12.5	185
N,Al6061T6,GL	39.11	0.86/.058	0.9/-.006	211.4	12.5	223
N,Al6061T6,LG	39.11	0.86/.058	0.9/-.006	211.5	12.5	227
N,Ni200-G,Al6061T6-L	56.23	0.90/.048	1.1/-.008	104.3	12.5	168
N,Al6061T6-L,Ni200-G	56.23	0.90/.048	1.1/-.008	102.7	12.5	210
N,Al6061T6-G,Ni200-L	56.23	1.20/.057	1.03/-.001	108.1	12.5	135
N,Ni200-L,Al6061T6-G	56.23	1.20/0.057	1.03/-.001	108.8	12.5	125

Table A.40: Comparison between model and data, Antonetti,P3435, Ni200

F	$R_{\exp}$	R_j	$\frac{R_j - R_{\exp}}{R_j}\%$
N	K/W	K/W	$(-)$
366.01	1.54	1.55	0.75
625.62	0.93	0.91	-2.23
1019.83	0.53	0.56	4.64
1333.28	0.42	0.43	0.92
1742.88	0.32	0.33	0.56
2200.55	0.28	0.26	-7.34

Table A.41: Comparison between model and data, Antonetti,P2627, Ni200

F	$R_{\exp}$	R_j	$\frac{R_j - R_{\exp}}{R_j}\%$
N	K/W	K/W	$(-)$
398.70	0.59	0.69	15.40
628.18	0.37	0.44	15.30
1040.98	0.24	0.27	9.69
1349.31	0.18	0.21	13.67
1818.52	0.15	0.15	4.68
2249.91	0.12	0.12	3.21

Table A.42: Comparison between model and data, Antonetti,P1011, Ni200

F	$R_{\exp}$	R_j	$\frac{R_j - R_{\exp}}{R_j}\%$
N	K/W	K/W	$(-)$
328.19	1.25	1.36	7.97
737.15	0.62	0.61	-1.79
933.94	0.47	0.48	1.40
1171.11	0.38	0.38	-0.02
1378.15	0.36	0.32	-11.52
2060.82	0.21	0.22	2.07

Table A.43: Comparison between model and data, Antonetti,P0809, Ni200

F	$R_{\exp}$	R_j	$\frac{R_j - R_{\exp}}{R_j}\%$
N	K/W	K/W	$(-)$
447.42	0.89	1.00	10.65
765.35	0.57	0.58	2.68
999.32	0.40	0.45	11.63
1233.93	0.36	0.36	1.11
1570.45	0.30	0.28	-5.83
1852.49	0.24	0.24	1.71
2330.68	0.18	0.19	5.56

Table A.44: Comparison between model and data, Antonetti,P1617, Ni200-Ag

F	$R_{\exp}$	R_j	$\frac{R_j - R_{\exp}}{R_j}\%$
N	K/W	K/W	$(-)$
346.58	0.13	0.11	-15.39
636.78	0.07	0.06	-16.20
956.46	0.05	0.04	-11.58
1274.85	0.03	0.03	-7.27
1622.71	0.03	0.02	-29.42
1958.40	0.03	0.02	-28.89
2353.67	0.02	0.02	0.98

Table A.45: Comparison between model and data, Antonetti,P3233, Ni200-Ag

F	$R_{\exp}$	R_j	$\frac{R_j - R_{\exp}}{R_j}\%$
N	K/W	K/W	$(-)$
369.64	0.16	0.14	-17.42
703.41	0.09	0.07	-21.38
956.46	0.07	0.05	-26.97
1298.55	0.05	0.04	-20.95
1735.46	0.04	0.03	-19.10
2354.31	0.03	0.02	-23.26

Table A.46: Comparison between model and data, Hegazy,PNI0102, Ni200

F	$R_{\exp}$	R_j	$\frac{R_j - R_{\exp}}{R_j}\%$
N	K/W	K/W	$(-)$
242.98	0.64	0.92	30.68
288.63	0.57	0.78	26.85
360.30	0.48	0.62	22.64
422.64	0.43	0.53	19.80
494.80	0.39	0.45	14.86
556.65	0.36	0.40	11.18
665.13	0.31	0.34	7.18
772.14	0.28	0.29	3.37
885.05	0.25	0.25	0.98
991.57	0.23	0.23	0.37
1104.96	0.21	0.20	-3.18
1314.07	0.18	0.17	-6.27
1540.36	0.16	0.15	-9.60
1765.18	0.15	0.13	-14.97
2005.22	0.12	0.11	-9.76
2199.61	0.11	0.10	-11.47
2413.14	0.10	0.09	-11.97
2644.83	0.09	0.08	-7.62
2848.05	0.09	0.08	-9.48
3092.01	0.08	0.07	-7.73
3522.51	0.07	0.06	-8.97
3955.46	0.06	0.06	-8.26
4334.42	0.06	0.05	-9.46

Table A.47: Comparison between model and data, Hegazy,PNI0304, Ni200

F	$R_{\exp}$	R_j	$\frac{R_j - R_{\exp}}{R_j}\%$
N	K/W	K/W	$(-)$
234.15	1.16	1.70	31.63
290.11	1.06	1.37	22.88
359.32	0.90	1.11	19.30
424.61	0.80	0.94	15.32
489.89	0.73	0.81	10.51
559.60	0.66	0.71	7.32
668.08	0.58	0.60	3.13
802.09	0.51	0.50	-2.46
890.45	0.47	0.45	-4.07
990.58	0.43	0.40	-7.23
1109.37	0.39	0.36	-8.49
1342.05	0.32	0.30	-9.14
1546.25	0.28	0.26	-10.16
1760.27	0.25	0.23	-10.18
1997.37	0.22	0.20	-10.51
2206.48	0.19	0.18	-7.81
2419.52	0.18	0.16	-10.02
2639.43	0.17	0.15	-14.16
2865.23	0.16	0.14	-11.90
3094.96	0.15	0.13	-12.97
3559.82	0.13	0.11	-16.19
3951.53	0.12	0.10	-17.74
4319.69	0.11	0.09	-15.61

Table A.48: Comparison between model and data, Hegazy,PNI0506, Ni200

F	$R_{\exp}$	R_j	$\frac{R_j - R_{\exp}}{R_j}\%$
N	K/W	K/W	$(-)$
242.00	1.56	1.94	19.61
287.65	1.43	1.64	12.62
354.90	1.21	1.33	8.45
427.06	1.06	1.10	3.47
494.80	0.95	0.95	0.29
555.18	0.88	0.85	-3.72
662.68	0.76	0.71	-6.83
775.09	0.68	0.61	-11.87
887.50	0.62	0.53	-16.16
996.96	0.55	0.47	-15.72
1151.59	0.47	0.41	-16.11
1322.41	0.42	0.36	-17.27
1533.49	0.36	0.31	-16.19
1764.20	0.32	0.27	-18.37
1973.80	0.28	0.24	-16.32
2203.53	0.25	0.21	-16.99
2424.92	0.23	0.19	-18.79
2632.07	0.21	0.18	-18.00
2862.78	0.20	0.16	-20.24
3084.65	0.18	0.15	-20.14
3517.11	0.16	0.13	-19.01
3963.32	0.14	0.12	-19.34
4361.91	0.14	0.11	-26.71

Table A.49: Comparison between model and data, Hegazy,PNI0708, Ni200

F	$R_{\exp}$	R_j	$\frac{R_j - R_{\exp}}{R_j}\%$
N	K/W	K/W	$(-)$
226.29	2.05	3.29	37.68
292.56	1.90	2.54	25.51
356.87	1.69	2.09	19.20
426.08	1.51	1.75	13.67
490.87	1.37	1.52	9.76
559.11	1.24	1.33	7.02
671.52	1.07	1.11	3.66
780.98	0.95	0.95	0.48
896.83	0.85	0.83	-2.97
997.95	0.79	0.75	-5.39
1103.48	0.70	0.67	-4.01
1318.00	0.59	0.56	-4.00
1540.36	0.50	0.48	-3.72
1766.16	0.45	0.42	-6.30
1989.51	0.41	0.37	-8.39
2225.62	0.36	0.33	-8.23
2419.52	0.34	0.31	-9.45
2645.32	0.31	0.28	-11.86
2864.74	0.29	0.26	-10.74
3079.25	0.26	0.24	-9.24
3516.62	0.24	0.21	-12.44
3953.99	0.21	0.19	-11.90
4309.38	0.19	0.17	-10.08

Table A.50: Comparison between model and data, Hegazy,PNI0910, Ni200

F	$R_{\exp}$	R_j	$\frac{R_j - R_{\exp}}{R_j}\%$
N	K/W	K/W	$(-)$
232.18	3.04	4.18	27.21
290.60	2.90	3.34	13.17
356.87	2.49	2.72	8.47
421.66	2.17	2.30	5.47
468.78	1.98	2.07	4.30
556.16	1.79	1.74	-2.39
682.31	1.50	1.42	-5.23
780.49	1.35	1.24	-8.72
894.86	1.18	1.08	-8.66
996.96	1.08	0.97	-11.16
1106.92	0.96	0.88	-10.09
1333.21	0.81	0.73	-11.26
1534.96	0.70	0.63	-10.35
1763.22	0.62	0.55	-12.30
1997.37	0.54	0.49	-11.85
2213.35	0.49	0.44	-11.82
2428.35	0.46	0.40	-14.42
2656.61	0.41	0.37	-13.31
2854.92	0.39	0.34	-14.38
3082.69	0.36	0.31	-14.89
3526.44	0.31	0.28	-14.00
3967.73	0.28	0.24	-14.44
4315.76	0.26	0.22	-14.83

Table A.51: Comparison between model and data, Hegazy,PSS0102, SS304

F	$R_{\exp}$	R_j	$\frac{R_j - R_{\exp}}{R_j}\%$
N	K/W	K/W	$(-)$
218.93	2.89	3.64	20.68
290.60	2.14	2.74	22.08
358.34	1.74	2.22	21.72
425.10	1.50	1.87	19.81
494.80	1.32	1.61	17.81
546.34	1.20	1.46	17.55
668.57	1.04	1.19	13.01
781.47	0.92	1.02	10.00
912.53	0.82	0.87	5.50
987.64	0.78	0.81	3.57
1104.47	0.71	0.72	1.87
1320.94	0.60	0.60	1.06
1545.27	0.51	0.52	0.41
1762.24	0.46	0.45	-1.14
1988.04	0.40	0.40	0.75
2205.50	0.36	0.36	1.65
2420.50	0.33	0.33	-1.02
2636.97	0.31	0.30	-2.34
2818.11	0.26	0.28	6.27
3066.98	0.26	0.26	1.60
3511.22	0.23	0.23	0.21
3953.01	0.20	0.20	0.13
4329.51	0.18	0.18	2.17

Table A.52: Comparison between model and data, Hegazy,PSS0304, SS304

F	$R_{\exp}$	R_j	$\frac{R_j - R_{\exp}}{R_j}\%$
N	K/W	K/W	$(-)$
211.57	6.79	9.93	31.63
293.05	5.67	7.17	20.86
362.26	4.93	5.80	14.96
423.62	4.43	4.96	10.72
494.80	3.97	4.25	6.49
552.23	3.66	3.81	3.88
664.15	3.19	3.16	-0.92
774.11	2.84	2.71	-4.52
878.17	2.63	2.39	-9.85
989.60	2.33	2.12	-9.52
1100.54	2.14	1.91	-11.84
1314.07	1.82	1.60	-13.54
1547.73	1.54	1.36	-13.33
1769.11	1.37	1.19	-15.50
1984.11	1.19	1.06	-12.75
2200.10	1.09	0.96	-14.31
2419.52	1.00	0.87	-14.70
2638.45	0.91	0.80	-14.86
2874.07	0.84	0.73	-15.19
3080.23	0.79	0.68	-15.08
3527.91	0.70	0.60	-18.14
3983.44	0.61	0.53	-15.66
4331.47	0.56	0.49	-15.43

Table A.53: Comparison between model and data, Hegazy,PSS0506, SS304

F	$R_{\exp}$	R_j	$\frac{R_j - R_{\exp}}{R_j}\%$
N	K/W	K/W	$(-)$
200.77	8.45	16.06	47.37
296.00	7.28	10.89	33.22
356.87	6.45	9.04	28.66
425.10	5.74	7.59	24.35
494.80	5.17	6.52	20.66
562.05	4.73	5.74	17.62
667.10	4.12	4.83	14.69
775.58	3.68	4.16	11.56
888.48	3.30	3.63	9.18
1014.15	2.95	3.18	7.15
1101.03	2.76	2.93	5.75
1334.69	2.31	2.42	4.51
1533.00	2.04	2.10	2.96
1752.91	1.79	1.84	2.69
1989.02	1.60	1.62	1.06
2226.60	1.45	1.45	-0.19
2424.43	1.35	1.33	-1.16
2632.56	1.24	1.22	-1.53
2890.27	1.14	1.12	-2.29
3086.12	1.09	1.04	-4.37
3521.04	0.96	0.92	-5.32
3968.22	0.86	0.81	-6.00
4329.02	0.80	0.74	-7.54

Table A.54: Comparison between model and data, Hegazy,PSS0708, SS304

F	$R_{\exp}$	R_j	$\frac{R_j - R_{\exp}}{R_j}\%$
N	K/W	K/W	$(-)$
218.44	11.01	19.49	43.51
286.67	9.94	14.85	33.10
354.41	8.56	12.02	28.76
414.30	7.43	10.28	27.67
491.86	6.84	8.66	21.04
557.14	6.33	7.64	17.23
693.11	5.52	6.14	10.14
774.11	4.87	5.50	11.41
879.16	4.39	4.84	9.36
1008.25	4.01	4.22	5.05
1098.08	3.64	3.88	6.20
1311.61	3.08	3.25	5.07
1538.40	2.66	2.77	3.92
1787.76	2.30	2.38	3.47
1991.97	2.12	2.14	0.74
2200.59	1.92	1.94	0.59
2415.59	1.77	1.76	-0.40
2632.56	1.63	1.62	-0.91
2867.19	1.50	1.49	-0.78
3080.23	1.42	1.38	-2.40
3525.46	1.25	1.21	-3.66
3967.73	1.11	1.07	-3.33
4307.42	1.04	0.99	-4.92

Table A.55: Comparison between model and data, Hegazy,PZ40102, Zircaloy4

F	$R_{\exp}$	R_j	$\frac{R_j - R_{\exp}}{R_j}\%$
N	K/W	K/W	$(-)$
205.68	3.94	4.68	15.79
291.58	2.99	3.30	9.50
355.39	2.45	2.71	9.58
438.35	2.06	2.20	6.17
494.31	1.81	1.95	6.82
562.05	1.63	1.71	5.04
667.10	1.37	1.44	5.35
775.58	1.18	1.24	5.04
896.34	1.05	1.07	2.30
996.96	0.94	0.97	3.01
1122.14	0.85	0.86	0.90
1319.47	0.72	0.73	1.34
1556.56	0.62	0.62	-0.70
1762.73	0.55	0.55	0.09
1976.26	0.49	0.49	0.25
2210.40	0.44	0.44	0.06
2436.70	0.39	0.39	1.11
2649.25	0.36	0.36	1.07
2847.56	0.34	0.34	0.27
3102.81	0.31	0.31	-0.40
3519.07	0.27	0.27	0.96
3973.13	0.24	0.24	0.00
4327.54	0.22	0.22	-0.18

Table A.56: Comparison between model and data, Hegazy,PZ40304, Zircaloy4

F	$R_{\exp}$	R_j	$\frac{R_j - R_{\exp}}{R_j}\%$
N	K/W	K/W	$(-)$
214.02	4.53	6.00	24.59
293.54	3.53	4.38	19.34
364.23	2.99	3.53	15.32
430.50	2.62	2.98	12.27
494.31	2.34	2.60	9.92
538.49	2.17	2.39	8.98
665.62	1.84	1.93	4.66
772.64	1.64	1.66	1.29
878.66	1.46	1.46	0.35
987.15	1.32	1.30	-1.24
1101.03	1.18	1.17	-1.38
1312.60	1.01	0.98	-2.82
1541.83	0.85	0.83	-2.24
1762.24	0.77	0.73	-5.24
1974.29	0.69	0.65	-5.86
2226.60	0.61	0.58	-6.56
2419.03	0.56	0.53	-6.13
2631.57	0.51	0.49	-5.26
2864.74	0.47	0.45	-4.51
3080.23	0.45	0.42	-7.74
3551.47	0.36	0.36	0.85
3981.97	0.35	0.32	-8.95
4302.02	0.33	0.30	-10.68

Table A.57: Comparison between model and data, Hegazy,PZ40506, Zircaloy4

F	$R_{\exp}$	R_j	$\frac{R_j - R_{\exp}}{R_j}\%$
N	K/W	K/W	$(-)$
203.71	4.72	7.47	36.83
295.51	3.87	5.15	24.74
364.23	3.32	4.18	20.54
432.95	2.91	3.51	17.03
491.86	2.60	3.09	15.85
558.61	2.36	2.72	13.19
668.57	2.05	2.27	9.72
770.18	1.83	1.97	7.22
889.95	1.62	1.71	5.08
974.88	1.50	1.56	3.91
1102.01	1.35	1.38	1.85
1333.21	1.15	1.14	-0.62
1547.73	1.01	0.98	-2.49
1789.73	0.88	0.85	-3.21
1970.86	0.80	0.77	-3.70
2220.22	0.72	0.68	-5.39
2429.33	0.66	0.63	-5.66
2638.94	0.61	0.58	-5.94
2844.12	0.56	0.53	-5.28
3066.98	0.52	0.50	-5.53
3561.78	0.46	0.43	-7.17
3953.99	0.41	0.38	-6.83
4307.42	0.38	0.35	-6.48

Table A.58: Comparison between model and data, Hegazy,PZ40708, Zircaloy4

F	$R_{\exp}$	R_j	$\frac{R_j - R_{\exp}}{R_j}\%$
N	K/W	K/W	$(-)$
216.97	6.72	10.29	34.69
297.47	5.79	7.51	22.92
359.81	5.06	6.21	18.57
427.55	4.42	5.22	15.41
497.75	3.99	4.49	10.99
591.99	3.21	3.77	14.84
671.02	3.03	3.33	9.06
772.64	2.73	2.89	5.54
876.70	2.43	2.55	4.70
990.09	2.18	2.26	3.32
1086.79	2.00	2.06	2.82
1316.03	1.69	1.70	0.39
1529.56	1.47	1.46	-0.94
1760.76	1.30	1.27	-2.61
2002.27	1.16	1.12	-3.88
2203.04	1.07	1.01	-5.09
2434.73	0.98	0.92	-6.40
2635.99	0.90	0.85	-6.52
2877.01	0.83	0.78	-7.28
3076.31	0.79	0.73	-8.33
3509.75	0.69	0.64	-8.55
3942.70	0.61	0.57	-8.12
4345.22	0.56	0.51	-8.75

Table A.59: Comparison between model and data, Hegazy,PZN0102, Zr2.5Nb

F	$R_{\exp}$	R_j	$\frac{R_j - R_{\exp}}{R_j}\%$
N	K/W	K/W	$(-)$
237.58	2.37	3.81	37.63
288.63	2.07	3.13	33.79
361.77	1.80	2.50	28.01
423.13	1.63	2.14	23.57
489.89	1.50	1.85	18.92
558.61	1.36	1.62	16.17
662.68	1.22	1.36	10.78
774.60	1.10	1.17	5.64
893.88	0.99	1.01	2.02
995.00	0.92	0.91	-1.32
1104.47	0.83	0.82	-1.54
1321.43	0.72	0.68	-5.47
1542.33	0.61	0.59	-4.48
1758.80	0.55	0.51	-6.90
1977.24	0.50	0.46	-8.73
2213.84	0.46	0.41	-12.34
2435.23	0.41	0.37	-11.29
2640.41	0.39	0.34	-13.80
2870.63	0.36	0.32	-14.58
3037.04	0.31	0.30	-4.33
3505.82	0.27	0.26	-4.97
3943.19	0.25	0.23	-7.44
4294.66	0.23	0.21	-8.31

Table A.60: Comparison between model and data, Hegazy,PZN0304, Zr2.5Nb

F	$R_{\exp}$	R_j	$\frac{R_j - R_{\exp}}{R_j}\%$
N	K/W	K/W	$(-)$
226.78	3.11	5.09	39.03
292.56	2.72	3.95	31.12
356.87	2.38	3.24	26.48
422.64	2.16	2.73	21.04
490.87	1.96	2.35	16.60
557.63	1.81	2.07	12.51
670.53	1.61	1.72	6.30
774.60	1.45	1.49	2.56
889.95	1.30	1.30	0.10
1019.05	1.14	1.13	-0.23
1144.72	1.05	1.01	-3.58
1308.67	0.88	0.88	0.73
1537.91	0.77	0.75	-2.00
1782.85	0.67	0.65	-3.91
1988.04	0.60	0.58	-2.82
2187.82	0.54	0.53	-2.48
2416.57	0.50	0.48	-4.25
2651.21	0.46	0.44	-6.36
2882.41	0.42	0.40	-6.01
3086.12	0.39	0.37	-5.17
3538.22	0.35	0.33	-7.60
3955.95	0.32	0.29	-8.11
4289.26	0.29	0.27	-7.95

Table A.61: Comparison between model and data, Hegazy,PZN0506, Zr2.5Nb

F	$R_{\exp}$	R_j	$\frac{R_j - R_{\exp}}{R_j}\%$
N	K/W	K/W	$(-)$
200.77	6.23	9.92	37.21
286.18	5.16	6.96	25.91
362.76	4.46	5.49	18.82
420.68	3.99	4.74	15.81
492.35	3.56	4.05	11.97
565.98	3.24	3.52	7.83
672.50	2.85	2.96	3.68
772.64	2.54	2.58	1.60
919.41	2.22	2.17	-2.54
992.06	2.07	2.01	-3.31
1110.36	1.89	1.79	-5.43
1328.30	1.58	1.50	-5.55
1505.51	1.37	1.32	-3.54
1757.33	1.21	1.13	-6.53
1999.33	1.06	1.00	-6.60
2200.10	0.97	0.91	-6.89
2437.68	0.88	0.82	-7.55
2651.21	0.82	0.75	-8.80
2901.06	0.76	0.69	-10.17
3073.85	0.71	0.65	-9.11
3516.13	0.63	0.57	-10.37
3958.90	0.55	0.50	-10.08
4312.33	0.52	0.46	-11.85

Table A.62: Comparison between model and data, Hegazy,PZN0708, Zr2.5Nb

F	$R_{\exp}$	R_j	$\frac{R_j - R_{\exp}}{R_j}\%$
N	K/W	K/W	$(-)$
210.58	7.69	11.80	34.83
287.65	6.57	8.64	23.90
362.26	5.71	6.86	16.78
426.08	5.07	5.83	13.08
490.38	4.53	5.07	10.63
562.54	4.08	4.42	7.55
673.97	3.51	3.69	4.70
776.07	3.11	3.20	2.98
881.12	2.81	2.82	0.19
988.13	2.54	2.51	-1.04
1105.45	2.33	2.25	-3.84
1339.10	1.92	1.86	-3.70
1553.62	1.68	1.60	-4.78
1757.82	1.49	1.41	-5.30
1976.26	1.32	1.26	-5.17
2217.77	1.21	1.12	-8.00
2417.55	1.11	1.03	-7.69
2664.95	1.01	0.93	-8.30
2874.56	0.93	0.86	-7.59
3118.52	0.88	0.80	-10.00
3510.24	0.78	0.71	-9.75
3977.06	0.69	0.62	-9.89
4344.72	0.63	0.57	-9.70

Table A.63: Comparison between model and data, Milanez et al.,T1, SS304

F	$R_{\exp}$	R_j	$\frac{R_j - R_{\exp}}{R_j}\%$
N	K/W	K/W	$(-)$
7.74	145.41	221.40	34.32
22.87	60.29	74.94	19.55
42.75	29.98	40.09	25.22
90.06	16.57	19.03	12.91
180.64	9.33	9.49	1.62
365.04	5.33	4.69	-13.50
594.56	3.51	2.88	-21.75
977.63	1.78	1.75	-1.56
1027.12	1.46	1.67	12.67
1205.77	1.27	1.42	10.86
1358.66	1.04	1.26	17.69

Table A.64: Comparison between model and data, McWaid,T1, SC1SC2

F	$R_{\exp}$	R_j	$\frac{R_j - R_{\exp}}{R_j}\%$
N	K/W	K/W	$(-)$
262.98	7.02	9.75	27.94
724.59	3.34	3.54	5.44
1216.10	2.28	2.11	-8.12
1702.54	1.70	1.51	-13.01
2031.90	1.41	1.26	-11.75
2432.20	1.20	1.05	-13.50
2943.97	1.00	0.87	-15.06
3394.94	0.89	0.75	-17.75
3987.79	0.77	0.64	-19.47

Table A.65: Comparison between model and data, McWaid,T1, SM1SM2

F	$R_{\exp}$	R_j	$\frac{R_j - R_{\exp}}{R_j}\%$
N	K/W	K/W	$(-)$
280.72	5.64	7.72	26.96
729.66	2.79	2.97	6.02
1216.10	1.92	1.78	-7.52
1631.60	1.48	1.33	-11.71
2062.30	1.23	1.05	-16.65
2452.46	1.09	0.88	-23.39
2873.03	0.91	0.75	-20.57
3339.20	0.82	0.65	-25.65
3997.92	0.71	0.54	-31.43

Table A.66: Comparison between model and data, Nho,Al,G-Ni,L

F	$R_{\exp}$	R_j	$\frac{R_j - R_{\exp}}{R_j}\%$
N	K/W	K/W	$(-)$
269.98	0.30	0.40	26.86
348.52	0.27	0.31	12.49
402.52	0.24	0.27	10.39
495.78	0.22	0.22	-0.91
574.32	0.19	0.19	-2.22
662.68	0.17	0.16	-0.40
770.67	0.16	0.14	-13.07
878.66	0.15	0.12	-17.27
1079.92	0.12	0.10	-22.87
1207.55	0.10	0.09	-15.92
1452.99	0.10	0.07	-28.10
1673.88	0.08	0.07	-27.20
1929.13	0.07	0.06	-28.01

Table A.67: Comparison between model and data, Nho,Al,L-Ni,G

F	$R_{\exp}$	R_j	$\frac{R_j - R_{\exp}}{R_j}\%$
N	K/W	K/W	$(-)$
220.89	0.43	0.41	-4.67
255.25	0.35	0.35	-0.01
309.25	0.32	0.29	-9.03
338.70	0.28	0.27	-5.40
382.88	0.26	0.24	-9.33
427.06	0.23	0.21	-8.70
530.14	0.18	0.17	-8.44
657.77	0.15	0.14	-11.60
736.31	0.14	0.12	-13.78
937.57	0.12	0.10	-24.24
1035.74	0.11	0.09	-24.59
1212.46	0.09	0.07	-25.51
1408.81	0.08	0.06	-22.23
1654.24	0.06	0.05	-18.70
2012.58	0.06	0.04	-23.17
2307.11	0.05	0.04	-23.97

Table A.68: Comparison between model and data, Nho,Al6061T6,G-L

F	$R_{\exp}$	R_j	$\frac{R_j - R_{\exp}}{R_j}\%$
N	K/W	K/W	$(-)$
191.44	0.14	0.18	25.99
269.98	0.11	0.13	15.88
309.25	0.10	0.11	15.21
338.70	0.09	0.10	12.97
436.88	0.07	0.08	11.97
530.14	0.06	0.07	10.67
647.95	0.05	0.05	13.26
760.85	0.04	0.05	5.47
883.57	0.04	0.04	5.70
1251.73	0.03	0.03	2.07
1295.91	0.02	0.03	10.07
1482.44	0.02	0.02	1.12
1801.51	0.02	0.02	3.88
1978.22	0.02	0.02	5.87

Table A.69: Comparison between model and data, Nho,Al6061T6,L-G

F	$R_{\exp}$	R_j	$\frac{R_j - R_{\exp}}{R_j}\%$
N	K/W	K/W	$(-)$
176.71	0.17	0.20	15.00
225.80	0.14	0.16	11.91
274.89	0.12	0.13	7.79
338.70	0.10	0.10	0.21
412.33	0.08	0.09	3.27
544.87	0.07	0.06	-2.02
643.04	0.06	0.05	-4.99
731.40	0.05	0.05	-4.56
878.66	0.04	0.04	-7.47
1021.02	0.04	0.03	-6.38
1227.18	0.03	0.03	-9.47
1467.71	0.03	0.02	-10.20
1668.97	0.02	0.02	-11.10
2002.77	0.02	0.02	-10.84
2316.92	0.02	0.02	-5.50
2719.44	0.01	0.01	-10.71

Table A.70: Comparison between model and data, Nho,Ni200,G-Al6061T6,L

F	$R_{\exp}$	R_j	$\frac{R_j - R_{\exp}}{R_j}\%$
N	K/W	K/W	$(-)$
215.98	0.39	0.50	22.28
245.44	0.39	0.44	11.99
269.98	0.36	0.40	10.03
323.98	0.40	0.33	-19.90
387.79	0.31	0.28	-9.96
436.88	0.28	0.25	-10.93
525.24	0.23	0.21	-13.92
598.87	0.20	0.18	-12.41
687.22	0.18	0.16	-13.49
805.03	0.15	0.13	-9.22
1011.20	0.12	0.11	-11.00
1217.37	0.10	0.09	-8.14
1418.63	0.07	0.08	4.24
1580.61	0.06	0.07	14.20
1988.04	0.04	0.05	20.05

Table A.71: Comparison between model and data, Nho,Ni200,L-Al6061T6,G

F	$R_{\exp}$	R_j	$\frac{R_j - R_{\exp}}{R_j}\%$
N	K/W	K/W	$(-)$
235.62	0.40	0.45	9.77
284.71	0.33	0.37	10.03
319.07	0.30	0.33	9.24
373.06	0.26	0.28	8.90
436.88	0.23	0.24	4.27
535.05	0.19	0.20	5.30
589.05	0.18	0.18	-2.35
711.77	0.16	0.15	-5.17
854.12	0.12	0.12	-0.94
952.30	0.12	0.11	-7.46
1109.37	0.10	0.10	-1.34
1354.81	0.08	0.08	-3.01
1605.16	0.07	0.07	-2.02
1909.50	0.06	0.06	-2.62

Table A.72: Comparison between model and data, Nho,Ni200,G-L

F	$R_{\exp}$	R_j	$\frac{R_j - R_{\exp}}{R_j}\%$
N	K/W	K/W	$(-)$
309.25	0.69	1.17	40.77
343.61	0.64	1.06	39.02
446.70	0.55	0.81	31.74
535.05	0.52	0.68	23.76
579.23	0.49	0.63	21.86
672.50	0.44	0.54	19.18
785.40	0.39	0.46	14.68
957.20	0.36	0.38	5.24
1040.65	0.32	0.35	7.55
1237.00	0.28	0.29	5.18
1477.53	0.25	0.25	-0.12
1703.33	0.21	0.21	1.49
2027.31	0.18	0.18	-0.19
2326.74	0.16	0.16	-3.17
2793.07	0.13	0.13	-2.11
3180.86	0.11	0.11	2.61
3568.65	0.10	0.10	4.11

Table A.73: Comparison between model and data, Nho,Ni200,L-G

F	$R_{\exp}$	R_j	$\frac{R_j - R_{\exp}}{R_j}\%$
N	K/W	K/W	$(-)$
304.34	0.69	1.18	41.96
377.97	0.60	0.95	37.03
461.42	0.55	0.78	29.04
613.59	0.45	0.59	22.66
657.77	0.42	0.55	22.63
775.58	0.39	0.46	15.64
913.03	0.33	0.39	16.45
1178.10	0.28	0.31	8.11
1340.09	0.25	0.27	7.98
1462.80	0.22	0.25	11.03
1629.70	0.20	0.22	11.67
2027.31	0.16	0.18	8.44
2302.20	0.14	0.16	9.59
2788.16	0.12	0.13	8.00
2930.52	0.11	0.12	12.15

Appendix B

Uncertainty Analysis

B.1 Introduction

The following is a discussion of the analysis made to estimate the maximum uncertainity in the experimental measurements and the theoritical predictions of the thermal joint resistance in a vacuum. The accuracy of the measurement system and the procedure and uncertainity of the methods used for estimation of the surface parameters are discussed in Chapter six.

B.2 Differential Error Analysis Method

In order to estimate the uncertainty in the calculated result on the basis of the uncertainties in the primary measurements, we will use the method explained as follows. Suppose the result R is a given function of the independent variables $x_1, x_2, ..., x_n$. Thus,

$$R = R(x_1, x_2, ..., x_n)$$

Let w_R be the uncertainty in the result and $w_1, w_2, ..., w_n$ be the uncertainties in the independent variables. According to [83]:

$$w_R = \left[\left(\frac{\partial R}{\partial x_1} w_1 \right)^2 + \left(\frac{\partial R}{\partial x_2} w_2 \right)^2 + ... + \left(\frac{\partial R}{\partial x_n} w_n \right)^2 \right]^{1/2} \tag{B.1}$$

B.3 Thermal Measurements Uncertainty Analysis

The experimental joint resistance, of a particular joint was determined from the estimated heat flux and the temperature drop across the interface.

$$R_{\text{exp}} = \Delta T/Q \tag{B.2}$$

As explained in Chapter six, the heat flux through the interface was measured by the Armco iron flux meter. The heat loss was less than 6.7% under vacuum condition. The estimated uncertainity in the heat flux was, therefore, $\pm 3.35\%$.

The uncertainity in the temperature drop across the interface was the result of the uncertainities associated with the thermocouple readings and the extrapolated temperatures. The thermocouple readings were estimated to be accurate to $\pm 0.1^{\circ}C$. The estimated uncertainity in the interface temperature drop by extrapolation of the temperature gradients was approximately $\pm 0.1^{\circ}C$. Therefore, the overall uncertainity in the temperature drop across the joint was, therefore, $\pm 0.2^{\circ}C$.

The recorded maximum temperature drop was as large as $103.4^{\circ}C$ and the minimum value was approximately $50.2^{\circ}C$. Thus, the fractional uncertainity in the temperature drop could be as small as 0.2% and as much as 0.4%. Using a simple differential error analysis, Eq. (B.1) the estimated uncertainity in the maesured joint resistance can be found from

$$w_{R_{\text{exp}}} = \left[\left(\frac{\partial R_{\text{exp}}}{\partial \Delta T} w_{\Delta T} \right)^2 + \left(\frac{\partial R_{\text{exp}}}{\partial Q} w_Q \right)^2 \right]^{1/2} \tag{B.3}$$

substituting partial derivates, it simplifies to

$$w_{R_{\text{exp}}} = \left[\left(\frac{w_{\Delta T}}{Q} \right)^2 + \left(\frac{\Delta T}{Q^2} w_Q \right)^2 \right]^{1/2} \tag{B.4}$$

where $w_{\Delta T} = 0.2^{\circ}C$ and w_Q is considered to be 3.35% of actual measurements. Tables B.1 to B.3 list the estimated uncertainities associated with the experimental data sets T1 to T3 in percent, respectively. As can be seen, the uncertainity of thermal contact resistance measurements is less than 4 percent.

B.4 Uncertainty in TCR Predictions

Thermal joint resistance R_j is predicted by Eq. (5.25). For convinience, a summary of the model is shown here.

$$R_j = \frac{(1 - a_L/b_L)^{1.5}}{2k_s a_L} + \frac{0.565\,(\sigma/m)\,H^*}{k_s F}$$

where,

$$a_L = 1.80\ a_H\ \frac{\sqrt{\alpha + 0.31\tau^{0.056}}}{\tau^{0.028}}$$

where $\alpha = \sigma\rho/a_H^2$, $\tau = \rho/a_H$, $H^* \equiv c_1\,(\sigma/m\sigma_0)^{c_2}$, and $a_H = (0.75F\rho/E')^{1/3}$. The uncertainty associated with the prediction of the joint resistance is a function of $\sigma, m, \rho, c_1, c_2, F, E', k_s$, and b_L. Therefore, one can write.

$$R_j = R_j(\sigma, m, \rho, c_1, c_2, F, E', k_s, b_L) \tag{B.5}$$

Using a simple differential error analysis method, i.e., Eq. (B.1), the uncertainty associated with the model can be found from

$$\begin{aligned} w_{R_j} = \Bigg[&\left(\frac{\partial R_j}{\partial \sigma} w_\sigma\right)^2 + \left(\frac{\partial R_j}{\partial m} w_m\right)^2 + \left(\frac{\partial R_j}{\partial \rho} w_\rho\right)^2 + \left(\frac{\partial R_j}{\partial c_1} w_{c_1}\right)^2 + \\ &\left(\frac{\partial R_j}{\partial c_2} w_{c_2}\right)^2 + \left(\frac{\partial R_j}{\partial F} w_F\right)^2 + \left(\frac{\partial R_j}{\partial E'} w_{E'}\right)^2 + \left(\frac{\partial R_j}{\partial k_s} w_{k_s}\right)^2 + \left(\frac{\partial R_j}{\partial b_L} w_{b_L}\right)^2 \Bigg]^{1/2} \end{aligned} \tag{B.6}$$

The estimated uncertainties for, effective surface roughness w_σ, surface slope w_m, and radius of curvature w_ρ for tests T1 to T3 are listed in Table B.4. Uncertainties for other input parameters are estimated as, microhardness coefficents ±5%, thermal conductivity ±3.1%, applied load ±0.1%, and the effective elasticity modulus ±2.5%; it is assumed that these uncertainties are constant for all tests.

Using Maple [**?**], the uncertainties associate with experimental sets T1 to T3, i.e. Eq. (B.6), are calculated and shown in Tables B.5 to B.7.

It can be seen that the uncertainties associated with data points decreases as the applied load increases in all three tests. Also, as expected, the maximum uncertainty occurs in the minimum applied load in T3. The averaged uncertainty associated with the joint resistance prediction is 4.3 percent.

Table B.1: Uncertainty associated with thermal joint resistance measurements, T1

Q	ΔT	R_{exp}	w_Q	w_R	$w_R/R_{\text{exp}}\%$
W	K	K/W	W	K/W	$(-)$
6.00	84.56	14.08	0.20	0.47	3.36
6.29	76.65	12.19	0.21	0.41	3.36
7.03	66.18	9.42	0.24	0.32	3.36
9.18	70.54	7.68	0.31	0.26	3.36
12.94	86.85	6.71	0.43	0.23	3.36
19.31	103.40	5.35	0.65	0.18	3.36

Table B.2: Uncertainty associated with thermal joint resistance measurements, T2

Q	ΔT	R_{exp}	w_Q	w_R	$w_R/R_{\text{exp}}\%$
W	K	K/W	W	K/W	$(-)$
3.96	85.06	21.50	0.13	0.72	3.36
5.02	87.80	17.50	0.17	0.59	3.36
5.09	70.25	13.80	0.17	0.46	3.36
5.76	62.79	10.90	0.19	0.37	3.37
6.05	61.07	10.10	0.20	0.34	3.37
9.37	66.54	7.10	0.31	0.24	3.36

Table B.3: Uncertainty associated with thermal joint resistance measurements, T3

Q	ΔT	R_{exp}	w_Q	w_R	$w_R/R_{\text{exp}}\%$
W	K	K/W	W	K/W	$(-)$
0.78	62.25	79.93	0.03	2.69	3.37
1.45	70.47	48.50	0.05	1.63	3.36
2.60	76.84	29.60	0.09	0.99	3.36
3.62	78.89	21.80	0.12	0.73	3.36
5.87	80.99	13.80	0.20	0.46	3.36
6.93	79.74	11.50	0.23	0.39	3.36
7.70	74.67	9.70	0.26	0.33	3.36
9.72	76.80	7.90	0.33	0.27	3.36
10.38	77.88	7.50	0.35	0.25	3.36
13.98	81.07	5.80	0.47	0.19	3.36

Table B.4: Input parameters uncertainties

Parameter	T1	T2	T3
w_σ μm	0.17	0.09	0.18
w_m $(-)$	0.009	0.004	0.009
w_ρ m	0.02	0.018	0.02

Table B.5: Uncertainty associated with thermal joint resistance predictions, T1

F	k_s	R_j	w_{Rj}	$w_{Rj}/R_j\%$
N	W/mK	K/W	K/W	$(-)$
373.15	18.57	13.67	0.71	5.20
495.33	18.51	11.94	0.55	4.65
869.38	18.47	9.33	0.36	3.90
1381.50	18.67	7.64	0.27	3.50
1740.90	19.08	6.82	0.23	3.35
2656.10	19.71	5.57	0.18	3.16

Table B.6: Uncertainty associated with thermal joint resistance predictions, T2

F	k_s	R_j	w_{Rj}	$w_{Rj}/R_j\%$
N	W/mK	K/W	K/W	$(-)$
210.95	18.50	20.46	0.68	3.32
303.64	18.65	17.05	0.59	3.47
445.73	18.56	14.58	0.48	3.27
883.56	18.74	11.25	0.35	3.10
1116.90	19.02	10.24	0.31	3.07
2577.40	19.42	7.59	0.23	3.07

Table B.7: Uncertainty associated with thermal joint resistance predictions, T3

F	k_s	R_j	w_{Rj}	$w_{Rj}/R_j\%$
N	W/mK	K/W	K/W	$(-)$
31.25	18.08	81.74	8.44	10.33
48.50	18.19	49.71	5.10	10.26
110.09	18.30	29.21	2.26	7.73
189.24	18.39	20.68	1.29	6.23
409.29	18.49	13.12	0.61	4.66
600.53	18.57	10.90	0.44	4.06
795.78	18.60	9.63	0.36	3.76
1110.20	18.70	8.38	0.29	3.49
1338.64	18.81	7.69	0.26	3.40
2561.50	18.93	5.89	0.19	3.20

Appendix C

Computer Program

A computer code in Visual Basic is written to solve the governing mechanical relationships discussed in chapter three. Thermal joint resistance is claculated according to the procedure explained in chapter four.

The code is written based on the algorithms described in chapter three.

C.1 The Code

```
Dim Omega() As Double ' half-space deformation
    Dim PS() As Double ' Pressure
    Dim Hard() As Double ' MicroHardness
    Dim PSNew() As Double ' Pressure new value
    Public uR0 As Double ' Max. Sphere indentation (m)
    Public C1 As Double ' Const.1 for Hegazy's microhardness correlation
    Public C2 As Double ' Const.2 for Hegazy's microhardness correlation
    Public Hcont As Double ' effective contact microhardness defined by Heggazy (GPa)
    Public Sigma As Double ' Equivalent Roughness (m)
    Public Sigma1 As Double ' Roughness surface 1 (micro m)
    Public Sigma2 As Double ' Roughness surface 2 (micro m)
    Public Rho As Double ' Equivalent Sphere Radius (m)
    Public NPoint As Integer ' No of points in r-direction
```

```
Public Ep As Double ' Equivalent elastic modulus (Pa) "E Prime"
Public drS As Double 'increment in the r-direction
Public rInfS As Double ' infinity r
Public Fext As Double ' External Force (N)
Public Counter As Integer ' counter of the Main Loop
Public AEPS As Double ' Max error of pressure distribution
Public pHertz0 As Double ' Max. Pressure in Hertz
Public aH As Double ' Hertz contact radius (m)
Public uH As Double ' Hertz Max. indentation (m)
Public bLg As Double 'Outer radius of the sample (m)
Public MeanSlope ' Mean absolute profile Slope
Public ForceError As Double ' Force Error
Public Gamma As Double ' Plasticity index
Public ModelFlag As Integer ' plastic=2, elastic=1
Public Alpha As Double ' Alpha roughness level
Public TOL1 As Double ' Tolerance of the first iteration loop
Public mCounter As Integer ' The main loop counter
Public PlasticIndex As Double ' The plastic index (-)
Public u0 As Double
Public u1 As Double
Public UnderRFac As Double ' Under relaxation Factor , when =1 no relaxation !
Public Pi As Double ' Pi Number

Private Sub Command1_Click()
Dim dRh As Double
Dim rsH As Double
Dim ICheck As Integer
Dim m1 As Double ' mean slope of surface 1
Dim m2 As Double ' mean slope of surface 2
Dim v1 As Double ' Poisson Ratio 1
Dim v2 As Double ' Poisson Ratio 2
```

```
Dim rho1 As Double ' radius 1
Dim rho2 As Double ' radius 2
Dim E1 As Double ' Young Modulus 1
Dim E2 As Double ' Young Modulus 1
' Dummy variables
Dim iG As Integer
Dim IaL As Integer
Dim tau As Double 'tau
NPoint = 50
Pi = 3.141592654
TOL1 = 0.0001
ReDim Omega(NPoint + 1)
ReDim PS(NPoint + 1)
ReDim PSNew(NPoint + 1)
ReDim Hard(NPoint + 1)
' Input data
' E prime
v1 = 0.3
v2 = 0.3
E1 = 204000000000#
E2 = 204000000000#
Ep = ((1 - v1 ^2) / E1 + (1 - v2 ^2) / E2) ^(-1) '(Pa)
'Ep = 112600000000#
' Rho
Rho = 150 '(m)
'Sample radius (m)
bLg = Rho
' Sigma
Sigma1 = 1 ' Micrometer
Sigma2 = 1 ' Micrometer
```

'Sigma = 0.000001 * Sqr(Sigma1 ^2 + Sigma2 ^2) ' (m)

Sigma = 20 * 0.000001

' Hegazy's Microhardness Coefficients (GPa)

C1 = 6.23

C2 = -0.23

' External Force (N)

Fext = 200

UnderRFac = 0.25 ' under relaxation factor

' Finding the range for the solution, i.e. ef0*ef1 < 0

u0 = -4.1 * Sigma

'eF0 = (Fext - IntFextS) / Fext

u1 = -4.3 * Sigma

' Mean slope using Lambert Correlation

m1 = 0.076 * Sigma1 ^0.52

m2 = 0.076 * Sigma2 ^0.52

MeanSlope = Sqr(m1 ^2 + m2 ^2)

MeanSlope = 0.076 * (Sigma * 1000000#) ^0.52

' Hegazy's effective contact microhardness

Hcont = C1 * (0.95 * Sigma * 1000000# / MeanSlope) ^C2

' Plastic Index

PlasticIndex = Ep * MeanSlope / (C1 * 1000000000# * (Sigma * 1000000# / MeanSlope) ^C2)

' Hertz parameters (smooth surfaces)

aH = (3 * Fext * Rho / 4 / Ep) ^(1 / 3) ' from Hertz's solution

uH = aH ^2 / Rho

pHertz0 = 3 * Fext / 2 / Pi / aH ^2

' Johnson's alpha

Alpha = Sigma * Rho / aH ^2

tau = Rho / aH

IaL = 1.5 * Sqr(Alpha + 0.46) + 1

```
rInfS = aH * IaL
If rInfS > bLg Then rInfS = bLg
'rInfS = bLg
drS = rInfS / NPoint
' Mikic's plasticity index
Gamma = Hcont * 1000000000# / MeanSlope / Ep
' Elastic or plastic deformation of asperities
'ModelFlag = 1 ' elastic model
ModelFlag = 2 ' plastic model
' Itteration on uR0 (Main Loop)
HalvingDistance
'FactorMethod
MsgBox "All Done!", 0 + 48, ""
Label24.Caption = IntFextS
Results
End Sub

Public Function EllipticK(xK As Double) As Double
' Calculate Compelete Elliptic Integral of the first kind "K", using Yovanovich, Lemczyk 1988
Dim xp As Double ' Complementary modulus
Dim e As Double
Dim u As Double
Dim q As Double
Dim K As Double
Pi = 3.141592654
xp = Sqr(1 - xK ^2)
u = Sqr(xK)
up = Sqr(xp)
If xK < 0.9999 Then
If xK < 1 / Sqr(2) Then
```

```
e = (1 - up) / (1 + up) / 2
Else
e = (1 - u) / (1 + u) / 2
End If
q = e + 2 * e ^5 + 15 * e ^9 + 150 * e ^13
K = Pi * (1 + 2 * q + 2 * q ^4 + 2 * q ^9) ^2 / 2
If xK < 1 / Sqr(2) Then
EllipticK = K
Else
EllipticK = -K * Log(q) / Pi
End If
Else
EllipticK = 10 '....not to get the division by zero!!
End If
End Function

Public Function EllipticE(xE As Double) As Double
' Calculate Compelete Elliptic Integral of the Second kind "E", using Yovanovich, Lemczyk 1988
Dim xp As Double ' Complementary modulus
Dim e As Double
Dim u As Double
Dim q As Double
Dim K As Double
Dim Kp As Double
Dim Elp As Double
Pi = 3.141592654
xp = Sqr(1 - xE ^2)
u = Sqr(xE)
up = Sqr(xp)
If xE = 1 Then
```

```
EllipticE = 1
Else
If xE < 1 / Sqr(2) Then
e = (1 - up) / (1 + up) / 2
Else
e = (1 - u) / (1 + u) / 2
End If
q = e + 2 * e ^5 + 15 * e ^9 + 150 * e ^13
K = Pi * (1 + 2 * q + 2 * q ^4 + 2 * q ^9) ^2 / 2
Elp = Pi ^2 * ((1 + 9 * q ^2 + 25 * q ^6 + 49 * q ^12) / (1 + q ^2 + q ^6)) / 4 / K
If xE < 1 / Sqr(2) Then
EllipticE = Elp
Else
Kp = -K * Log(q) / Pi
EllipticE = (Pi / 2 + Kp * (K - Elp)) / K
End If
End If
End Function

Public Function IntFextS() As Double
' Integrate over 0...r Infinity interval using n panels " cal. External Force"
Dim DeltaInt As Double ' Integration differential
Dim P1 As Double ' Numerical Integration point 1
Dim P2 As Double ' Numerical Integration point 2
Dim Intsum As Double ' Numerical Integration
Dim iInt As Integer ' an Integer Countor
Dim aa As Double ' Internal variable
DeltaInt = drS
Intsum = 0
For iInt = 1 To NPoint
P1 = (iInt - 1) * DeltaInt
```

```
P2 = iInt * DeltaInt
Intsum = Intsum + (P1 * PSNew(iInt) + P2 * PSNew(iInt + 1)) * DeltaInt / 2
Next
IntFextS = 2 * Pi * Intsum
End Function

Public Function IntOmega(iLocation As Integer) As Double
' Integrate over 0...r Infinity interval using n panels " omega(r)"
Dim DeltaInt As Double ' Integration differential
Dim P1 As Double ' Numerical Integration point 1
Dim P2 As Double ' Numerical Integration point 2
Dim Pave As Double ' Average value of pressure
Dim Intsum As Double ' Numerical Integration
Dim ii As Integer ' an Integer Countor
Dim r As Double
Intsum = 0
If iLocation = 1 Then ' Case r=0
DeltaInt = drS
For ii = 1 To NPoint - 1
Intsum = Intsum + (PS(ii) + PS(ii + 1)) * DeltaInt / 2
Next
Intsum = Intsum + PS(NPoint) * DeltaInt
IntOmega = 2 * Intsum / Ep
Else ' Case r>0
r = (iLocation - 1) * drS ' calculating r
' first Summation, integral from 0 to r , r>t
For ii = 1 To iLocation - 1
Pave = (PS(ii) + PS(ii + 1)) / 2
P1 = (ii - 1) * drS / r
P2 = (ii) * drS / r
Intsum = Intsum + Pave * (LEI(P2) - LEI(P1))
```

```
Next
' second summation, integral from r to rInf , t> &=r
For ii = iLocation To NPoint - 1
Pave = (PS(ii) + PS(ii + 1)) / 2
P1 = (ii - 1) * drS / r
P2 = (ii) * drS / r
Intsum = Intsum + Pave * (P2 * EllipticE(1 / P2) - P1 * EllipticE(1 / P1))
Next
IntOmega = 4 * r * Intsum / Pi / Ep
End If
End Function

Public Function PStar(iP As Integer) As Double
'calculate the effective local microhardness based on the Hegazy's correlation for plastic model
'calculate the effective elastic hardness based on Mikic model
Dim dv As Double 'Equivalent Vickers's diameter
Dim LambdaMe As Double ' the lambda this routine is called for!
Dim ErfLam As Double
Dim HMin As Double ' Min. Limit for Hardness
Dim aContact As Double 'Microcontact spot radius (m)
LambdaMe = LambdaS(iP)
ErfLam = ERFC(LambdaMe)
If ModelFlag = 2 Then ' plastic
If ErfLam > 0 Then
aContact = (Sqr(8 / Pi) * Sigma / MeanSlope) * Exp((LambdaMe) ^2) * ErfLam
dv = 1000000# * Sqr(2 * Pi) * aContact 'a Mic. should be in Micrometer
Hard(iP) = C1 * dv ^C2 ' gives in GPa
Else
Hard(iP) = 0
End If
```

```
    Hard(iP) = Hard(iP) * 1000000000# ' Convert to (Pa)
    'Hard(iP) = C1 * 1000000000#
    PStar = Hard(iP) * ErfLam / 2
    Else ' elastic
    PStar = Ep * MeanSlope * ErfLam / 4 / Sqr(2)
    End If
    End Function
    Public Function aMic(iA As Integer) As Double
    'Calculate the contact spots radius
    aMic = (Sqr(2 * ModelFlag ^2 / Pi) * Sigma / MeanSlope) * Exp((LambdaS(iA)) ^2) *
ERFC(LambdaS(iA))
    End Function
    Private Sub Command3_Click()
    End
    End Sub

    Public Function ERFC(x As Double) As Double
    ' Calculate Efrc using numerical Integration
    Dim DeltaInt As Double ' Integration differential
    Dim P1 As Double ' Numerical Integration point 1
    Dim P2 As Double ' Numerical Integration point 2
    Dim Intsum As Double ' Numerical Integration
    Dim ii As Integer ' an Integer Countor
    Pi = 3.141592654
    If x < 1 Then
    n = 30
    ElseIf x > 1 And x < 2 Then
    n = 70
    ElseIf x > 2 And x < 4.2 Then
    n = 150
    Else
```

```
n = 1
End If
DeltaInt = x / n
Intsum = 0
For ii = 1 To n
P1 = (ii - 1) * DeltaInt
P2 = ii * DeltaInt
Intsum = Intsum + (Exp(-P1 ^2) + Exp(-P2 ^2)) * DeltaInt / 2
Next
If x > 4.2 Then
ERFC = 0
Else
ERFC = 1 - 2 * Intsum / Sqr(Pi)
End If
End Function

Public Sub ShowTrend()
' internal variables
Dim tt As String
Dim tj As String
Dim qj As String
Dim J As Integer
Dim q As Double
Dim I As Integer
Dim ii As String
I = Int(NPoint / 2)
J = Int(NPoint / 4)
Label2.Caption = PSNew(1) / pHertz0
Label3.Caption = PSNew(3) / pHertz0
Label4.Caption = PSNew(J) / pHertz0
Label5.Caption = PSNew(I) / pHertz0
```

```
Label6.Caption = PSNew(NPoint - 4) / pHertz0
Label15.Caption = Omega(1) / Sigma
Label16.Caption = Omega(3) / Sigma
Label17.Caption = Omega(J) / Sigma
Label18.Caption = Omega(I) / Sigma
Label19.Caption = Omega(NPoint - 4) / Sigma
'Label9.Caption = uR0S(Counter)
MsgBox "Ready to Go!", 0 + 48, ""
End Sub

Public Function LambdaS(iL As Integer) As Double
' calculate the non-dimensional separation with the new value of deformation "omega new"
Dim rS1 As Double
Dim uRr As Double ' Sphere profile at radial location
rS1 = (iL - 1) * drS
uRr = uR0 - rS1 ^2 / 2 / Rho
LambdaS = (Omega(iL) - uRr) / Sigma / Sqr(2)
'LambdaS = (uR0 + Omega(iL) + rS1 ^2 / 2 / Rho - Omega(1)) / Sigma / Sqr(2)
End Function

Public Sub Conv1()
Dim iconv As Integer
Dim IEMax As Integer
Dim PMax As Double
Dim dmax As Double
IEMax = 1
AEPS = Abs(PSNew(1) - PS(1))
For iconv = 2 To NPoint
dmax = Abs(PS(iconv) - PSNew(iconv))
If dmax > AEPS Then
IEMax = iconv
```

```
AEPS = dmax
End If
Next
PMax = PSNew(IEMax)
If PSNew(IEMax) < PS(IEMax) Then PMax = PS(IEMax)
AEPS = AEPS / PMax
Label25.Caption = IEMax
End Sub

Public Sub FirstLoop()
'First itteration loop calculating proper omega and pressure distribution
Dim Cont1 As Integer
Dim TOL As Double ' Tolerance of the first iteration loop
Dim iLoop1 As Integer
TOL = 0.001
Cont1 = 0
Do
If Cont1 > 0 Then ' if not the first iteration , update the pressure & deformation
For iLoop1 = 1 To NPoint + 1
PS(iLoop1) = UnderRFac * PSNew(iLoop1) + (1 - UnderRFac) * PS(iLoop1)
Next
End If
' Calculate omega(r) and new press. distribution
For iLoop1 = 1 To NPoint + 1
Omega(iLoop1) = IntOmega(iLoop1)
PSNew(iLoop1) = PStar(iLoop1)
Next
Conv1 ' calculates the Max. difference in press. distribution
Cont1 = Cont1 + 1
Label13.Caption = Cont1
Label14.Caption = AEPS
```

```
' ShowTrend
Loop Until (AEPS < TOL)
End Sub
Public Sub Results()
Dim I As Integer
Dim IaL As Integer ' Location of aL in the mesh
Dim rS1 As Double
Dim III As Integer
Dim Epsilon As Double ' epsilon sqrt(Ar/Aa)
Dim AveEps As Double ' Average epsilon in aL
Dim aMic As Double 'Local Contact spot size (m)
Dim AveaMic As Double 'average Contact spot size (m)
Dim ErfcLam As Double
Dim eta As Double ' Local density of contact spots (ns/Aa)
Dim Aveeta As Double ' Ave density of contact spots (ns/Aa)
Dim MacArea As Double ' Macrocontact area (m^2)
Dim aL As Double ' macro contact radius based on 99% of total load (m)
Dim nss As Double ' local no of micro contact spots, nss(r)
Dim Tnss As Double ' Total no of micro contact spots
Dim Intsum As Double ' summation
Dim AveHard As Double ' Average Microhardness (Pa)
Dim Rss As Double ' Local Non-dimensional micro resistance
Dim dRss As Double ' Non-dimensional element micro resistance
Dim RssT As Double ' Non-dimensional Micro resistance
Dim RLL As Double ' Non-dimensional macro resistance
Dim RLHz As Double ' Non-dimensional Hertz macro resistance
Dim Rj As Double ' Non-dimensional joint resistance
Dim hCs As Double ' Thermal Conductance for each element / by ks [1/m]
Dim RjhC As Double 'Non-dimensional Joint Thermal ressitance using Conductance method
Dim P1 As Double ' dummy
```

```
Dim P2 As Double ' dummy
Dim hc1 As Double ' dummy
Dim hc2 As Double ' dummy
Dim averageNum As Integer
Dim PressFac As Double ' the factor for macro area calculating
' calculate aL based on 1% of the max pressure
DeltaInt = drS
Intsum = 0
For I = 1 To NPoint - 1
P1 = (I - 1) * DeltaInt
P2 = PSNew(I) / PSNew(1)
If (P2 < 0.01) Then
IaL = I
Exit For
End If
Next
aL = P1
MacArea = Pi * aL ^2
III = IaL
If IaL = 0 Then
III = NPoint
aL = bLg
End If
If aH < bLg Then
If aL < aH Then aL = aH
End If
' calculating Macro thermal resistance
If aL > bLg Then
RLL = 0
Else
```

```
RLL = (1 - aL / bLg) ^(1.5) * (Rho / aL)
End If
If aH < bLg Then
RLHz = (1 - aH / bLg) ^(1.5) * (Rho / aH)
Else
RLHz = 0
End If
'output general parameters
Open "C:\Documents and Settings\majid\Thesis\ResultOut.txt" For Output As #2
Print #2, NPoint, aH, pHertz0, Rho, Ep, C1, C2, Fext, Sigma, aL, MacArea, MeanSlope, bLg, Hcont
AveaMic = 0 ' summation average aMic
Tnss = 0 ' summation total ns
AveEps = 0 'summation average epsilon
RssT = 0 ' summation of micro resiatnace
Aveeta = 0 ' summation average eta
AveHard = 0 ' summation average microhardness
averageNum = 0
' output local parameters
For I = 1 To NPoint
rS1 = (I - 1) * drS
ErfcLam = ERFC(LambdaS(I))
' calculate local epsilon
Epsilon = Sqr(ModelFlag * ErfcLam / 4)
If ErfcLam > 0 Then
' calculate local contact spot size
aMic = Sqr(2 * ModelFlag ^2 / Pi) * (Sigma / MeanSlope) * Exp((LambdaS(I)) ^2) * ErfcLam
' calculate local spot density
eta = (MeanSlope / Sigma) ^2 * Exp(-2 * LambdaS(I) ^2) / ErfcLam / 16
```

```
' calculate local number of spots
nss = eta * 2 * Pi * rS1 * drS
Else
eta = 0
nss = 0
aMic = 0
End If
If aMic = 0 Then
Rss = 100000000000#
Else
'calculating local non-dimensional micro thermal resistance
Rss = (1 - Epsilon) ^(1.5) * (Rho / aMic)
End If
dRss = nss / Rss ' reciprocal of the element resistance
'calculating average parameters
If I < III Then
averageNum = averageNum + 1
AveaMic = AveaMic + aMic
AveEps = AveEps + Epsilon
Aveeta = Aveeta + eta
Tnss = Tnss + nss
RssT = RssT + dRss
AveHard = Hard(I) + AveHard
End If
'RssT = RssT + dRss
If I > III Then
If rS1 < bLg Then RssT = RssT + dRss
End If
If Hard(I) = 0 Then
hCs = 0
```

```
    Else
    hCs = 1.25 * (MeanSlope / Sigma) * (PSNew(I) / Hard(I)) ^0.95
    End If
    Print #2, rS1, PSNew(I), Omega(I), LambdaS(I), Epsilon, aMic, eta, nss, Rss, Hard(I),
hCs
    Next
    AveaMic = AveaMic / averageNum
    AveEps = AveEps / averageNum
    Aveeta = Aveeta / averageNum
    AveHard = AveHard / averageNum
    If ModelFlag = 1 Then AveHard = Ep * MeanSlope / 2 / Sqr(2) ' elastic microhardness
    RssT = 1 / RssT
    Rj = RssT + RLL ' non-dimensional joint resistance
    If ModelFlag = 2 Then ' plastic model
    'calculating the total thermal conductance (non-dimensional)
    DeltaInt = drS
    Intsum = 0
    For I = 1 To NPoint
    P1 = (I - 1) * DeltaInt
    P2 = I * DeltaInt
    If Hard(I - 1) = 0 Then
    hc1 = 0
    Else
    hc1 = 1.25 * (MeanSlope / Sigma) * (PSNew(I - 1) / Hard(I - 1)) ^0.95
    End If
    If Hard(I) = 0 Then
    hc2 = 0
    Else
    hc2 = 1.25 * (MeanSlope / Sigma) * (PSNew(I) / Hard(I)) ^0.95
    End If
```

```
Intsum = Intsum + (P1 * hc1 + P2 * hc2) * DeltaInt / 2
Next
RjhC = 1 / (Intsum * Pi / Rho)
End If
'printing average values
Print #2, Tnss, AveaMic, AveEps, Aveeta, AveHard, RLL, RLHz, RssT, Rj, RjhC, PlasticIndex, Alpha
Close #2
End Sub

Public Function LEI(x As Double) As Double
' calculate needed function for r>t
If x < 0.999 Then
LEI = (x ^2 - 1) * EllipticK(x) + EllipticE(x)
Else
LEI = 1
End If
End Function

Public Sub FactorMethod()
Dim ErF(2) As Double ' Error of external force (–)
Dim Eu0(2) As Double ' Deflection point 1&2
Dim iLoopM As Integer
Dim ForceRatio As Double ' ratio of calculated to real external load
Dim Beta As Double ' Correction factor for UR0
mCounter = 1
uR0 = -2.64 * Sigma
'uR0 = 0.01 * uH
Do
For iLoopM = 1 To 2
If iLoopM = 2 Then 'if not the first point
```

```
If ErF(1) < 0 Then '———calculated force is bigger
Beta = (1.01151) ^(1 / 2 ^mCounter) ' old version
Else
Beta = (0.9995) ^(1 / 2 ^mCounter) ' old version
End If
uR0 = Beta * uR0
End If
FirstLoop
' calculate the Force due to the press. dist.
ForceRatio = Fext / IntFextS
ErF(iLoopM) = (Fext - IntFextS) / Fext
Eu0(iLoopM) = uR0
Next
Label7.Caption = mCounter
Label20.Caption = Eu0(2) / Sigma
Label9.Caption = Eu0(1) / Sigma
Label21.Caption = ErF(2)
Label11.Caption = ErF(1)
mCounter = mCounter + 1
uR0 = ((ErF(1) * Eu0(2) - ErF(2) * Eu0(1)) / (ErF(1) - ErF(2)))
FirstLoop
ForceError = (Fext - IntFextS) / Fext
Label23.Caption = ForceError
MsgBox "Ready to Go!", 0 + 48, ""
Loop Until (Abs(ForceError) < TOL1)
End Sub

Public Sub HalvingDistance()
' The Secant variables
Dim CCC As Double ' the coefficent to estimate the other bound of the solution
Dim u2 As Double
```

```
Dim eF0 As Double
Dim eF1 As Double
Dim eF2 As Double
mCounter = 1
uR0 = u0
FirstLoop
eF0 = (Fext - IntFextS) / Fext
If Abs(eF0) < TOL1 Then Exit Sub
uR0 = u1
FirstLoop
eF1 = (Fext - IntFextS) / Fext
If Abs(eF1) < TOL1 Then Exit Sub
Label9.Caption = u0 / Sigma
Label20.Caption = u1 / Sigma
Label11.Caption = eF0
Label21.Caption = eF1
Label7.Caption = mCounter
MsgBox "Ready to Go!", 0 + 48, ""
' Halving the distance method
Do
mCounter = mCounter + 1
u2 = u1 - eF1 * (u1 - u0) / (eF1 - eF0)
uR0 = u2
FirstLoop
eF2 = (Fext - IntFextS) / Fext
If Abs(eF2) < TOL1 Then Exit Do
Label23.Caption = eF2
If eF0 * eF2 < 0 Then
u1 = u2
eF1 = eF2
```

```
Else
u0 = u2
eF0 = eF2
End If
Label9.Caption = u0 / Sigma
Label20.Caption = u1 / Sigma
Label11.Caption = eF0
Label21.Caption = eF1
Label7.Caption = mCounter
MsgBox "Ready to Go!", 0 + 48, ""
Loop Until (Abs(eF2) < TOL1)
End Sub
```

Appendix D

Radiation Conductance

The following is an investigation to study the relative importance of the radiation heat transfer in thermal joint conductance in a vacuum. In order to perform this analysis, the relative magnitude of the radiation over conduction is calculated over an applicable joint temperature for a typical contact. The radiation heat transfer between two contacting bodies can be found from

$$Q_r = \sigma_{SB}\ A_a F_{12} \left(T_{j,1}^4 - T_{j,2}^4\right) \tag{D.1}$$

where $\sigma_{SB} = 5.67 \times 10^{-8}\ W/\left(m^2 K^4\right)$ and F_{12} are the Stefan-Boltzmann constant and the radiative parameter, respectively. Absolute joint temperatures $T_{j,1}$ and $T_{j,2}$ are found by extrapolating the temperature profiles in body 1 and 2, respectively. The radiative parameter is given by $F_{12} = 1/\epsilon_1 + 1/\epsilon_2 - 1$ where ϵ_1 and ϵ_2 are the emissivities of the contacting surfaces. Using the definition of the thermal conductance, $h_r = \Delta T/Q_r$, the radiative conductance can be calculated from [72]

$$h_r \equiv 4\sigma_{SB}\ F_{12}\ T_j^3 \tag{D.2}$$

where

$$\frac{T_{j,1}^4 - T_{j,2}^4}{T_{j,1} - T_{j,2}} \approx 4T_j^3$$

where $T_j = 2\left(T_{j,1} + T_{j,2}\right)$ is the mean joint temperature.

The microcontacts conductance for conforming rough joints is [8]

$$h_c = 1.25 k_s \left(\frac{m}{\sigma}\right) \left(\frac{P}{H_{mic}}\right)^{0.95} \tag{D.3}$$

Thus ratio of radiation conductance over the microcontact conductance is

$$\frac{h_r}{h_c} = \frac{4\sigma_{SB}\ F_{12} T_j^3}{1.25\ k_s\,(m/\sigma)\,(P/H_{mic})^{0.95}} \tag{D.4}$$

If we assume black body radiation across the gap, $\epsilon_1 = \epsilon_2 = 1$ gives $F_{12} = 1$; also we consider a relatively low contact pressure and low thermal conductivity with contact parameters as follows: $k_s = 20\ W/mK$, $\sigma = 1\ \mu m$, $m = 0.1$, and $P/H_{mic} = 10^{-4}$. These assumptions give the upper bound on the radiation conductance. Using these input parameters, the ratio of h_r/h_c can be calculated as a function of the mean joint temperature T_j. Table D.1 lists the ratio of h_r/h_c, for an upper bound of radiative conductance, over a wide range of joint temperatures.

Table D.1: Relative importance of radiative conductance as function of joint temperature, upper bound

T_j	h_r/h_c
K	$(-)$
300	0.015
400	0.037
500	0.072
550	0.095
600	0.124
650	0.157
700	0.196

If a typical rough interface is considered, with $\epsilon_1 = \epsilon_2 = 0.8$, $k_s = 20\ W/mK$, $\sigma = 1\ \mu m$, $m = 0.1$, $300 \leq T_j \leq 400$ and $P/H_{mic} = 5 \times 10^{-4}$. The ratio of h_r/h_c for the range of interest of the joint temperature T_j will be 0.005 and 0.012, respectively. It means, the relative magnitude of the radiative heat transfer to the microcontacts conduction is less than 1.2 percent for the range of interest and can be neglected. As shown in Table D.1, the radiation conductance becomes relatively important when the interface is formed by two very rough, very hard low-conductivity solids under very light contact pressure at very high joint temperature. Therefore, for many practical applications, the radiative conductance can be neglected.